NORTHWESTERN UNIVERSITY

Experimental and Computational Study of Surfaces, Interfaces and Thin Films

A DISSERTATION

SUBMITTED TO THE GRADUATE SCHOOL

IN PARTIAL FULFILLMENT OF THE REQUIREMENTS

for the degree

DOCTOR OF PHILOSOPHY

Field of Materials Science and Engineering

By

Erman Bengu

EVANSTON, ILLINOIS

June 2000

UMI Number: 9974248

Bell & Howell Information and Learning Company
300 North Zeeb Road
P.O. Box 1346
Ann Arbor, MI 48106-1346

ABSTRACT

Experimental and Computational Study of Surfaces, Interfaces, and Thin Films

Erman Bengu

The trend toward synthesizing structures at ever decreasing sizes in nearly every field of industry is leading to the realization of nanomachines. This would require better techniques for the synthesis and characterization of novel materials at the atomic level. Another challenge is to develop computational methods capable of processing data from characterization methods at higher speeds and accuracy.

A new ion-beam assisted deposition chamber has been designed, built, and attached to an existing in situ characterization and analysis system. This system is used to investigate cubic boron nitride thin film growth and examine the chemical and structural evolution of the films at early stages of nucleation. The results from these experiments indicated the presence of transient nanostructures at the conditions promoting the nucleation of cubic boron nitride. Some of these structures are identified as single-wall boron nitride nanotubes and multi-walled nested boron nitride fullerenes (onions). In addition, the growth conditions for these novel two-dimensional phases of boron nitride has been identified, and the atomic structures were investigated using high-resolution electron microscopy and molecular modeling.

A new computational method for the analysis of x-ray reflectivity has been developed based on phase restoration concepts. This new model-independent method extracts the density profiles across interfaces by restoring the missing phase information. Several cases using simulated and experimental data have been analyzed. The results from these test cases were very encouraging for the widespread application of this technique.

Finally, high-resolution electron microscope images of the Si (111)-(7x7) surface in the plan-view geometry have been analyzed. A numerical technique is developed allowing for the separation of the overlap of the top and bottom surfaces. The resultant images show all of the atoms in the top three layers, including the dimers in the third layer.

Approved by

Professor Laurence D. Marks (Thesis advisor)

Department of Materials Science and Engineering

Robert R. McCormick School of Engineering and Applied Science

Northwestern University, Evanston, IL 60208

To my daughter, my wife, my family whom I owe so much.

ACKNOWLEDGEMENTS

First, I would like to thank my advisor, Professor Laurence D. Marks, for introducing me to *mare clausum* of science and for allowing me to swim freely. I am also indebted to Chris Collazo-Davila and Dan Grozea for their sincere friendship, support, and patience (especially when things go wrong and I become the *enfant terrible* of the lab). Without you and your sense of humor, this would have been an awfully prosaic and boring journey. By the way, thank you very much for taking time to teach me the intricacies of SPEAR and UHV microscope.

I would like to thank my classmate Mike Carmody for being such a good sport and sharing some of the pain and joy of these long years. I would like to acknowledge the friendship of Murat Guruz, Ian Widlow, Monica Salud, Natasha Erdman, Chris Own, and Arun Subramanian. Finally, thanks to everybody who helped me during the course of this work in any way, shape, or form.

This work was funded by the Air Force Office of Scientific Research on grant number F49620-94-1-0164.

LIST OF ABREVIATIONS

ACF	Auto-Correlation Factor
AES	Auger Electron Spectroscopy
AFM	Atomic Force Microscopy
BN	Boron Nitride
c-BN	Cubic Boron Nitride
CTF	Contrast Transfer Function
DAS	Dimer Adatom Stacking fault (model)
DM	Direct Methods
ECR	Electron Cyclotron Resonance
FOM	Figure of Merit
GMR	Giant Magneto-Resistance
h-BN	Hexagonal Boron Nitride
HREM	High Resolution Electron Microscopy
ISS	Ion Scattering Spectroscopy
LB films	Langmuir-Blodgett films
LEED	Low Energy Electron Diffraction
LEEM	Low Energy Electron Microscopy
ME	Maximum Entropy
PEELS	Parallel Electron Energy Loss Spectroscopy
PFA	Amphiphile Perfluorododecyl Aspartate
POCS	Projection Onto Convex Sets
REM	Reflection Electron Microscopy
RHEED	Reflection High Energy Electron Diffraction
r-BN	Rhombohedral-BN
RT	Room Temperature
SESM	Scanning Electron Surface Microscopy
SINDAD	Stabilizing Ion and Neutral Beam Assisted Deposition System
SLD	Scattering Line Density
SK	Stranski-Krastanov (growth mode)
SPEAR	Sample Preparation Evaluation Analysis Reaction (chamber)
STEM	Scanning Transmission Electron Microscopy
STM	Scanning Tunneling Microscopy
t-BN	Turbostratic Boron Nitride
TED	Transmission Electron Diffraction
TEM	Transmission Electron Microscopy
UHV	Ultrahigh Vacuum

XPS	X-ray Photoelectron Spectroscopy
XRD	X-ray Diffraction
XRR	X-ray Reflectivity
XTEM	Cross-sectional Transmission Electron Microscope
w-BN	Wurtzitic Boron Nitride

TABLE OF CONTENTS

FIGURES

TABLES

CHAPTER 1: INTRODUCTION

1.1 Why Is It Interesting to Study Thin Films and Surfaces?

For billions of years, nature was able to control processes and build *things* at an atomic scale in cells using DNA, RNA, enzymes, and proteins. Throughout the history of mankind, scientists have struggled to understand, control, and eventually mimic these feats of nature. During the last two decades, the electronics industry fueled a significant amount of research on building features and controlling processes on surfaces (10^{15}-10^{16} atoms/cm^2) at ever decreasing dimensions. However, we are still trailing the nanomachines of nature in size, precision, and quality.

Ultimately, artificial self-replicating nanomachines will be a reality, since the fundamental scientific building blocks are already nearing realization. These nanomachines or robots should have programmable brains (CPU) and memory (data storage), and should be equipped with nanoscopic manipulator arms (nano-features) that are capable of managing individual atoms. However, current challenges are for the *semiconductor industry* to manufacture microprocessors, the *computer hardware industry* to manufacture storage facilities, and *researchers working on nanotubes* to develop mechanical appendages that are small enough to fit in an enclosure not larger than a cubic micron. The major portion of the work presented in this thesis is a compilation of case studies in these areas, which could eventually lead the way to such accomplishments.

The push for a smaller lateral feature size in the semiconductor industry has been a significant motivator for studies investigating atomic scale phenomena, especially on

surfaces. A lesser-known field, the hard disk drive (HDD) industry, is also another important contributor. Hard disk drives employ a thin protective layer with good tribological properties (i.e. low friction coefficient and high hardness) on the magnetic media. This protective overcoat prevents the wear that occurs when read/write heads contact the magnetic media during operation. It is estimated that protective overcoat thickness for future HDD applications will be less than five nm, approximately several hundred atoms across (Chung and Bhatia 1998).

Protective thin films find practical applications in nearly every field of industry. Corrosion resistant thin films have major applications in jet engines; hard and wear-resistant protective thin films are used for cutting tools; thin diffusion barriers are used in composite materials and in electronics industry. The impetus behind studies on ultrahard thin films has both scientific and technological aspects. Synthesis of materials with hardness close or even higher than that of diamond has been a long-standing scientific curiosity and motivated research on the origins hardness at atomic scale (Lui and Cohen 1989). Moreover, technological aspects of ultrahard films helped initiate the introduction and adaptation of laboratory scale processes, such as ultrahigh vacuum (UHV) ion-beam deposition techniques (Brown 1998), to production line.

Despite the progress in ultrahard coatings field there are still many areas that need further study. Some challenging issues are the development of better deposition and characterization techniques and synthesis of *intrinsic* ultrahard coatings (Veprek 1999). One particular issue is thin film deposition of cubic phase of boron nitride (c-BN). In this

thesis, nucleation of c-BN thin films under ion-beam irradiation is investigated. In addition, *in situ* processing concepts has been applied to the deposition and characterization of the ultrahard films.

For a long time researchers have been aware of the need for *in situ* characterization and processing of thin films and surfaces (Pashley et al.1964). However, most of the essential technical advancements arrived nearly two decades later. *In situ* studies on the initial stages of film growth on oxide, semiconductor, and metal surfaces followed the introduction of UHV transmission electron microscopy (TEM), one of the best known *in situ* techniques (Yagi et al. 1982; 1985). The progress in the instrumentation led to an increased interest in other surface related phenomena such as surface reconstructions and catalysis. As described in Chapter 4 of this thesis, data from *in situ* electron microscopy can be used to solve notoriously difficult problems such as the atomic structure of the Si (111) 7×7 reconstruction (Zangwill 1992).

In this thesis, a unique ion-beam assisted deposition unit was designed and built for an existing special *in situ* UHV surface analysis system coupled with an UHV-TEM. The details about the experimental equipment used in this study are given in section 1.2. This deposition unit was used for the investigation of the mechanisms responsible for the nucleation and growth of cubic boron nitride on various substrates, which is described in Chapter 3. In addition, the same unit was used for the synthesis and characterization of single-walled BN nanotubes. Nanotubes are ideal candidates for appendages for nanomachines (Smalley et al. 1997), among other potential applications. Finally,

computational treatment of surface analysis data is also covered in various forms; for instance, analysis of relaxed surface structures on silicon using images from high-resolution transmission electron microscopy (HRTEM) is addressed in Chapter 4. A new method for the numerical treatment of x-ray reflectivity is also presented in Chapter 4.

1.2 Instrumentation and Experimental Details

A unique UHV surface analysis system (SPEAR) at Northwestern University, and an ion-beam assisted deposition unit (SINBAD) attached to SPEAR has been used for nearly all of the research involved with the BN thin films. A mobile magnetron and ion-beam epitaxy system (MIBE) attached to SPEAR is also worth mention. For most of the computationally involved studies described in this dissertation, a number of HP 9000 Class UNIX workstations at the computer labs of Prof. L.D. Marks's group has been employed. The following sections will give a detailed description of the SPEAR and SINBAD systems. Also included is a brief description of the computer facilities.

1.2.1 SPEAR

SPEAR is a multi-chamber, UHV surface analysis system. The acronym SPEAR stands for Sample Preparation Evaluation Analysis and Reaction System (Collazo-Davila, Landree, Grozea et al. 1995). A schematic layout of SPEAR, SINBAD, and MIBE (top-view) is shown in Figure 1.2.1, and photographs are given in Figure 1.2.2a and b. SPEAR was designed to replace the older and limited UHV-surface science chamber

(SSC) (Dunn, Zhang and Marks 1991; Bonevich and Marks 1992) attached to a Hitachi UHV H-9000 microscope (Marks et al.1988; 1991).

The major target in designing SPEAR was to achieve a simple and effective way to marry the capabilities of a high-resolution TEM with a UHV surface characterization and modification (film deposition) system. This goal was achieved by the use of separate UHV chambers for analysis and other units linked to each other and the UHV-TEM through a central chamber that ensures transfer of samples from one unit to another. Thus, the SPEAR system consists of four separate chambers, as shown in Figure 1.2.2a.

Samples to SPEAR system are introduced from a load-lock chamber that can hold five samples at a time, and this is achieved without breaking the vacuum in any other chamber. The central component of SPEAR is the transfer chamber equipped with a carrier assembly that can shuttle samples between different units. A separate storage module in the transfer chamber can hold up to eight samples and four microscope cartridges. At any time, one can transfer a sample through the transfer chamber to any part of SPEAR including the UHV H-9000 microscope or SINBAD.

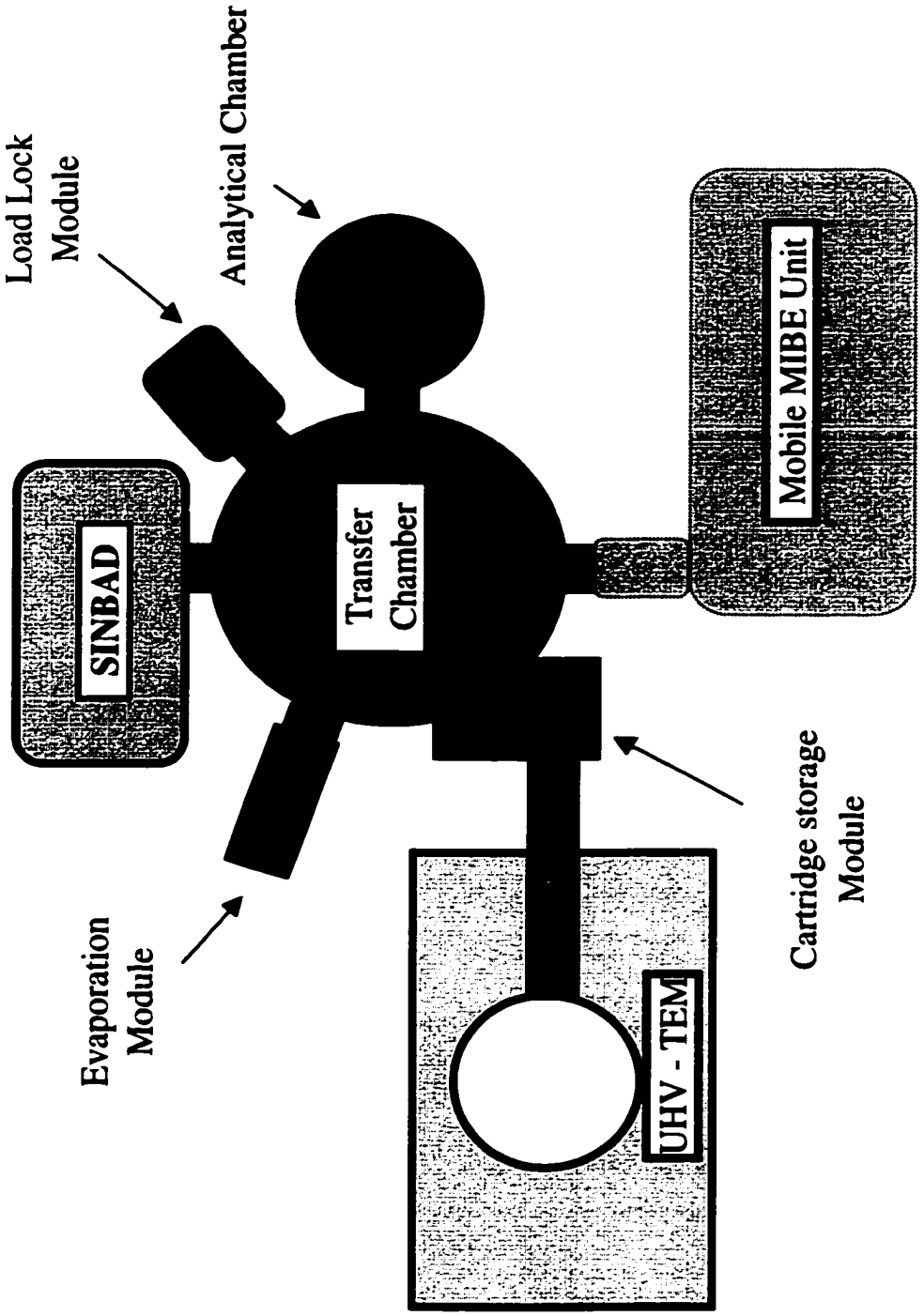

Figure 1.2.1 **Schematic diagram of the SPEAR surface analysis system viewed from the top.**

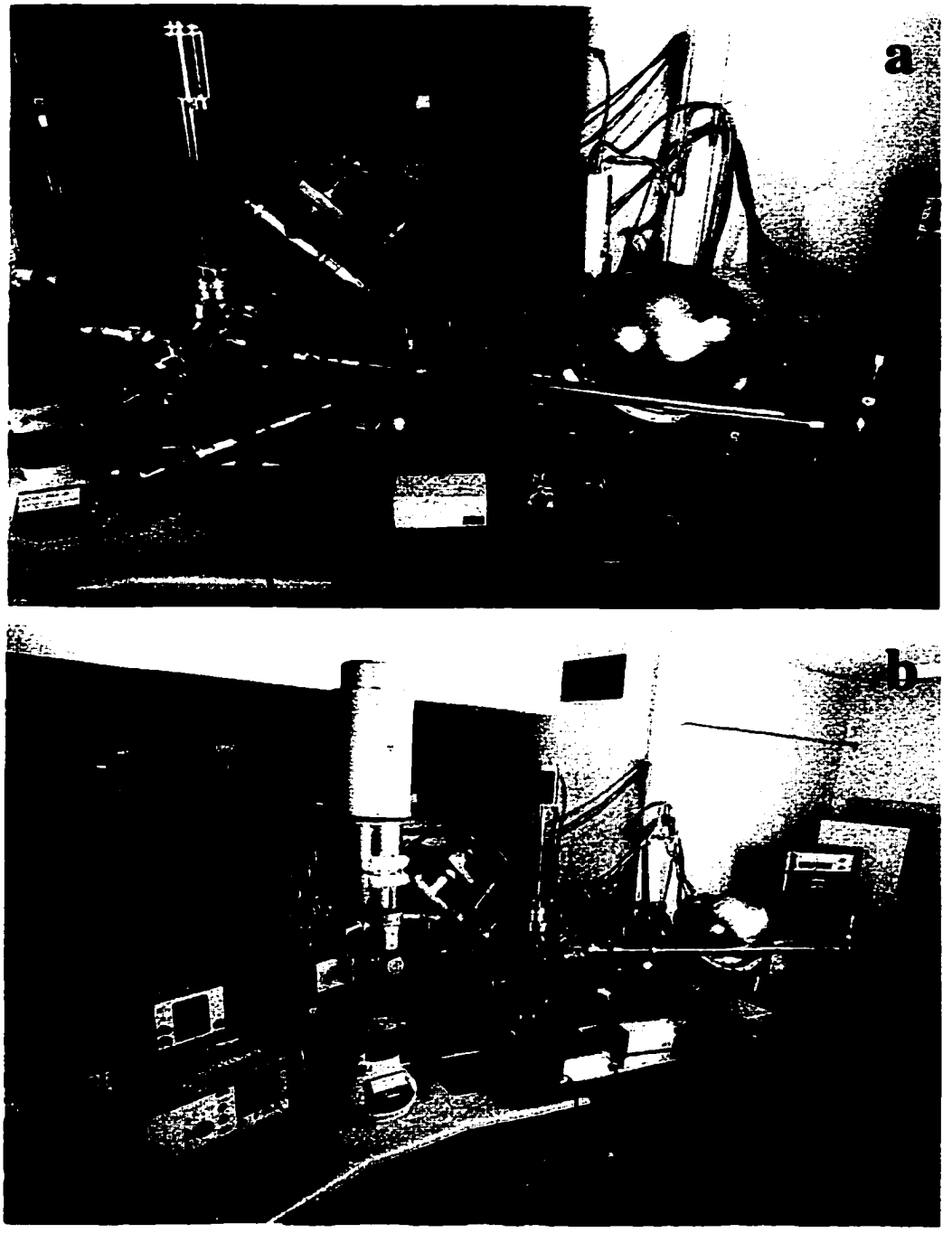

Figure 1.2.2 **a) and b) Photographs of the SPEAR and SINBAD systems from two different perspectives.**

In addition, a 4.5-inch four-way cross, modified to be an evaporation station, has been added to the transfer chamber with five different metal boats that are mostly used in semiconductor/metal interface studies.

The analytical chamber is capable of carrying out both sample preparation and surface sensitive chemical analysis. For sample preparation, the analytical chamber houses a PHI 6050 duoplasmatron microbeam ion-gun for ion-beam milling/cleaning, a 10 keV electron gun (Kimball Physics, LaB_6) for direct beam annealing, and a multi-purpose sample manipulation stage capable of 360° of rotational freedom, d.c. biasing, resistive heating, and liquid nitrogen cooling. Chemical characterization tools are a Perkin Elmer 04-548 dual anode x-ray tube (Mg and Al sources) with a PHI 10-360 spherical capacitance electron energy analyzer (SCA) operated either for acquisition of Auger electron spectra (AES) or X-ray photoelectron spectra (XPS) from the surface of samples. AES data is available using a FEI single lens field-emission scanning electron gun. Scanning electron microscopy (SEM) images are acquired from the surfaces by a secondary electron collector (Channeltron detector) using the FEI single lens field-emission scanning electron gun or the ion gun. Also available are SEM images of the surfaces while cleaning using a duoplasmatron microbeam ion-gun (probe size ~ 5μm).

1.2.2 SINBAD

SINBAD is a UHV ion-beam assisted deposition chamber attached to SPEAR for the investigation of in-situ processing and characterization of ultrahard thin films. SINBAD stands for Stabilizing Ion and Neutral Beam Assisted Deposition (Bengu,

Collazo-Davilla, Grozea et al. 1998). The author was responsible for designing and building SINBAD, Chris Collazo-Davila assisted during the final assembly of the chamber. The main building block of SINBAD is the MBE chamber on the SPEAR system which had two effusion cells configured for thin film deposition of GaAs. Figure 1.2.3a and b are schematic representations of the MBE and SINBAD chambers, respectively. The main chamber for MBE unit was redesigned and fitted with a new flange capable of housing a variety of equipment. Figure 1.2.4 shows schematical drawings of the new flange design. This flange contained enough space to house the deposition tools, such as the ion-beam source and the electron-beam source. It also had several view-ports that served different purposes; a pyrometer attached to one of the view ports is used to monitor the temperature of substrate. Another is used for visual observation of the process during deposition.

SINBAD is equipped with a single position 4kW electron-beam evaporator (Thermionics Inc., Hayward, CA), a 4 keV ion-gun (Perkin-Elmer Model 04-300, Eden Prairie, MN), and a compact electron cyclotron resonance (ECR) plasma source (AX-4300 Astex Inc., Boston, MA). Relative positions of the deposition equipment and the target are depicted at Figure 1.2.4. Both the ECR and the 4keV ion-gun can be utilized as ion-sources for purposes other than deposition. A differential pumping assembly with a 50 l/s turbo molecular pump is also set up for the 4keV ion-gun.

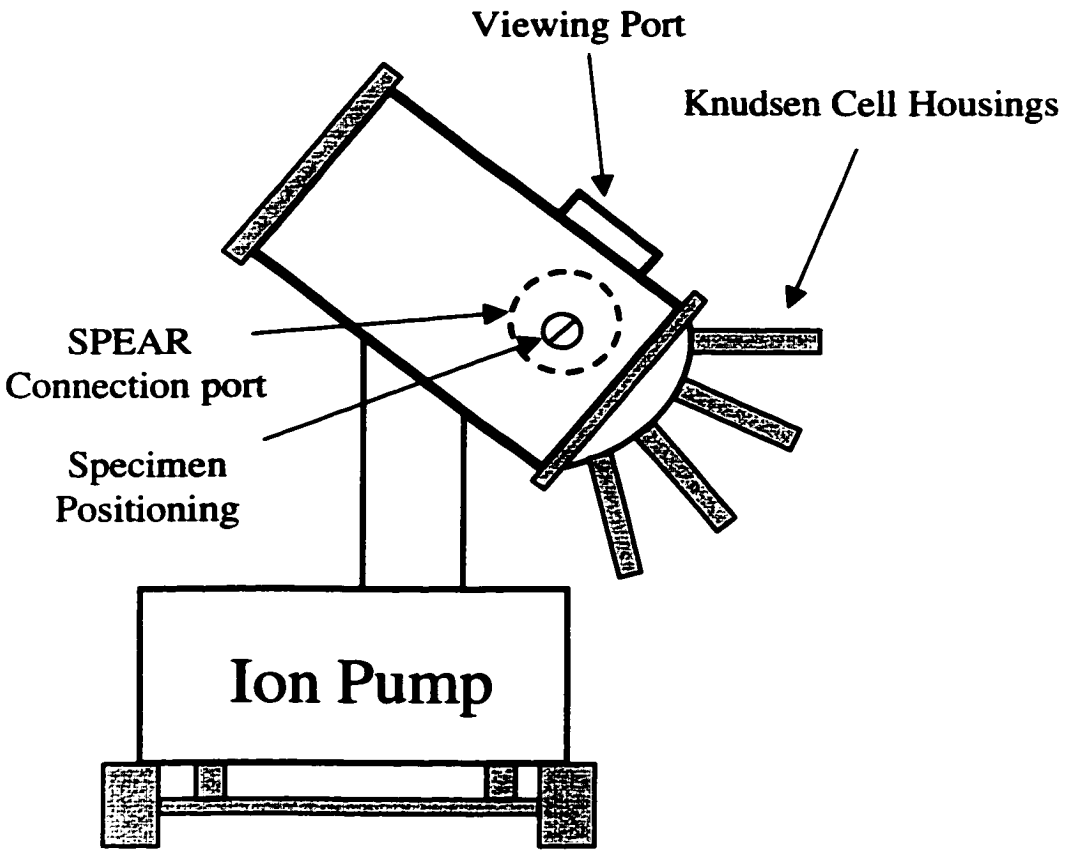

Figure 1.2.3 **a) An illustration of the MBE chamber originally installed with the SPEAR system, before modifications.**

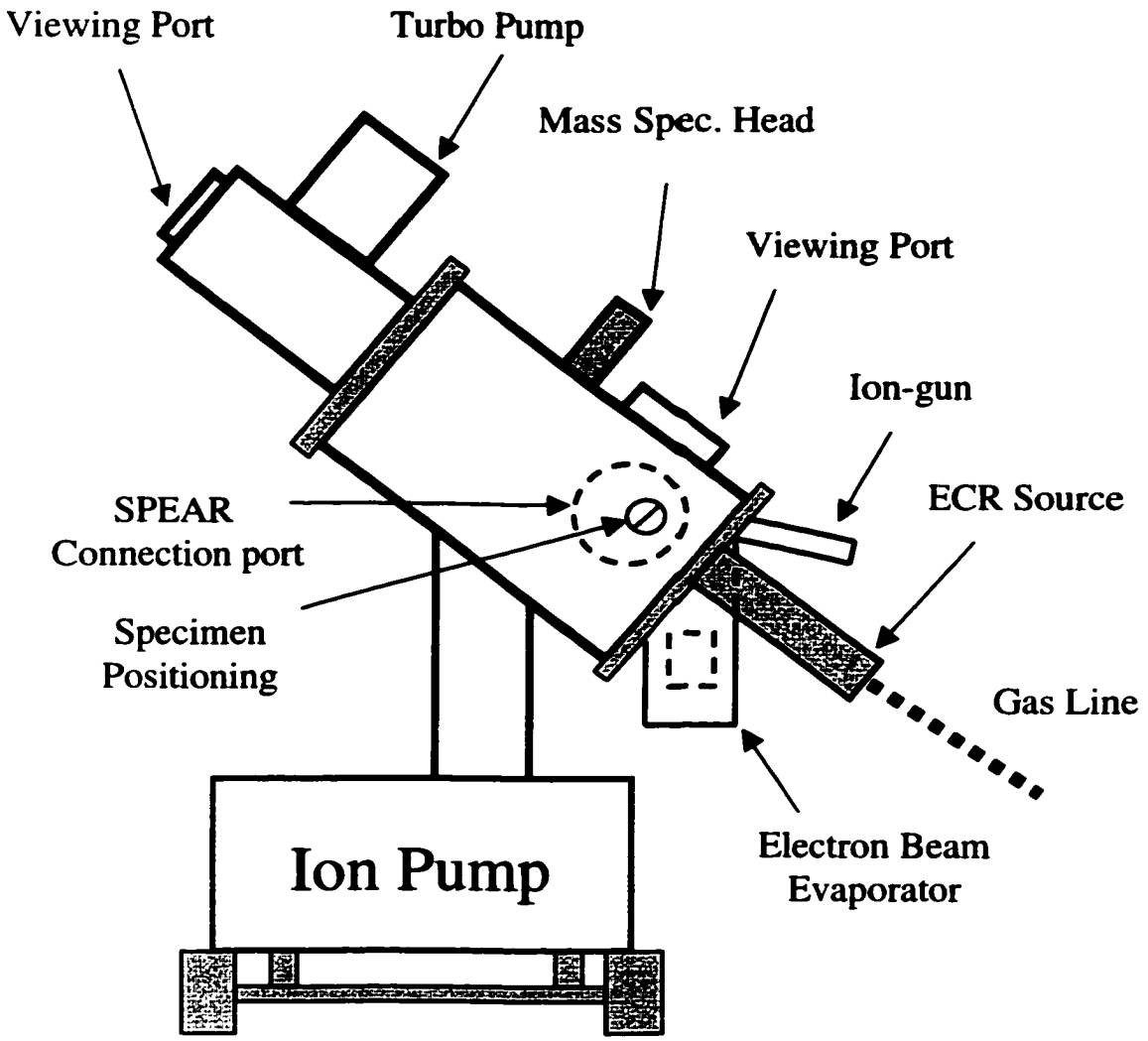

Figure 1.2.3 b) Illustration describing the SINBAD system after the modifications.

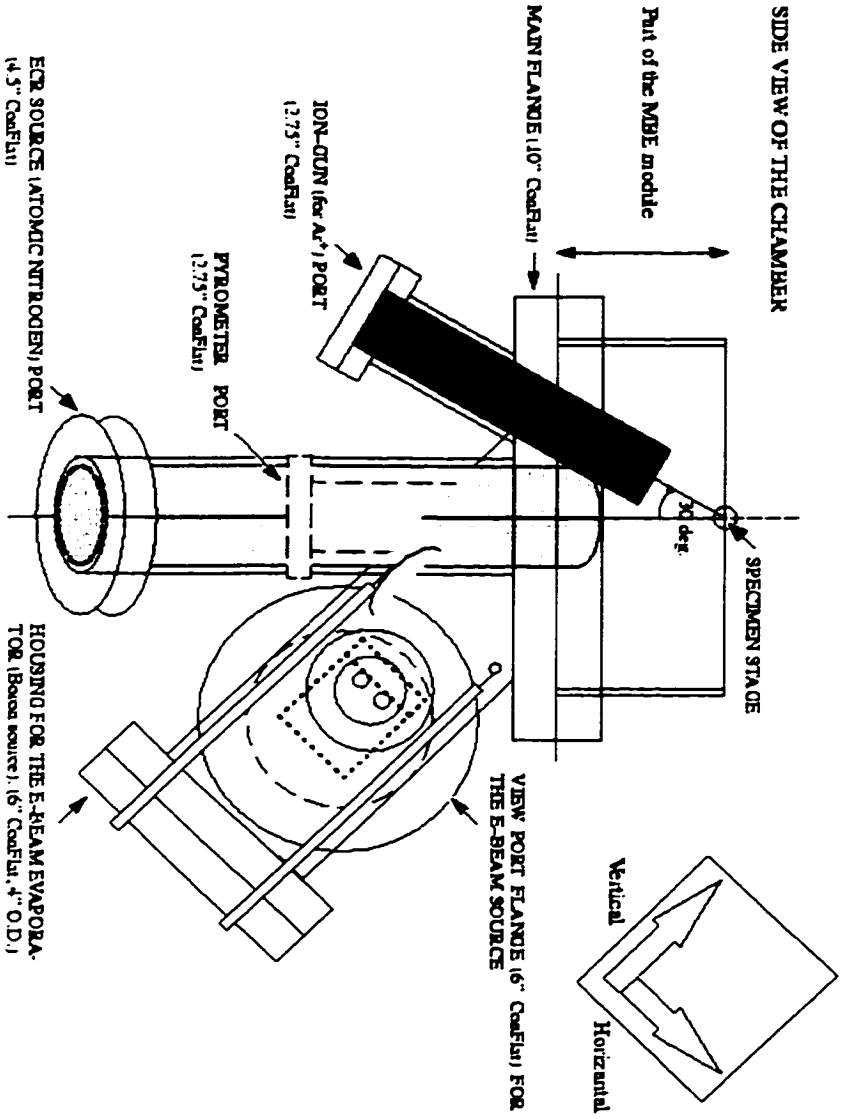

Figure 1.2.4 **Drawing of the flange designed to house the ECR, ion-gun, and the e-beam source for the SINBAD. View port for the pyrometer is behind the ECR port so it is shown with dashed lines.**

The new unit is also fitted with a 280 l/s turbo-molecular pump (Varian Vacuum, Lexington, MA), supplementary to the existing 220 l/s ion pump (Physical Electronics, Eden Prairie, MN). The base pressure of the system after a bake is approximately 10^{-10} torr. The sample manipulation stage was modified for d.c. biasing of the sample as well as resistive heating during deposition. Like the SPEAR system, SINBAD is designed to transfer, handle, and deposit on thin 3mm TEM ready samples.

1.2.3 Computer Facilities

Chapter 4 of this thesis describes the two computationally and numerically intensive studies. A new model-independent technique for the analysis of x-ray reflectivity and a numerical method for extraction of high-resolution electron microscopy (HREM) images of Si (111) surface are explained. For these studies, Hewlett-Packard HP 9000 series 700 workstations running on HP-UX 9.0X and 10.20 operating systems were used. Most of the HREM images presented in this thesis have been enhanced in terms of image contrast and brightness using an image manipulation language called SEMPER. SEMPER is comparable to another software package, MATLAB, although SEMPER is arguably much faster. Other computer programs were written using the FORTRAN computer language on the UNIX workstations.

1.3 Substrate Preparation

For the deposition of BN films, silicon, copper, and tungsten substrates were used. The surface structure and chemistry of these were closely controlled. For the irradiation

studies, TEM samples were prepared from h-BN and c-BN. The standard TEM sample geometry applies to substrates for deposition. For instance, all samples have to be in the form of a 3 mm diameter disc. Moreover, they must have regions that are only a few hundred angstroms thick in order to be electron transparent (crucial for TEM investigation).

TEM bulk sample preparation for metals and silicon vary. Silicon samples (3 mm discs) were cut from a commercial Si wafer (~500 μm thick) using an ultrasonic cutter. After thinning these discs to 200 μm using standard 600 grid SiC sandpaper, they are dimpled at the center to a thickness of 20 μm to 30 μm. A VG1000 dimpler with a force of 10 to 20 g. and a grinding wheel speed of 20 rpm to 40 rpm was used. The samples were polished using the same dimpling equipment with first a 1 μm diamond paste, and then a 0.1 μm syton colloidal suspension. Finally, the sample preparation is concluded by a chemical etch using a nitric (HNO_3) and hydrofluoric (HF) acid solution (9:1). The etching reaction was stopped as soon as a hole was observed forming at the center of the 3 mm disc.

Metal bulk TEM sample preparation follows a similar route without the dimpling of the 3 mm discs. Single crystal Cu samples (110 and 100 orientations) were obtained from Prof. Julia Wertmann. They were cut into 5 mm × 20 mm strips that were then thinned to 150 to 200 μm. Following a vacuum annealing at around 500C to remove defects generated during cold working, 3 mm discs were punched out from these foils. Final treatment of Cu samples involved jet polishing these discs using 67%methanol +

33%nitric acid solution at –30C until a hole formed at the center. Finally, a very similar route for W was also followed, but a solution made by diluting 5 to 7 grams of sodium hydroxide in 100ml of water was used for jet polishing. Polycrystalline W was bought from Alfa Cesar, Inc in the form of a thin slab (100 mm × 100 mm, 1 mm thick). A plasma-arc cutter was used to cut 3 mm tungsten discs which were thinned to 150 μm for subsequent jet-polishing.

Explosively synthesized cubic-BN powder was acquired from Dr. Vasant Joshi with an average particle size of 5 μm (Joshi 1999). In addition, polycrystalline h-BN (99.5% purity) in the form of a sintered rod (150 mm long, 10 mm diameter) was obtained from Advanced Ceramics Corp. Flakes of h-BN and c-BN (separately) mixed with copious amounts of methanol were placed in to a glass mortar. The BN particles in the mixture were crushed by hand until slurry was formed. A drop of the slurry was then left to dry on a 1000-mesh gold or molybdenum grid. After the methanol evaporated, loosely attached microscopic BN pieces were left on the grid.

Regular TEM samples are very fragile, and they cannot be handled without danger of breaking or permanent damage in the SPEAR system without an effective and secure way of treatment. This is accomplished by mounting the samples in a specially designed ring made out of molybdenum. A schematic drawing and a picture of these rings is given in Figure 1.2.5a and b. The Mo ring acts as a protective shell around the TEM sample and allows *rough* handling of these inside the SPEAR and the

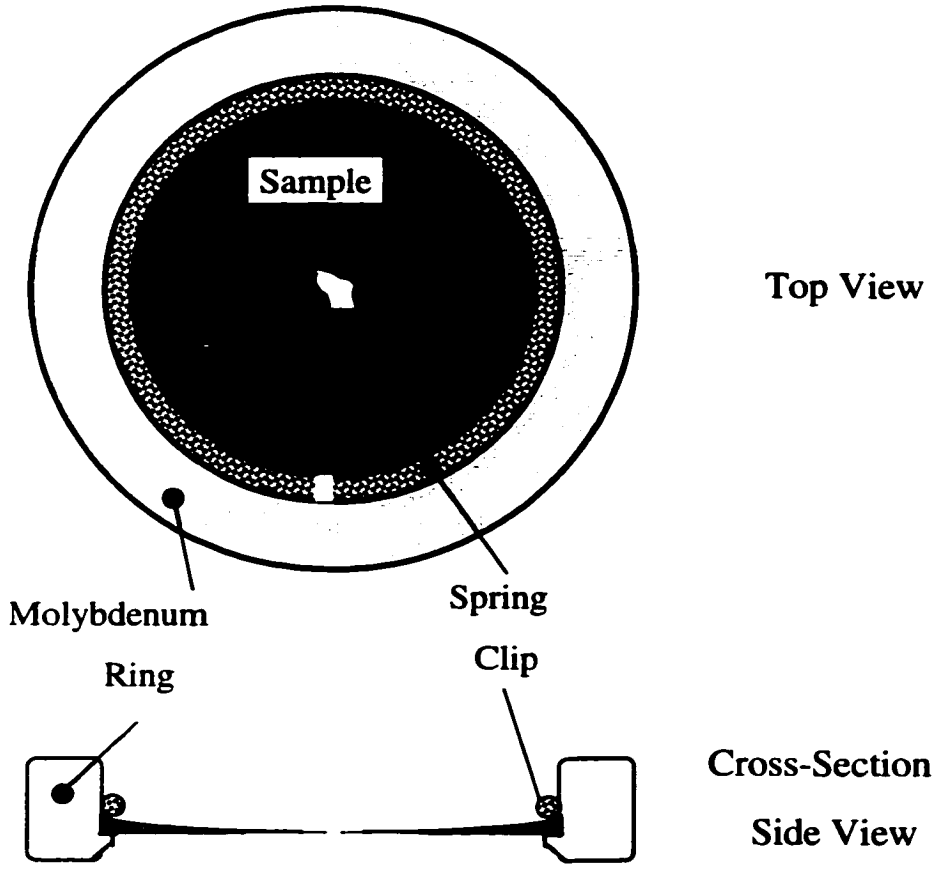

Figure 1.2.5 a) Drawing of the molybdenum ring for the manipulation of samples in the SPEAR system. The spring clip can be either tungsten or tantalum.

Figure 1.2.5 b) An image of the Mo ring with a sample. (After Collazo-Davila et al. 1995)

UHV-TEM. The Mo ring also allows resistive heating of the TEM samples by passing a current directly through the molybdenum. Stability of the TEM samples in Mo rings is arranged by sandwiching the sample between the brim of the Mo ring and an o-ring spring clip made out of tantalum or tungsten wire. In this arrangement, stability of the sample is guaranteed even though, the sample is rotated 90 and/or 180 degrees.

The samples in Mo rings are introduced to the SPEAR system through the load-lock chamber after a 24-hour bake. However, the sample is not usable, as the surface of the sample is actually covered by chemical impurities primarily due to ex-situ chemical processing. The typical surface chemistry of a Si (001) sample freshly introduced to SPEAR analyzed by XPS is given in Figure 1.2.6. This impurity layer was removed by cycles of ion milling (sputtering) and electron-beam annealing inside the analytical chamber. Figure 1.2.6 displays the surface chemistry at different sequences of sample preparation investigated using XPS. Before and during the cleaning process, the chemical content of the surface was monitored using XPS. Chemical analysis is limited by the sensitivity limit of the XPS, which is generally 1% of a monolayer. After the chemical characterization, the sample is transferred to UHV- H9000 microscope for structural characterization of the surface. Details about the structural characterization of the TEM samples will be given in detail in Chapter 3 in a discussion of BN deposition on these surfaces.

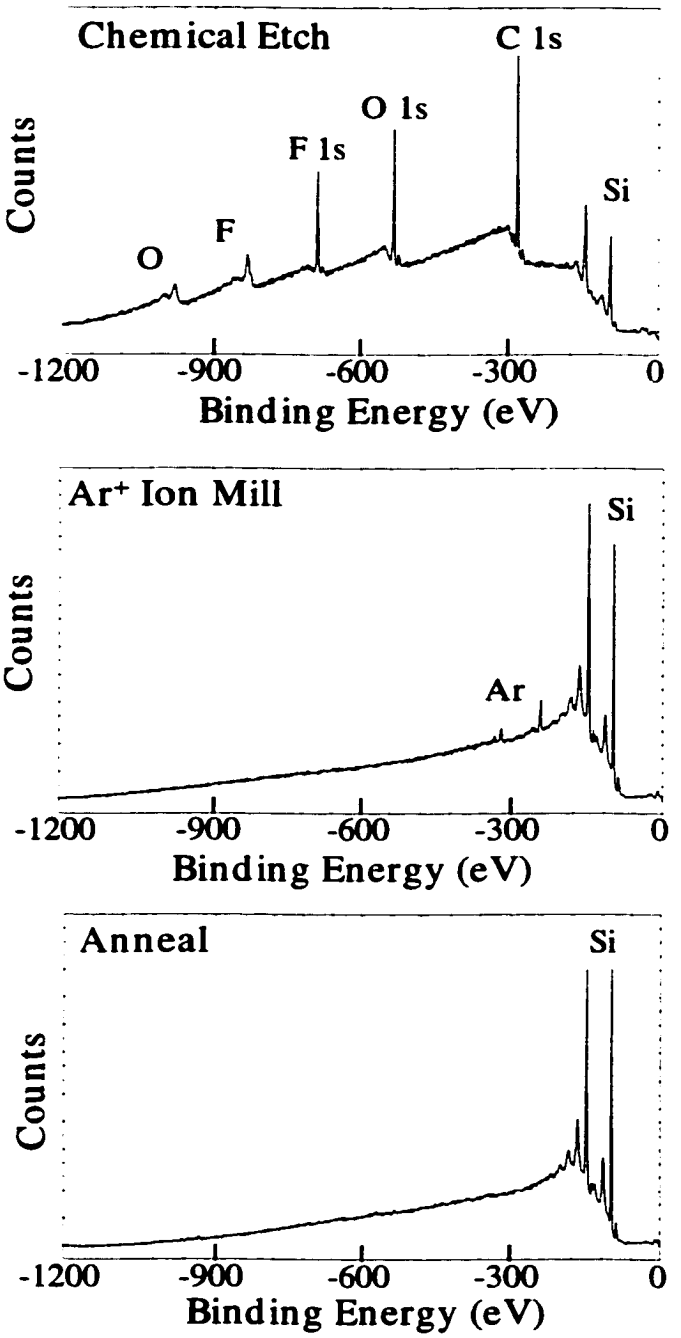

Figure 1.2.6 **XPS spectra from various stages of sample preparation of Si (100) (Courtesy of Dan Grozea).**

CHAPTER 2: IN SITU GROWTH AND ANALYSIS OF ULTRAHARD BN THIN FILMS

2.1 Boron Nitride

Diamond is the hardest and the most thermally conductive of all substances. Cubic-boron nitride (c-BN) is second to diamond in hardness and somewhat less thermally conductive, but it has a much less reactive character. Charcoal, graphite, and diamond are all allotropes of carbon, and are found readily in nature in varying abundance. Hexagonal-boron nitride (h-BN) and c-BN are also allomorphs, analogous to diamond and graphite, but both are synthetic compounds.

Several researchers announced a successful process for synthesizing diamond from graphite using a high temperature and pressure technique (Bundy, Hall, and Wentorf 1955). C-BN was first discovered in 1957 by Wentorf, but the first direct conversion from h-BN to c-BN using a similar high temperature and pressure method was performed by Bundy and Wentorf (1963). Although similar to diamond in terms of crystal structure, the c-BN unit cell is slightly larger, 3.615 Å vs. 3.56 Å for diamond.

First experiments regarding the direct conversion of h-BN to the cubic phase took place in the high pressure, temperature region of the phase diagram of BN (Bundy and Wentorf 1963). The low pressure, temperature region of the BN phase diagram has not been investigated due to remarkable fit of the existing data to the so-called "Berman-Simon" equilibrium boundary. This boundary has been determined for the graphite-diamond equilibrium using thermodynamic considerations. According to the "Berman-

Simon" equilibrium boundary, at standard temperature and pressure, h-BN is the stable phase, whereas c-BN is the metastable phase. However, Solozhenko in 1993 challenged the position of the h-BN/c-BN equilibrium line by proposing a new phase diagram where c-BN is the thermodynamically stable phase at ambient conditions. It is generally agreed that c-BN is the stable structure whereas h-BN becomes stable at temperatures around 900 C - 1500 C (Albe 1997; Bohr et al. 1995; Kuznetsov et al. 1997; Kern et al. 1999; Sachdev et al. 1997; Solozhenko et al. 1999).

BN has two more allomorphs: rhombohedral-BN (r-BN) and wurtzitic-BN (w-BN). Figure 2.1.1 displays the four basic crystal structures of BN. H-BN and r-BN share a similar ordered stacking sequence of sp^2-bonded sheets made up of six-membered rings where each boron atom is bonded to (in plane) three nitrogen atoms, and vice versa. On the other hand, in c-BN and w-BN each atom makes four bonds and forms sp^3-bonded six-membered ring networks analogous to diamond. Another form of sp^2 BN, turbostratic-BN (t-BN) has a stacking sequence in which each sheet is randomly rotated about an axis parallel to the stacking direction. (During discussions regarding the BN film growth, h-BN and t-BN has been used interchangeably).

C-BN is extremely hard (60 - 70 GPa), has a high thermal conductivity (2 - 13 W $cm^{-1} K^{-1}$), and possesses a wide band gap ($E_g \approx 6.4$ eV) (Vel, Demazeau, and Etourneau 1991). It has been successfully doped both p- and n-type with Be and Si, respectively, which makes it a strong candidate for wide band gap semiconducting applications (Era et al. 1989), whereas diamond can only be p-type doped. In addition, c-BN is chemically

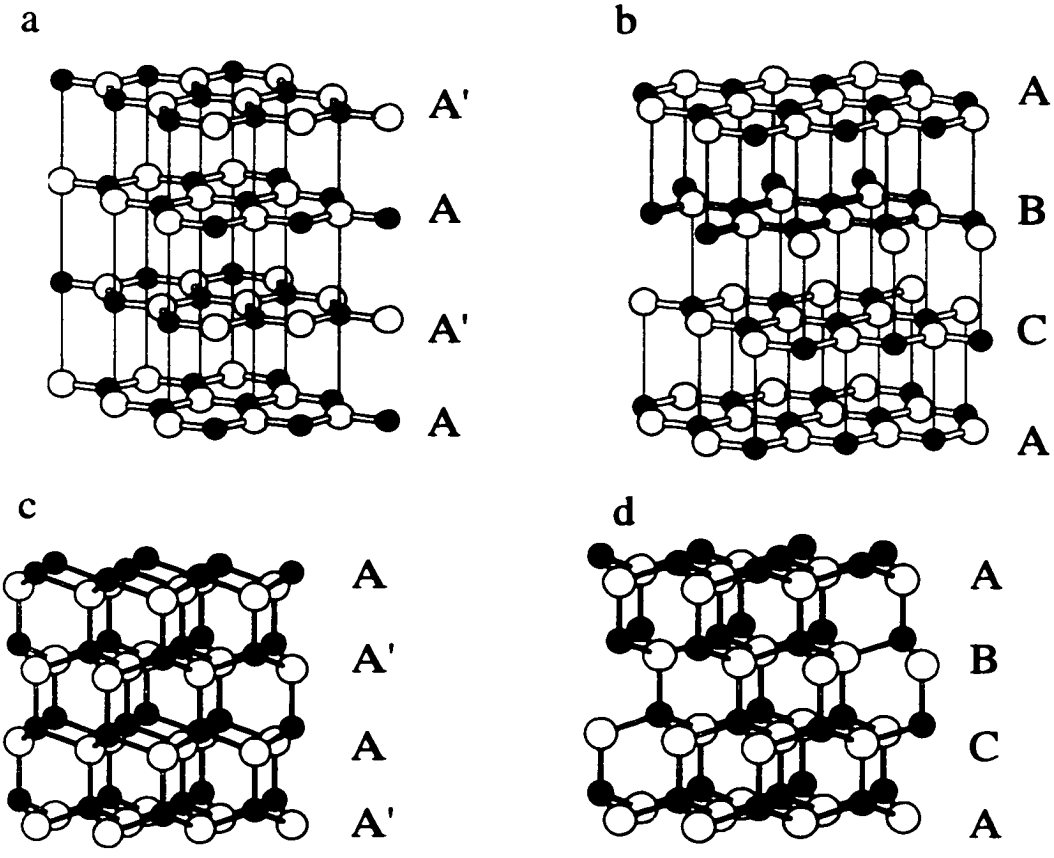

Figure 2.1.1 **Four crystal structures of BN: a) hexagonal b) rhombohedral c) wurtzitic d) cubic.**

more stable than diamond; c-BN does not react with iron and is resistant to oxidation at high temperatures. Hence, c-BN is considered as a potential material for use in ultra-violet light-emitting diodes, high power/high temperature solid state electronic devices, and wear-resistant coatings used on machining tools in the manufacturing industry.

2.2 Ultrahard BN Thin Films

The performance requirements from ultrahard coatings are multi-faceted and are ever increasing as the application fields expand. There is a growing demand for better surface modification techniques and superior coating materials that can retain their properties under extreme conditions. In fact, a high hardness is only one of the properties that is required from the protective coatings. For instance, nearly 40% of cutting tools are coated with hard, wear resistant overcoats, and more than 70% of these tools are used to machine steel or other ferrous alloys. Diamond coated tools are not compatible for use with ferrous alloys due to the high reactivity of carbon with iron, whereas c-BN coatings would be ideal even at very high temperatures due to the superior chemical stability of the compound.

Following the first synthesis of w-BN film (Sokolowski 1979) and c-BN film (Sokolowski et al. 1981), there has been significant progress in the synthesis of BN in thin film form. Figure 2.1.2 gives the yearly distribution of the citations regarding BN

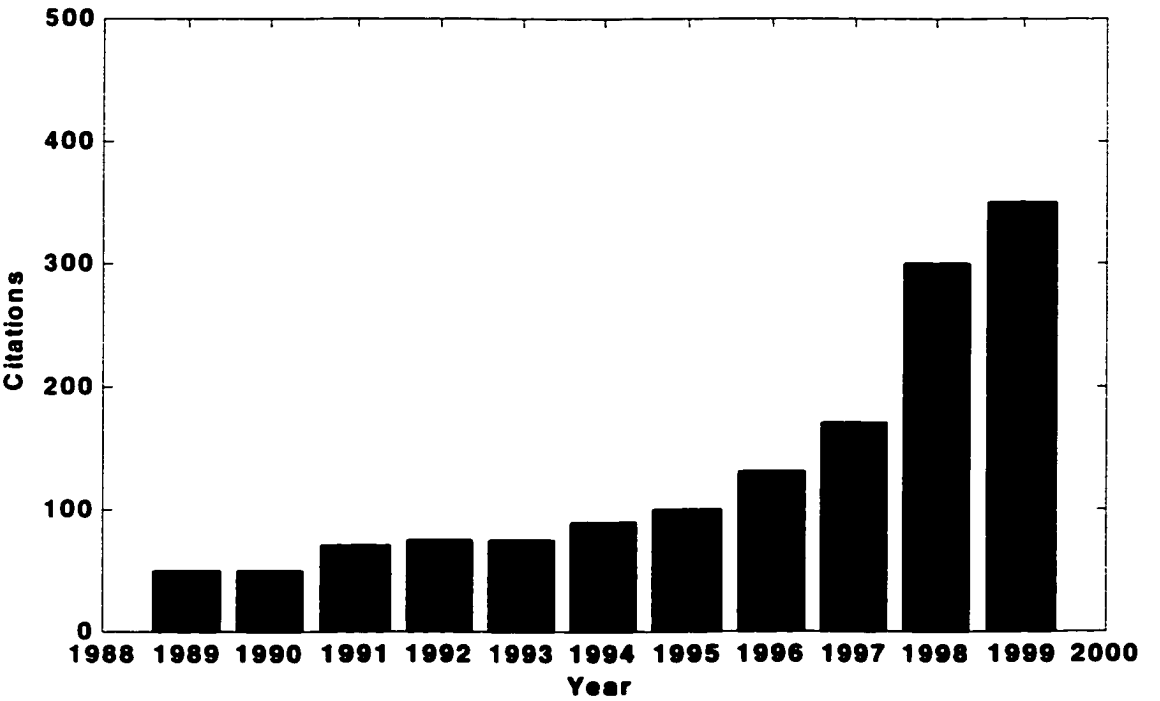

Figure 2.1.2 **The yearly distribution of citations on c-BN films.**

thin films. Polycrystalline hard c-BN films can be deposited using lower substrate temperatures than are required for polycrystalline diamond films, < 200 C vs. ~700 C, respectively. However, the quality of the c-BN films is still not good relative to the diamond films; extensive cracking and adhesion problems are commonly encountered. These phenomena are generally attributed to the compressive stresses typically observed in c-BN films (McKenzie 1993; McKenzie et al. 1993), ranging from 0.5 GPa to 25.5 GPa (Cardinale et al. 1996 and Ulrich et al. 1995, respectively). Cardinale et al. (1994) reported that ambient water vapor was also a contributing factor as the c-BN films stored in dry gas and vacuum did not indicate adhesion problems. Murakawa et al. (1991) and Okamoto et al. (1990) reported an enhancement in the adhesion of the c-BN films deposited using B and Ti buffer layers. Murakawa et al. (1991) also employed post-deposition annealing of the c-BN films for stress relief. Although studies for the stress-free synthesis of c-BN films are continuing, McKenzie (1993) claimed that the compressive stresses are necessary for stabilizing the c-BN phase on these films.

The compressive stress build up in c-BN films is attributed to compaction and distortion of the growing surface layer by ion-bombardment. Early findings indicated a relationship between the percentage of the cubic phase and the compressive stress, which was suggested to be proportional to ion energy to a certain degree (McKenzie 1993). Later, it was shown that once the c-BN nucleation was achieved on the growing film, less ion energy and/or flux was required for sustaining the growth of c-BN (McKenzie et al.

1995; Hahn et al. 1997; Litvinov and Clarke 1997). Following the same path, Mirkarimi, Medlin et al. (1997) were able to grow c-BN films up to 700 nm without any delamination. Although the substrate temperature, in excess of 1000 C, helped minimize the residual compressive stress and enhance the adhesion, high substrate temperatures will not be commercially feasible. Finally, the insight gained from such studies convincingly hints to a nucleation barrier for the stabilization of the cubic phase.

A common route for overcoming the problems with nucleation is through heteroepitaxial templating using suitable substrates. Even the biaxial compressive stress field due to ion-bombardment could be simulated by the epitaxial stresses due to lattice mismatch, if in fact it is the main mechanism for stabilizing the c-BN phase. Thus, it may be possible to exploit epitaxy in achieving the growth of single crystal c-BN films. In this respect, the first step is to find suitable templates for the growth of c-BN. Some candidate materials are Cu (a=3.6148 Å, 0.06% mismatch), and austenite (a=3.555+0.044x Å, x= weight percent carbon, 0.5% mismatch). Lately, a 45 degree rotated cube on cube epitaxial configuration has been considered using face-centered cubic rare-earth nitrides, such as CeN (5.02 Å, 1.85% mismatch), and NdN (5.15 Å, 0.7% mismatch).

Diamond (a=3.5671 Å, 1.33% mismatch) is also one of the suitable substrates for the epitaxial growth attempts. While diamond has been used widely in the attempts for the epitaxial growth of c-BN (Okamoto, Utsumi, Osaka 1990; Saitoh and Yarbrough 1991; Liao and Wang, 1994; Pascallon et al. 1999a, 1999b), the results failed to display

any epitaxial relationship between the c-BN films and the diamond substrates. On the other hand, epitaxial growth of diamond films on c-BN substrates has been reported (Friedmann et al. 1993; Chai et al. 1994a; Jin et al. 1995).

Several theoretical studies suggested the direct epitaxial growth of c-BN on silicon would be possible under certain circumstances (Verwoerd, 1994; Verwoerd et al. 1994; Zhang et al. 1997). In one of the studies, Doll et al. (1991), using pulse-excimer-laser-ablation method claimed depositing epitaxial c-BN films on Si (001) substrates. Song et al. (1994) and Zhang et al. (1994) also reported growing epitaxial c-BN films on nickel substrates. Moreover, homoepitaxial growth of c-BN films on c-BN seed particles has been claimed by Saitoh et al. (1994). However, there has not been any recent independent study reporting further evidence supporting the claims regarding epitaxial growth of the c-BN films. In fact, in a commentary by McCarty et al. (1994), it has been shown that the evidence presented by Doll et al. (1991) did not support the epitaxy of c-BN on Si (001) surface at all. In light of these facts, it is safe to conclude that epitaxial growth of c-BN has not been achieved yet.

It is also worth briefly mentioning epitaxial h-BN films. Ultrathin insulating h-BN films would interact very weakly with metal surfaces. The abrupt electronic structure at the interface between the metal surface and the h-BN layer could allow for the development of unique devices (Nagashima et al. 1996). This invoked a limited interest in synthesizing epitaxial h-BN films. Nagashima et al. (1995), and Oshima and Nagashima (1997) reported of epitaxial monolayer films of h-BN on several metal

surfaces. Long and Grabke (1992) also reported epitaxial growth of h-BN films on Fe-37Ni alloy, which are being considered for making inert surfaces on stainless steel chambers for UHV applications.

2.3 Cubic-BN Film Growth

The nucleation and growth process for c-BN films is very complex and has a very large combined parameter space for simple trial-and-error based parameter-property response curves to address the problems with c-BN growth. A feasible model for the nucleation and growth of c-BN films is necessary for identifying the mechanisms of c-BN stabilization and controlling them for the synthesis of ultrahard, low stress, and thick coatings. In the following sections, a detailed description of the microstructural evolution in c-BN thin films is given. In addition, a discussion about the current growth models for c-BN films will be presented.

Deposition of c-BN films is possible with a variety of techniques, such as plasma enhanced chemical vapor deposition (PECVD), ion-beam-assisted deposition (IBAD), and reactive magnetron sputtering (RMS). For instance, Okamoto et al. (1990), Saitoh and Yarbrough (1991), Ichiki et al. (1994), and Dworschak, Jung, and Ehrhardt (1995) employed PECVD. Another group of researchers, such as Bouchier and Moller (1992), Ikeda (1992), and Friedmann et al. (1994) used ion-beam assisted deposition techniques. Mieno and Yoshida (1990) and Kidner et al. (1994) employed sputter deposition techniques. Several studies using chemical vapor deposition techniques for the synthesis of c-BN films without ion-bombardment were also reported (Saitoh et al. 1994; Zhang et

al. 1994; Manorama et al. 1993). However, the evidence indicating the presence of c-BN in these films is inconclusive at best. A detailed discussion and review of these techniques is given by Yoshida (1997).

It is important to note that all of the techniques for the c-BN growth mentioned involves bombardment of the growing film with energetic ions from a plasma or a dedicated ion source. The cross-sectional TEM sample of c-BN films also display another commonality, which is the textured growth of h-BN layer preceding the c-BN layer, as shown in Figure 2.1.3. The characteristic microstructure for c-BN films starts with an amorphous layer (a-BN) forming over the substrate, which is 10 to 20 Å thick. Sometimes, a buffer layer is used to modify and enhance the adhesion between the film and the substrate. The thickness of a-BN layer is comparable to the range of ions with energies 100-1000eV (Collazo-Davila et al. 1999; Hofsass et al. 1995; 1997), and thus this layer is probably due to ion-mixing of the film material with the substrate. Hofsass et al. (1995) reported the growth of h-BN films on c-BN films without the a-BN layer in support of this argument. However, McFall et al. (1996) suggested that the a-BN layer observed was h-BN with no preferred orientation based on the data from *in situ* ellipsometry experiments.

The a-BN layer is followed by the highly textured sp^2-bonded h-BN with the basal (002) planes growing perpendicular to the plane of substrate surface. This textured layer is better described with the turbostratic arrangement of h-BN basal planes (t-BN) due to evidence for random rotational stacking in the TED patterns from this layer, such as larger interlayer spacing and diffuse rings (Mirkarimi, Medlin et al.1997). The thickness

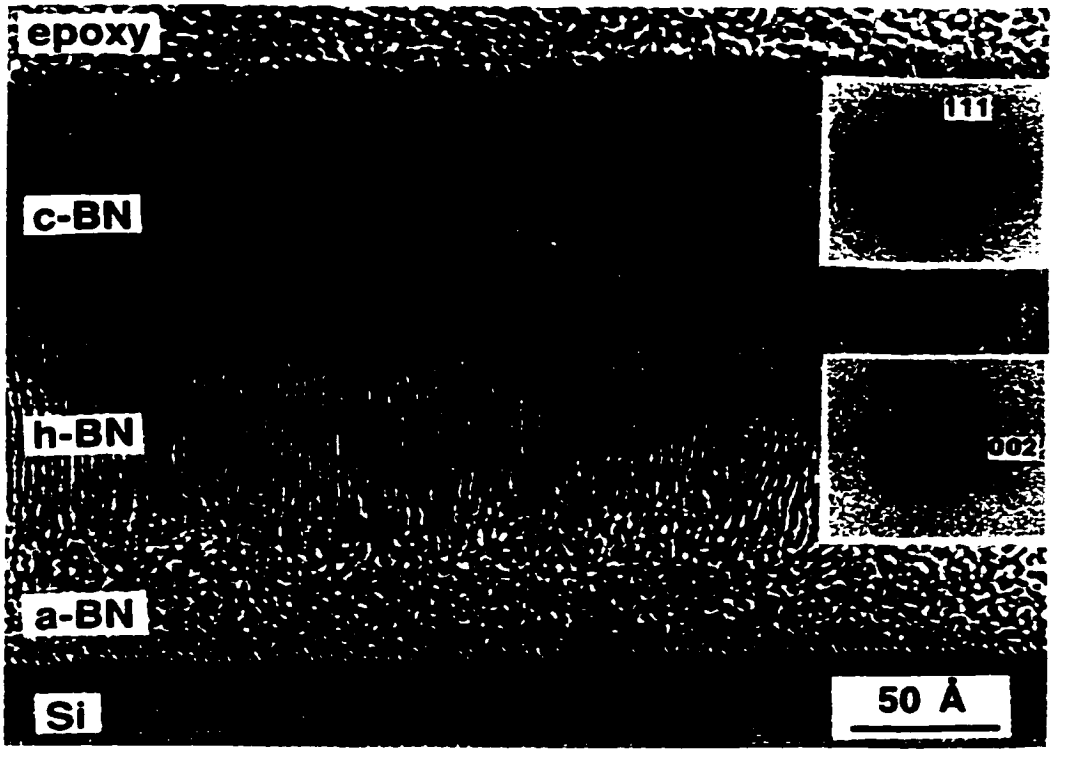

Figure 2.1.3 **A cross-sectional TEM sample showing the c-BN growth (after D.J. Kester, K.S. Ailey, et al. 1993).**

of this t-BN layer varies between 20-100 Å. McKenzie (1993) used the Gibbs free energy expression extended to include the strain energy argument due to the biaxial compressive stress field to explain the texture for the t-BN layer. The strain energy component was calculated for the c-BN and h-BN crystals with {111} and {002} planes either normal or parallel to the biaxial stress field. The results showed that calculated Gibbs free energies were lower if the planes were oriented perpendicular to the stress field. These results strongly correlate with the experimental observations where (002) planes of t-BN were always found growing normal to the substrate surface even with low ion incidence angles (Medlin et al. 1994).

The Gibbs energy expression was revised by Cardinale et al. (1997), and minimized for all possible orientations. The results showed that the minimum energy configuration was achieved when the basal planes of h-BN sheets were tilted 45° to the stress field. Cardinale and coworkers proposed that the texture was the result of plastic deformation of the h-BN to relieve the stress induced by ion-irradiation rather than a minimum energy configuration. In support of this model, McCarty and Medlin (1997) explained the rotation of the basal planes during plastic deformation, using the modes of deformation observed for hexagonal close-packed metals. Later, McKenzie and Bilek (1998) responded by suggesting that the original results would be consistent with the experimental observations if the elastic constants –shear modulus parallel to the basal plane, S_{44} or C_{44}^{-1}- were adjusted to compensate for the disordered structure of t-BN. Finally, McCarty (1999) suggested the total dismissal of thermodynamic theory of elastic

strain energy in explaining the texture. He argued that the stresses generated in the system are much larger than the elastic limit of the materials in question, and McKenzie and Bilek (1998) used incorrect elastic constants. Recently, Zeitler et al. (1998 and 1999) made *in situ* measurements of the stress evolution growing t-BN films. Interestingly, Zeitler and coworkers reported a tensile stress for the textured t-BN films that increases with the thickness of the t-BN layer. This tensile stress in the textured t-BN layer was observed to dramatically transform to a large compressive stress at the onset of the c-BN growth.

The cause of stress in films synthesized with ion-beam assisted deposition is ion-induced defect creation, such as vacancies and interstitials (Windischmann 1991). Both the swelling and compaction of materials have been observed depending on the condition for irradiation (Hobbs et al. 1994). The experiments on bulk graphite using neutron irradiation with dosages around 1-5 displacements per lattice atom indicated that at low temperatures (200 C) the volume of the graphite increases, whereas at high temperatures (450 C) shrinkage was observed (Simmons 1965). Furthermore, McCulloch et al. (1995) measured 4-5 GPa of tensile stress in the carbon samples irradiated with 50 keV C^+ ions with dosages ~10^{17} ions/cm^2. They also reported a sharp transformation of tensile stress to compressive stress when the dosage was increased to ~10^{18} ions/cm^2.

The textured t-BN layer is followed by the c-BN layer. Several studies of the h-BN/c-BN interface using cross-sectional TEM technique showed the presence of a 2:3 lattice match between the h-BN (002) planes and the c-BN (111) planes (Zhou et al.

1995; Reinke et al. 1996; Medlin et al. 1996; Hofsass et al. 1997). Li et al. (1992) also reported a similar epitaxial relationship between the basal planes of graphite and (111) planes of diamond. The atomic structure and the stability of the t-BN/c-BN interface have been studied using molecular and quantum mechanical methods, and results indicated such an interface to be stable at ambient temperatures (Widany et al. 1996; Zhang et al. 1997). Some studies reported the presence of 1 nm to 2 nm of sp^2-bonded material on top of the cubic BN layer (Friedmann et al. 1994; Sene et al. 1996; Park et al. 1997; Hofsäss et al. 1997). Although these findings merit further analysis, sp^2-bonded surface layers may have important implications for some of the proposed growth models.

2.3.1 Film Properties

2.3.1.1 Hardness

Hardness of bulk c-BN varies between 47 GPa to 75 GPa using both Vickers and Knoop hardness methods (Vel et al. 1991). Although the reported hardness values for c-BN films vary considerably, in general the average hardness is roughly around 55 GPa. Early reports indicated the hardness of c-BN films were around 42 GPa to 61 GPa using a Knoop tester (Watanabe et al. 1991). Bouchier and Moller (1992) reported a hardness value of 25 GPa, where as Verinaud et al. (1992) reported 48 GPa. Mirakarimi, McCarty et al. (1997) reported the hardness values for *thick* c-BN up to 70 GPa. Although some of the c-BN hardness values reported are higher than the bulk values, this is not uncommon.

Some of the reasons for this observation could be smaller crystal sizes in the films, and especially for the hot-pressed ceramics, density of the structure may play a major factor.

2.3.1.2 Stress

Compressive stresses in c-BN films have been often found to in the GPa range. As mentioned earlier, compressive stresses with chemical attack take part in the poor adhesion observed in c-BN films. It is found that compressive stress has a strong dependency on the energy of ionic species (Reinke et al. 1996). Highest stresses observed were often reported for two separate and distinct ion energy ranges. The first starts around 100eV and extends up to 200 eV, whereas the second is from 550 eV to 800 eV (Kulisch and Reinke 1997). The stress in c-BN films is determined using two principal methods. The first one is accomplished by profilometry or optical interference (McKenzie 1993; Cardinale et al. 1996) through measuring the radius of curvature of the substrate before (R_O) and after the deposition (R_F). The second method uses the shift of the frequency of the c-BN TO vibration mode ω_{TO} from its zero position at 1054 cm^{-1} to higher wave numbers observed through Fourier transformation-infrared (FT-IR) spectroscopy. This corresponds to a transverse optical phonon mode that requires long-range order, and is the only indicator for the presence of the c-BN phase. However, the IR peak position is affected by stoichiometry, contamination, or grain size.

2.3.1.3 Stoichiometry

Hackenberger et al. (1994) using neutron depth profiling, investigating the effect of stoichiometry to the c-BN content. The results of this study suggest that stoichiometry has a significant effect on the cubic phase stabilization. Films with B/N ratios close to one displayed higher c-BN content (Kaneda and Shibata 1994), whereas deviations from the stoichiometry decrease the cubic phase content. The carbon inclusion observed for c-BN films deposited using B_4C targets seems to have less effect on the films, and is observed to decrease with increasing nitrogen ion flux (Mirkarimi et al. 1997). In addition, Luthje et al. (1995) reported a decrease in the cubic phase content with rising oxygen inclusion in the films.

2.3.2 Modeling of the c-BN Film Growth

There are a large number of models on c-BN film growth, and detailed reviews of these models have been provided by Mirkarimi et al. (1997) and Kulisch, Reinke (1997). In this section, first, ion-induced processes in a growing film will be outlined. Then, some of the current theories on c-BN growth will be examined in light of the experimental data and basic concepts of ion-beam/surface interactions. The energetic particles bombarding the growing front of the film can lead to extensive changes in the physical and chemical properties of the final film. Some of the basic mechanisms leading to these changes can be outlined by considering the fundamental processes during ion-solid interactions, as shown in Figure 2.1.4. The energetic ions and neutral species

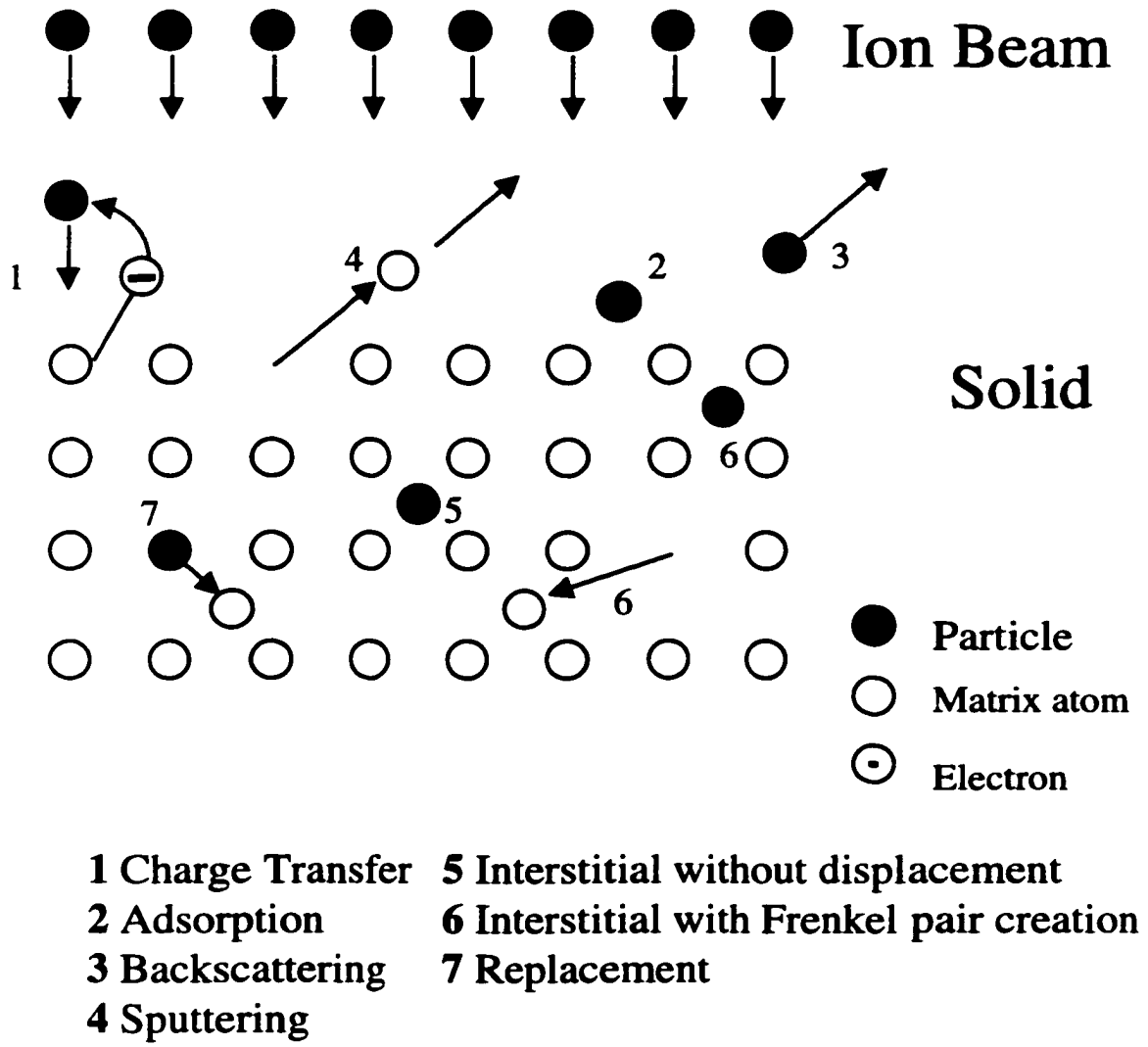

Figure 2.1.4 **Illustration of ion-solid processes.**

impinging on the film may become embedded in the growing surface, where they transfer their energy to the surrounding atoms through atomic collisions. As a result, an impacting ion may become trapped, reflected, or penetrate deep into the film. If it stays under the surface, it becomes an implanted particle either as an interstitial or by displacing a substrate atom. If the energy transferred to the lattice atom is greater than the displacement energy of the solid, the incoming ion can also displace that atom. Thus, the displacement energy is defined as the minimum energy that must be transferred to a substrate atom in order to create a stable Frenkel pair (vacancy-interstitial pair). If the energy transferred is sufficient, the displaced atoms may either initiate other defects, collisions, or escape through the surface as sputtered particles. Another important effect of the low-energy ion-beam bombardment on growing films can be described as enhanced diffusion. It was found that during the early stages of film formation, ion bombardment provides enough activation energy to enhance mobility of lattice and surface atoms through ballistic collisions or lattice excitations. On surfaces, low-energy ion-irradition was found to increase the average size of adatom clusters. The change in the cluster size is attributed to the enhanced surface adatom mobility and dissociation of smaller clusters due to ion bombardment.

There are four major models attempting to explain the exact nature of c-BN film growth. All of the models are based on the direct or secondary effects ion-beam – solid interactions as discussed earlier. However, there is still an argument regarding the details of c-BN formation. Two of the models, the thermal spike and the preferential sputtering

models, treat the growth of c-BN films using ion-beams with extra emphasis on the direct effects of ion-beam damage. The compressive stress and subplantation models are more interested in examining the c-BN through the secondary effects of ion-beam induced damage.

Seitz and Koehler (1956) were the first to accurately describe and treat the thermal spike concept. They assumed that a fast ion trapped in a lattice can transfer all of its energy to the atoms adjacent to the site of impact, which creates a short living ($\sim 10^{-12}$ sec) pocket of very energetic atoms. Subsequent calculations suggested the temperature at this region could reach several thousands of degrees Kelvin. Furthermore, the presence of large hydrostatic pressures (up to10 GPa) has been claimed for this region. Such thermally agitated regions in a solid caused by the energy transferred from impinging ions are called thermal spikes. Weissmantel et al. (1980) proposed that rapidly quenched spike region ($\sim 10^{14}$ K sec^{-1}) may trap the "metastable" phases for both carbon (diamond) and BN (c-BN) formed in the high-temperature/high-pressure spike region. Recently, Hofsäss et al. (1998) reconsidered the thermal spike theory by using a cylindrical spike region along the path of an ion implanted in the growing film.

The thermal spike approach can explain sp^3-bonding in films, however besides ion flux and energy it assumes no other parameters likely to be effective on the final properties of the films. Hence, the threshold temperature observed for the c-BN films by McCarty, Mirkarimi et al. 1996 and Tanabe and Hayashi 1992 cannot be explained. In support of the thermal spike model, Dworschak, Jung, and Ehrhardt (1995) argued that

below a certain temperature, the spike might quench too fast for atoms to rearrange themselves for the c-BN phase to form. However, even if a threshold temperature of 200 C (~0.06 eV) is considered, it would be too small with respect to the thermal energy transferred to the spike zone in the substrate by the impinging ions (~100-1000eV). In addition, Mirkarimi, McCarty, and Medlin (1997) reported the results of computational studies which showed melting within the thermal spike pockets may not occur for high-melting-point ceramics like h-BN and c-BN.

As a part of this study, ion-irradiation experiments on h-BN using 50 keV Xe^+ ions has been performed by Dr. Collazo-Davila (the author worked together with Dr.Collazo-Davila in this study) at Argonne National Labs with Dr. Mark Kirk, which indicated that 50 keV Xe^+ ions were not able to produce significant atomic rearrangements in h-BN at room temperature (Collazo-Davila 1999). The sample was viewed in dark-field mode while being bombarded with 50 keV Xe^+ ions at a dose rate of 10^{10} cm^{-2} s^{-1}. The ions in this experiment, 50 keV Xe^+, had enough energy to create substantial cascade regions that would have been easily visible with the help of a TEM during irradiation, if the effected region amorphized or transformed into another phase apart from h-BN. These observations also suggest that the point defects created in the h-BN are mobile even at RT. Similar anomalous ion damage behavior was observed for ZnSe by Man-Yu and Bourret-Courchesne (1996). Based on the observations presented and evidence from the literature, it would be unlikely that the thermal spikes can account for the synthesis of c-BN.

The preferential sputtering model was proposed by Reinke et al. (1995), Kulisch and Reinke (1997). This model is directed towards explaining the c-BN growth rather than the nucleation of the phase. In order to incorporate the data in the literature to their model Reinke et al. (1995) defined a flux ratio parameter, F, (the ratio of the flux of ions to the flux of boron atoms). Subsequently, a plot of F vs. ion energy, E_{ion} was plotted, which indicated a region where c-BN formation has been observed. Later Reinke et al. (1995) defined two boundary lines F_h and F_c on the plot, which separated the h-BN and c-BN regions, and c-BN and complete sputtering regions, respectively. Due to this empirical approach, the sputter model can correctly predict effects of some of the parameters involved in the growth process, such as the substrate temperature. However, Robertson (1996) pointed out the first shortcoming of this model, which is very low sputter yields for the first row elements in the periodical table, i.e. C and B. Robertson also indicated that the difference in the sputtering yield between sp^2 and sp^3 sites was too low to account for c-BN formation. Furthermore, the most important evidence against the sputter model was the reports of the 10-20 Å surface layer of sp^2-bonded BN sitting on the c-BN layer (Friedmann et al. 1994; Bouchier et al. 1994; Park et al. 1997). Some of the other deficiencies of this model are its inability to explain the layered growth of the c-BN. Finally, according to this model, there should not be any obstacles to the growth of pure c-BN films, which has not been achieved yet.

Lifshitz et al. (1990) described the growth of tetrahedral amorphous carbon (ta-C) by "subplantation" (shallow implantation) of ions in the energy range of 10 eV to 1000

eV. As described earlier, one of the processes that an ion transfers its energy to the substrate is through the displacements of the substrate atoms and creation of the interstitial-vacancy pairs. According to this model, when the local the density of the film due to the interstitials exceeds a critical value, a "spontaneous athermal transformation" to sp^3-bonded phase takes place. Lifshitz et al. explained the preferential displacement of sp^2-bonded atoms by pointing to the difference between the displacement energy of carbon atoms in graphite (25 eV) and in diamond (80 eV). However, Robertson (1996) and Marton (1994) pointed out that most recent measurements of the displacement energies were different than those used by Lifshitz et al. They reported that the displacement energy for diamond and graphite were 38 eV and 33 eV, respectively. The small difference between these displacements energies and its potentially adverse implications are yet to be accounted for by the supporters of this model.

The compressive stress model proposed by McKenzie et al. (1993) was already discussed earlier in Section 2.3, where it was shown that the recent in situ measurements of the evolution of stress in c-BN films seriously questioned the validity of this model. Recently, Mirkarimi et al. (1994) proposed a dynamic stress model. In this model, Mirkarimi et al. suggested that the local stress in the c-BN films was controlled by the steady state production and annihilation of the defects created by the ion-bombardment. According to their model, diffusion of the defects to viable sinks may help increase the local distortions, which can induce very high stresses. Mirkarimi et al. claimed these local stresses could help the nucleation of c-BN. However, this model cannot explain the

effect of temperature on the c-BN growth, as the defect mobility in h-BN was shown to be almost independent of the temperature by the earlier experiments.

2.4 Nucleation of c-BN on h-BN

All of the models proposed for the c-BN growth had significant difficulty in explaining the c-BN film formation, as shown in the previous section. This was expected as their concepts were directly adopted from ta-C deposition with little or no care for the unique aspects of the c-BN/h-BN system. First instance, BN has a strong ionic character (0.48 on the Philips scale, where NaCl is 1 and graphite is 0), which indicates a significant difference in the response of the lattice to the ion-bombardment (Robertson 1996). Polycrystalline diamond films has been deposited using chemical vapor deposition (CVD), however c-BN requires ion-beam involved techniques. In addition, there is strong evidence for the stability of c-BN at room temperature and pressure, where as diamond is the metastable phase. In fact, a better approach for the understanding of c-BN formation would be the application of the methods previously used to *investigate* the diamond/graphite interface rather than directly *adopting* the models proposed for diamond formation. In the rest of this section, a brief summary of the studies on diamond nucleation from a unique perspective will be discussed, and experimental application of some the fundamental aspects to the BN will presented.

Mehandru et al. (1992) considered the hydrogenation induced arch-like edge structures of the graphite sheets as the preferential sites for diamond nucleation. They found that the local atomic structure optimized using quantum chemical calculations

closely resembled the bonding of diamond, as shown in Figure 2.4.1. Later, Lambrecht et al. (1993) and De Vita et al. (1996) modeled the diamond/graphite interface using the epitaxial geometry observed by Li et al. (1992) which is also consistent with the geometry due to hydrogenation. These studies actually formed the basis of models that explain the growth of diamond in thin films and the graphite/diamond interface.

In an earlier study, the tendency of graphitic sheets to form curved surfaces was shown by Ugarte (1992) who irradiated carbon soot by the electron-beam of a TEM. Ugarte managed to form closed concentric-shells of graphite (onions). Qin and Iijima (1996) also reported the formation of similar onions during electron-beam irradiation of diamond particles. However, in another study Banhart and Ajayan (1996) reported the formation of diamond particles while in situ heating the onions during electron-beam irradition in a TEM. The common point for these experiments was the use of electron-beams to simulate the conditions for ion-beam deposition and investigate resulting structures at an atomic scale.

Using the same investigative tool (high-resolution transmission electron microscopy (HREM)) and methodology (electron-beam irradiation), the h-BN/c-BN system can be investigated in detail. Sample preparation for h-BN on gold grids has been described in Chapter 1. Due to the extremely brittle nature of h-BN, bulk microscope preparation is extremely difficult.

It was shown by Collazo-Davila et al. (1999) that the electron-beam in a TEM is capable of producing similar amount of damage through ballistic displacement of atoms.

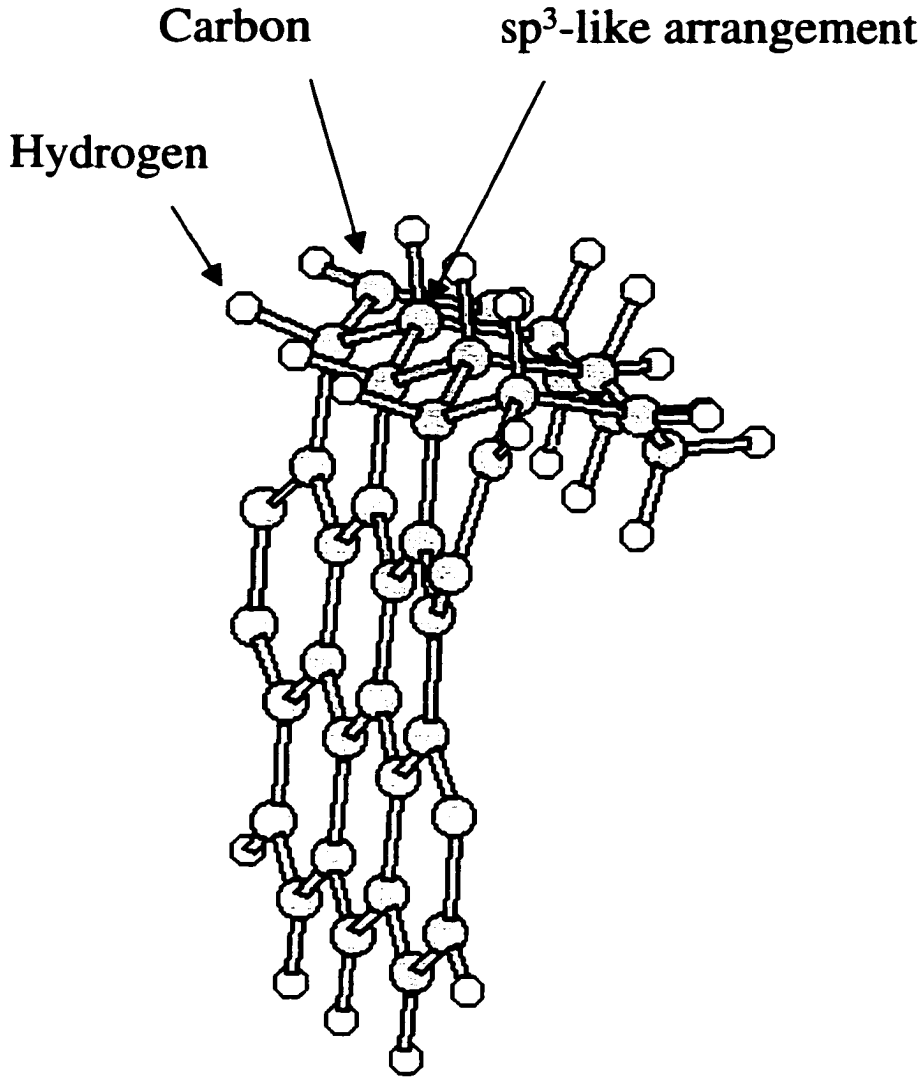

Figure 2.4.1 **Buckling of the hydrogenated graphite sheets, and creation of sp^3-like bonding arrangement.**

The list in Table 2.1.1 summarizes the amount of damage in terms of average number of displacements per atom (dpa) that can be imparted to every boron and nitrogen atom in a BN flake during 1 minute exposure to an electron flux of 100 Amp/cm^2 (6.24 x 10^{20} electrons cm^{-2} s^{-1}). Sene et al. 1996, by using computer simulations, reported a tentative value of five dpa for the amount of damage that is created during the c-BN film growth, which is very close to what is estimated for a 300keV electron-beam, as shown in Table 2.1.1.

The electron-beam irradiation experiments that will be presented in the next section were conducted together with Dr. Collazo-Davila using the UHV-TEM at Northwestern University.

Table 2.1.1
Energy Transfer from Electrons to Boron and Nitrogen Atoms in a TEM

	Boron		Nitrogen	
Accelerating Voltage (kV)	**Max Energy Transfer (eV)**	**Estimated dpa†**	**Max Energy Transfer (eV)**	**Estimated dpa†**
1,000	402	1.9	310	2.6
400	113	1.1	87	1.3
300	79	0.9	61	1.0
200	49	0.6	38	0.6
100	22	0.2	17	0.0

†The dpa are calculated for 1 minute of electron bombardment at a current density of 100 Amp/cm^2 assuming a displacement energy of 20 eV for both B and N. The total displacement cross sections were calculated using the McKinley and Feshbach (1948) approximation to the Mott series (1929). The modified Kinchin and Pease (1955) relation was used to account for secondary displacements occurring for primary energy transfers greater than twice the displacement energy. (After Collazo-Davila et al. 1999)

2.4.1 Nanoarch Formation

First, two suitable (thin) h-BN flakes on the gold grid are selected. In order to view the resulting structure in three dimensions, the h-BN flakes were chosen such that different lattice planes were perpendicular to the incident electron beam direction. HREM images of these two flakes are shown in Figure 2.4.2a and b. In Figure 2.4.2a, the h-BN crystal is oriented with its basal planes (0002) parallel to the direction of the beam. In Figure 2.4.2b, the basal planes of h-BN are perpendicular to the beam direction. These regions were then subjected to a current density of 50-100 A cm^{-2} for 10 min. This condition at the subject regions was obtained by removing the condenser aperture from the beam path and adjusting the bias on the Wehnelt cup (Collazo-Davila et al. 1999). In Table 2.1.1, it is shown that similar experimental conditions can induce up to 10 dpa, comparable to c-BN growth. The results from this experiment are given in Figures 2.4.3a and b. The unusually layered, dome-like structures formed under electron-beam irradiation, as shown in Figure 2.4.3a, are called nanoarches (Collazo-Davila et al. 1998). A basic atomic model for the nanoarch structure is proposed by Collazo et al. (1998) are given in Figure 2.4.4. Similar curving of the graphite sheets was reported earlier (Ugarte 1992). In addition Banhart, Zwanger, and Muhr (1994) reported the formation of BN onions and other curved BN features formed under intense electron-beam irradiation.

Two other important sets of experiments were also conducted. In the first one, similar thin h-BN particles were exposed to intense electron-beam irradiation using

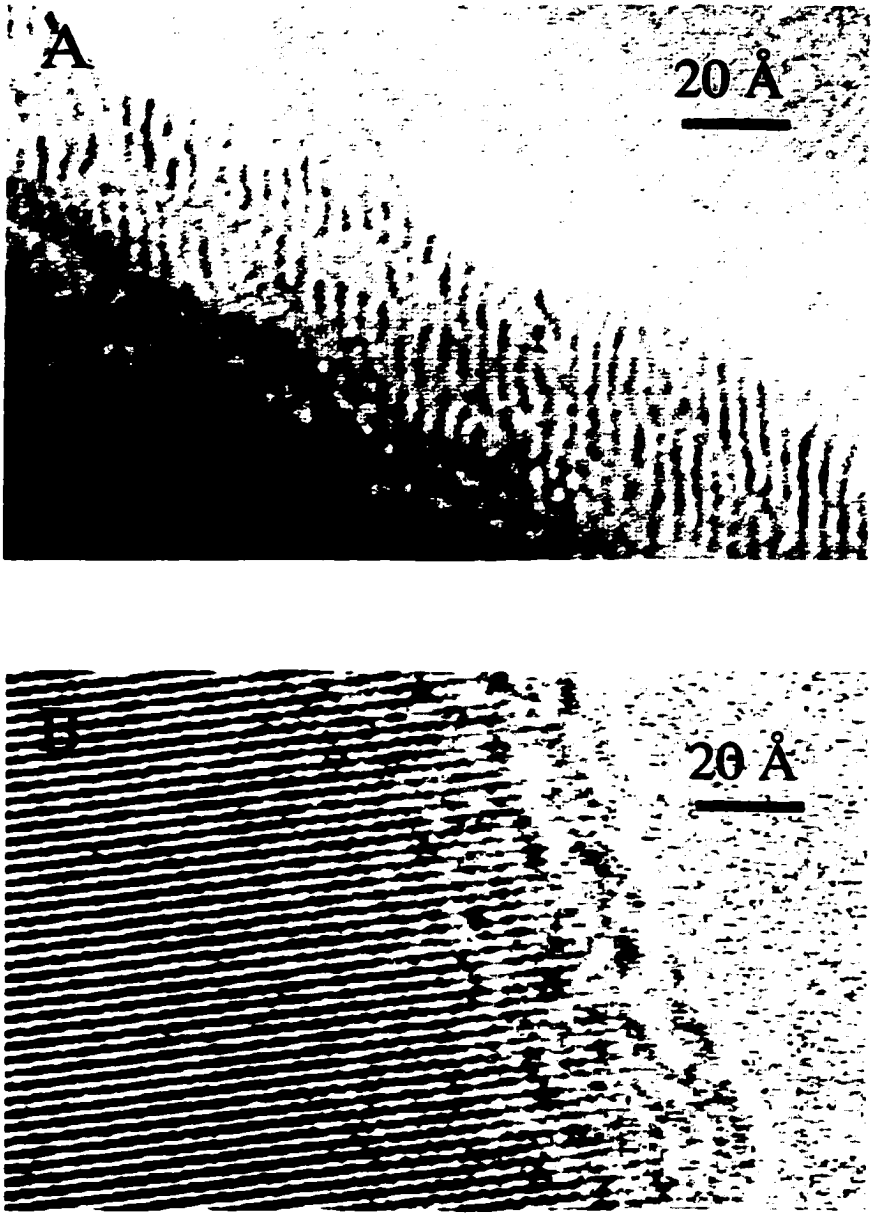

Figure 2.4.2 **High resolution TEM images of h-BN with the basal plane oriented a)parallel to the beam and b) perpendicular to the beam.**

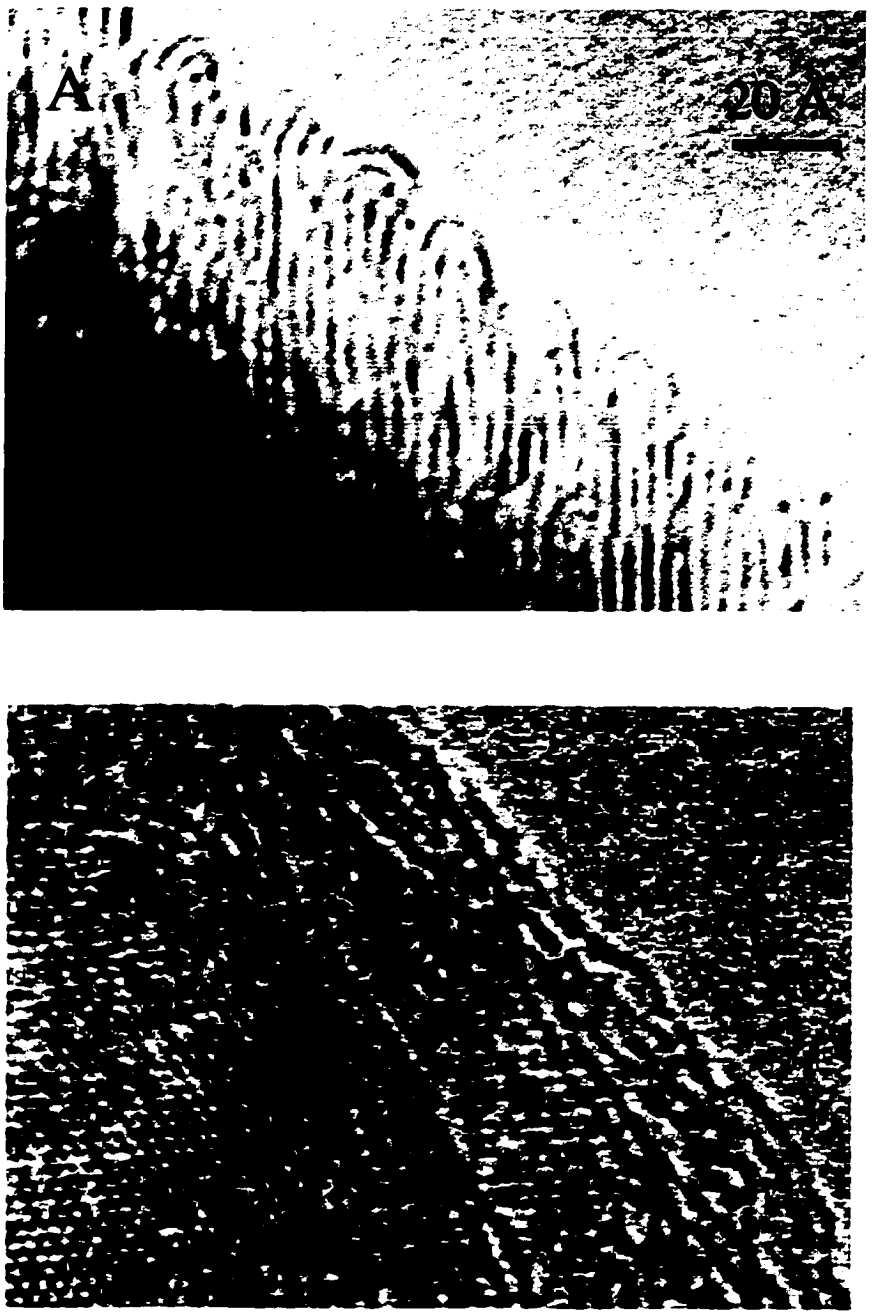

Figure 2.4.3 **The same regions in Figure 2.4.2 after 10 minute electron-beam irradiation (300 keV, with 50 - 100 A/cm^2 current density); basal plane is a)parallel to the beam and b) perpendicular to the beam. Arrows in (b) indicate the arches which are located at the edges of surface steps.**

Figure 2.4.4 **Basic model of nanoarch with 10 Å diameter superimposed on the HREM image**

accelerating voltages 200kV and 100 kV. The results from these experiments indicated the presence of nanoarches on the irradiated regions, although it took longer for nanoarches to form. In the second set, similar experiments were conducted using TEMs with conventional vacuum ($\sim 5\times10^{-7}$ Torr) using accelerating voltages of 300 kV and 1000 kV. The experiments with the 1000 kV microscope were conducted by Prof. L. D. Marks using the facilities of National Research Institute of Metals in Japan. Although arch formation was observed for the 1000 kV irradiation, 300 kV irradiation of the h-BN did not induce any nanoarches. Collazo et al. (1999) attributed this observation to the contamination of the edges of basal planes by the contaminant gases (H_2O, CO_2, and CO). Later, it was proposed that the sputtering rate for the 1000 keV electron beam was high enough to allow the "clean" basal planes to saturate the dangling bonds by forming arches before the contaminants poison the edges. It is also possible that nanoarch formation follows a route similar that proposed for the hydrogenation of the graphite sheets by Mehandru et al. (1992).

The observation of nanoarch formation under conditions similar those in c-BN formation provide an important clue about the nucleation of c-BN over the h-BN layer during film growth. Especially, the presence of a curvature in this structure is very encouraging as Iijima et al (1980) discussed the presence of sp^3-bonding in highly curved structures for graphite. This structure behaves like a semiconductor surface reconstruction in a way. It saturates the dangling bonds and converts the excess energy by forming a curved structure. Collazo et al. (1999) calculated the minimum bending

angle would be ~ 11° as projected along the [1120] direction that the B-N-B at the apex of the arch will suffer.

If one considers the geometry of the sp^3-bonding, it can be said that nanoarches forming on the h-BN layer during the c-BN film growth can decrease the energy required to nucleate sp^3-bonded nuclei, or at least act as preferential nucleation sites. Once the sp^3-bonded nucleus is formed, the growth can take place by incorporating some of the nanoarch atoms to the nuclei and thereby reducing the strain energy due to the curvature. In Figure 2.4.5, possible sequences from the c-BN nucleation at the h-BN interface through the nanoarch route are described with the help of the interface model of Widany, Frauenheim, and Lambrecht (1996). It is based on the texture observed for the c-BN thin films and diamond films, where (0002) basal planes in the hexagonal phases are parallel to the (111) planes in the cubic phase.

One of the strengths of this view is that it can explain some of the unreported problems regarding irreproducibility of c-BN growth. Several research groups were unable to grow c-BN films, or films with similar c-BN contents, although they used the same deposition parameters published by other researchers. The reported sensitivity of nanoarches to the chemistry of the vacuum can explain this behavior. In addition, some of the aspects of the sputtering model can be incorporated to this model as nanoarch formation relies on the sputtering of the contaminants. In addition, the threshold temperature can be explained by the thermal activation energy required for the formation of a nanoarch by the bonding of the clean edges of two BN sheets.

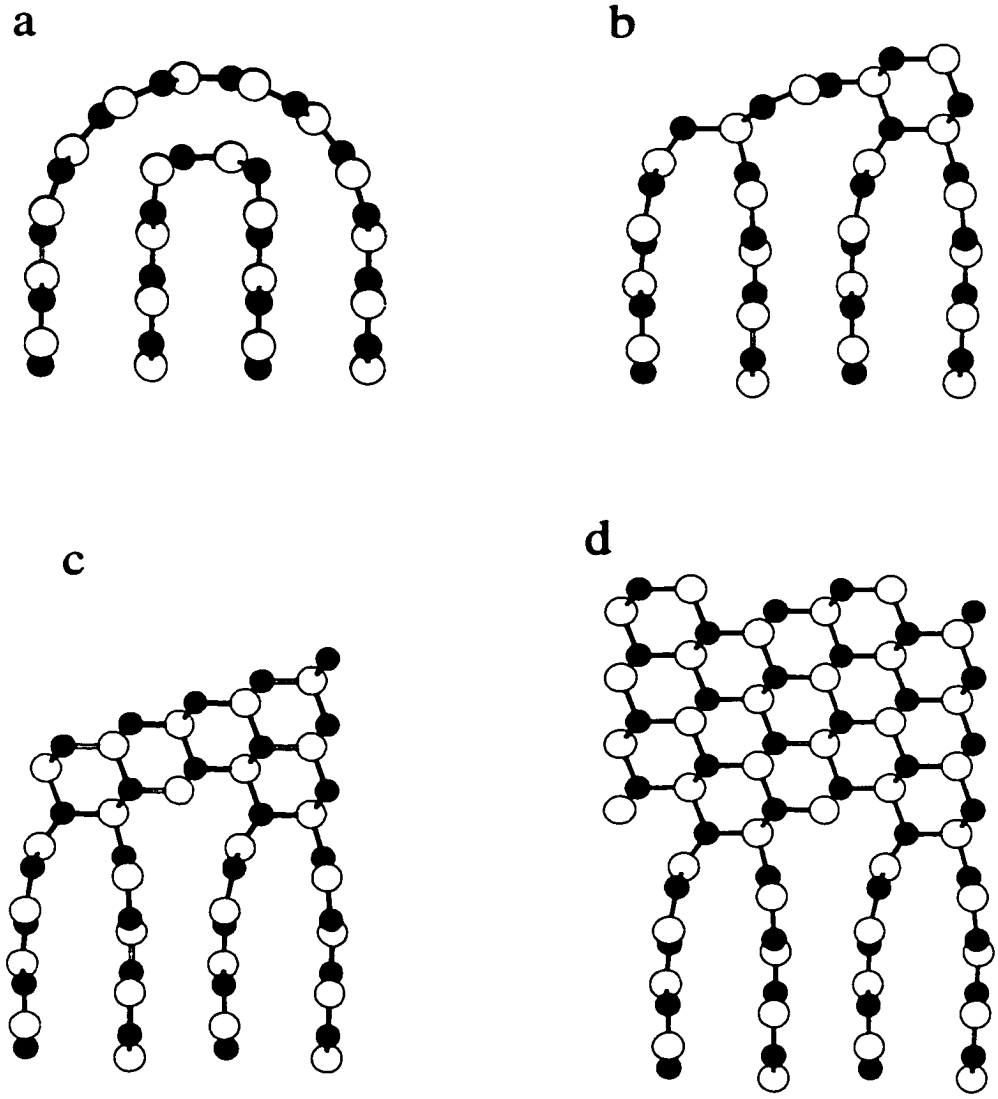

Figure 2.4.5 **Nucleation and growth of c-BN on a nanoarch. The interface in (d) has been proposed by Widany et al. (1996) to be a stable interface configuration. (After Collazo-Davila et al. 1999)**

However, there are some questions that needs to be addressed, such as the texture of the h-BN layer, which can no longer be explained by the compressive stress model. Moreover, at this stage this model cannot explain the sp^2-bonded layer observed on the c-BN. Another point that needs to be addressed is the variation in the h-BN layer thickness with temperature, which cannot be explained by this model.

As a summary, an investigation of the c-BN nucleation at the h-BN layer at an atomic scale has been conducted using methods similar those used for diamond/graphite interface. A new and unique model for the explanation of the c-BN nucleation at the h-BN layers has been developed. This model can account for some of the important aspects of the deposition process. In addition, it also agrees very well with the theoretical interface proposed for the c-BN/h-BN model.

CHAPTER 3: BN FILMS AND NANOSTRUCTURES

3.1 In situ Processing of BN Films

One of the few applications of in situ techniques to c-BN growth has been the confirmation of the layered growth using in situ spectroscopic ellipsometry (Pascual, Andujar, Gimeno et al. 1996; McKenzie, McFall, Smith et al. 1995; McFall, McKenzie, Netterfield 1996). However, there has not been a further attempt to examine the interface between these layers using other in situ methods. On the contrary, most of the studies on the c-BN growth rely on the property-response relationships for modeling the c-BN nucleation at the h-BN/c-BN interface.

In situ methods require precise control of the film deposition parameters, a clean environment for the deposition, and a well-characterized substrate surface. Structural and chemical characterization of the substrate and the film system are also essential for a complete *in situ* examination. There are only a limited number of systems capable of examining thin films and surfaces, which satisfy these requirements (Collazo-Davila, Landree, Grozea et al. 1995). Even fewer are capable of synthesizing of films using ion-beams required for c-BN growth (Bengu, Collazo-Davila, Grozea et al. 1998). The SPEAR system at Northwestern University with the new SINBAD chamber is one of the pioneering systems in applying the in situ processing concepts for the study of hard coatings. In this chapter, the results from in situ BN film deposition experiments using the SINBAD processing chamber will be presented. The results of these experiments are used to characterize the structural and chemical evolution of BN films at an atomic scale.

The effects of various deposition parameters on the h-BN morphology will be described. Finally, some of the novel phases observed on the h-BN films such as single-wall BN nanotubes and fullerenes will be covered.

3.1.1 Deposition of h-BN Films

In Chapter 2, evidence for the presence of BN nanoarches was presented and the tips of these nanoarches are offered as preferential nucleation sites for the sp^3-bonded cubic phase (Collazo-Davila, Grozea, Marks 1998). Widany, Frauenheim, Kohler (1996), in an earlier theoretical study, proposed a fundamental interface between h-BN and c-BN employing structures similar to nanoarches. Collazo-Davila et al. (1999) also showed that the formation of these nanoarches depends on the imbalance between the rate of contaminant arrival (quality of the vacuum) and sputter cleaning at the h-BN sheet edges. One can suggest that the formation of nano-features at the interface during growth is one of the essential elements for the onset of c-BN nucleation.

Similar observations have been reported for the graphite/diamond interface. Li et al. (1992) noticed that graphite powder and fibers acted as nucleation centers for diamond on the surface of silicon substrates. Furthermore, Li et al. reported that there was a preferential epitaxial relationship between the prism planes of graphite (edges of graphite sheets) and the (1 1 1) planes of diamond, where graphite (0001) || diamond (111) and graphite [1 1 $\bar{2}$0] || diamond [10 $\bar{1}$]. Later, others (Lambrecht, Lee, Segall et al. 1993; De Vita, Galli et al. 1996) modeled this interface configuration using 2:3 matching of buckled hexagonal networks of diamond to the flat hexagonal network of graphite sheets.

A similar interface during the transformation of graphite onions to diamond under electron-beam irradiation has been observed by Banhart (1997).

Several studies of the h-BN/c-BN interface using XTEM technique also showed the presence of a 2:3 lattice match between the h-BN (002) planes and the c-BN (111) planes (Zhou, Ikuhara, Suzuki 1995; Reinke, Kuhr, Kulisch 1996; Medlin, Friedmann et al. 1996; Hofsass et al. 1997). In addition, the general morphology of the sp^2-bonded layers underlying the c-BN films (McCarty, Mirkarimi et al. 1996), and the highly curved character of the structures observed for h-BN and graphite subjected to electron-beam irradiation (both covered in Chapter 2) are very similar. The data in the literature for the deposition of c-BN films unequivocally points to the fact that nucleation of the cubic phase depends on the initial sp^2-bonded network. From this perspective, a close examination of the sp^2-bonded nanostructures of BN and the conditions promoting their synthesis might reveal some of the important mechanisms responsible for the phase transformation of h-BN to c-BN. Structures such as multi-wall tubular networks, onions, and nanoarches of BN can be considered as transient metastable phases.

In this study, three different types of substrates are used (i.e. single crystal silicon, copper, and polycrystalline tungsten) for the examination of BN deposition using a low-energy ion-beam assisted technique. In the following sections, details about the chemical and structural characterization of the substrates and the films will be described. The effects of deposition parameters on the morphology of BN thin films will be discussed. The role of the nanoarches and other nano-features in BN thin films for the nucleation of the cubic phase will also be examined. Synthesis and structural characterization of other

novel BN structures such as single-wall nanotubes and fullerenes are also examined, and evidence for their presence in BN thin films is given. In this study, some of the XTEM examinations of the BN films were done together with Dr. Chris Collazo-Davila.

3.1.1.1 Growth on Si (001)

After Si (001) samples were loaded to the SPEAR system, an initial chemical characterization of the silicon surface was conducted using the XPS equipment on the analysis chamber. Typical sequence of XPS spectra acquired from the surface are provided summarizing the initial cleaning process in Chapter 1, which describes the chemical state of the surface during cycles of ion milling with 1keV Ar^+ ions and electron-beam annealing inside the analytical chamber. The primary reason for annealing the sample using 3keV electron beam is to annihilate the defects generated on the surface of the silicon substrate. It also helps the desorption of Ar atoms trapped below or physi-absorbed on the surface, which could be substantial depending on the duration of cleaning. Some of the fine details of Si surface preparation, such as surface roughening, using the SPEAR system is reviewed by Collazo-Davila et al. (1995) and Grozea, Landree, Marks (1997).

XPS is capable of nondestructively detecting all elements from Li to U, and it can provide information about the composition of the surface layers down to a depth of 50 to 70 Å. Furthermore, XPS cannot only identify the presence of an element (at levels down to 0.05 at%), but it can also distinguish different chemical states of elements in different environments.

An unlikely method, TED, primarily used to characterize the surfaces structurally has also been used to provide chemical information about impurities not detectable by XPS (i.e. hydrogen) on Si (001) surface. The presence of Si (001)-2×1 reconstruction was verified using TED. This also served as a reference point in terms of atomic scale control of the substrate surface structure. Figure 3.1.1 displays the diffraction pattern corresponding to the Si (001)-2×1 native reconstruction. This reconstruction is found to form on clean (001) surface during annealing for defect annihilation. Atomic hydrogen and impurity atoms are known to disorder this structure (Jarayam, Xu, and Marks 1993); thus, UHV conditions and extra care in substrate preparation are essential.

The structural and chemical analyses of the Si (001) samples were finalized after verifying the presence of 2×1 superlattice diffraction spots under TED examination. Then the samples were transferred to the SINBAD chamber, where the deposition of the BN films will take place over the clean and reconstructed Si (001) substrate at RT. During deposition experiments, the substrate bias was kept between –20 to –200 Volts (d.c.), and the range for ECR power was adjusted to be between 90 and 200 Watts with 1 to 2 sccm of N_2 (99.999 at%) flow. The substrates were resistively heated and the substrate temperatures were kept between RT and 550 C, measured with an optical pyrometer. The deposition rates of the boron, using the electron-beam source, was

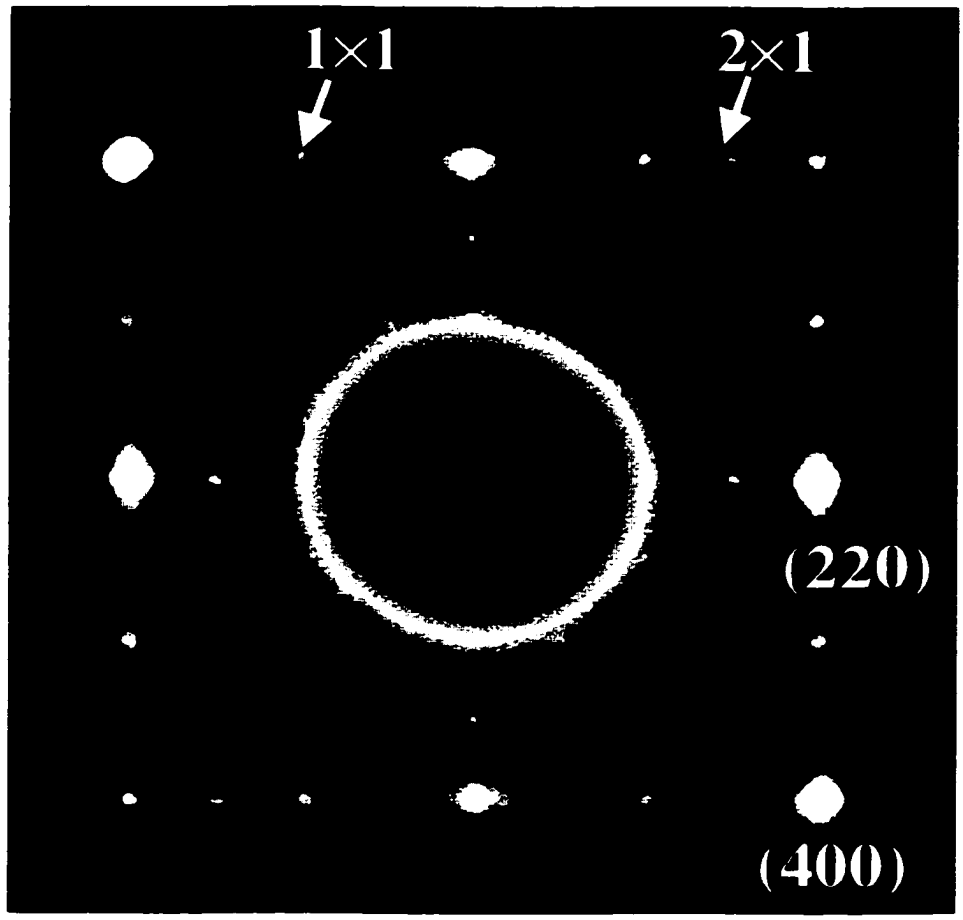

Figure 3.1.1 **The TED pattern from Si (001) substrate displaying reflections from the 2×1 native reconstruction.**

calibrated beforehand by measuring the boron thickness on the bulk Si (001) samples using XPS measurements and direct measurements through cross-sectional TEM samples (XTEM). For BN deposition experiments a constant boron deposition rate was chosen (~10 Å/min), which resulted in an average of 0.5-3 Å/min BN growth rate at the substrate. The conditions for the ECR plasma source was adjusted to stabilize the ion-flux at $5\times10^{14} - 10^{15}$ ions/cm^2.s (Fan and Newman 1998a; 1998b). The duration for deposition experiments was kept between 30 minutes to 120 minutes for plan-view samples and up to 360 minutes for XTEM samples. Unless indicated otherwise, the same deposition parameters have been used for the experiments on Cu (110) and tungsten substrates.

Once the deposition is finished, the system was pumped down to the UHV range, and then the sample was transferred back to the SPEAR system for further analysis. In the SPEAR system, the films were first chemically analyzed with the help of the XPS equipment in the analytical chamber. Two reference spectra were acquired from the powder h-BN and c-BN samples on un-thinned bulk Si (001) wafers, as shown in Figure 3.1.2. Detailed scans for the N1s and B1s core levels loss peaks are given in Figure 3.1.3, there is a systematic shift in the spectra (~2.5eV) from the literature values probably due to charging effects. The N1s core level spectra for h-BN shows a loss feature at ~9 eV higher binding energy than the core peak. This has been identified as the π plasmon loss feature (πP), which is absent for the N1s spectra from the c-BN sample. These measurements agree with the previously reported results for h-BN

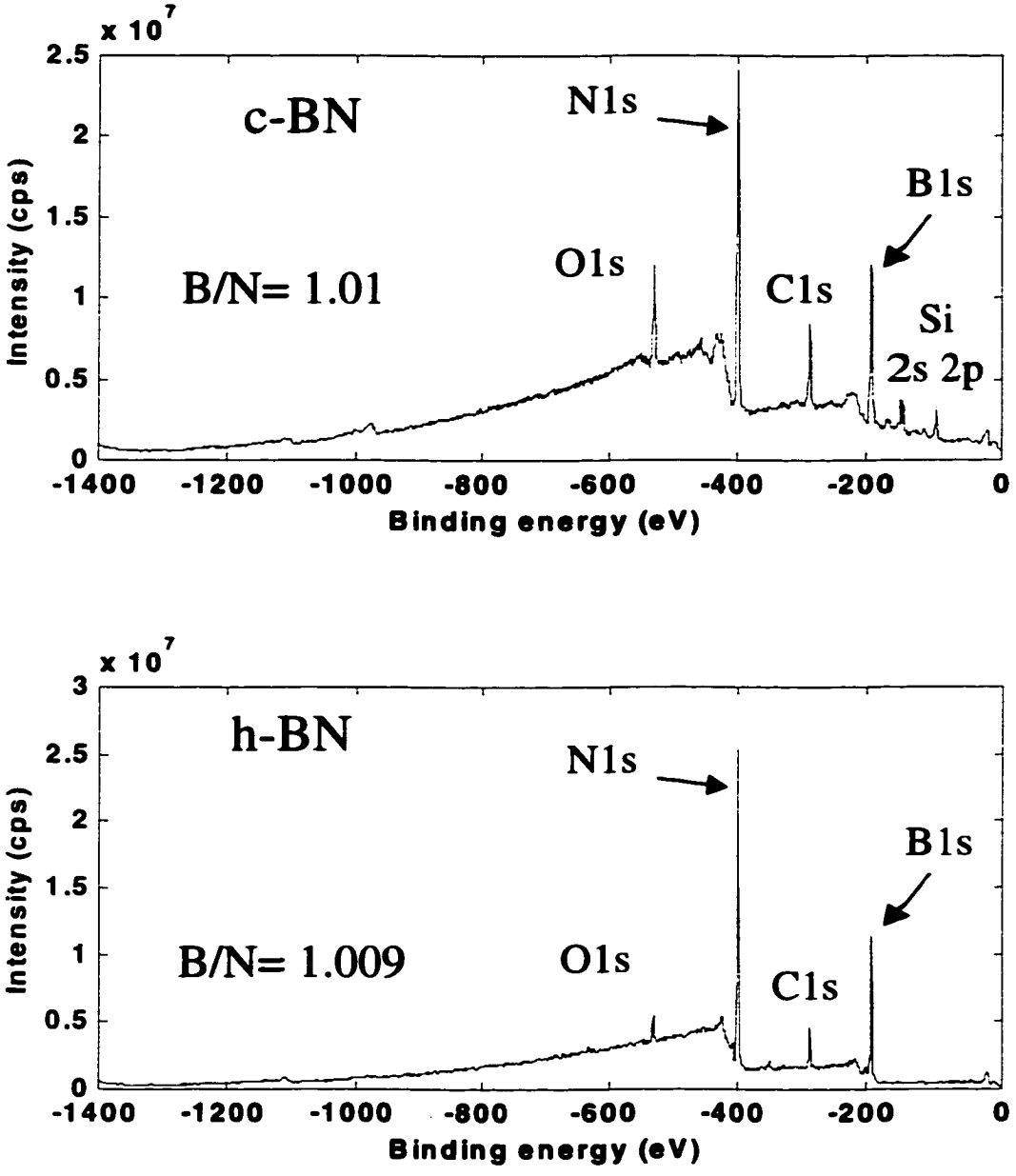

Figure 3.1.2 The XPS spectra from the powder reference samples on un-thinned bulk Si(001) wafers.

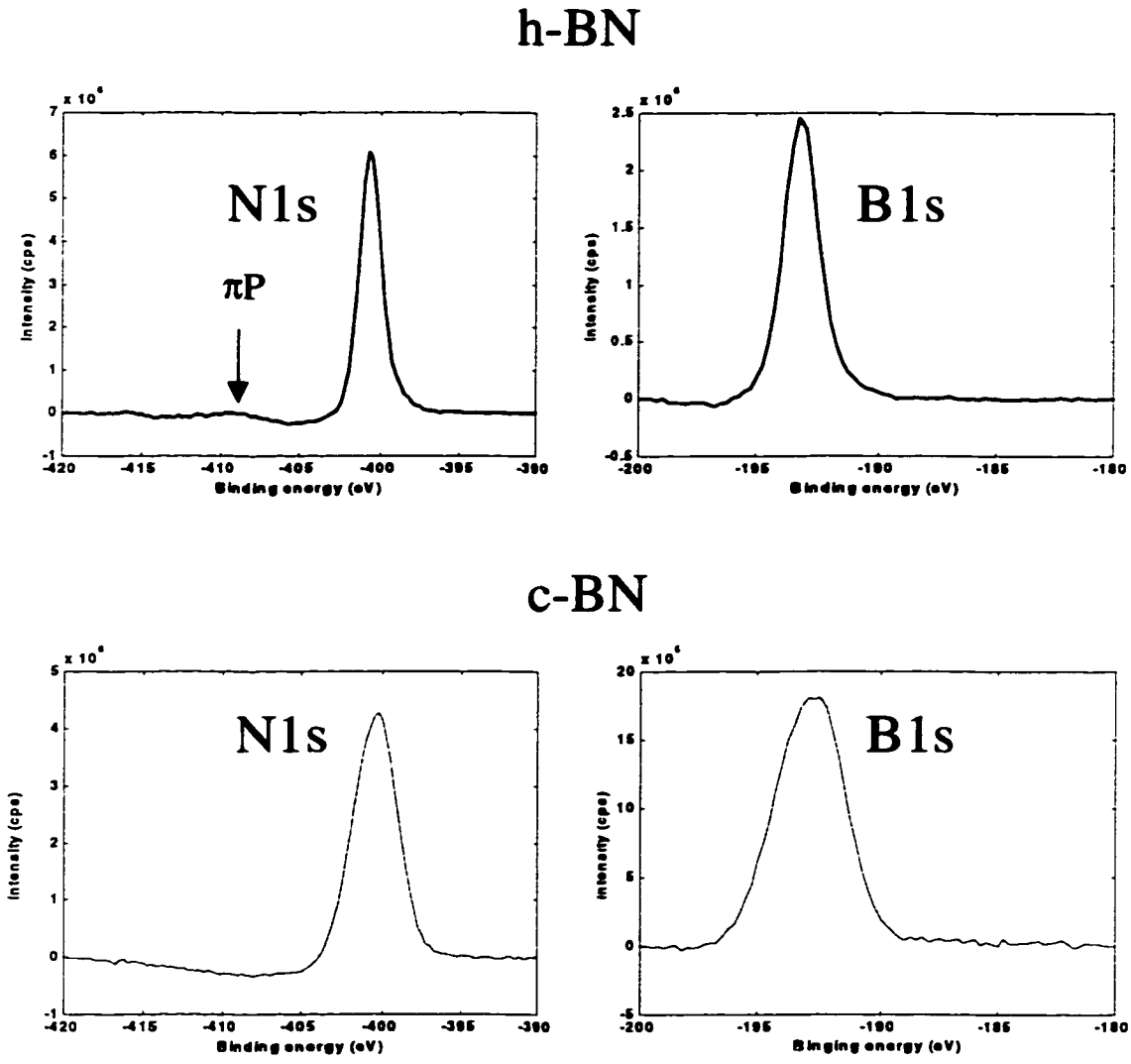

Figure 3.1.3 Detailed scans of the N1s and B1s core levels for the h-BN and c-BN.

and c-BN by Berns and Capelli (1996) and Trehan, Lifshitz and Rabalais (1990). Finally, the core loss peaks measured in the c-BN spectrum are wider than those for the h-BN spectrum. This is probably due to inelastic energy loss events that electrons suffered going through the relatively thicker impurity (carbon and oxygen) layer.

Some of the examples of the XPS spectra acquired from the films synthesized with various deposition parameters are given in Figure 3.1.4. The results of the chemical analysis indicated that the boron-to-nitrogen ratio in the films was close to those in the reference samples. Individual core loss peaks for the N1s and B1s are shown in Figure 3.1.5a and b, respectively. The πP features for films 1 and 2 are roughly 9 eV away from the core loss peak. However, for film 3 a similar feature is located at 5 eV away from the core loss peak for N1s. One can speculate that this could be the result of ion-induced damage to the BN structure. However, in the previous study by Trehan et al. (1990) on 1keV N_2^+ irradiated BN, only the formation of the πP feature has been observed. Other studies employing XPS for the chemical analysis of BN films reported only the presence of πP feature ~9 eV away from the core loss peaks (Ichiki, Amagi, Yoshida 1996; Wada and Yamashita 1992; Mineta, Kohata et al. 1990). Although Zunger, Katzir, Halperin (1976) and Zunger (1974) report experimental and theoretical values for a π-π^* interband transition in h-BN 6.0 – 6.5 eV away from the N1s peak corresponding to a direct optical band gap, the real nature of this feature is not clear and is still under investigation.

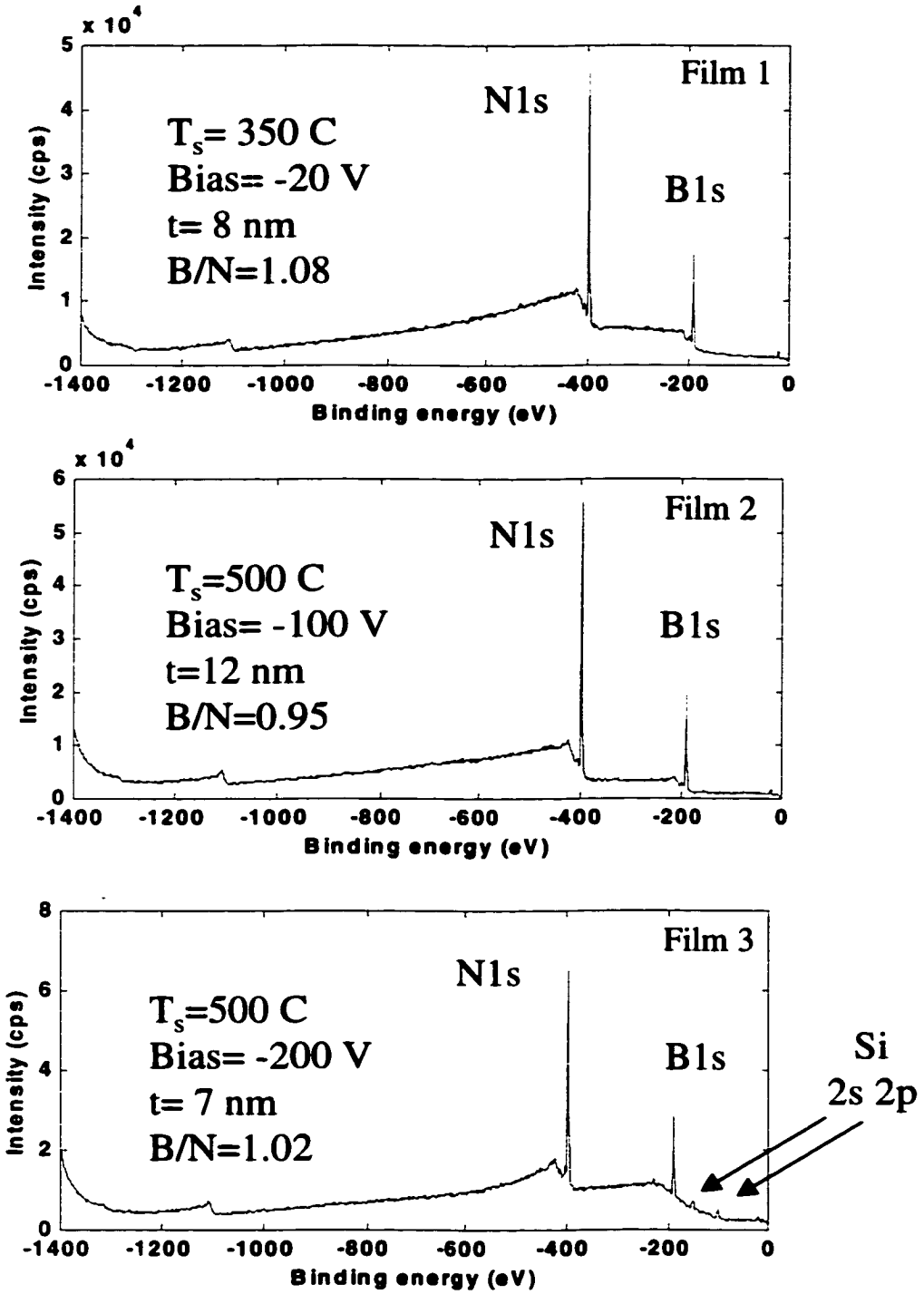

Figure 3.1.4 XPS spectra from BN films deposited on Si(001) substrates.

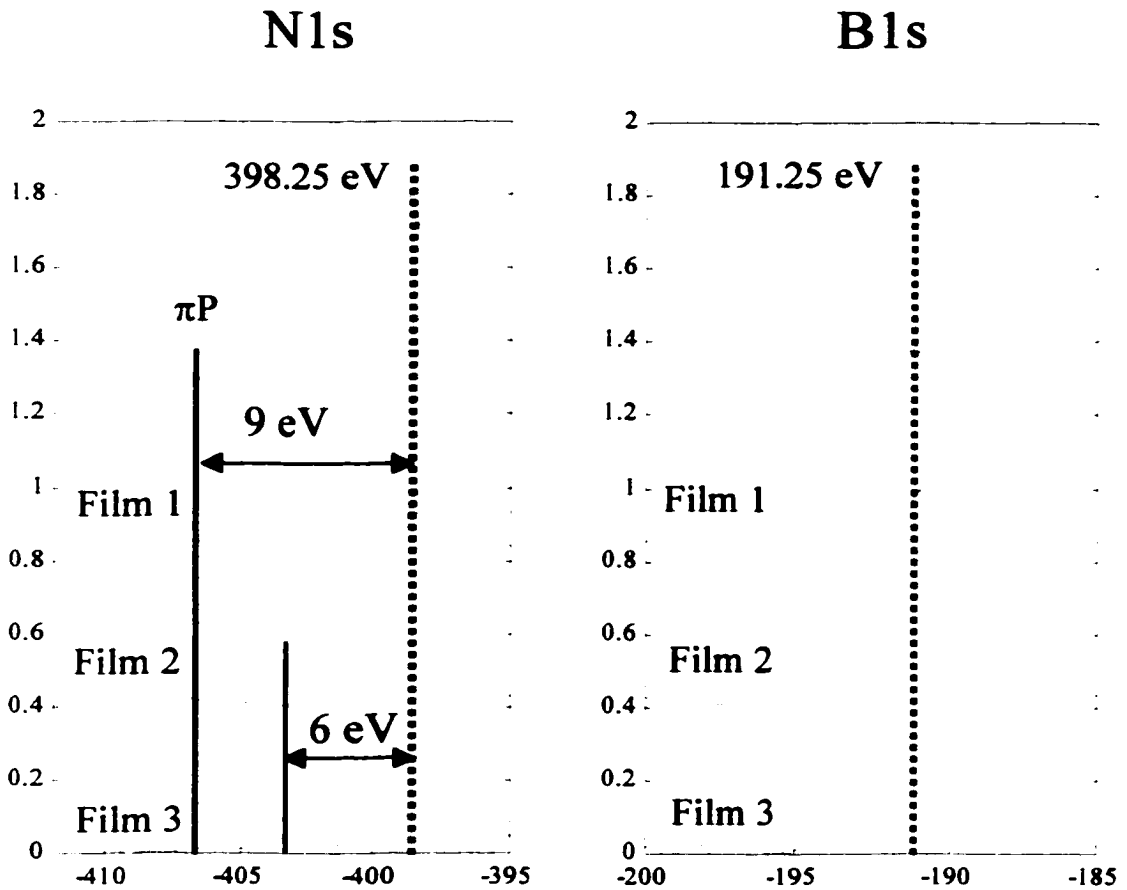

Figure 3.1.5 **Detailed XPS spectra of the N1s and B1s of the BN films deposited on Si (001) substrates. For films 1 and 2, the πP peak due to interlayer interactions for the basal planes is visible. For film 3, a loss feature was observed at approximately around ~6eV away.**

The morphology and the atomic structure of the films on the silicon substrates were investigated using the UHV-TEM attached to the SPEAR system. Figure 3.1.6 shows the plan-view HREM image from one of the films with the TED pattern inset. The presence of diffuse rings in the diffraction pattern suggests that the film did not have a well-defined crystal structure. The measurements on the diffraction pattern suggested that the three diffuse rings can be identified as (002), (100), and (102) planes of h-BN. However, the rings are too diffused to make accurate measurements for unambiguous identification of the planes. Under HREM scrutiny, it was observed that the film consisted of h-BN nano-crystallites (~2 nm, arrow A) with (002) planes oriented parallel to electron beam direction. Similar spaghetti-like morphologies were previously observed by Ikeda (1992) in plan-view as the underlying matrix for the c-BN containing films. The highly curved morphology also strongly suggests that these films are more likely to be turbostratic (t-BN) as the curvature disorders the intra-planar rotational registry and stacking.

The lattice spacing for the (002) planes was measured using the power spectra (~3.4 Å) from regions of the BN films under HREM examination where the underlying Si (220) lattice fringes were visible. The value found from power spectra was comparable to those measured from TED pattern (~3.36 Å). The BN films on bulk Si (001) substrates were also examined by preparing XTEM samples. In Figure 3.1.7, an XTEM image from one such film displays the well-known textured and columnar growth of t-BN layers. The structures of the films were inspected further using the dark

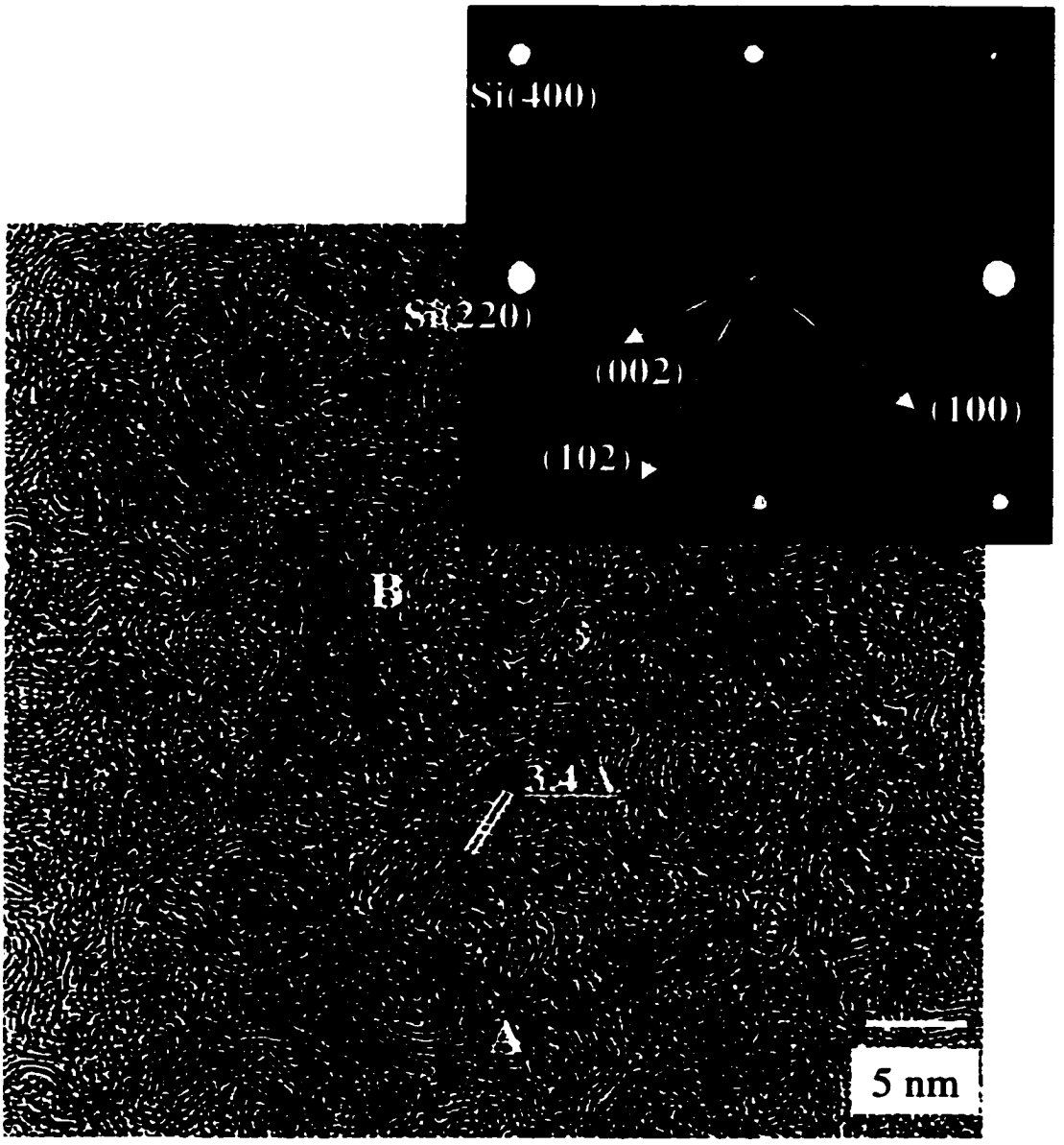

Figure 3.1.6 **The HREM image from the BN films deposited on Si (001) surface with the TED pattern inset. Arrows A and B point to BN crystallites with and without curved crystallites, respectively.**

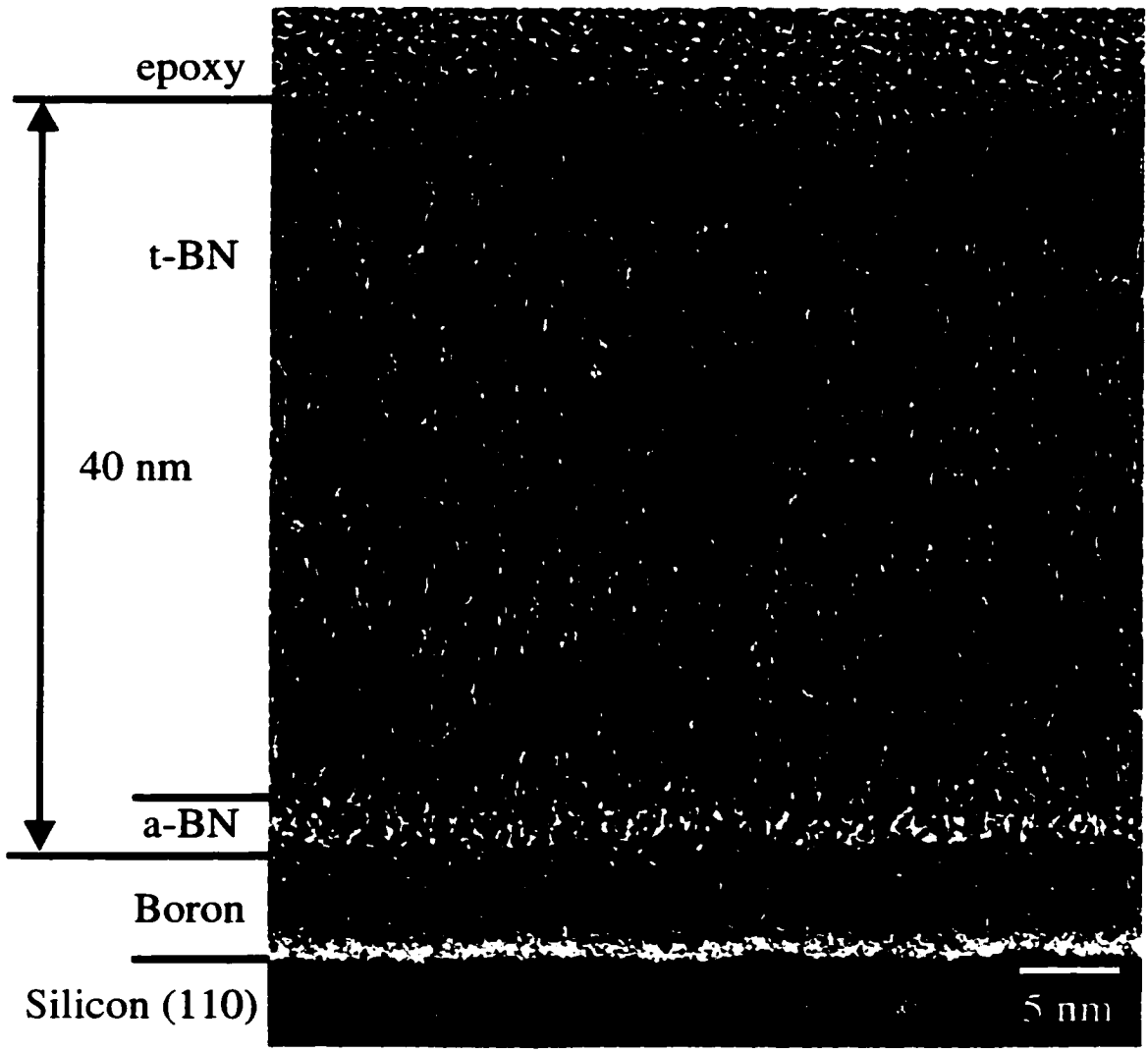

Figure 3.1.7 **The XTEM image from a BN film deposited on bulk Si (001) substrate. The film is approximately 40 nm thick and highly textured with (002) planes (basal) of t-BN growing perpendicular to the plane of the substrate.**

field mode of the TEM by centering the aperture on the spot from the (002) planes of t-BN. (Figure 3.1.8).

3.1.1.2 Growth on Cu (110)

Other than Si (001) substrates, thin films of BN were also deposited on Cu (110) substrates. Cu is a potential substrate for study of epitaxial growth as it has a lattice parameter very close to that of c-BN. It is also known that h-BN powder in Cu powder matrices and containers subjected to shock compression results in a higher yield of w-BN and c-BN (Sekine, Kobayashi, Nameki 1996). However, two previous studies (Kester, Ailey et al. 1994; Luthjie, Bewilogua et al. 1995) which used Cu substrates reported little or no presence of c-BN on the films. In the study by Mirkarimi et al. (1995), although some c-BN was detected on Cu substrates, presence of an epitaxial or other novel mechanism promoting the c-BN formation has not been verified. In addition, Cu (110) surface has been used to study stacking of C_{60} on metal surfaces (Murray, Pedersen et al. 1997; Fasel, Agostino et al. 1999; Fasel, Aebi et al. 1996).

Clean Cu (110) surfaces do not reconstruct, and therefore do not require heat treatment for a native reconstruction. The XPS spectrum from a typical Cu (110) substrate before cleaning is shown at Figure 3.1.9. The main impurity was found to be oxygen, which was cleaned by ion milling with 1 keV Ar^+ ions; the XPS spectrum for the clean Cu surface is provided in Figure 3.1.9 also.

The films on Cu were prepared using parameters similar to those used for the ones on Si. However, the substrate temperature for Cu samples was kept below 300 C

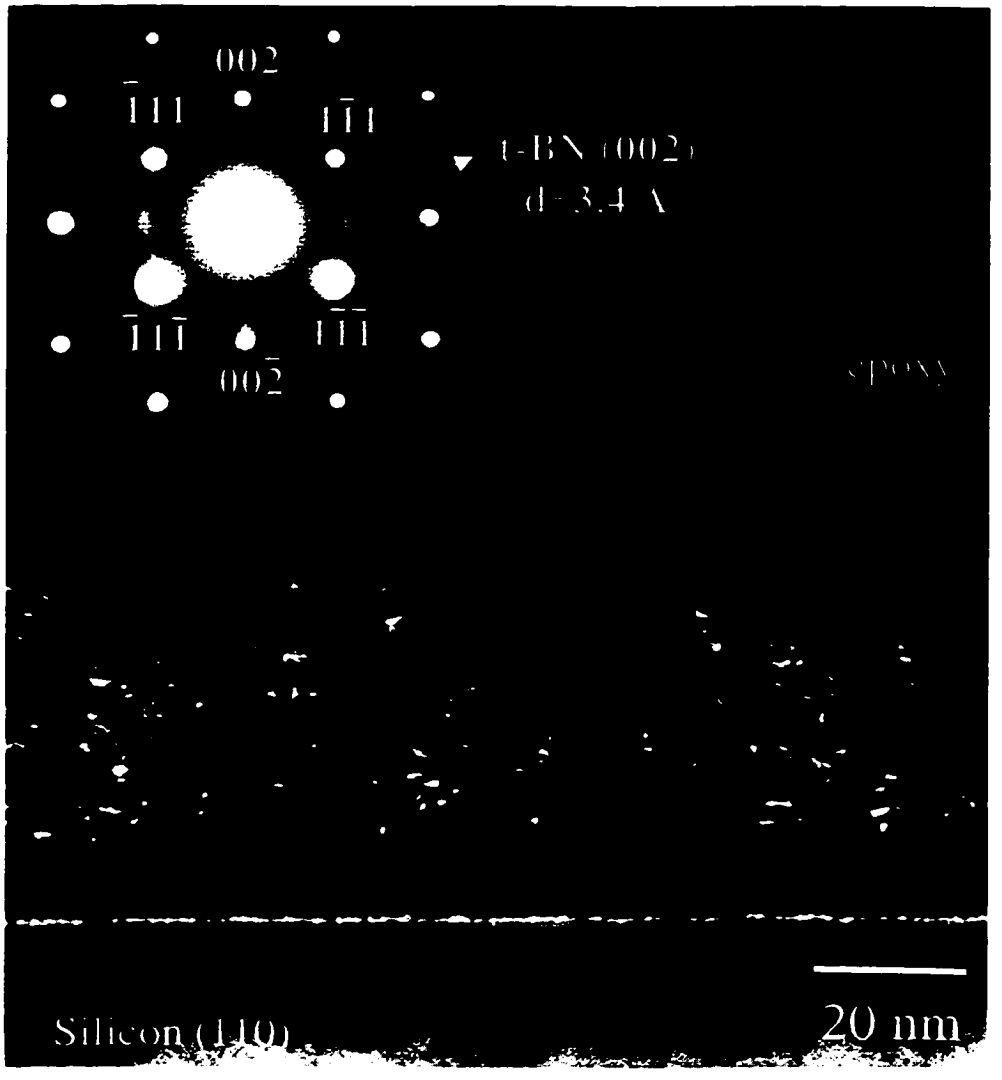

Figure 3.1.8 **The XTEM sample of the BN film imaged in the dark field mode using the (002) reflection from the t-BN. The columnar growth of t-BN is visible.**

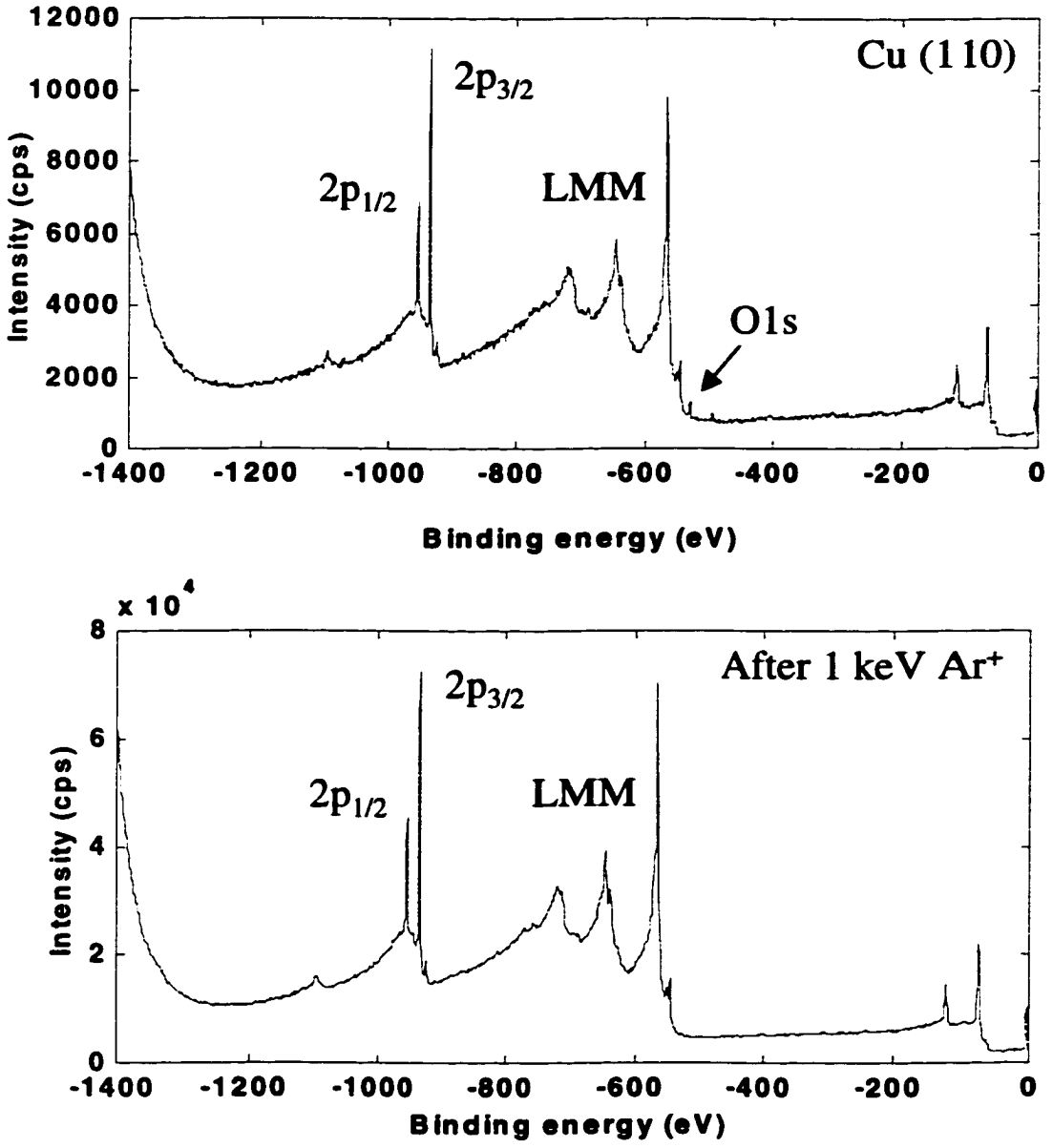

Figure 3.1.9 The XPS spectra acquired from the surface of Cu (110) substrates before and after cleaning with 1 keV Ar^+ ions.

(< ½ T_{melt} Cu) as the edges of Cu samples thicken very quickly due to surface diffusion, limiting the examination of thin films using the electron microscope.

In Figure 3.1.10, the XPS spectrum from a BN film deposited on Cu (110) is shown; the thickness of the film was calculated to be roughly 120 Å. The close-up of the N1s core loss peak (as mentioned earlier) displays the presence of a feature which is ~5-6 eV away. The Cu (110) substrates were investigated by the UHV-TEM after the chemical analysis of the films. The morphology of the BN films, as shown in Figure 3.1.11, was very similar to the spaghetti-like structure on Si (001) substrates. The (002) spacing for the t-BN was ~3.5 Å.

3.1.1.3 Growth on Polycrystalline Tungsten

Tungsten substrates were mainly used for depositions made at high temperatures (600C- 800C), as tungsten has excellent high temperature properties. In most cases, the duration for deposition experiments on tungsten substrates was kept shorter (15 to 20 minutes) in order to study the early stages of h-BN nucleation and effects of growth parameters. The procedure followed for the preparations of tungsten samples was very similar to those used for the silicon and copper substrates. Some oxygen was found on the surfaces, and upon ion milling with 1 keV Ar^+ ions and annealing at 1000C the surface was ready for subsequent BN deposition. (Figure 3.2.12).

The XPS spectrum from a BN film on tungsten substrate is shown in Figure 3.2.13. The nitrogen-to-boron ratio of the films was close to unity. In addition, the πP feature is visible ~9 eV away from the N1s peak suggesting that the sp^2-bonding was dominant in the film. The images from HREM investigation of the films also showed

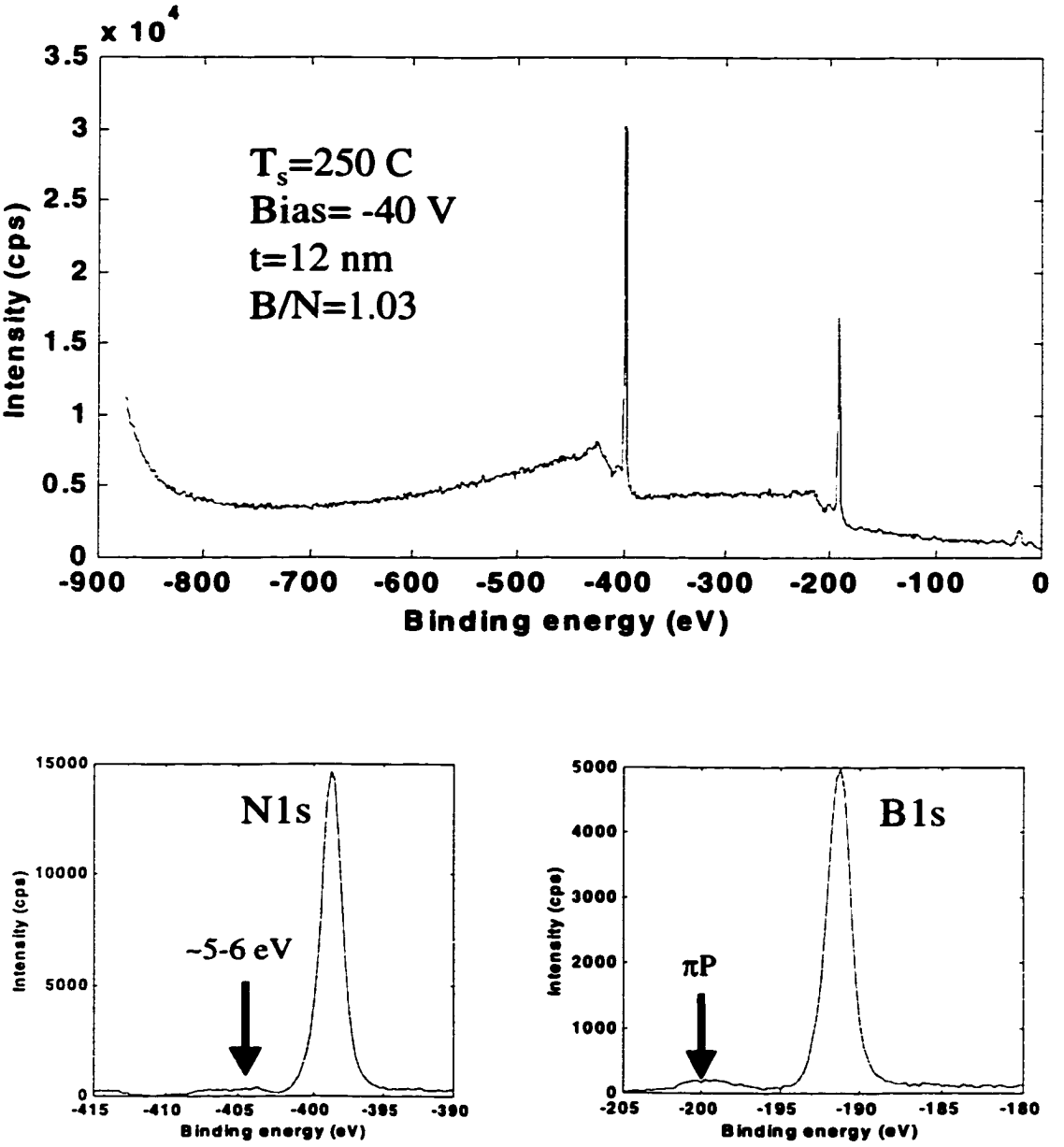

Figure 3.1.10 The XPS spectrum acquired from the BN film deposited on the surface of Cu (110) substrate. The detailed N1s core level indicate the presence of a feature ~5-6 eV away.

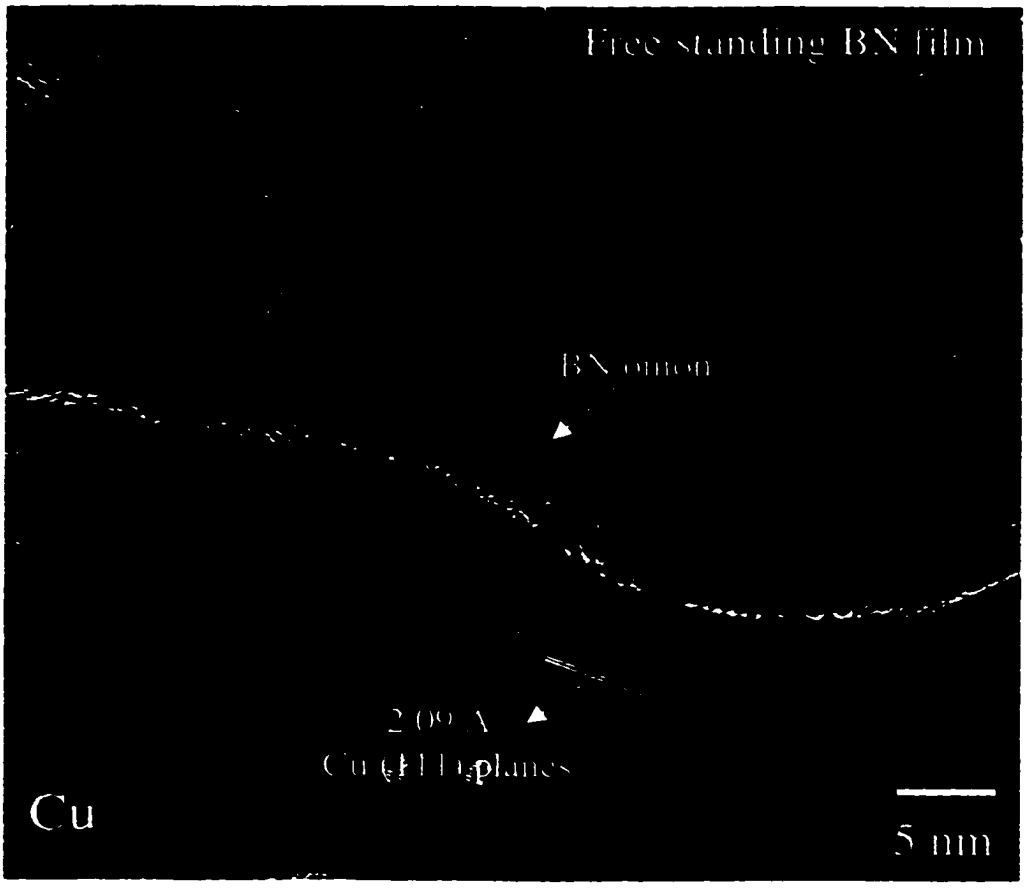

Figure 3.1.11 **The HREM image from the BN film deposited on Cu (110) surface with the TED pattern inset. Arrows A and B point to BN crystallites with and without curved crystallites, respectively.**

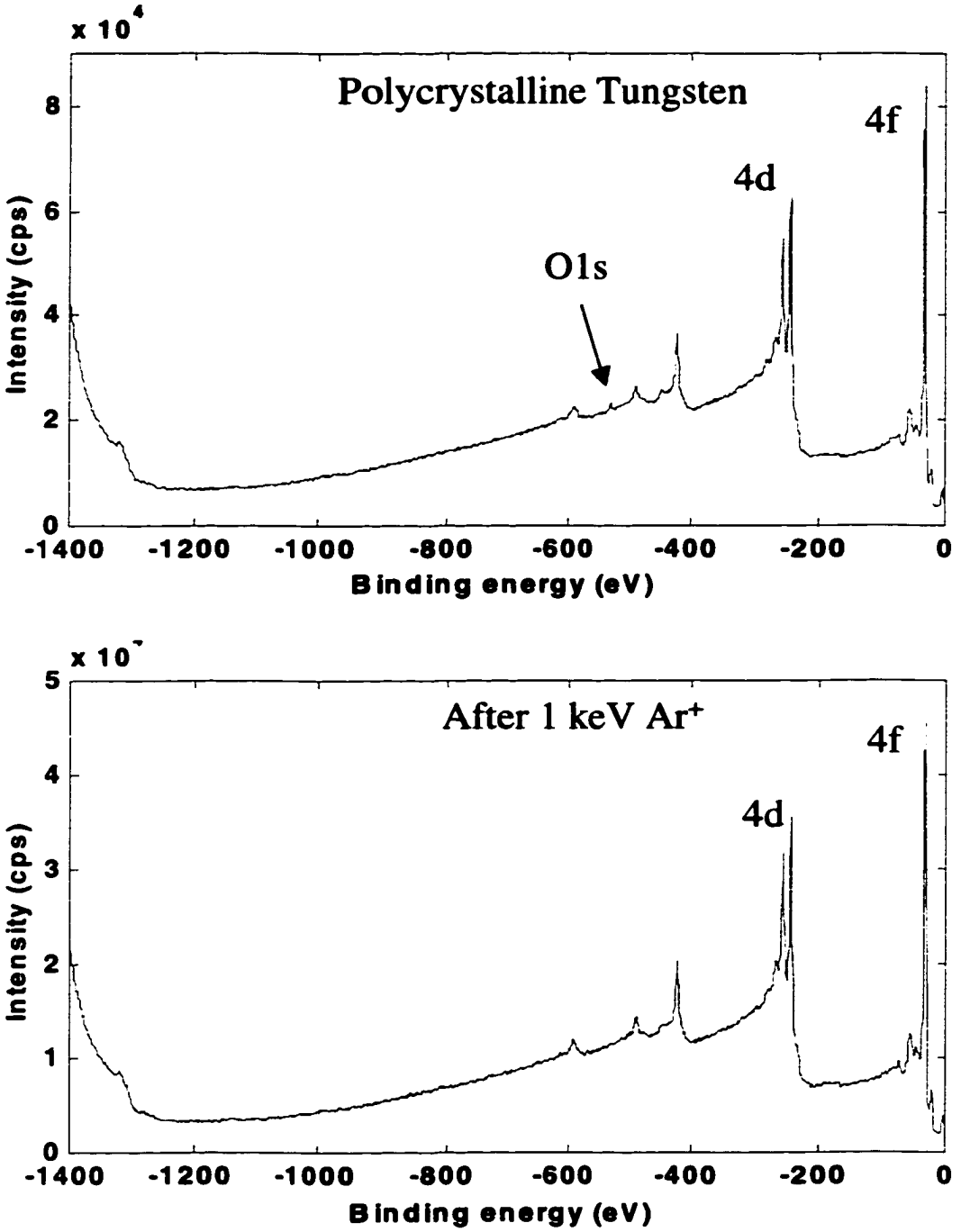

Figure 3.1.12 **The XPS spectra acquired from the surface of polycrystalline tungsten substrates before and after cleaning with 1 keV Ar^+ ions.**

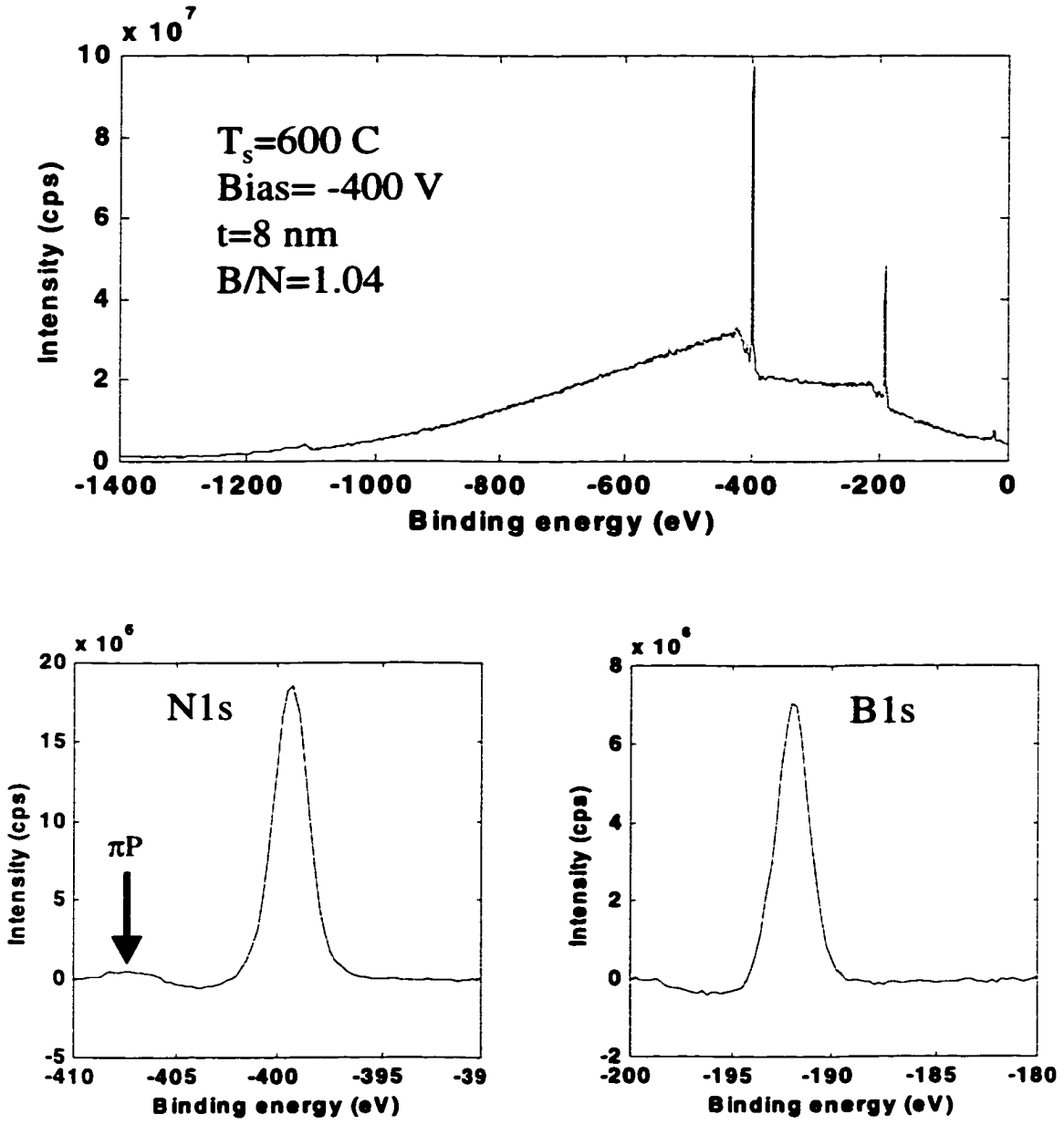

Figure 3.1.13 The XPS spectrum acquired from the BN film deposited on the surface of polycrystalline tungsten substrate.

presence of h-BN nano-crystallites embedded in a spaghetti-like BN matrix similar to those observed for on Si and Cu substrates. In addition, single-walled BN features were observed, as shown in Figure 3.1.14. These single-walled structures ranged from fullerene-like closed structures to one described as "nanohorns" by Iijima et al. (1999). Detailed reviews of these structures are made in the following sections on BN nanotubes and fullerenes.

3.2 Effect of Growth Parameters on BN Film Morphology

Variations in the morphology of BN films deposited using the SINBAD system were investigated with respect to the deposition parameters used during growth. It was observed that substrate temperature, bias, and the flux used during the experiments were the main parameters effecting the atomic structure of these films. In fact, these parameters control the essential processes during film growth with energetic particles such as the diffusion, damage, and the growth rate. The illustration in Figure 3.2.1 summarizes some of the thermally activated processes (substrate temperature) and processes activated by the momentum transfer (ion-bombardment) at the substrate. In this section, the emphasis will be on defect formation mechanisms and subsequent defect annihilation mechanisms observed for BN thin films.

The effect of substrate temperature on c-BN nucleation has been studied in detail (Friedmann, Mirkarimi et al. 1994; McCarty, Mirkarimi et al. 1996; Tanabe, Hayashi 1992). Depositions at very high temperatures (~1000 C) were found to decrease the

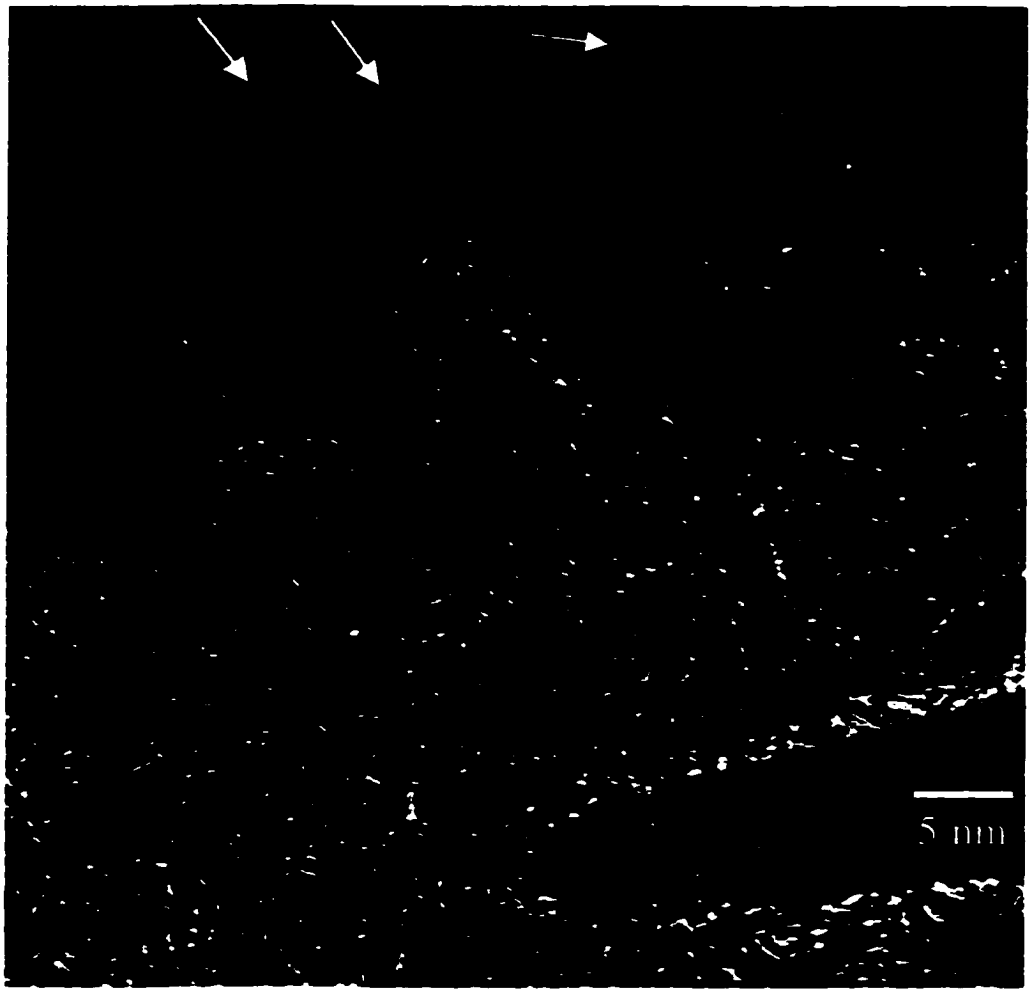

Figure 3.1.14 **Plan view HREM image from a BN film deposited on tungsten. Arrows point the single-wall features on the sample. In addition, plate-like h-BN crystallites were observed.**

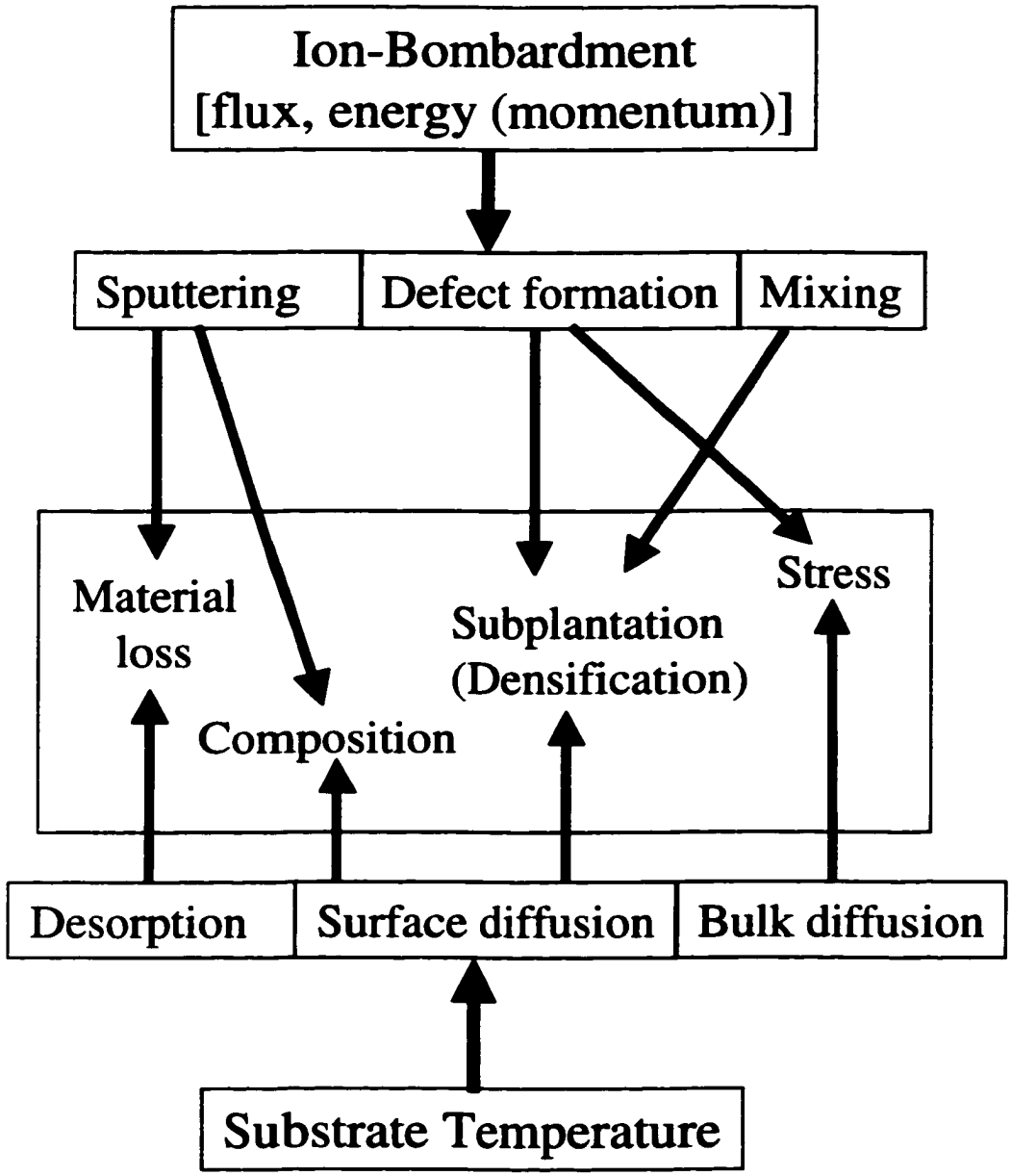

Figure 3.2.1 **Summary of the main process variables employed during ion-beam assisted deposition of thin films and their effects on the film formation processes.**

stress and allow for thicker c-BN films. In addition, substantially thicker t-BN layers for high temperature growth experiments were recorded by Kester et al. (1994). Although the results from these studies reported a strong tendency toward a threshold temperature for c-BN growth (~100 C) below which only t-BN could be synthesized, they contradict with the recent thermodynamic treatments, suggesting c-BN as the stable phase at ambient conditions (Solozhenko 1995). In addition, the thicker h-BN layers in films deposited at high substrate temperatures are consistent with this new view of the P-T phase diagram of BN, which predicts hexagonal phase as the stable one for high temperature and pressure regions. However, the threshold temperature for c-BN hints possible thermally activated processes, such as a diffusion-related mechanism, promoting the conversion of sp^2-bonded planar hexagonal networks to sp^3-bonded puckered hexagonal networks. In this study, morphological characterization of BN films deposited at various temperatures has been used to investigate the effects of substrate temperatures.

Figure 3.2.2 illustrates the effect of increasing substrate temperatures on the BN films. The film deposited at 300 C is covered with single-wall BN nano-features; a single-wall BN nanotube and a fullerene like feature are found in the film. The rest of the film is also made up of similar single-walled structures, and overall the morphology can be described as a loose *woolen yarn*. The films deposited at temperatures well above 300 C displayed the presence of onions and other multi-walled BN structures. The film synthesized at 600 C had dense morphology with a few single-wall features buried under the *spaghetti* matrix, as mentioned earlier.

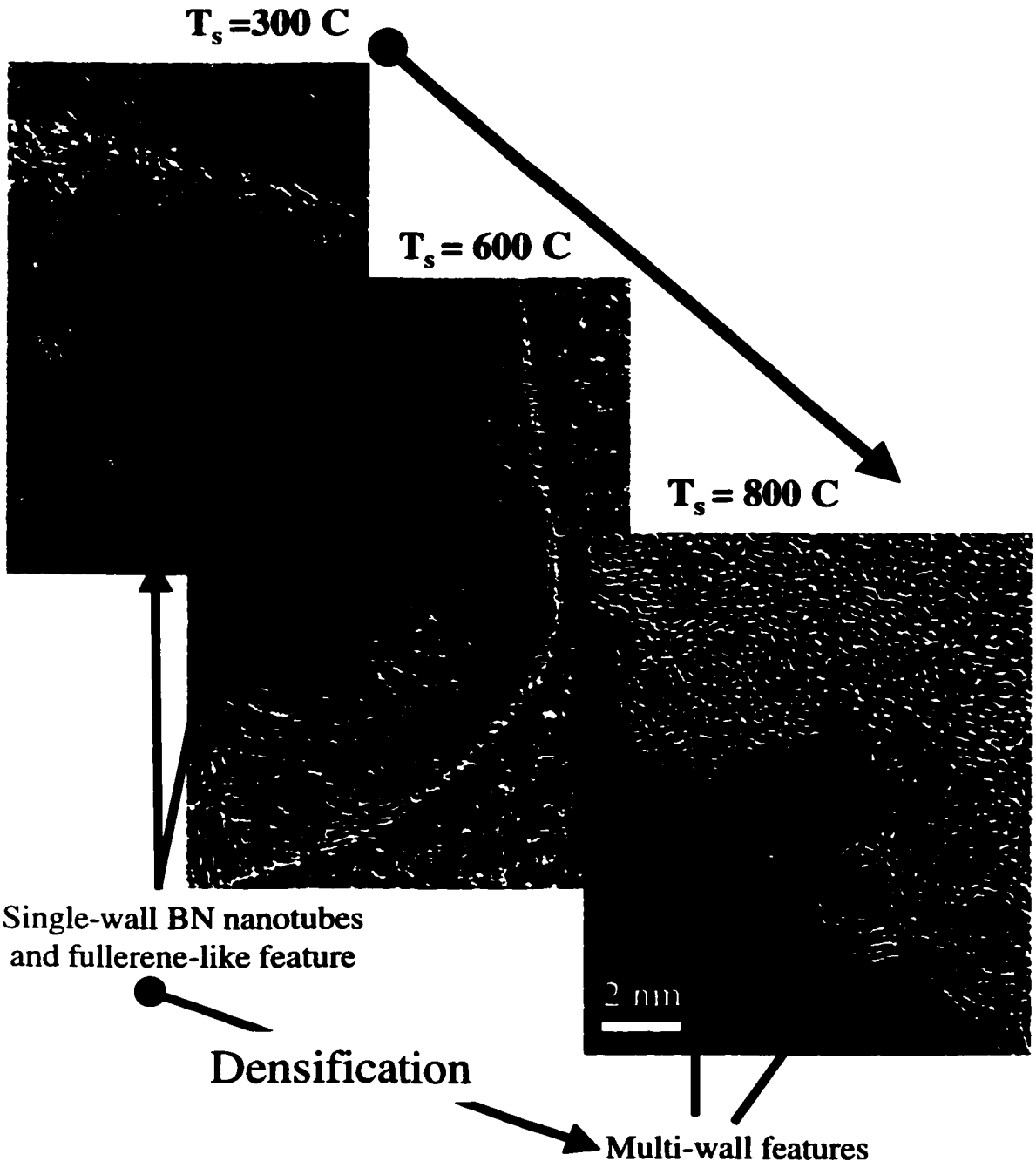

Figure 3.2.2 **Collage of HREM images from BN films on tungsten substrates displaying the variation in the morphology of the films at increasing substrate temperatures. Films deposited at higher temperatures display higher density of multi-wall features.**

Aside from the large onion, the HREM image of the film deposited at 800 C displayed the *spaghetti* structure, also. The major difference between the films deposited at 600 C and 800 C is that the features in the latter are denser and more circular in shape. Hence, the net effect of using higher substrate temperatures is the densification of the films.

The as-deposited films on Si were also subjected to electron beam heating (550 C, 10 min) as a continuation of experiments on BN films, which were mentioned earlier. The purpose of these experiments was to obtain information about the thermally activated processes under steady state conditions. The 3 keV electron beam was applied to the samples from the non-film side of the substrate in order to isolate the thermal effects from those of the momentum transfer (Grozea, Landree, Marks 1997). The XPS spectrum, Figure 3.2.3, acquired from the film on Si (001) after the heat treatment experiment did not indicate significant deviations from the before spectrum. The HREM investigation of the surfaces, indicated densification of the spaghetti morphology in the films, helping with the overall ordering to the structure (Figure 3.2.4). H-BN onions and some crystallites were observed on the films. Furthermore, a small decrease in the (002) plane spacing for the heat-treated t-BN film was measured from the TED pattern (3.31 Å vs. 3.36 Å of as-deposited film).

Boulanger, Andriot et al. (1995) reported the growth of well-ordered h-BN plate-like crystallites (20-100nm, and $d_{002} \sim 3.4$Å) and large polygonal onions with radii over 10 nm from highly disordered pyrolytic BN particles at 1650 C by heating with CO_2

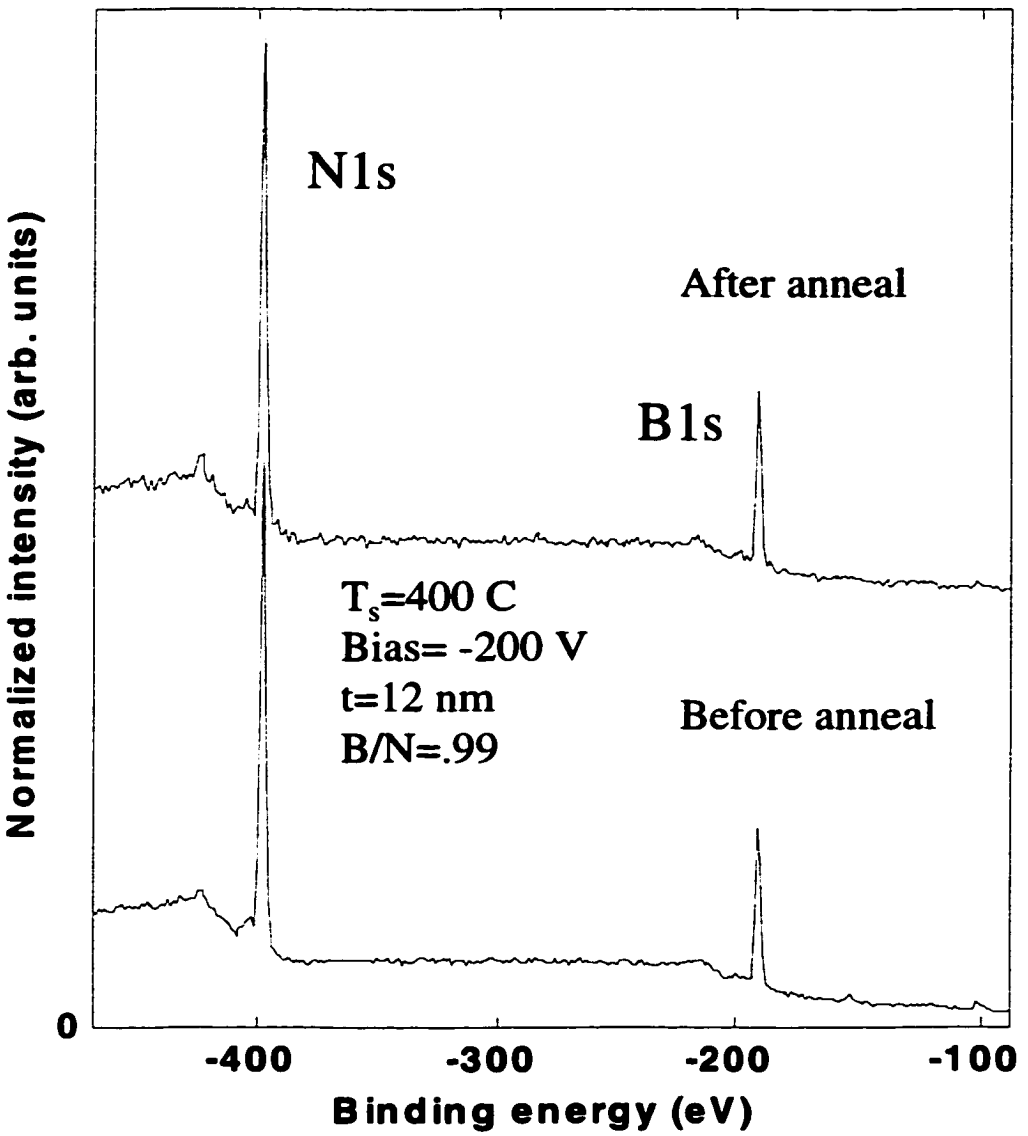

Figure 3.2.3 **XPS spectra acquired from BN films on Si (001) substrates before and after annealing with at 550 C for 10 minutes.**

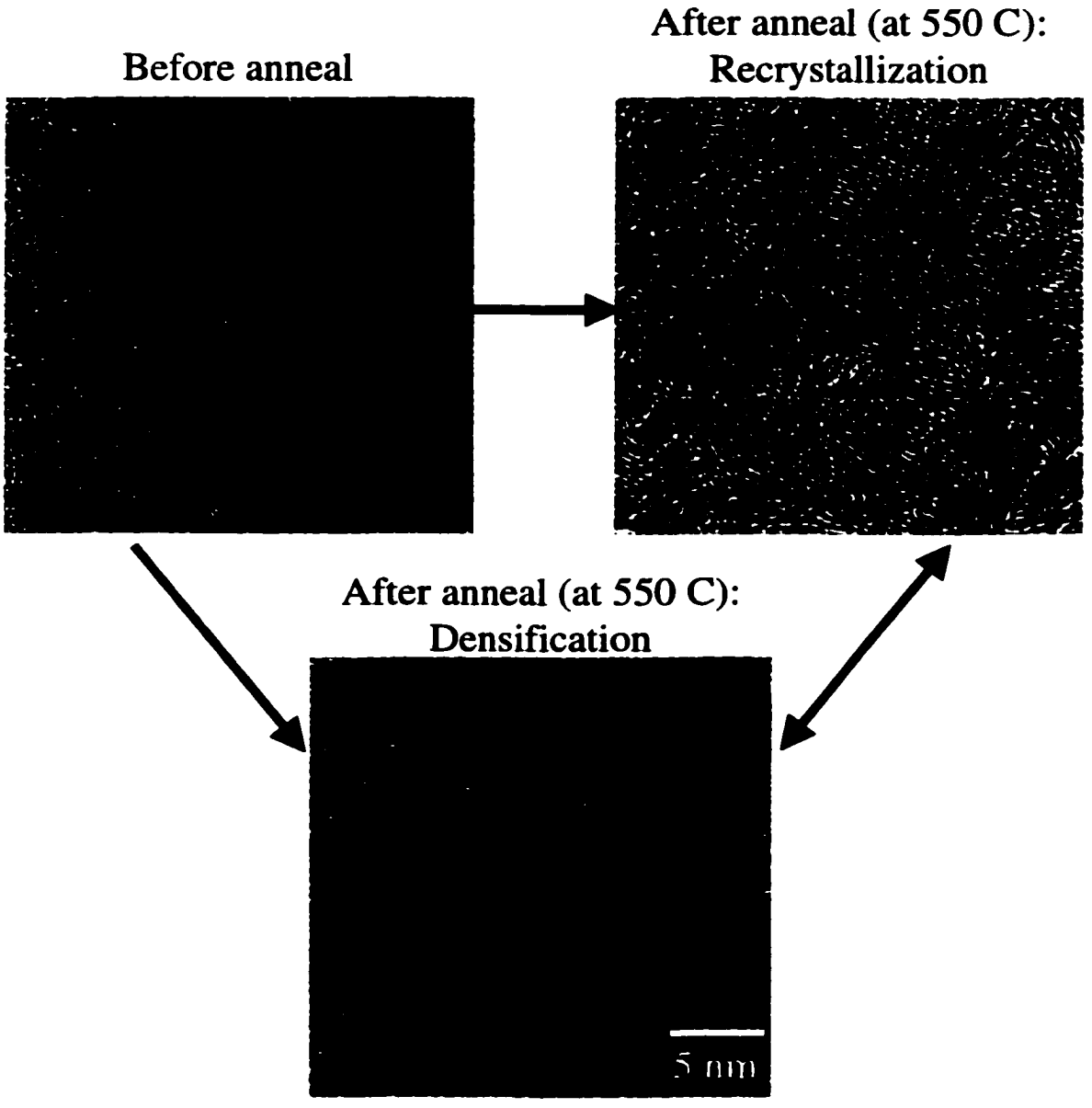

Figure 3.2.4 **HREM images from the BN films on Si (001) substrates displaying the change in the atomic morphology of the films before and after annealing. In general, the film indicates densification and at regions recrystallization takes place. Arrows point to crystallite and onion formations.**

laser. In these experiments, the growth of h-BN crystallites was expected due to thermodynamical considerations but, nucleation of onions or multi-walled circular features with extra strain energy, due to the curvature, could not be explained with this approach. However, Tomanek, Zhong and Krastev (1993) discussed the stability of single- and multi-wall carbon onions, cones, and tubes with respect to bulk graphite. They proposed that the destabilizing effects of bending decreases as the number of walls increase in a multi-wall nested structure. They reported formation energies of such multi-wall structures to approach to that of graphite. As a summary, heat treatment of as-deposited films helped the local ordering of t-BN matrix and induced grain growth in the form of onions. In addition, the depositions on the tungsten substrates suggested that higher substrate temperatures allowed for the growth of multi-walled BN structures, and the number of shells increased as the substrate temperatures were increased.

Another important factor effecting the morphology of h-BN films in the early stages of growth was the substrate bias, which can be considered as the mean energy of the ions impinging on the growing films. The most important effect of ions during deposition can be identified as defect generation at the surface of the growing film. The effects of ion-bombardment such as enhanced diffusion (bulk and surface), sputtering and ion-induced mixing can be considered as lesser important factors. Interested readers can refer to Kinchin and Pease (1955), Hobbs et al. (1994), and Robinson (1994) for detailed treatments of ion-irradiation.

Figure 3.2.5 illustrates the difference between the films deposited on tungsten using no bias and –350 volts (d.c.) bias on films A and B, respectively.

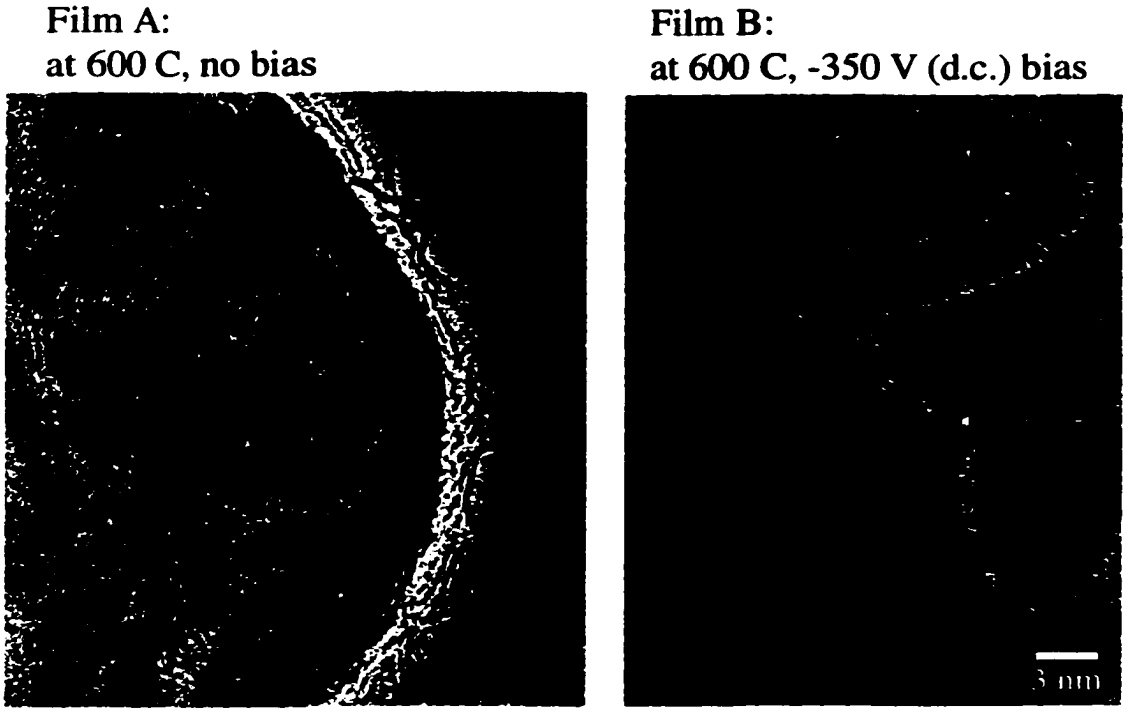

Figure 3.2.5 **HREM images from two different BN films on polycrystalline substrates deposited at different bias settings. The arrows point to single-wall structures on Film A, deposited without a bias. Film B, deposited using -350 V(d.c.) bias resulted in a denser morphology with some plate-like crystallites and onion-like features.**

Both of these films were deposited using a substrate temperature of 600 C. The general morphology of the film A indicated that the (002) planes of the t-BN film oriented themselves parallel to the substrate edge with some nanohorn-like features growing out toward the vacuum. On the other hand, the film B displayed a definite woolen-yarn structure with some plate-like crystallites and numerous single-wall BN nanohorns growing perpendicularly to the substrate edge. Overall, the differences in the morphology of films A and film B were dramatic. McCarty, Mirkarimi et al. (1996) also reported differences for films grown under ion-irradiation and without ions; they observed that h-BN films grown under ion-irradiation were better ordered and large curved crystallite formation was observed. Banhart, Zwanger, Muhr (1994) and Stephan et al. (1998) also reported crystallization of amorphous BN and onion formation in h-BN particles under electron-beam irradiation. In addition, Golberg et al. (1997) observed similar effects of electron beams on BN nanotubes. Hence, the ordering and crystallization of h-BN is expected at high substrate temperatures and pressures through thermodynamic considerations, which can be induced by irradiation locally.

The results of the current study summarized here also indicates that higher substrate temperature (300 C – 800 C) and high bias (~ -200 to -350 V d.c.) sustained at the substrate during the deposition of h-BN films promote the synthesis of onions, formation of crystallites, and related highly curved dense structures. In fact, the XTEM from a BN film deposited (T_s=550 C, -200 V d.c. bias) on a bulk Si (001) substrate displayed small crystallites buried at the surface region of the t-BN with fine lattice spacing, as shown in Figure 3.2.6.

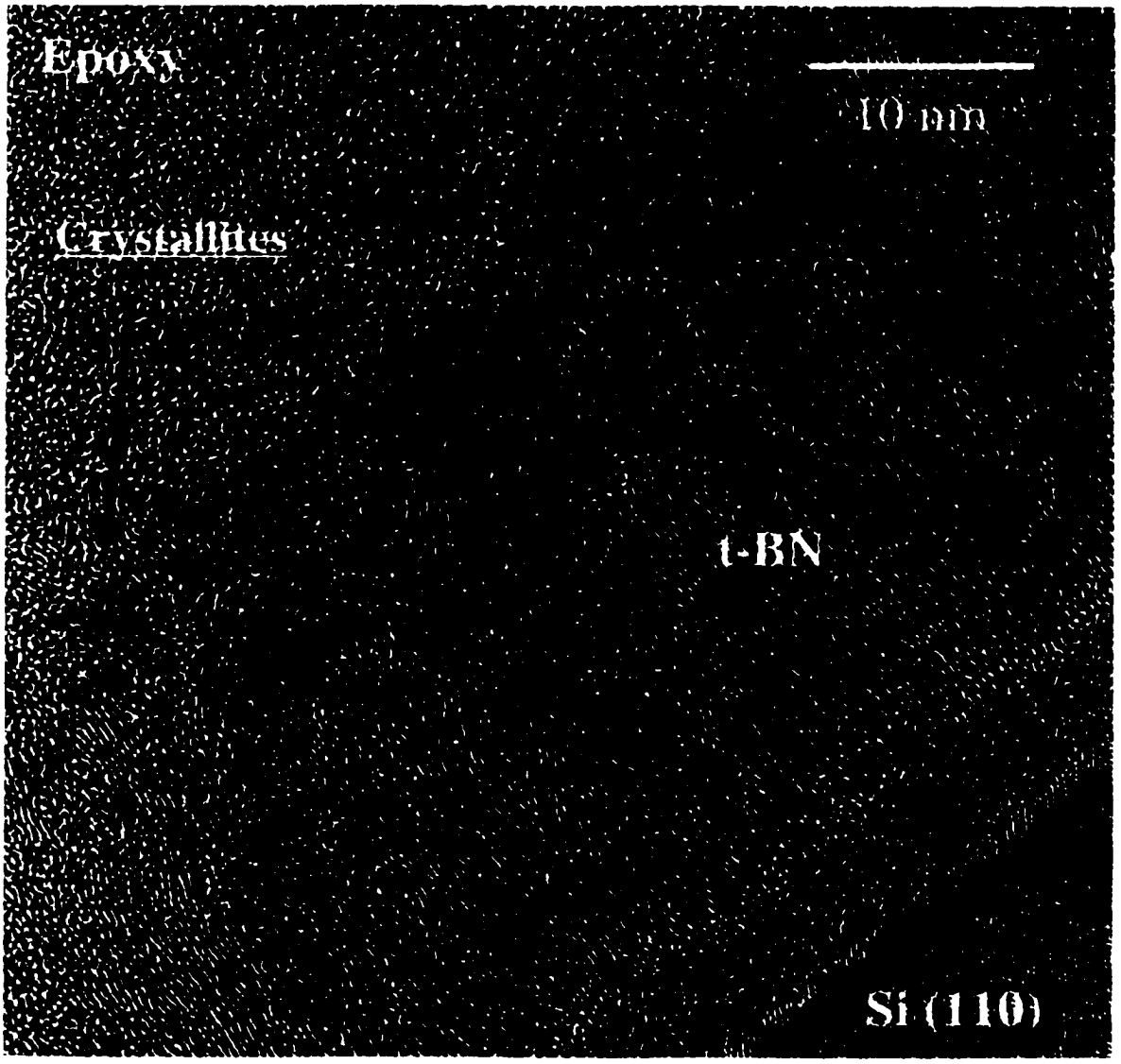

Figure 3.2.6 **The XTEM image from a BN film deposited on bulk Si (001) substrate deposited with parameters promoting ordering of h-BN crystallites and onion formation. The crystallites at the top region of the film display lattice spacing matching that of (111) c-BN planes.**

The spacing of these crystallites, approximately ~2.09 Å, does not match the possible metals and their nitrides that could be sputtered on the substrate during deposition, such as molybdenum and tungsten, but they matches (111) lattice spacing for c-BN.

It has been argued by Collazo-Davila, Bengu at al. (1999; 1998) that the distortion of the B-N bond at the curved ends of these structures could play an important role for the transition from a planar sp^2-bonding arrangement to curved sp^3-bonding. Thus, it can be suggested that the highly curved BN sheets in onions and similar curved structures that were observed in BN films deposited at highly energetic conditions also act as preferential nucleation sites for the sp^3-bonded cubic phase. In 1980, Iijima reported evidence for tetrahedral (sp^3) bonding in polygonal carbon onions and multi-wall cones. Most importantly, graphite-to-diamond transformation was observed at the centers of similar carbon onions, which are synthesized under intense electron-beam irradiation and heating (Banhart and Ajayan 1996; Zaiser and Banhart 1997). Although c-BN synthesis with a similar method is yet to be reported, the presence of onions and nanoarches under conditions promoting c-BN growth suggest that these are transient structures assisting the transition from h-BN to c-BN. In conclusion, the particular region in the parameter space for the substrate temperature and bias has been verified which is shown to promote deposition of structures in BN thin films that can be considered as the precursors for the sp^3-bonded c-BN.

3.3 Synthesis of BN Nanotubes and Fullerenes

3.3.1 Nanotubes and Fullerenes: An Introduction

Since the original discovery of C_{60} and the fullerenes by Kroto, (1985), a new region of science has begun to be unearthed. Fullerenes are simple closed sp^2-bonded carbon networks made up of primarily hexagons and 12 pentagons (due to Euler's theorem)[¥]. Some fullerenes of various sizes are shown in Figure 3.3.1. Innovative uses for fullerenes, such as superconductors, catalysts, ferromagnets, and photoconductors are proposed.

The methods for synthesizing fullerenes stemmed from the long known phenomenon of monocyclic carbon clusters in the carbonaceous gas phase generated by creating an arc-discharge between graphite rods or by laser-ablation of graphite in an inert atmosphere. Although the mechanism that leads to stable fullerene structures remains to be addressed, Smalley and Colbert (1995) argue that under certain circumstances these clusters grow or coalesce into single graphene sheets. The closed forms of these graphene sheets are suggested to be the result of defects in the hexagonal network such as pentagonal rings. This view is known as the "pentagon road" model. This model is also capable of explaining the formation of nanotubes with slight

---

[¥] According to Euler's theorem for polyhedra, the sum of the number of vertices and faces less the number of edges in a polyhedral closure is always equal to two:

$$V - E + F = 2$$

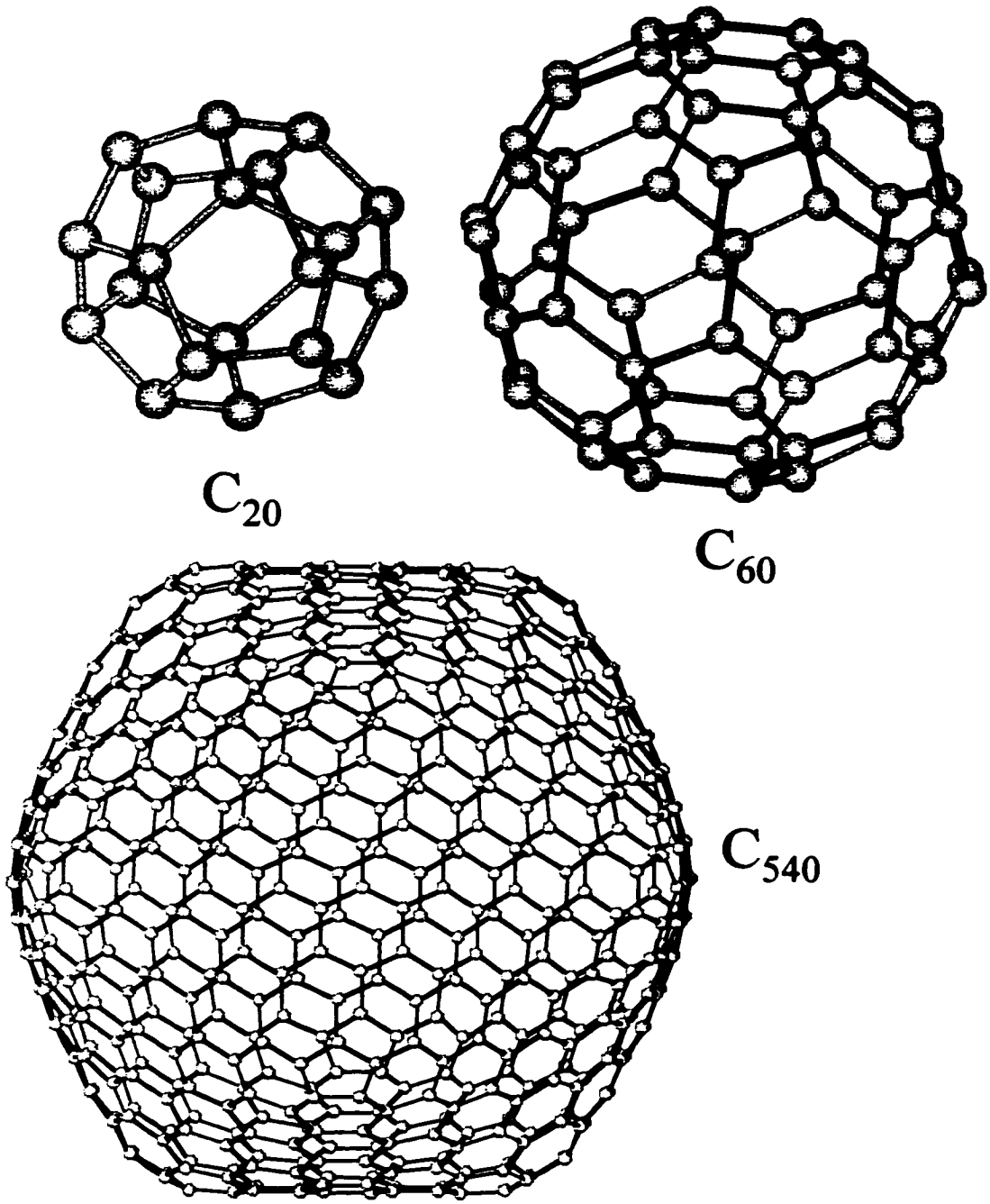

Figure 3.3.1 **Some carbon fullerenes; C_{20} is the smallest possible fullerene with no hexagons; C_{60} (Buckminsterfullerene) with 12 pentagons and 20 hexagons; C_{540} has 12 pentagons and 240 hexagons.**

modifications, the "tube detour". Nanotubes are simply elongated fullerenes lacking the curved closures, or caps. An example of a single-wall tube is shown in Figure 3.3.2.

Iijima (1991) reported the existence of multi-walled carbon nanotubes on the cathode of a Kratschmer-Huffmann fullerene reactor, originally designed for the mass production of fullerene molecules (Kratschmer et al. 1990). It was described that these nanotubes might be up to 1 μm in length, and have multiple layers of diameters ranging from 4 to 30 nm. The interlayer distance for the carbon sheets in these multilayers (d_{002} =0.34 nm) is found to be somewhat larger than that of graphite (d_{002} =0.335 nm), which is ascribed to the curvature of the tube. Later, Ebbesen and Ajayan (1992) optimized the process allowing for large-scale synthesis of carbon nanotubes. Consequently, other techniques such as laser ablation (Guo, Nicolev et al. 1995), hydrocarbon pyrolysis (Endo Takeuchi 1993; Amelinckx et al. 1994), CVD (Yudasaka et al. 1995; Huang, Xu, Ren and Wang 1998) and PECVD (Tsai et al. 1999) were also found to be successful in synthesizing multi-wall carbon nanotubes.

Theoretical calculations (Hamada et al. 1992) and measurements on nanotubes (Ebbesen, Lezec, Hiura et al.1996) suggested that electronic properties of nanotubes are strongly dependent on the helicity and the diameter of the tubules. Nanotubes could behave as semiconducting or metallic nanowires. Another material property of nanotubes that is a function of tube diameter and helicity is the Young's modulus (Yao and Lordi 1998).

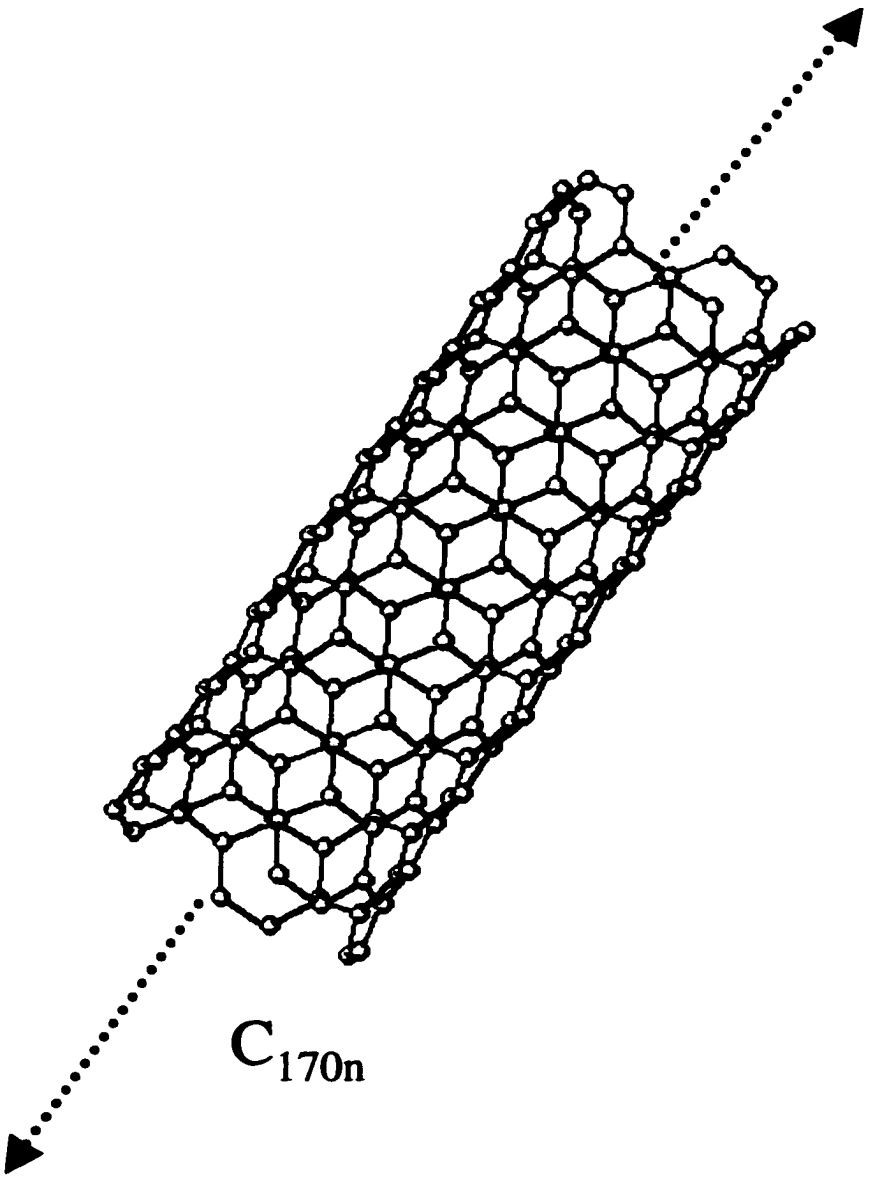

Figure 3.3.2 **A single-wall carbon nanotube.**

Both experimental measurements by Treacy et al. (1996) and calculations agree that nanotubes have Young's modulus close to in-plane single crystal graphite; thus, the nanotubes are far stronger than carbon fibers.

One of the first suggestions for the application of nanotubes was in the production of nanowires by filling them with metals through capillary suction (Broughton and Pederson 1992). In fact, Ajayan and Iijima (1993) successfully carried out experiments that resulted in Pb filled nanotubes. Some recent nano-engineering applications are as follows: (i) field emission sources (Rinzler, Hafner and Nikolev et al. 1995); (ii) STM tips (Dai et al. 1996); (iii) H_2 storage (Dillion et al. 1997); and (iv) nano-Velcro (Berber et al. 1999). Several commercial applications of nanotubes have also been developed such as the Samsung CNT/226FED, a matrix addressable diode-flat panel display with 4.5–inch fully sealed carbon nanotubes (Choi et al. 1999). Furthermore, using nanotubes as artificial muscles (Baughman et al. 1999), and even laser driven atomic pumps for single atom deposition machines (Kral and Tomanek 1999) are in the works.

Although most of the attention is directed towards carbon-related nanostructures, several other compounds were proposed to form fullerene-like structures and tubules. Miyamoto, Rubio et al. (1994a; 1994b) proposed nanotubes of p- and n-type semiconducting BC_2N and metallic nanotubes of BC_3. The plausibility of BN nanotubes has been argued by Blasé et al. (1994) and Rubio et al. (1994). Recently, Boustani et al. (1999) pointed out the remarkable structural stability of pure boron nanotubes.

In 1995, Chopra et al. reported the synthesis of BN multilayer nanotubes for the first time, which was followed by the Loiseau et al. (1996) observing single-layer BN

nanotubes. Later, studies reporting on the synthesis of BC_3 (Weng-Sieh et al. 1995), BC_2N (Stephan et al. 1994; Redlich et al. 1996) and other nanotubes followed. Nanotubes of some layered metal-sulfides were also synthesized, such as MoS_2 (Margulis et al. 1993) and WS_2 (Tenne et al. 1992). A recent review on the non-carbon nanotubes by Zettl (1996) is recommended for interested readers.

3.3.2 BN Fullerenes and Nanotubes

BN is the compound most closely related to carbon. The sp^2 and sp^3 bonded arrangements of both substances have similar structures and properties. Theoretical calculations by Blase et al. (1995) showed that BN nanotube formation from single sheets is slightly more favorable than for carbon. Furthermore, average energy per BN pair was calculated to be substantially lower for nanotubes than in BN fullerenes, indicating that it would be harder to synthesize BN fullerenes (Alexandre et al. 1999). In an earlier study, Jensen and Toflund (1993) suggested that failure in synthesizing BN fullerenes might be a result of dissociation of B_nN_m clusters ($n \neq m >> 1$) into N_2 and BN molecules. They suggested the use of a host substrate where these clusters could be annealed for the survival of such structures. A combination of these might explain the fact that there has been only one observation of a BN fullerene through electron beam irradiation of h-BN (Golberg 1998) which has not been repeatable. However, onions of BN have been synthesized earlier by irradiating BN with the electron beam of a TEM (Banhart et al. 1994). Similar structures have been also achieved by electron-beam irradiation of BN nanotubes (Stephan, Bando, and Loiseau et al. 1998) and by subjecting h-BN to high

temperature and pressure (Horiuchi, He, Akaishi 1995). It has been known that both bulk diamond and graphite convert to closed-concentric cages, or onions, under intense electron beam irradiation (Ugarte 1992; Ugarte 1993; Qin and Iijima 1996) and at high temperatures (Kuznetsov et al. 1994). In light of this evidence, it was logical to expect BN nanotube synthesis under conditions promoting carbon nanotubes. Finally, Chopra et al. (1995) observed multilayer BN nanotube formation in the soot gathered on the cathode of a Kratschmer-Huffmann type reactor that used a BN insert at the tungsten cathode.

Unfortunately, reports for successful synthesis of BN nanotubes have been scarce when compared to their carbon counterparts which reflects negatively on the available measured material properties of BN nanotubes. Almost all of the material properties regarding BN nanotubes are from theoretical calculations, which sharply contrast with carbon nanotubes. In fact, BN nanotubes are predicted to be stable wide-band-gap semiconductors (E_{gap}~ 5.5 eV) irrespective of the helicity and diameter of the tubes (Blasé et al. 1994; Rubio, Corkill and Cohen 1994). Helicity and diameter, on the other hand, were major factors for the electronic properties of carbon nanotubes. Moreover, BN nanotubes were found to be less reactive than carbon nanotubes; thus, they are potentially more suitable for highly oxidizing atmospheres (Rubio et al.1996). It is also reported that calculated strain energy is smaller for BN nanotubes than for carbon nanotubes (Charlier et al. 1999).

3.3.2.1 Deposition of BN Nanotubes and Fullerenes

There are a limited number of techniques used for BN nanotube formation. Loiseau et al. (1996) modified the standard method for carbon nanotubes using HfB_2 electrodes in the arc-discharge set-up. Yu et al. (1998) used excimer laser ablation of an h-BN substrate, depositing the ablated material on a cooled target. Another promising method that has been used for BN nanotube synthesis was the substitution reaction where carbon in multi-wall nanotubes (Golberg et al. 1999; Han, Bando et al.1999) was replaced by boron through this reaction:

$$B_2O_3 + 3C(\text{nanotubes}) + N_2 \Rightarrow 2BN(\text{nanotubes}) + 3CO.$$

Finally, Chen et al. (1999) claimed the synthesis of multi-wall BN nanotubes with bamboo-like morphology by ball-milling BN powders for 140h and annealing at 1300 C for 10h. Nearly, all of the arc-discharge or laser-related methods require the use of catalyst metals. There have not been any reports of deposition of BN nanotubes using CVD or PACVD related techniques.

In Figures 3.2.2 and 3.2.5, it was shown that certain conditions during the growth of BN films under low-energy ion-beam bombardment favored synthesis of single-wall BN structures. These structures are single-wall nanotubes, nanomountains, and fullerenes. A collage of such structures observed during this study is given in Figure 3.3.3. A large variation in the dimensions of these as single-wall nanotubes (SWNT) has been observed - diameter ranging from 5 Å to 30 Å. However, the length and assemblage of these BN structures were unlike carbon single-wall nanotubes synthesized using arc or laser ablation techniques, which are found to constitute relatively looser networks

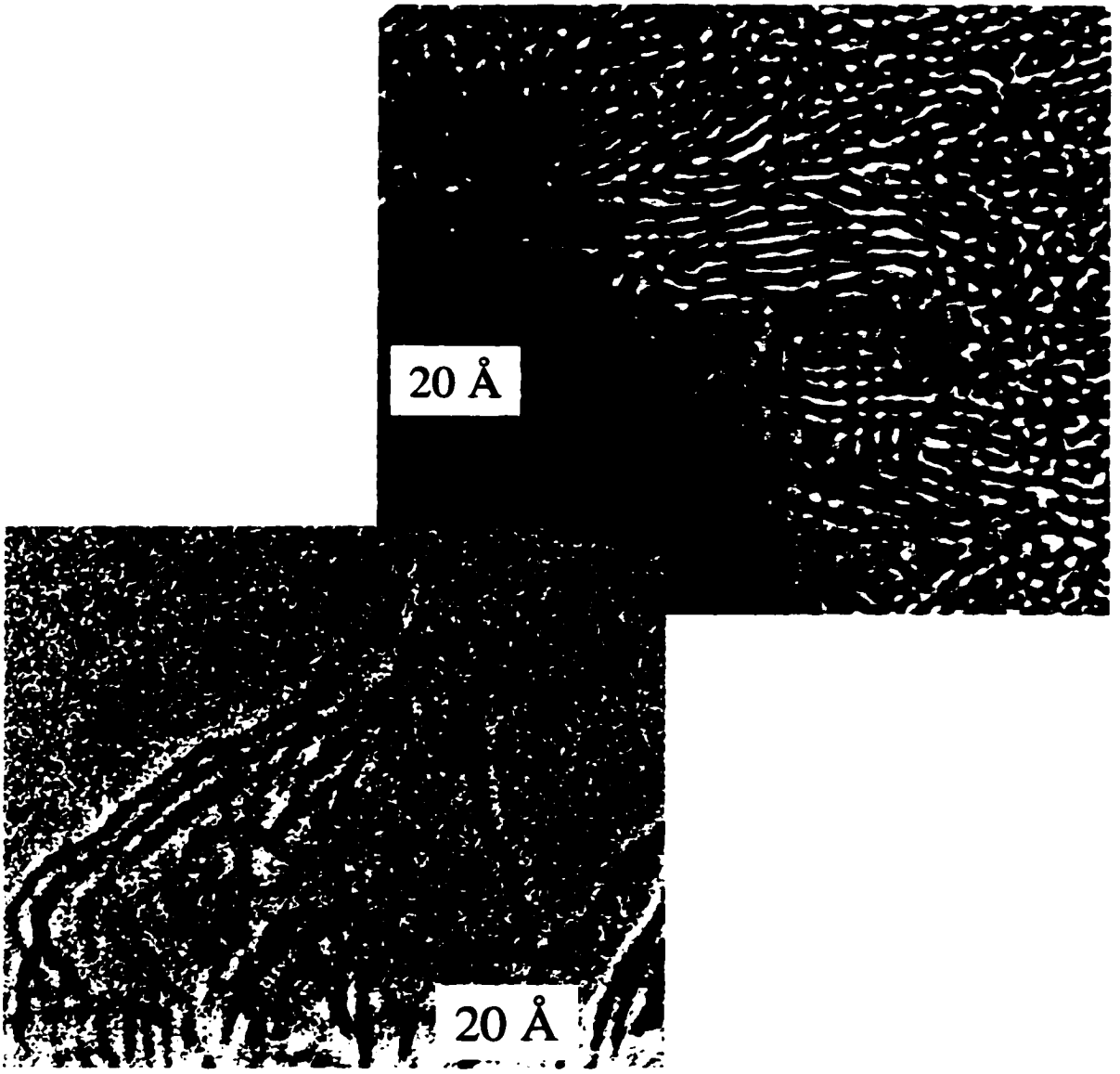

Figure 3.3.3 **HREM images of single-wall BN structures on tungsten substrates. Arrows point to single-wall BN nanotubes, fullerenes and nanomountains.**

between metal catalysts instrumental for their growth. The BN single-wall nanotubes observed, display curvilinear patterns with drastic changes in diameter over a relatively shorter length with no metal particles encapsulated inside or attached to the base. Typical processes such as arc discharge and laser ablation, employed for BN and carbon nanotube synthesis use metal catalysts, (e.g. Ni, Co, Fe_3C) which end-up occasionally at the tip of the nanotubes. Because of the metal particles located at the tips of the nanotubes, it is generally hard to investigate the capping arrangements. Loiseau et al. (1996) reported amorphous caps for single-wall BN nanotubes in one of the limited number of observations where the conditions were favorable for such an investigation.

Single-wall nanotubes are considered to be better field emitters than metal emitters, and are considered to have potential applications in field emission displays and other microelectronic device applications (Dean and Chalamala, 1999a). Tamuru and Tsukada (1995) suggested that the discontinuities in the electronic structure at the nanotube cap produce the distinct electronic states that enable device applications. The atomic structure of the nanotube at the cap was shown to have significant effects on the electronic properties of the nanotubes (Carroll, Redlich, Ajayan et al. 1997), in addition to carrying crucial information regarding the formation mechanisms (Charlier et al. 1999).

The major difficulty for theoretical studies examining the possible atomic arrangements at the BN nanotube caps has been the lack of experimental evidence (Fowler et al. 1999; Terrones et al. 1996). None of the proposed structures can be

supported by experimental evidence. In this study, the HREM images of some of the BN films on tungsten substrates were investigated closely and several single-wall BN nanostructures (among many) were identified as candidate structures for further atomic scale examination. These structures are shown in Figure 3.3.4.

An important point in the solution for the atomic structures of these features is the presence of particular angles, (arrows 1 and 2 in Figure 3.3.4), an acute angle ranging from 65° to 75° and an obtuse angle ranging from 115° to 125° which dominate the observed curvatures. During the early stages of the model building, a standard method for C nanostructure building was adopted which uses 5- and 7- membered rings (defects) in the hexagonal network for matching the concave and convex angles, respectively (Mackay and Terrones 1991). In order to make a closed surface, a combination 5- and 6- membered rings are enough (Euler's theorem), and the combination of 7- and 6- membered rings gives a convex surface. In the hexagonal network of BN structure, 5- and 7- membered rings induce B-B or N-N bonds, which increases the total energy of the system by 1.6 eV/pair (Blasé et al.1998) therefore, are not favored. In addition, none of the models with 5- and 7- build was able match the features in the experimentally observed structures. For further analysis, a new approach which utilizes 4-, 6- and 8-membered BN rings was adopted using a molecular modeling software package (HyperChem Standard 5.11). The final geometry of the models was optimized through molecular mechanics, since the average number of atoms in these models (~400) is rather large for more accurate methods, e.g. *ab-initio* quantum

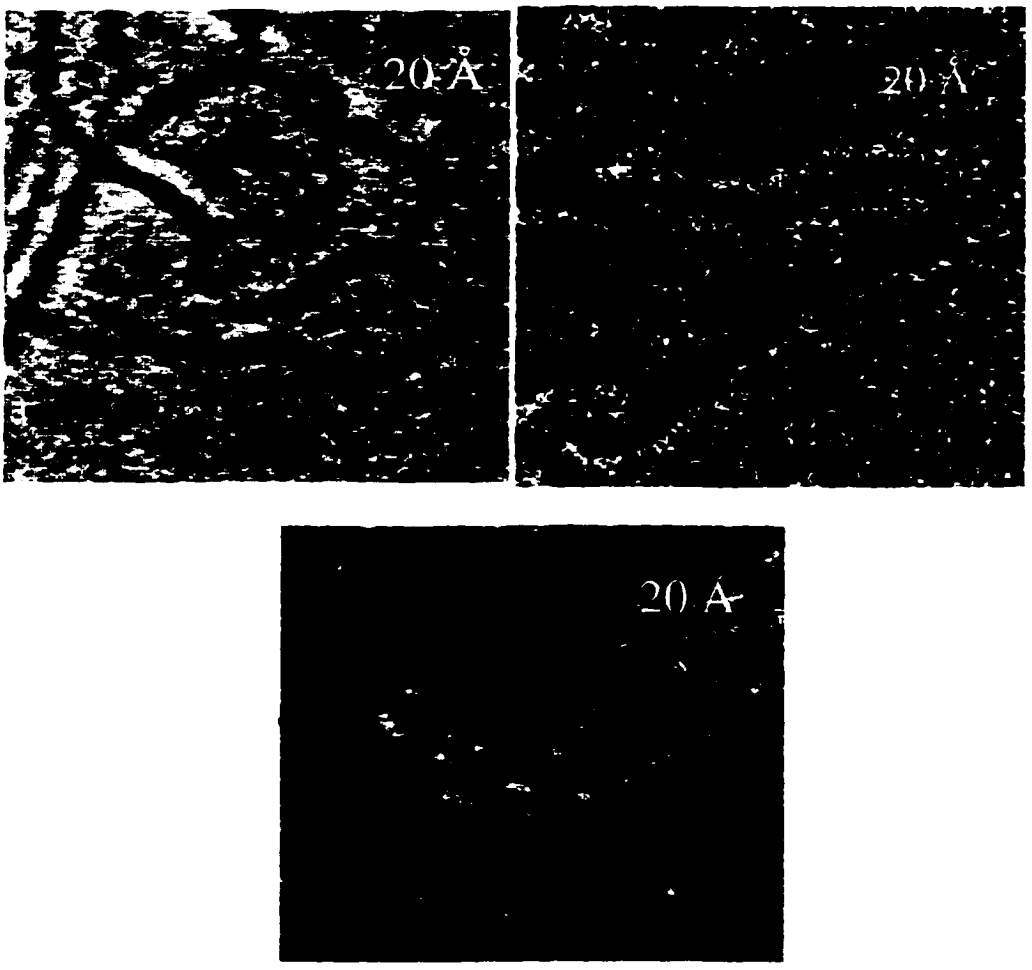

Figure 3.3.4 **Selected BN nano-structures for atomic modeling; a) spearhead model, arrow 1 and 2 point to typical obtuse and acute angles; b) t-rex model; c) fullerene model; arrow 1 points a capped nanotube of 5 Å, and arrow 2 points to a fullerene-like structure.**

mechanics. The relaxed atomic structures for candidate structures are given in Figure 3.3.5 a, b and c, with the simulated HREM images. The TEM image simulations were used to compare the model structures to the observed images during the building process; they were performed using a multislice algorithm. The arrows in Figure 3.3.5 a point to the most important characteristics of the original structure; the acute and obtuse angles, which were simulated by using 4-membered and 8-membered rings, respectively. The similarity between the simulated and experimental TEM images also confirm the theoretical findings pointing to a preference for 4- membered rings in single-walled closed BN structures. Additionally, 8-membered rings were critical for the accurate modeling of obtuse angles in BN nanotubes, in addition to helping attach the fullerenes caps to their nanotube bodies.

3.4 Implications

This study shows that cap structures for BN nanotubes would be markedly different than those observed for carbon. The main reason has been identified as the "frustration" associated with B-B and N-N bonds, as theoretically predicted by Blasé et al. (1998). This would also reflect upon the electronic structure of BN nanotubes, which may enable the manufacture of similar field emission devices to those of carbon nanotubes. Moreover, carbon nanotubes are prone to oxidation in air therefore, limited to vacuum applications (Dean and Chalamala, 1999b). However, BN is known to be an oxidation resistant compound.

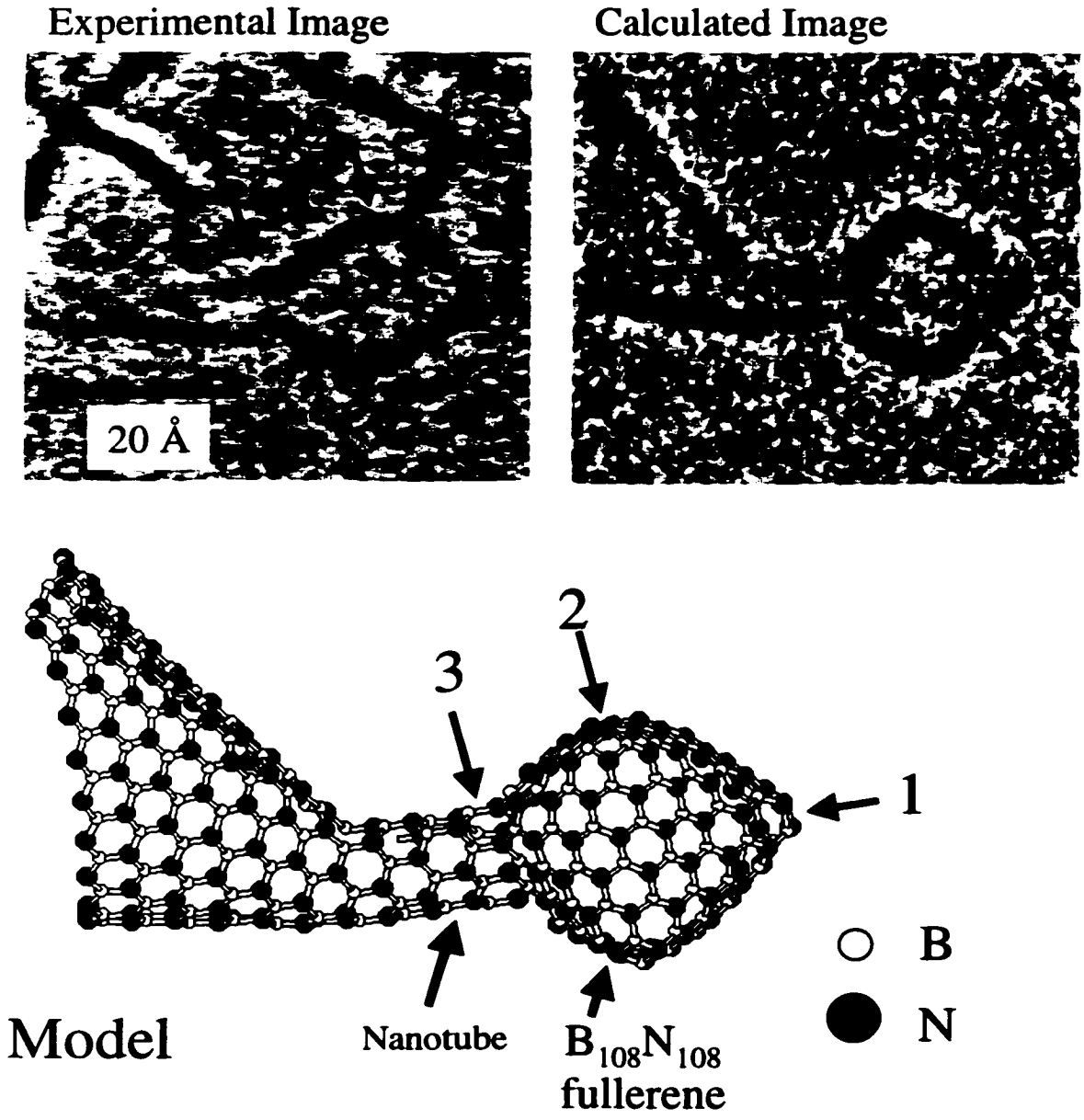

Figure 3.3.5 **a) Calculated image from the model proposed for the experimental image. Arrows 1, 2, and 3 point to the angles in the observed structure and corresponding ones in the model.**

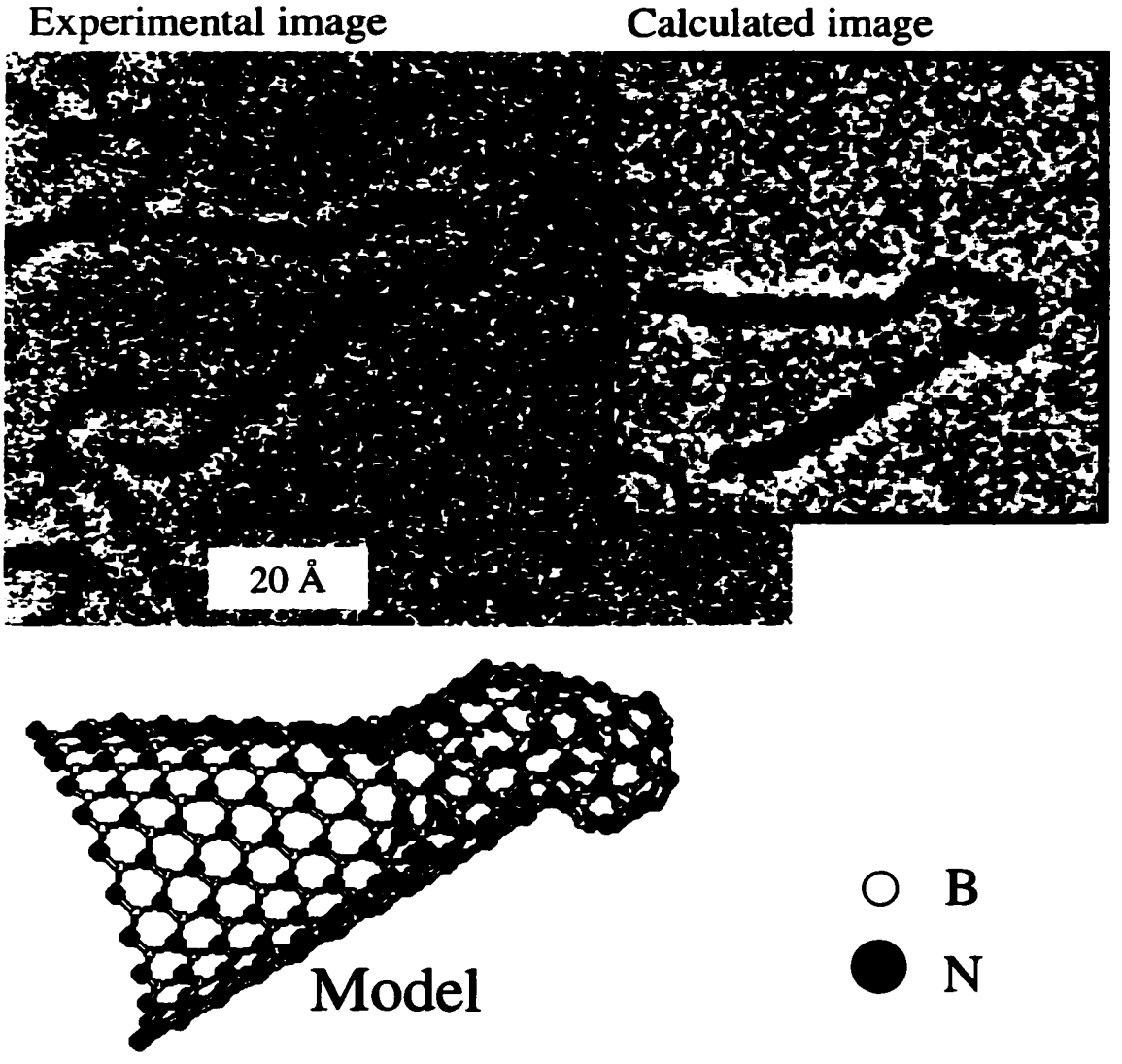

Figure 3.3.5 **b) Calculated image from the model proposed for the experimental image in Figure 3.3.4 b.**

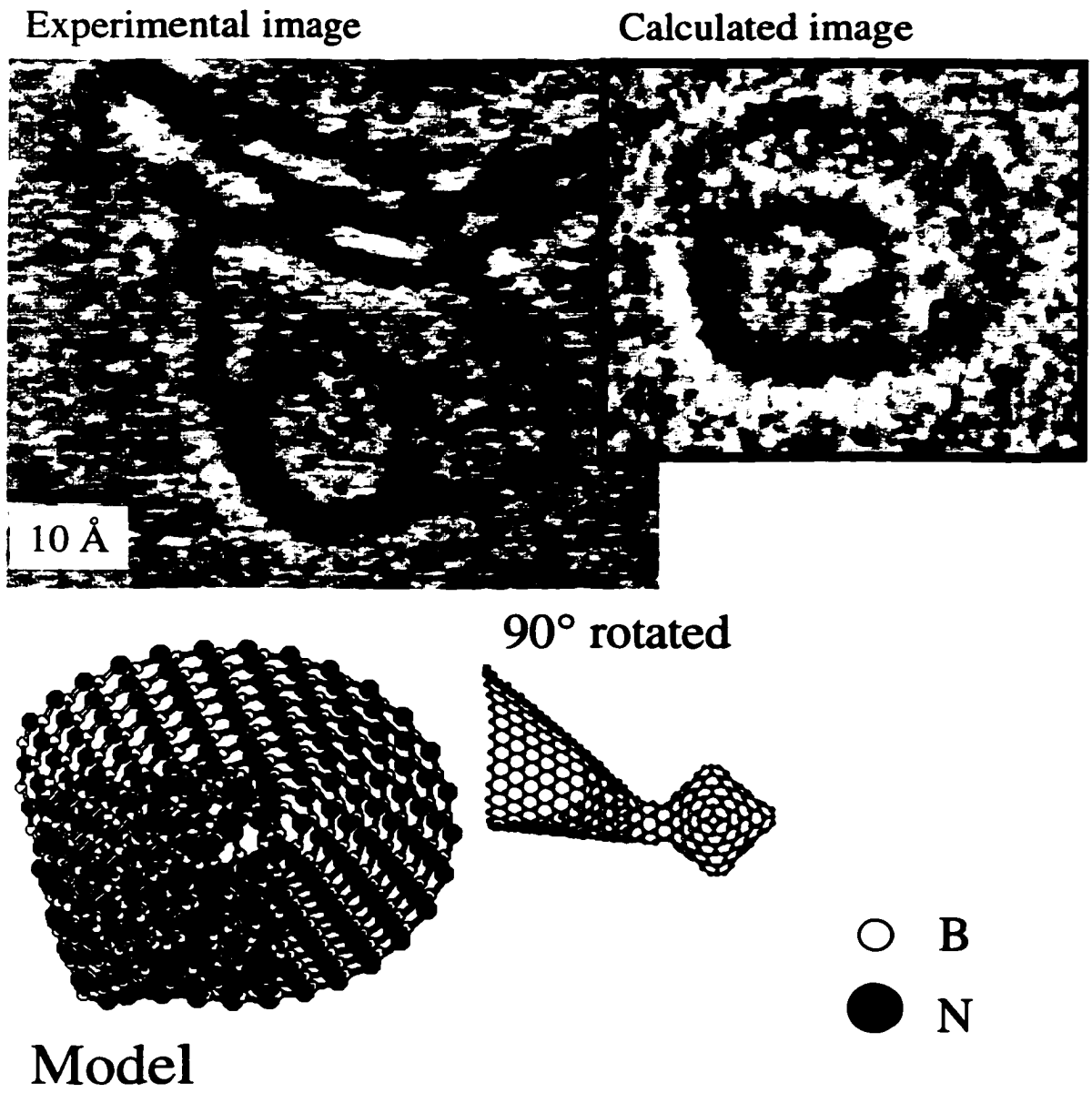

Figure 3.3.5 **c) Calculated image from the model proposed for the experimental image in Figure 3.3.4c.**

In this study, a new route has been used to synthesize single-wall BN structures that takes advantage of low-energy ionic species generated by an ECR-plasma source. Direct growth onto a substrate surface was achieved which enables the control of the nanostructure evolution using standard deposition parameters. In conventional techniques such as arc discharge and laser ablation using catalytic metal particles, gas-phase nucleation dominates, which does not readily allow for dynamical parameter control and process characterization.

Thousands of papers on fullerenes and nanotubes have been published since they are first observed, and many of them offered conflicting views on the growth mechanisms of fullerenes and nanotubes. In most of the models, nucleation was considered to take place in the vapor phase, or on a catalytic particle. The results from this study indicated that heterogeneous nucleation on a substrate is possible. In addition, a region has been identified for the growth of single-wall BN structures, as shown in Figure 3.3.6. This method is capable of producing single-wall structures therefore, may be suitable to produce a range of different nanotube coatings of well-controlled structure.

Another finding related to the use of 4-membered rings in BN nanotube caps was the bonding state of severely distorted nitrogen atoms in the 4-membered rings. Figure 3.3.7 shows a possible end cap arrangement with 4-membered and 8-membered rings for a commonly observed 9.6 Å diameter BN nanotube. The geometry of the BN nanotube in Figure 3.3.7 has been optimized by semi-empirical quantum mechanical calculations using AM1 method (Austin Model 1, Dewar et al. 1985). The results indicated two types of buckling of B-N bonds in this structure. The first one was at the nitrogen sites on the

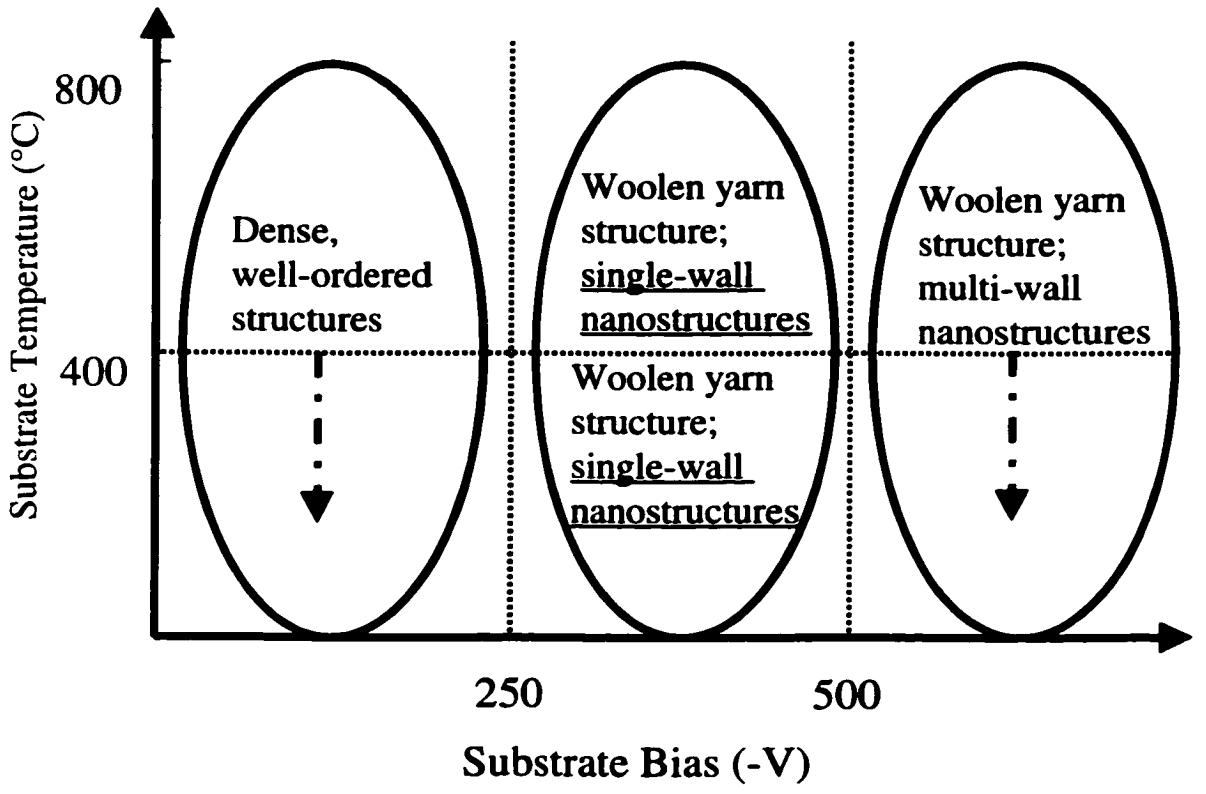

Figure 3.3.6 **The map of structures with regard to substrate bias and substrate temperature.**

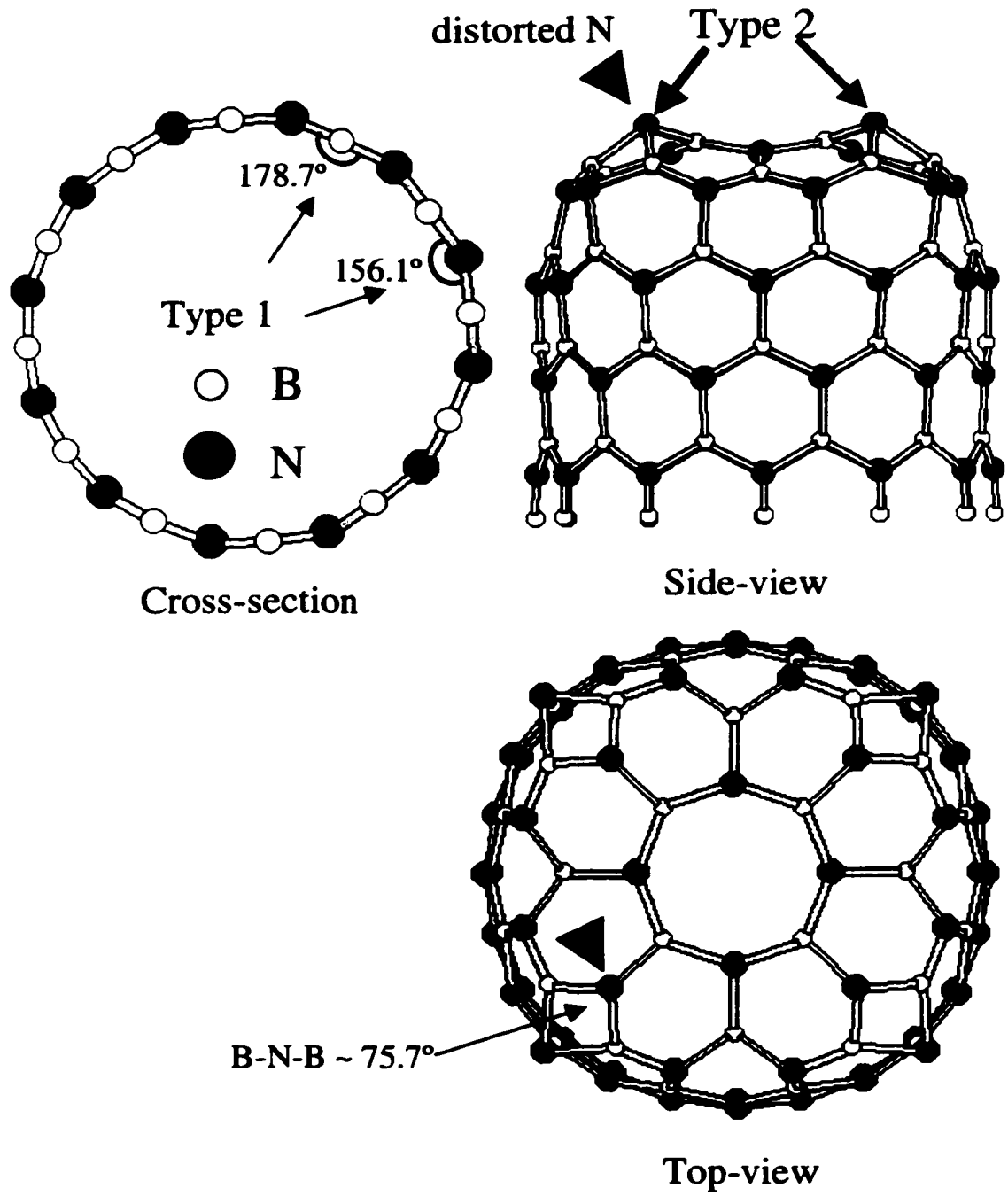

Figure 3.3.7 **BN nanotube with an end-cap containing four 4-member rings. Type 1 and type 2 are two different buckling mechanisms for B-N bond .**

nanotube walls, which allows for the curvature of the tube. In fact, Blasé et al (1994) was the first to propose this mechanism for the curvature of the BN sheets forming the BN nanotubes. The results from ab initio calculations by Blase et al. (1994), showed that while boron atoms sought to preserve sp^2 character by making planar bonds with neighboring nitrogen atoms in a nanotube, nitrogen atoms preferred to relax away from the plane of boron atoms by buckling the B-N bond. Other studies on the BN nanotubes and fullerenes also confirm these findings (Jensen and Toflund 1993; Menon and Srivastava 1999).

The second type of buckling of the B-N bonds was observed at the nitrogen atoms in the 4-membered rings, type 2 in Figure 3.3.7. The nitrogen atom in the 4-membered ring was perturbed 0.68 Å away from the plane formed by the three bonding boron atoms. The B-N-B angles were also measured to be 75.7°. Similar results for this unusual buckling of the nitrogen atoms in 4-membered BN rings were reported earlier for the $B_{36}N_{36}$ and $B_{12}N_{12}$ fullerenes by Alexandre et al. (1999) and Jensen and Toflund (1993), respectively. The similarity between the tetrahedral bonding (sp^3) observed for the c-BN and the distorted arrangement observed for the boron and nitrogen atoms in nanotube caps may imply that c-BN growth could be enhanced by presence of capped BN nanotubes.

CHAPTER 4: COMPUTATIONAL ANALYSIS OF SURFACE STRUCTURES

4.1 Imaging of Semiconductor Surfaces

The fundamental motivation behind studies investigating semiconductor surface structures is the technological importance of the electronic and structural properties of these structures to the modern semiconductor industry. Although skepticism regarding Moore's law remains to be addressed, the Semiconductor Industry Association (SIA) has made extensive revisions to its semiconductor technology road map in 1998 and has moved some of its major technology targets ahead by one year. In the 1999 edition of the International Technology Roadmap for Semiconductors, it is predicted that a 100 nm feature size, which is the physical limit of optical lithography, will be achieved in the year 2005 (see Figure 4.1.1). If this prediction holds, within five years the lateral feature size will be only forty times the Si (111)–7x7 unit cell size.

Semiconductor surfaces with their remarkable electronic and structural properties still challenge the researchers even at the current level of scientific progress. The main reason for this is that atoms at the surface of a semiconductor do not occupy the positions that would be expected from a simple continuation of the bulk structure. The excess energy due to incomplete bonding is released through rearrangement of the

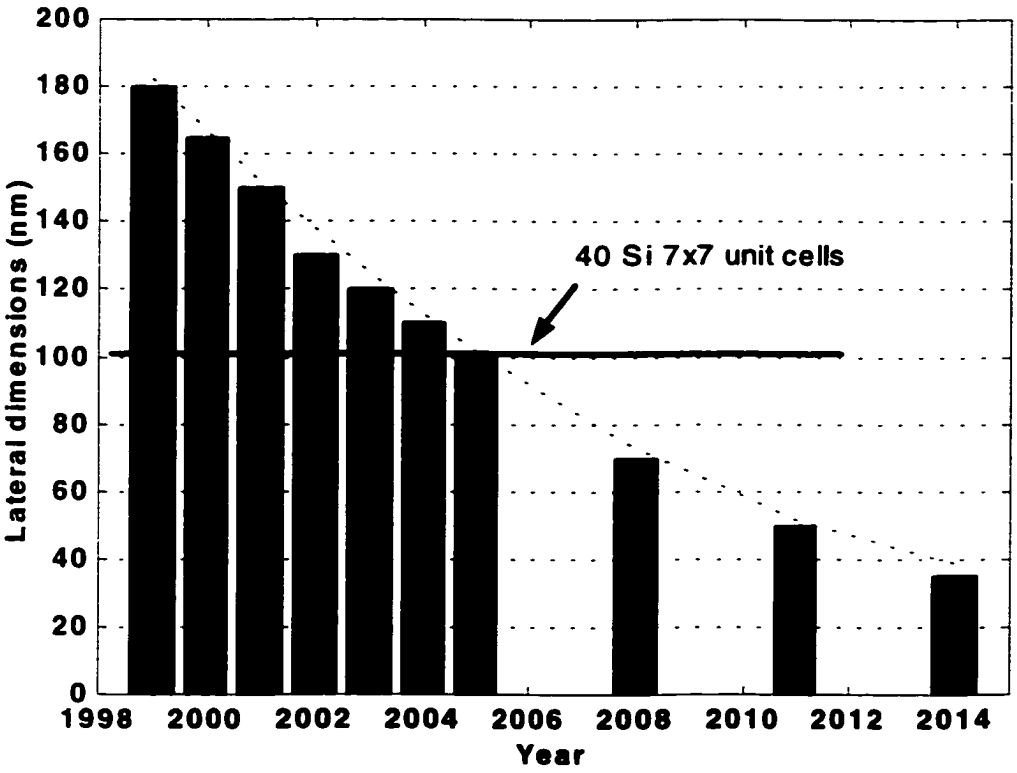

Figure 4.1.1 **Plot depicting the semiconductor industries set goals for the coming decades. The trend indicates a parabolic decrease until the year 2014.**

surface atoms and bonding changes. Thus, lateral or horizontal shifts in atom positions with respect to the surface plane can lead to a substantial decrease in the total energy of the system. This new atomic configuration on the surface is called a surface reconstruction. Sometimes, adsorption of foreign atoms on the native surface (usually less than one monolayer) may induce other surface reconstructions. These may be considered as a *frozen* instance of the early stages of nucleation and thin film growth.

Solving the atomic configuration of a reconstruction is a significant challenge, and incorrect solutions are frequent. Mostly, these are reconsidered and replaced in later studies. A dramatic example is the Si (111)-7×7 reconstruction, first observed by Schlier and Farnsworth by low-energy electron diffraction (LEED) in 1959. Until the widely accepted dimer, adatom, and stacking fault model (DAS) appeared (Takayanagi et al. 1985a and 1985b), there were a large number of models offered to explain this elusive reconstruction. Another more recent example is the arguments about the metal-induced (3×1) reconstruction of the Si (111) surface, which lasted nearly five years. It was generally accepted that the underlying structures were the same for both the alkali- and Ag-induced 3×1 structure. However, none of the dominant models proposed (variants of chain models) were able account for the band structure observations (Weitering et al. 1994; Erwin 1995). Finally, Collazo-Davila, Grozea, Marks (1998) came up with the "honeycomb chain-channel" model confirmed by Erwin and Weitering (1998) through *ab initio* calculations.

4.1.1 Analysis Techniques

Within the last thirty years, various new surface-sensitive techniques have been developed for the chemical and structural characterization of surface reconstructions. Together with the increase in the computing power, *ab initio* theoretical methods have enabled the investigation of the relationship between the atomic geometry and electronic properties of semiconductor surfaces. Even so, a simple technique capable of providing the position of surface atoms does not exist. Consequently, the processing of the raw data from the surface-sensitive methods is still a very involved and time-consuming task. The overall success of a study is disproportionately dependent on this step. There are two main classes of techniques for studying the structures on surfaces of crystalline materials: diffraction methods and imaging methods.

Diffraction methods take advantage of the interaction between X-rays or electron beams and the periodic arrangement of atoms on surfaces. For years, these methods have been the standard technique for the examination of crystal structures of 3-D bulk materials. Naturally, most of these methods are extended to the surfaces.

LEED is one of the earliest diffraction methods and it has been applied to the investigation of nearly all surfaces (Davisson and Germer 1927; Van Hove, Weinberg, and Chan 1986). A LEED apparatus can be attached to early any process chamber, and enables in situ characterization of surfaces with ease. However, modeling the interaction between the low-energy electrons and the substrate atoms is highly complicated, and thus, it is rather difficult to determine accurately the positions of atoms on the surface model using LEED data. Reflection high-energy electron diffraction (RHEED) is very

similar to LEED, but higher electron energies simplify the scattering process. The major disadvantage of RHEED is the multiple scattering issues due to use of reflection (Ino 1988).

Synchrotron radiation-based X-ray diffraction (XRD) is better understood and more interpretable than both LEED and RHEED, although substantially expensive. Grazing incidence X-ray diffraction (GIXRD) employs a geometry that enables the analysis of surfaces. In this format, incident angle α of X-rays is near α_c, the critical angle for total external reflection. It is possible to determine the positions of atoms vertically on a surface by scanning the intensity of crystal truncation rods normal to the surface. GIXRD was first used by Eisenberger and Marra (1981) for the investigation of surfaces and absorbed layers. Vineyard (1982) pointed to a simplified physical interpretation of GIXRD, otherwise a dynamical phenomenon due to refraction, as establishing the basis for a kinematical treatment. The weakness of the interaction between X-rays and surface atoms lengthens the time required for data acquisition, thus limiting the applicability of the method as an in situ method.

Transmission electron diffraction (TED) is another technique used for the determination of surface structures. The major advantage of TED is that it combines the ease of data acquisition of LEED and RHEED and the sensitivity of X-ray techniques. Data interpretation models are also well established. Electrons have a significantly higher scattering probability than X-rays, thus requiring a dynamical treatment. However, a kinematical theory of diffraction can be used to approximate the more rigorous dynamical case for very thin crystals and far off-zone conditions (Marks et al.

1991). In addition, multislice algorithms have been developed to describe accurately multiple scattering events (Goodman and Moodie 1974). Although TED introduces several improvements over the existing methods for surface science, the method and the instrumentation have some limitations. First, surface reconstructions on semiconductors can only survive under UHV conditions. UHV-TEMs are rare and require highly trained personnel for their operation and maintenance. Second, preparing sufficiently thin samples is very time consuming and laborious.

Ion scattering is a distinct approach to surface structural analysis based on Rutherford scattering. A monoenergetic, well-collimated beam of light ions (H^+ and He^+) is directed at a surface, and the energy distribution of ions scattered at various angles is measured to determine the location of the surface atoms. Other than the structural information, coverage and chemical composition of the surface can be determined. The reader is directed to reviews by Buck (1975) and Zangwill (1992) for further information on ion scattering techniques.

4.1.1.1 Diffraction Analysis

The success of classical diffraction analysis techniques depends on the quality of initial model. Collazo-Davila, Grozea et al. (1997) employed standard diffraction analysis to the case of Ge (001)- 2×1. In these methods, if the number of viable models is restricted, then the same approach can be used to differentiate between the possibilities through χ^2-minimization by refining the respective atom positions.

Within the last twenty years, alternative methods have been developed for the investigation of surface structures through diffraction data. The main limitation with diffraction methods is that only the intensity of the diffracted beams or the modulus of the structure factors can be captured on a negative or measured using a detector. Restoring the scattering charge density (x-ray diffraction) or potential (electron diffraction) requires the phase of the diffracted beams. This is referred to as the "crystallographic phase problem" of diffraction analysis.

Determining approximate values for the phase is accomplished using what are called direct methods. Direct methods (DM) apply the probability relationships that exist between the intensities and the phases of the diffracted beams for the solution of the phase problem. Fundamental concepts of the probabilistic approach for direct methods have been established by the works of Sayre (1952), Cochran (1955), and Karle and Hauptmann (1956). Direct methods have had significant success in solving single crystal bulk structures using XRD data. Initially, using TED data, DM was used to solve the structures or large organic molecules (Gilmore et al. 1993; Dorset 1996; and Dorset 1995).

A large number of algorithms have been developed for the implementation of DM using XRD or TED data, such as *SHELX* (Sheldrick 1990), and *MICE* (Gilmore, Bricogne, and Bannister 1990). Lately, Prof. Marks and his group at Northwestern University investigated the applicability of DM to two-dimensional surface diffraction data from either TED and/or GIXRD (Collazo-Davila, Marks et al. 1997; Gilmore, Marks et al. 1997; Marks, Plass, and Dorset 1997). Initially, Sayre-like sharpening operators,

with the help of multi-solution genetic-algorithms, has been the dominant format of the method (Landree, Collazo-Davila, Marks 1997; Marks and Landree 1998); later, this evolved to a feasible set type method used in image recovery problems (Marks, Sinkler, and Landree 1999). Surface structures investigated using these methods can be found in several review papers by Marks, Bengu et al. 1998; Grozea, Landree et al. 1999; and Leslie et al.1999.

4.1.2 Surface Sensitive Imaging

There are limitations to exploring surfaces using diffraction methods despite the recent progress in diffraction methods and analysis. One problem often encountered is that an important surface diffracted beam coincides with a bulk beam. Because the bulk intensity is much stronger than the surface diffraction intensity, the surface reflection cannot be measured. The success rate of direct methods employing a probabilistic approach is seriously hindered if some of the unmeasurable surface reflections are relatively strong. Diffraction data collected on negatives from TED is purely two-dimensional, but the actual surface structure may not be limited to a single layer. Although a potential or charge density map can be restored from the data available, the relative heights of the species will be unknown. For reconstructions extending into the bulk or with multiple layers, it is possible that a two-dimensional projection of the surface maps will contain overlapping sites, further complicating the height issue. There are at least two cases where direct methods were unable to provide unambiguous solutions. These are the Rb- and Ag-induced 3×1 reconstructions on the (111) surface of

germanium. In the case of Ge (111) - 3×1 Ag, Grozea et al. (1999) suggest that a limited number of reflections in the data set may have played a role. For such pathological cases where *ab initio* approaches fail to provide feasible solutions, critical information regarding the atom positions can be obtained by using imaging techniques.

Techniques used to image surfaces are the closest to providing an image of the atomic re-arrangement of the surface. One of the most common surface-imaging techniques used today is scanning-tunneling microscopy (STM), pioneered by Binnig and Rohrer in 1983. STM has a lateral resolution below 2 Å and a height resolution of around 0.01 Å. By rastering a very sharp metal tip over a surface at a constant height, STM correlates the tunneling current measured between the tip and the surface to map the surface density of states. However, mapping the density of surface states is far from answering the critical question about the locations of surface atoms; that is, STM cannot differentiate between a high density of states and a solitary adatom which may lead to a tenuous interpretation of results. In addition, STM is only sensitive to the topmost layer of the surfaces and reconstructions in 99% of cases, so the availability of data regarding multi-layered reconstructions and subsurface relaxations is limited.

Several new imaging techniques have been developed for imaging surfaces using electron beams. (see Figure 4.1.2). The imaging modes of LEED and RHEED, low-energy electron microscopy (LEEM) and reflection electron microscopy (REM), respectively, are valuable tools providing significant information regarding surfaces and their structure. LEEM has been developed and used extensively by Bauer (1985). REM, first attempted by Ruska in 1933, evolved to a powerful technique where in situ

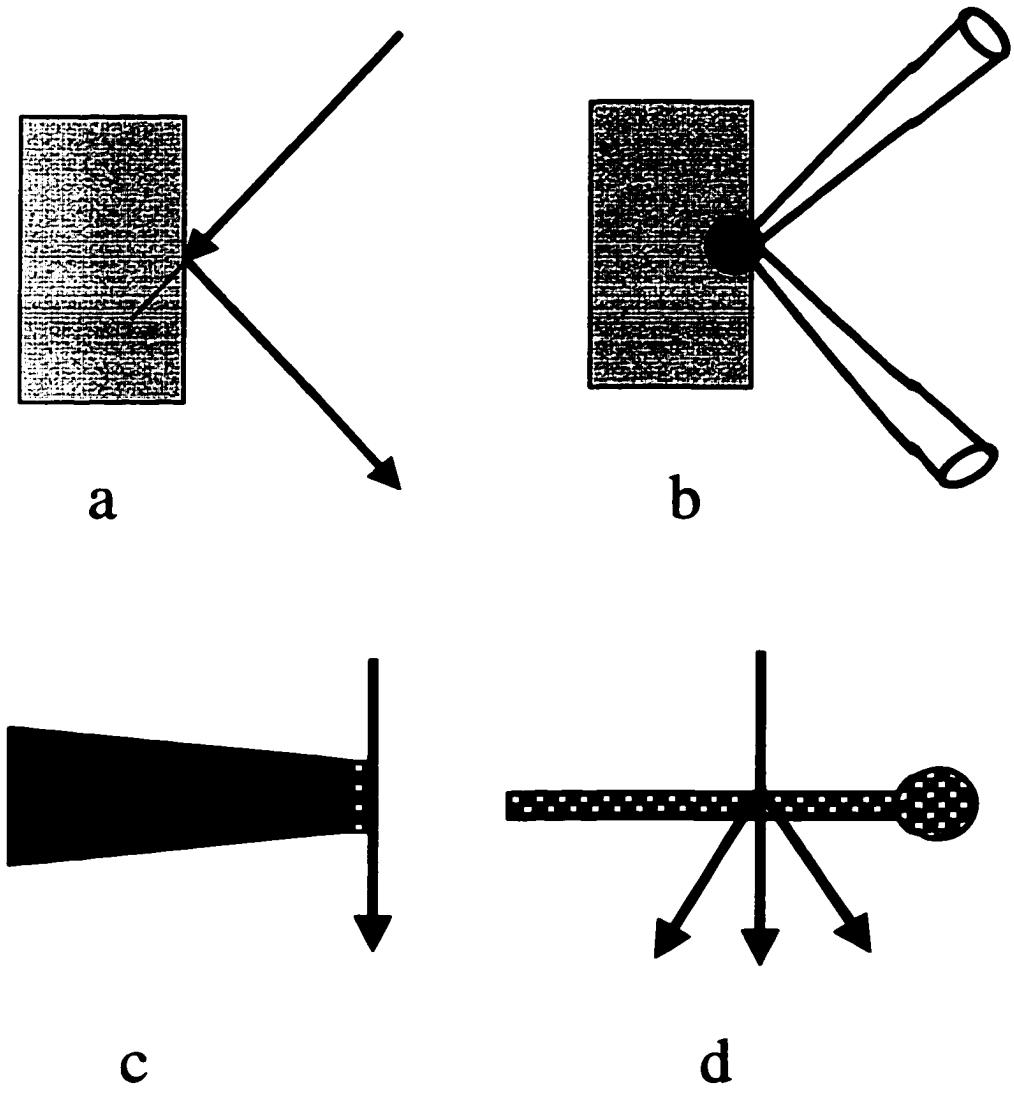

Figure 4.1.2 **Imaging techniques developed for use with surfaces: A) reflection electron microscopy (REM); b) scanning electron surface microscopy (SESM); c) profile imaging mode for HREM; d) Plan-view mode for HREM.**

observation of surface phase transformations is possible with high spatial resolution (Tanishiro et al. 1986). Recently, REM has been applied to investigate the motion of surface steps at elevated temperatures (Latyshev et al., 1995). Scanning-electron surface microscopy (SESM, closely related to scanning REM) is another technique applied to the investigation of domain boundaries and step-motion mechanisms on surfaces (Aizawa and Homma 1995). High-resolution transmission electron microscopy (HREM) with the help of advances in UHV technology (required for surface studies) experienced a transition from imaging of small particles to the surface structures. Marks and Smith (1983) applied the profile imaging geometry to the imaging of surface relaxation on clean metal surfaces. Barna et al. (1984) and Poppa (1983) also provided information on the surfaces of metal clusters using UHV-TEM. Finally, Gibson et al. (1985) imaged surface reconstructions using bulk-forbidden reflections.

While all of the techniques considered here can be used for in situ observations and have good image acquisition speeds, some image formation mechanisms are still under scrutiny (e.g. LEEM). In the following sections, a discussion of imaging theory will be provided with emphasis on HREM of surfaces, and its application to HREM of Si (111)-7x7 native surface reconstruction will be presented

4.1.3 HREM of Surfaces

One may ask the inevitable question "Is it possible to obtain an HREM image dominated with the contrast from the surface features, knowing that the bulk interactions

with the probe are stronger?" The answer is "yes," and there are several different ways to achieve this goal. The first attempts at imaging surfaces without using weak beam techniques emphasized using the objective aperture to isolate surface reflections (bulk forbidden), which resulted in the observation of surface steps (Cherns 1974). Later, this technique was adopted and improved by other researchers (Jarayam, Plass, and Marks 1995). Although dark-field related techniques proved the presence of adequate information relating to the surface, high-resolution methods initially did not take advantage of the surface information. Later, Dunn et al. (1993) studied the native 5×1 reconstruction on the (001) surface of iridium, and the step structure and the 1×1 terraces were also investigated. The images were numerically processed to reveal the symmetry elements of the 5×1 reconstruction. In this study, the electron beam was nearly perpendicular to the (001) surface, near on-zone imaging condition.

Xu and Marks in 1992 used PEELS measurements to study variations in the diffracted beam intensities with regard to crystal tilt. In their study Xu and Marks concluded that for off-zone conditions, the decrease in the surface spot intensity was much less than that is measured for the bulk spots. This result can easily be attributed to relative shapes of the bulk and surface spots (relrods) in the reciprocal space. While the relative intensity of the bulk spots are much higher ($\sim 10^{-1}$, transmitted beam is unity), the shape of the surface spots are much longer and interact with the Ewald sphere uniformly over an extended range (with $\sim 10^{-2}$-10^{-6} intensity). Experiments on Ir (001) surface using

far off-zone observations gave better results indicating the validity of the previous study (Xu, Dun, Zhang, and Marks 1993).

One can conclude that HREM imaging of surface with 1-5% of the total contrast is possible provided that:

(i) The sample is reasonably thin so that diffuse, inelastic scattering background due to bulk effects is minimized;

(ii) the surface consists of well-ordered, large uniform plateaus in order that large domains of reconstruction are available for sharp surface diffraction spots;

(iii) the bulk sample should be annealed well enough to minimize the defect concentration due to sample preparation.

Of these the most important is the first one, as the background noise is the major limitation to the information available in HREM images. The origin of the noise is not only the bulk inelastic effects, but also disorder and simple counting statistics involved. The critical point in extracting surface information form a HREM image is to find an *unbiased* way to manage noise. Noise filtering is a relatively mature field and it has been covered in the image-processing field extensively, although it has not been applied to electron microscopy widely.

For periodic images, the most common approach is to use Fourier filtering methods; however, extreme care should be taken as artifacts can be introduced to even

pure noise objects (Marks 1996). It is also possible to use maximum-entropy methods, which have been rather popular during the last years. Another school of thought exploits the noise estimates from the tail region of the power spectrum of a periodic image, which is an *unbiased* approach. Accordingly, it is possible to use a set of methods that can be collectively called Wiener filters for the noise-filtered reconstruction.

HREM images are generally periodic and an objective estimate of the noise can be made far away from diffracted spots at higher frequency regions. The observed image in the frequency space I can be defined as

$$I = S_t + \eta , \tag{4.1}$$

where S_t, is the sum of the true signal and η, the noise. In the Fourier space, a filter F can be construed as acting on image I to extract an estimate S of the true signal S_t through the relationship

$$F\,I = S . \tag{4.2}$$

The conventional Wiener filter (Wiener 1942) can be described minimizing the following expression:

$$W = \sum (F\,I - S_t)^2 , \tag{4.3}$$

which then reduces to

$$F = \frac{|S_e|^2}{|I|^2}, \tag{4.4}$$

with S_e being an estimate of the true signal

$$|S_e|^2 = \begin{cases} |I|^2 - |\eta|^2, & |I| > \eta \\ 0, & |I| < \eta \end{cases}. \tag{4.5}$$

This filter assumes that the noise and the signal are uncorrelated. The best estimate S_b of the signal in a least squares fashion is given by

$$S_b = \frac{I|S_e|^2}{|S_e|^2 + |\eta|^2}. \tag{4.6}$$

It is reported that the signal-to-noise ratio has been enhanced by a factor of six for 1024×1024 pixel images (Marks 1996). This is not surprising since the statistical noise scales with the square root of the number of pixels whereas the signal scales with the number of pixels. Thus, the enhancement for larger images is more pronounced (Marks 1996). Recently, a Random-Phase Parametric Wiener filter, an advancement over the conventional Wiener filter, has been successfully applied for the atomic-scale imaging of Si (111)-5×2 Au reconstruction by Plass and Marks (1995).

The main limitation to the use of Wiener and Wiener–like filter is when the surface spots are too weak to be observed in a power spectrum and/or HREM image does not reveal the presence of fringes of a structure on the surface. A second factor is the

estimation and modeling of the initial error. Currently, the noise estimate can only be modeled using either a gaussian or an exponential function with the algorithm written by Prof. Marks. Although it is possible to model the noise using higher order polynomials, aggressive filtering may induce loss of information and image artifacts; the final image should contain some residual noise.

4.1.4 Si (111)-7x7 Reconstruction

The Si (111) – (7×7) native reconstruction is one of the most, if not the most, complicated and celebrated surface structure in existence. It has been a dilemma since it was first observed by Schiller and Farnsworth in 1959. Takayanagi et al. (1985a and 1985b) proposed the dimer-adatom-stacking fault (DAS) model using TED data with the help of earlier STM observations identifying the adatoms (Binnig, Rohrer et al. 1983). The results of following studies employing GIXRD (Robinson et al. 1986 and Skov Pedersen et al. 1988), LEED (Huang, Tong, Packard, and Webb 1988), TED (Twesten and Gibson 1994), and *ab initio* computational methods (Takayanagi, Tanishiro, and Kajiyama 1986; Badziag and Verwoerd 1989; and LaFemina 1992) are consistent with the DAS model (see Figure 4.1.3). This model consists of 12 adatoms (first layer), a stacking fault bilayer (second and third layer) within which nine dimers (third layer) border the triangular subunits as the core structure of 1/6[112] screw dislocations, and a

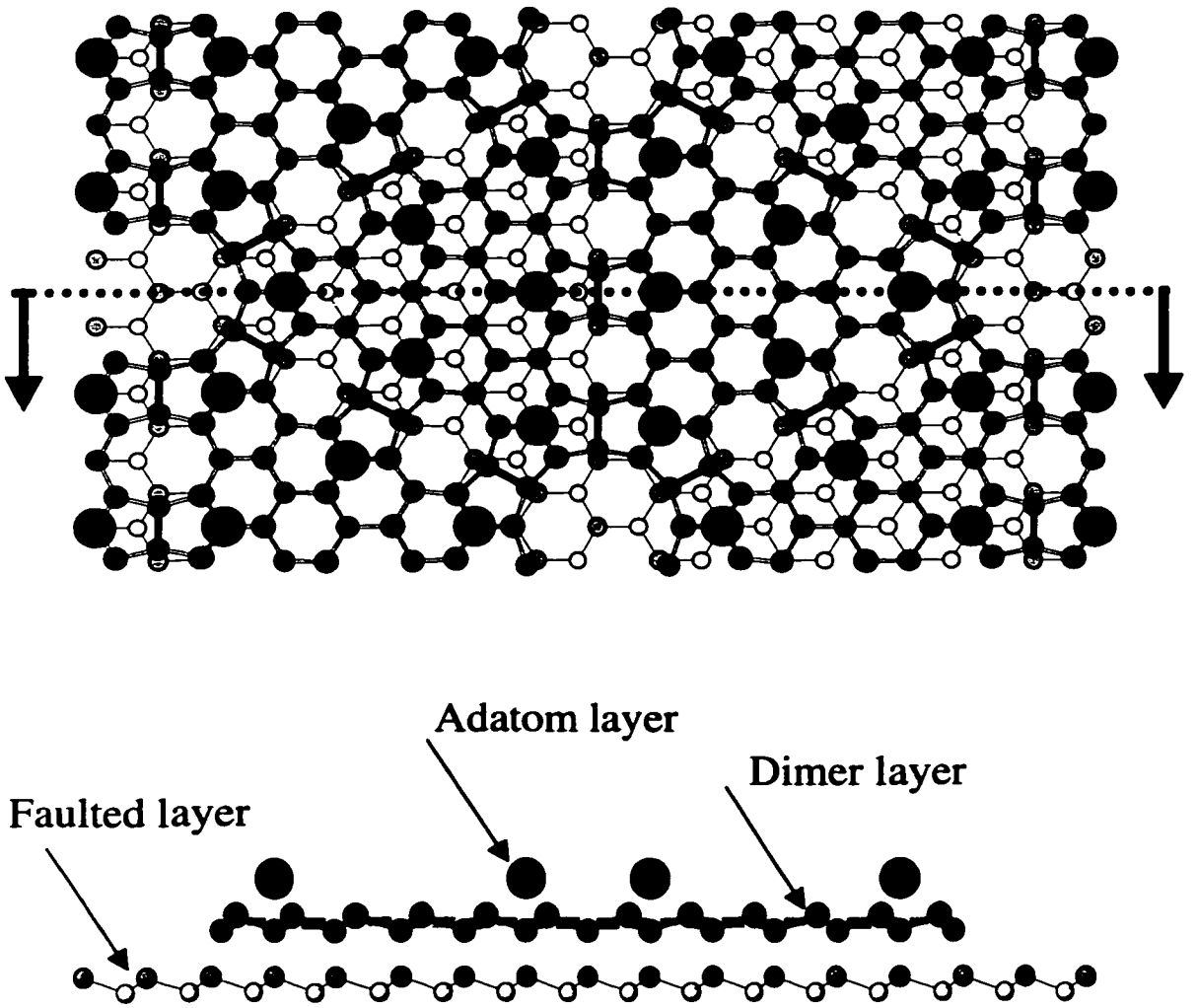

Figure 4.1.3 **Atom arrangement on Si (111) -7×7 reconstruction according to the dimer-adatom-stacking fault model (DAS). The 7×7 supercell consists of 12 atoms in the adatom layer, 42 atoms in dimer layer, and 48 atoms in the faulted layer.**

deep vacancy at each apex of the unit cell. While STM was used successfully to image the adatoms on the surface, many of the key features -for instance, the dimers in the third layer- are too deep in the structure. Figure 4.1.4 shows a typical STM image of the 7×7 reconstructed silicon surface; note that only the deep vacancies at the each apex of triangular subunits and adatoms are visible. In addition, STM, with its fine horizontal resolution, can discern between the faulted region and unfaulted regions using the height difference between them.

4.1.4.1 Imaging the Dimers

Ichihashi and Iijima (1994) took HREM images of 7×7 reconstructed silicon surfaces. The silicon sample was prepared from a p-type (111) oriented wafer of 10 - 20 Ohm-cm resistance. A 3 mm diameter disk was cut from the wafer, then mechanically thinned and dimpled. Chemical etching of the specimen was performed using a standard $HF+HNO_3$ solution. In this fashion, pits develop on the specimen surface and thin regions in the pits are less than 300 Å thick. The specimen surface was cleaned by heating using an infrared light in an ultra-high vacuum chamber linked to a newly developed UHV-TEM (JEM-2000FXV, operated at 200KV, resolution 2 Å). The vacuum around the specimen during observation was kept in the 10^{-10} Torr range. The images of the surface on negatives were digitized and transferred to Northwestern University for further processing. Figure 4.1.5 a) shows an unprocessed image of the Si surface with the b) power spectrum of the image as the inset.

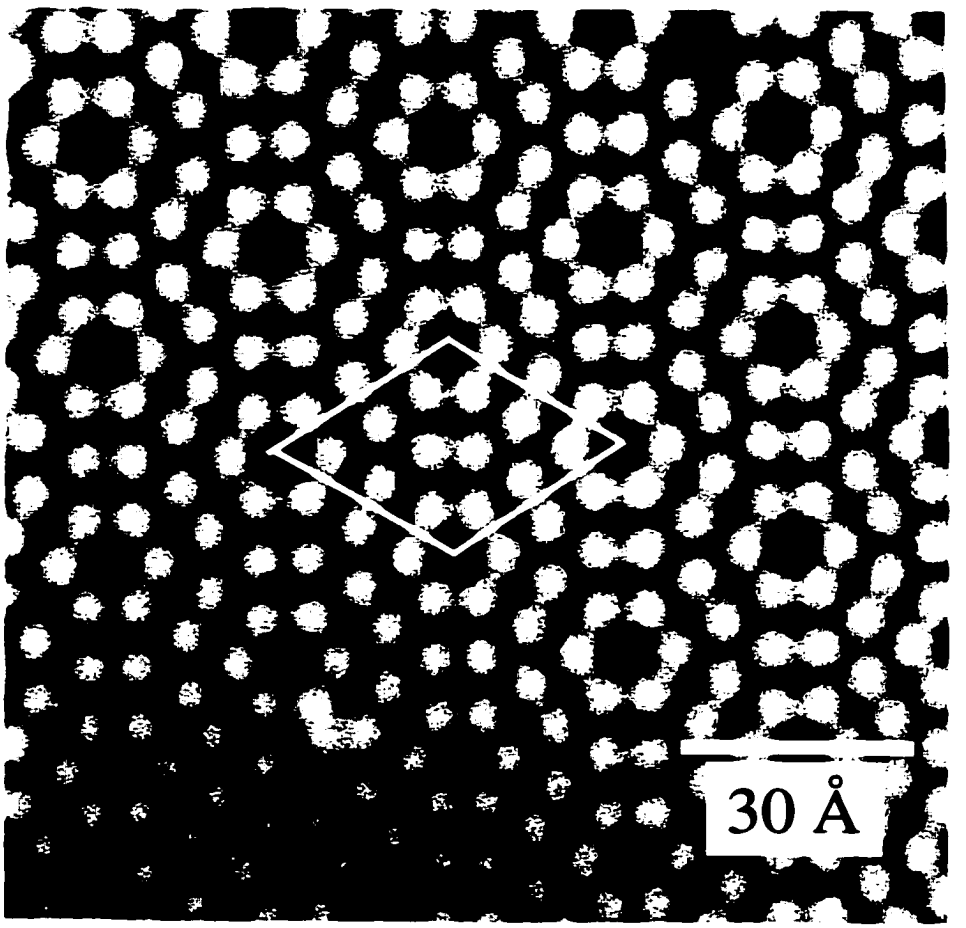

Figure 4.1.4 **Topographic image of Si (111)-7×7 reconstruction recorded using a scanning tunneling microscope (after Weisendanger et al. 1990).**

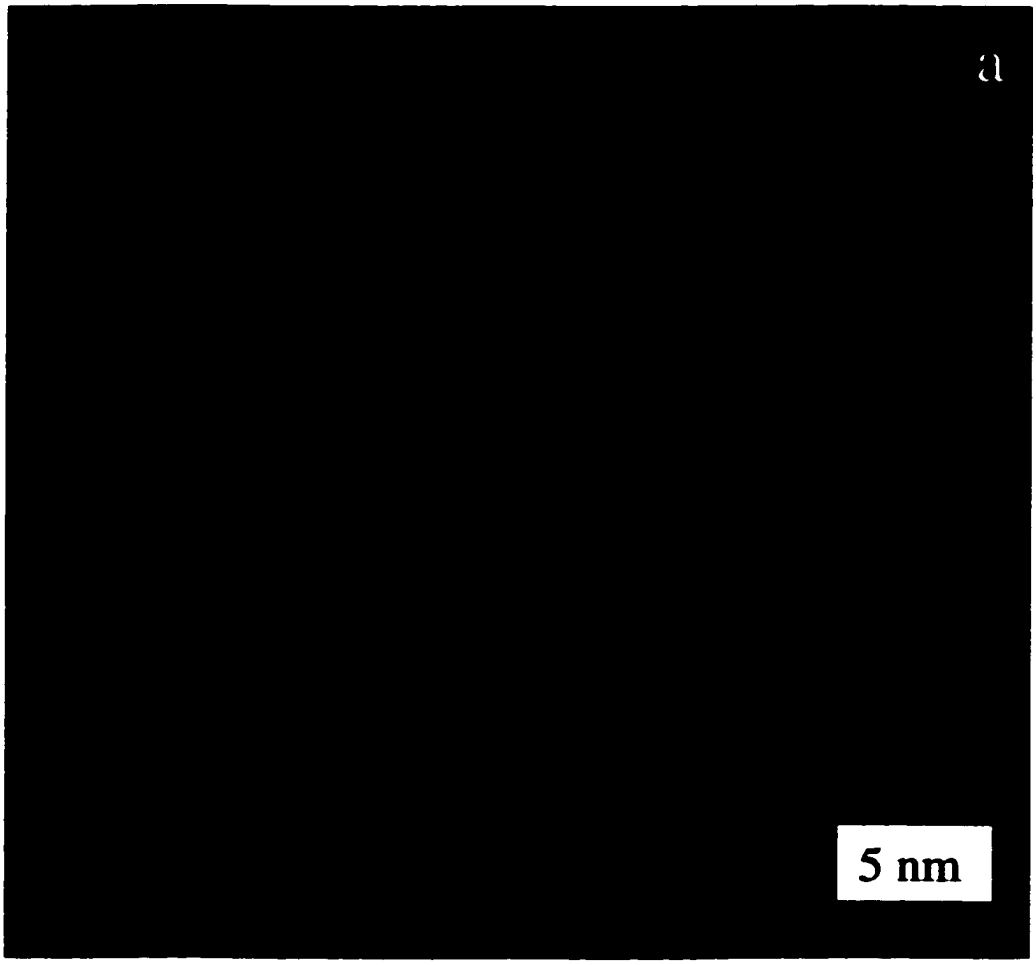

Figure 4.1.5 **a)Unprocessed image of Si surface. Although a periodic motif is observable, information at hand is not sufficient to draw conclusions.**

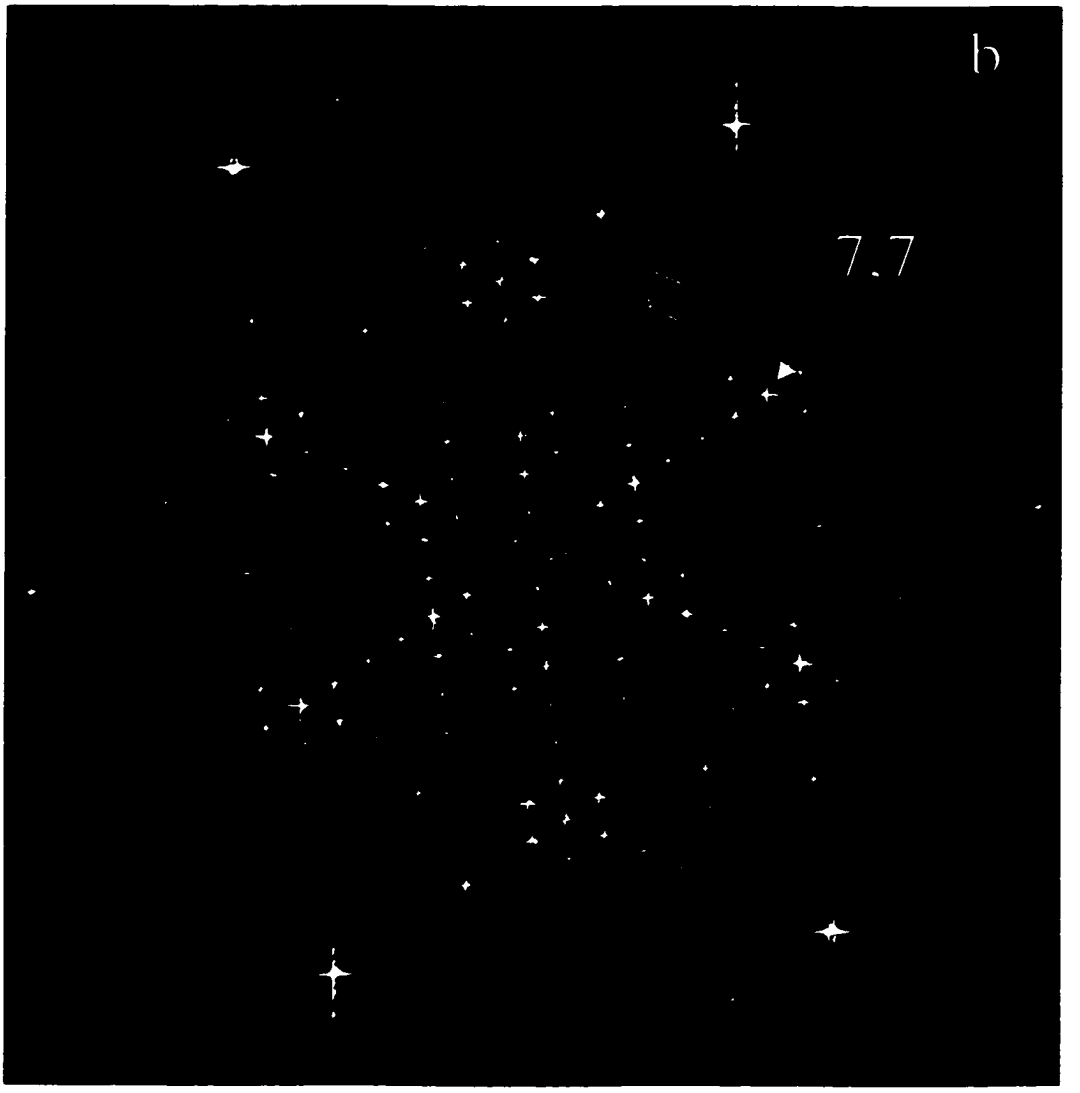

Figure 4.1.5 **b)Power spectrum of Si surface image displays 7×7 periodicity.**

HREM images of 7×7 reconstructed silicon surfaces were obtained under on-zone conditions (Ichihashi and Iijima 1994) hinting multiple scattering effects and forcing the use of nonlinear imaging conditions with the bulk beams. The TED study of Takayanagi et al. (1985) resulted in the precipitation of the DAS model for 7×7 employed kinematical approximation. Spence (1983), in his early analysis of surface diffraction, suggested that simple kinematical approximation could be used with surface beams. Strictly speaking, as pointed out by Marks (1991, 1992), one needs full dynamical treatment for complete analysis of a surface structure on a bulk-terminated layer. In our analysis of images, we have to remind ourselves that these images actually contain information from both the top and the bottom surfaces of the TEM sample convoluted in a nonlinear fashion. (see Figure 4.1.6). The image at the phosphorous screen can be easily expressed by:

$$I(\mathbf{r})=I_{top}(\mathbf{r})+I_{bot}(\mathbf{d}-\mathbf{r}) \qquad (4.7)$$

where $\mathbf{d}$ is some unknown translation vector and for periodic lattices the top ($I_{top}(\mathbf{r})$) and the bottom ($I_{bot}(\mathbf{d}-\mathbf{r})$) images will be related.

The first step is to handle the noise in these images using Wiener filters, discussed earlier, and the highly dynamical bulk Si {220} beams. After the application of the noise filter and a numerical soft aperture to {220} beams, the image and power spectrum are noticeably better. (Figure 4.1.7a and b, respectively). For the second step, we can neglect the Fresnel diffraction (focus variation) between the top and bottom

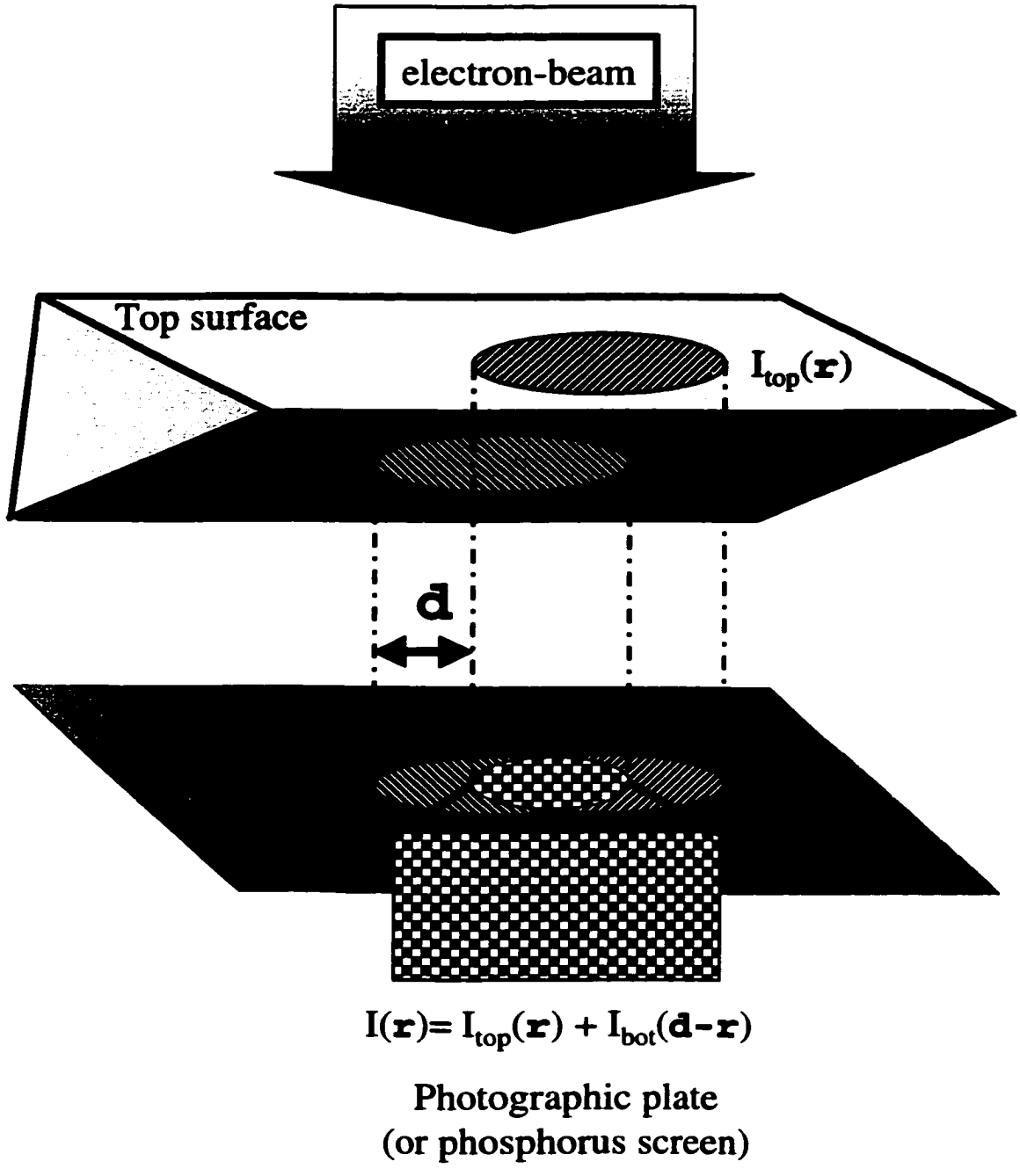

Figure 4.1.6 **Schematic illustration of the overlap image formation from the top- and bottom- surface images of wedge inside the electron microscope. The surface motifs are displaced with an unknown vector $\mathbf{d}$.**

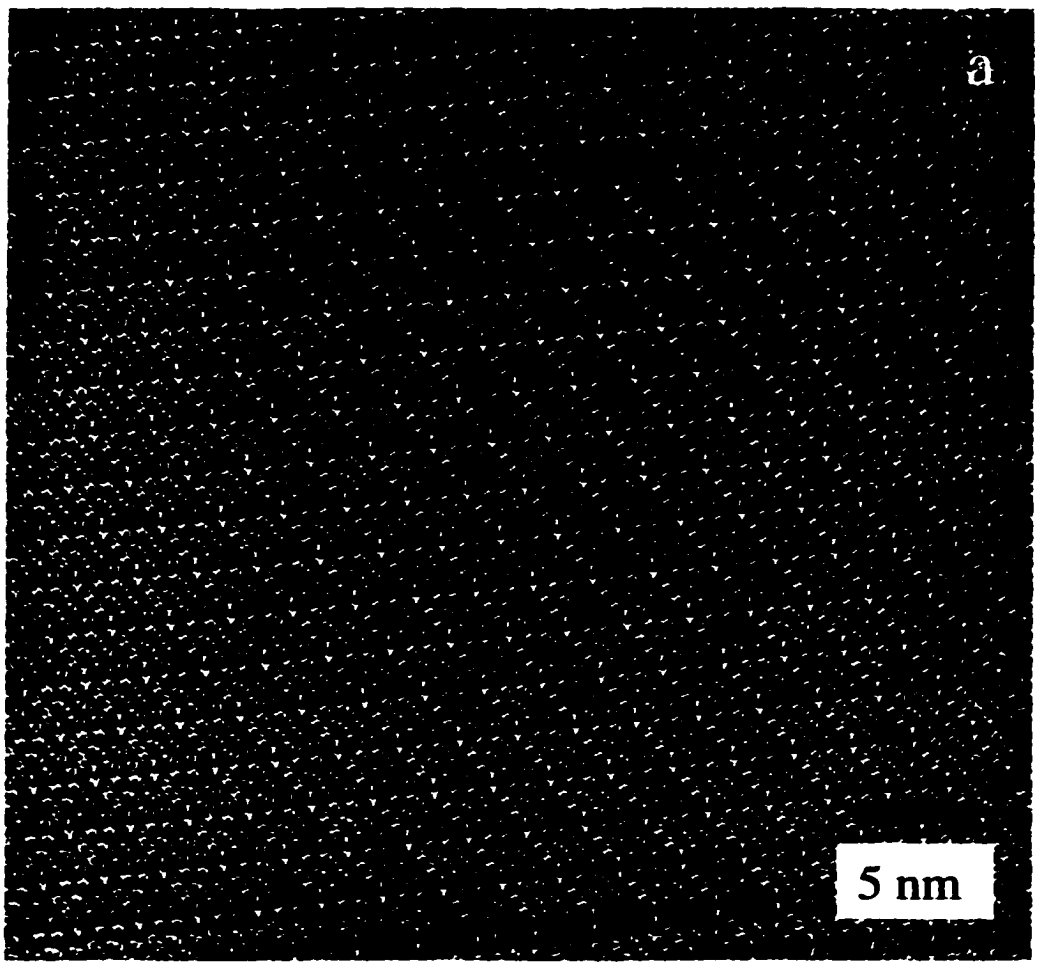

Figure 4.1.7 a) The image after the application of the noise filter and a numerical soft aperture to{220} beams.

Figure 4.1.7 **b) After the application of the noise filter and a numerical soft aperture power spectrum are noticeably better.**

surfaces, as these images are from a reasonably thin specimen and silicon is a relatively low-weight element.

Initially, in this approximation the electron wave leaving the sample can be written as:

$$\Psi_e(\mathbf{r}) = \exp(-i\sigma\phi_p(\mathbf{r})) \tag{4.8}$$

where $\sigma = 2\pi m e\lambda_r/h^2$ (relativistic interaction constant) and ϕ_p is the projected potential. However, here we are only interested in the weak surface reflections (1%-5%) for which the kinematical approximation will be reasonably accurate. We can also include the potentials due to surface structure as bulk effects ({220}'s) are partly handled by a digital aperture. Thus, equation 4.7 can be further approximated by:

$$\Psi_e(\mathbf{r}) \approx 1 - i\sigma[\phi^S(\mathbf{r}) + \phi^S(\mathbf{d}-\mathbf{r})], \tag{4.9}$$

where $\phi^S(\mathbf{r})$ is the potential of the top surface. This exit wave can be used to calculate the wave Ψ_d at the back-focal plane of the objective lens through a Fourier transformation given that $\phi^S(\mathbf{r})$ is a real function whose Fourier transform is $\phi^S(\mathbf{u})$. At this stage, a term representing the lens aberrations and microscope instabilities $A(\mathbf{u})$ is applied to the wave introduces the "damping envelope":

$$\Psi_d'(\mathbf{u}) = \delta(\mathbf{u}) - i\sigma A(\mathbf{u})\{\phi^S(\mathbf{u}) + \phi^{S^*}(\mathbf{u})\exp(2\pi i\mathbf{d}\cdot\mathbf{u})\} \tag{4.11}$$

Inverse transforming this term gives the image wave as:

$$\Psi_i(\mathbf{r}) = 1 - i\sigma\{\phi^S(\mathbf{r}) + \phi^S(\mathbf{d}-\mathbf{r})\} * \int A(\mathbf{u}) \times \exp(-2\pi i\mathbf{u}\cdot\mathbf{r})\,d\mathbf{u} \tag{4.12}$$

and then image $I(\mathbf{r})$ at the phosphorous screen can be approximated using only the first-order terms by:

$$I(\mathbf{r}) = \Psi_i(\mathbf{r})\Psi^*_i(\mathbf{r})$$
$$I(\mathbf{r}) \approx 1 + \int \sigma A(\mathbf{u})\{\phi^S(\mathbf{u}) + \phi^{S^*}(\mathbf{u})\exp(2\pi i\mathbf{d}\cdot\mathbf{u})\}\times\exp(-2\pi i\mathbf{u}\cdot\mathbf{r})\,d\mathbf{u} + \eta(\mathbf{r}) \quad (4.13)$$

where $\eta(\mathbf{r})$ is the noise in the images and d the translation between the top and bottom surfaces. This translation can take any of the 49 possible combinations of 1x1 lattice translations within the unit cell, plus one of the three translations (0,0), (1/3,2/3), and (2/3,1/3) due to the three different terminations A, B, or C of the AaBbCc stacking. Assuming p6mm symmetry, there are total of hundred and forty seven possible translations. Using appropriate symmetry elements, there is sufficient information in principle to determine the translation directly numerically as a free variable. However, in practice a less noise-sensitive methodology was employed finding the translations generating the best image of a single surface $I_s(\mathbf{r})^{\forall}$ using the following simple relationships:

$$I(\mathbf{u}) = I_s(\mathbf{u}) + I^*_s(\mathbf{u})\exp(2\pi i\mathbf{u}\cdot\mathbf{d}) \quad (4.14)$$

where $I(\mathbf{u})$ and $I_s(\mathbf{u})$ are the Fourier transform of the image and the single surface and $\exp(2\pi i\mathbf{u}\cdot\mathbf{d})$ the phase-shift term due to translation in the real-space image of the bottom surface.

The symmetry relationship between the top and bottom surfaces enables us to re-write equation 4.14 in the following fashion:

$$I(\mathbf{u}) = I_s(\mathbf{u})(1 + \exp(2\pi i \mathbf{u} \cdot \mathbf{d}))$$

(4.15)

thereby, in the Fourier space we can define the $I_s(u)$ with the help of a pseudoinverse of the phase-shift term by:

$$I_s(\mathbf{u}) = \frac{I(\mathbf{u})R(\mathbf{u})^*}{[|R(\mathbf{u})|^2 + |\eta(\mathbf{u})|^2]}, \qquad (4.16)$$

where

$$R(\mathbf{u}) = 1 + \exp(2\pi i \mathbf{u} \cdot \mathbf{d}). \qquad (4.17)$$

This methodology has been used for determining the surface structure of Si (111) - 7×7 using two 1024×1024 regions of two images recorded at different defocus values. For image 1, given in Figure 4.1.7a, this was done for three different regions; for image 2, for one region. The separated image (rotationally) from image 1 is shown in Figure 4.1.8 with the raw image from the separation in the inset. All the main details of the structure are evident, not just the adatoms but also the dimers. This is even more apparent for the translationally and rotationally averaged image in Figure 4.1.9 with inset; a multislice image simulation for a defocus of -36 nm was performed using a 3-layer model.

The image in Figure 4.1.10 shows the results from image 2, with again a multislice simulation inset. Although the atomic structure is not visible, the

---

[v] Best in the sense of least squares error between symmetry equivalent Fourier coefficients.

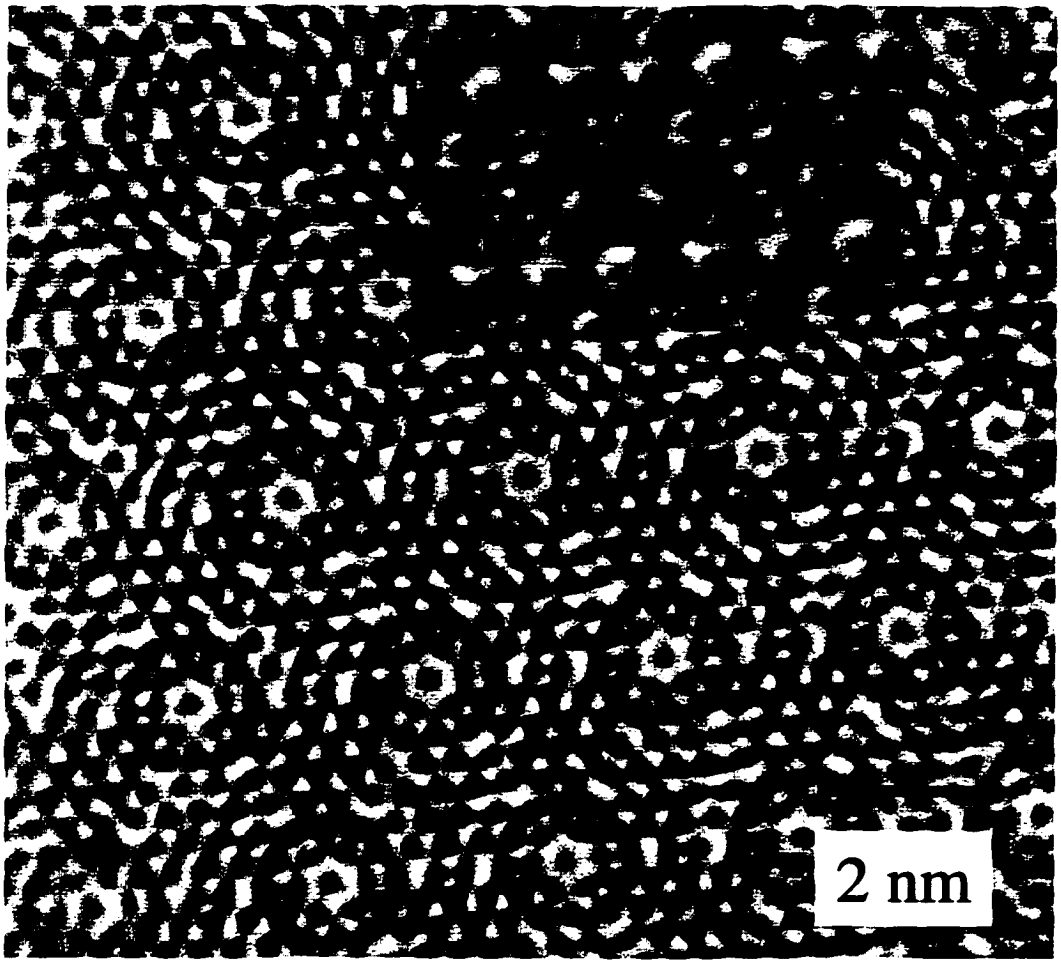

Figure 4.1.8 **Numerically extracted image of the single surface from the overlap image in Figure 4.1.7a. The raw separated image (inset) is rotationally (threefold) averaged.**

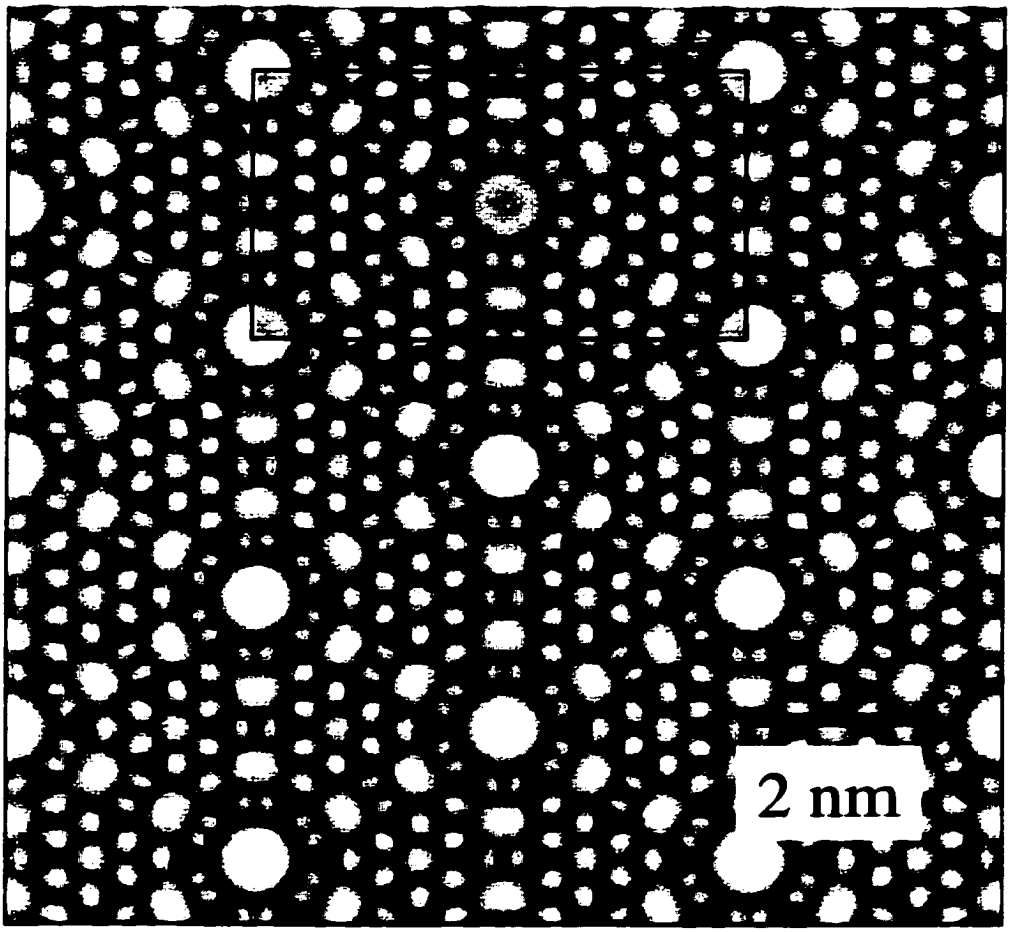

Figure 4.1.9 **Rotationally and translationally averaged image. The inset is a multislice image simulation.**

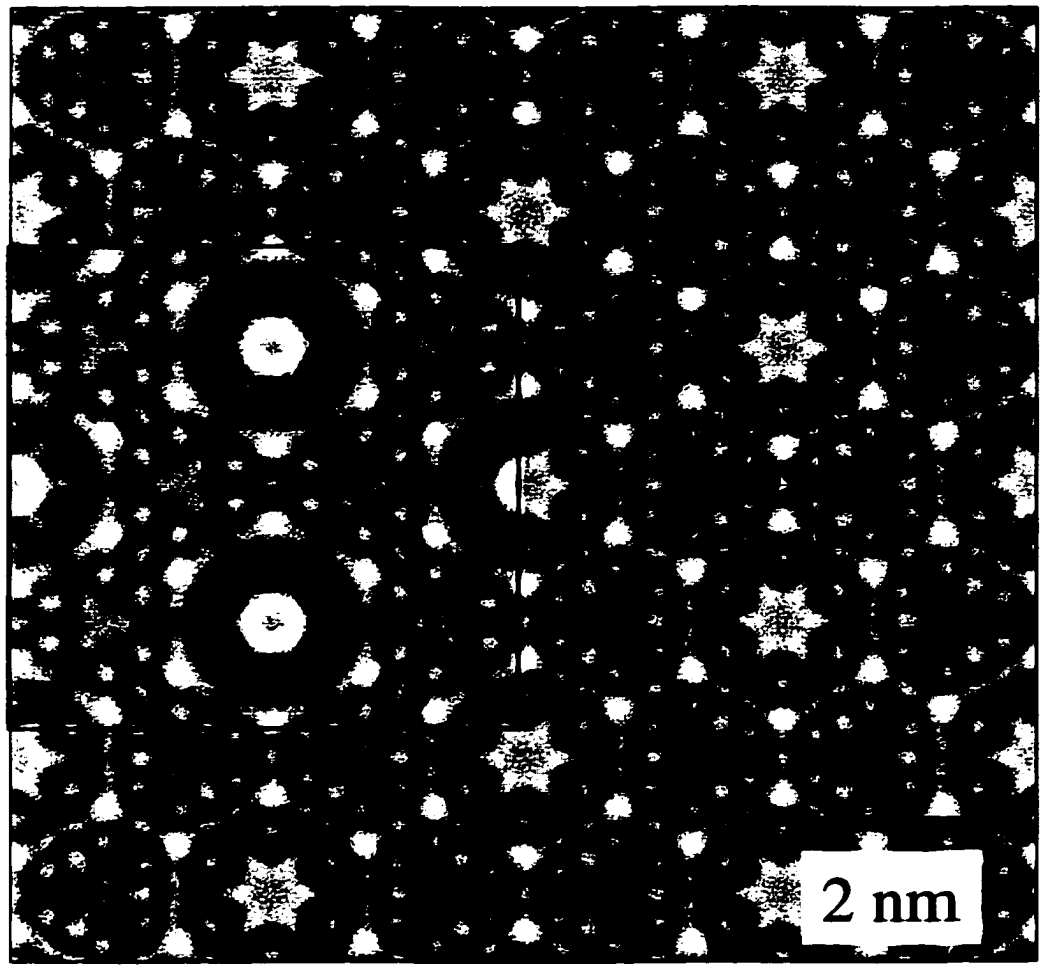

Figure 4.1.10 **Rotationally and translationally averaged image for another defocus. The inset is a multislice image simulation.**

correspondence between the experimental and calculated images is good for a defocus value of -136 nm.

In fact, there are differences between the images; the calculated image has the opposite phase compared to the experiment for three reflections ((5,0), (7,2), and (4,4)). The low signal levels, omission of multiple scattering and subsurface strains, as well as the microscope effects such as astigmatism are possible reasons for this. Nevertheless, such as match will not be acceptable for conventional HREM bulk crystal analysis.

4.1.4.2 Domain Boundary

Numerical manipulation of HREM images of the Si (111) - 7×7 reconstruction enabled us to overcome both the low contrast levels and the overlap issue helping us obtain the first direct images of the dimers in the DAS structure (Bengu et al. 1996). Another area where atomic level imaging might help is the domain boundaries and phase-transitions on the semiconductor surfaces. Boundaries between different domains of Si (111)-7×7 structure have been observed using LEEM (Telieps et al. 1985; Bauer et al. 1991), REM (Osakabe et al. 1980), and mainly STM (Becker et al. 1986; Tanaka et al. 1992). In contrast to incommensurate-commensurate (I-C) phase transitions and resulting boundary motion on surfaces where only the top layer absorbate monolayers are active, most surface phase transitions and domain boundaries (e.g. '1×1'-to-'7×7' on Si) involve atoms that are deeper in the structure.

Becker et al. (1985) claimed that 7×7 reconstruction on Si (111) surface nucleates by developing a dimer-row along a step edge; thus, it is possible that a number of DAS

domains can nucleate on a single terrace. If the phases of these domains do not match, a 1-D defect-fault line-forms where they meet on the terrace. Recently, the domain boundaries observed for 7×7 and other DAS structures has been characterized in a semi-empirical sense using STM images (Itoh et al. 1993). Their findings indicated the nucleation of DAS structures to be instigated by the corner holes rather than the dimer rows. Furthermore, they suggested surface reconstructions to follow a layer-by-layer procedure, thus indicating that factors triggering phase transitions on surfaces follow a bottom-to-top path. In order to identify correctly the transition mechanics of a process under the topmost layers (in buried interfaces), one must be able to image atoms below the surface, a process that is not available with STM (Marks, Bengu, and Gilmore 1997).

The numerical methodology developed for the extraction of HREM images of the Si (111) - 7×7 surface reconstruction is applied to a region with a noticable 1-D defect, such as the domain boundary in Figure 4.1.11. While these methods proved to be invaluable for extracting atomic detail in the previous section, extending them towards surface defects is a difficult task. The reason for this is two-folds: first, the filters tend to lose information; and second, when one moves from a 2-D periodic object to a 1-D defect (or less, point defects) there is a greater possibility of introducing artifacts. The basic strategy is that one generates an image of the defect-free "common surface," and then subtracts this from the experimental data to obtain an image which contains only the surface of interest, which, for instance, has a surface step. The one-dimensional periodicity of the defect if it exists can then be exploited to improve the results.

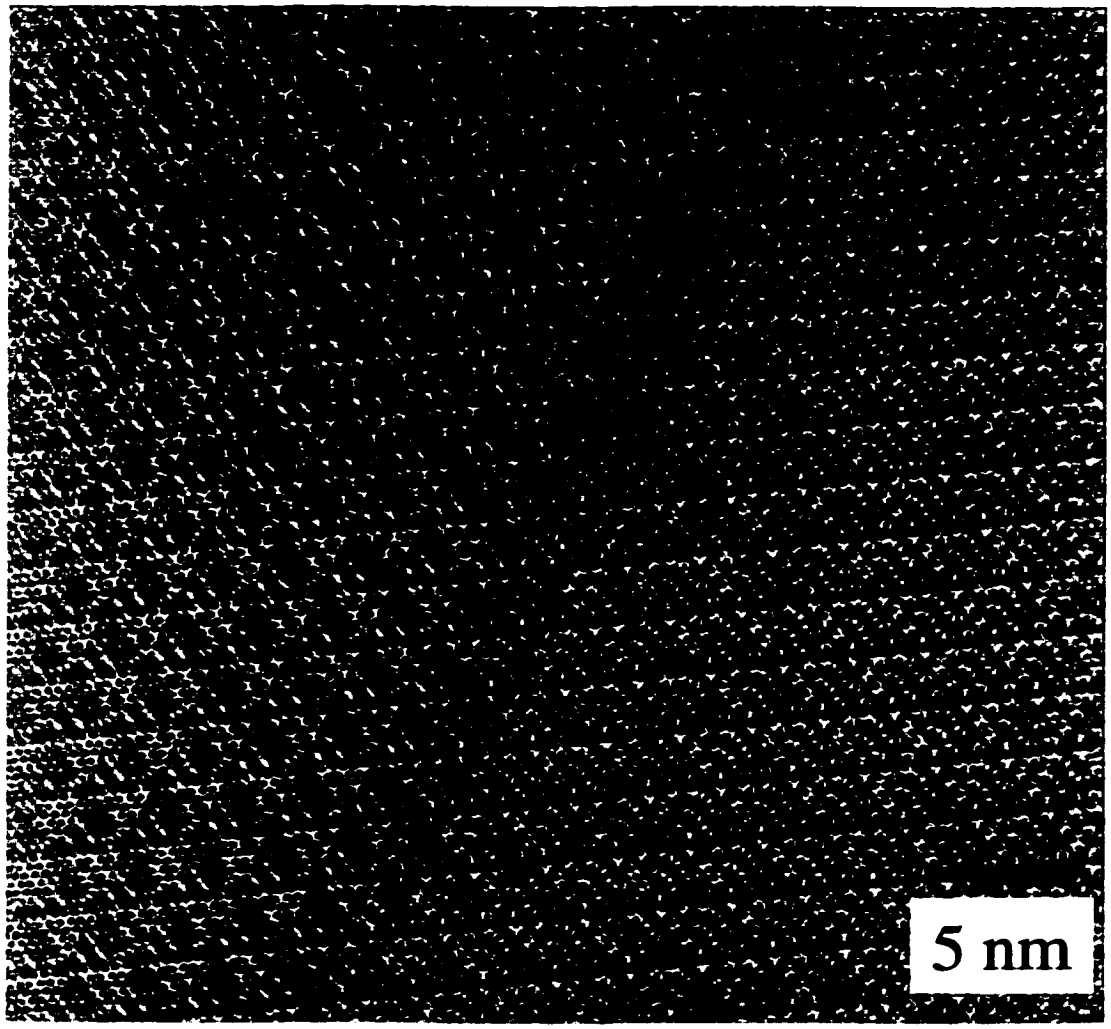

Figure 4.1.11 **Image of a step on the Si(111)-7×7 surface. The separation has been performed for the region A far away from the boundary (depicted by dashed lines).**

An example of this is shown in Figure 4.1.12. While one can start to see information close to the defect -for instance, the adatom configuration- it is not yet at a level where the dimer configuration around the step can be isolated.

4.1.5 Summary and Conclusion

Here, the results from the numerical extraction of the overlapped images of the top and bottom surfaces resulted in images that clearly show nearly all of the primary features of the DAS model. The final images show detailed features both deep inside the structure: e.g. dimers, stacking fault, and from the top surface, adatoms. Such detail escapes observation with STM, as it is sensitive to only the top surface. Application of this method to the imaging of 1-D domain boundary also seems to be at least conceptually possible, although much more work is definitely required if the defect structure at the interface is not periodic.

One of the obstacles that has to be dealt with in obtaining surface images is the noise due to poor counting statistics and low contrast levels for the surfaces (2-3% maximum). Although longer exposures or higher beam fluxes (field emission sources) can help to increase signal-to-noise ratio, there might be limitations to the degree that these are directly applicable or useful. In this exercise, we successfully used Wiener filters for unbiased treatment of the noise. However, a combination of high performance CCD cameras with online Wiener filtering could be the best way for tackling the noise problem.

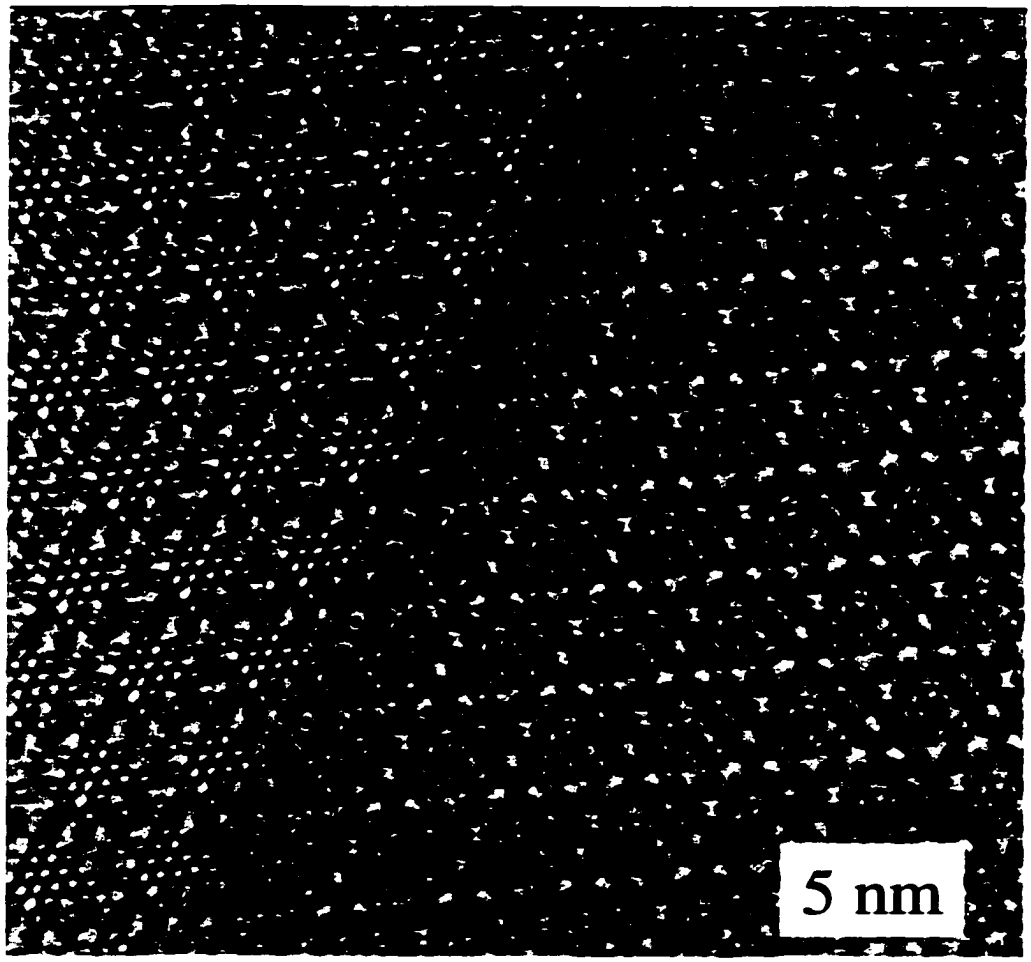

Figure 4.1.12 **Domain boundary solution.**

4.2 Model-Independent X-ray Reflectivity Analysis

One of the X-ray analysis techniques routinely employed is reflectivity. Small-angle X-ray specular reflectivity was first demonstrated by Compton in 1922. X-ray reflectivity under grazing incidence conditions is a powerful technique to study density profile, surface roughness, and multilayer structures without lengthy sample preparation steps in a non-destructive fashion. In fact, UHV or even low vacuum is not required for reflectivity analysis, unlike other surface sensitive methods. For instance, Braslau et al. (1988) investigated the surfactant-induced structures at liquid-vapor interfaces and Stone et al. (1999) compared the surface roughness of amorphous polymers using X-ray reflectivity and non-contacting atomic force microscopy.

Reflectivity has been established as one of the fundamental analysis techniques for investigating surfaces and interfaces in Langmuir and Langmuir-Blodgett (LB) films (Als-Nielsen and Mohwald 1991). LB technique may enable the synthesis of new stratified materials with tailored properties by controlling the layer constituents and sequences (Malik et al. 1995). Langmuir layers consist of organic molecules with well-distinguished hydrophilic (head) and hydrophobic (tail) segments spread at gas-water interfaces, forming a regular monomolecular layer. Incidentally, there are not many atomic-scale characterization techniques suitable for such structures. A rich variety of structural and chemical phenomena observed for Langmuir films are of great interest from both the scientific and industrial points of view. Recently, Geer et al. (1995) investigated the effect of surface roughness to the quasi-long-range order in LB films of

liquid crystalline copolymers, which is also an issue for inorganic multilayers. The molecular mechanism of bulk phase anchoring behavior during layer-by-layer growth in liquid crystal display devices has been studied by Ibn-Elhaj et al. (1997) using X-ray reflectivity (XRR) methods.

Biological functions such as nerve conduction, mass transport across cellular membranes, and molecular recognition depend on the integral membrane proteins. Structure-function relationships for cellular membranes are also immensely critical in terms of biotechnological applications. In a pioneering study, Koltover et al. (1998) probed highly aligned multilayers containing the membrane protein bacteriorhodopsin with the help of XRR, revealing the structural features of protein-induced membrane conformation on mesoscopic length scales.

XRR method also helped non-destructive analysis of surfaces, interfaces, and functional multilayers in hard solids, such as multilayer hard a-C films (Logothetidis et al. 1999), diamond-like-carbon films (Zhang et al. 1999), and GaAs/InP epitaxial multilayer gratings (Mikulik and Baumbach 1999). Steinfort, Scholte, and Tuinstra (1998) investigated the effects of miscut induced substrate surface steps on epitaxial multilayer systems through analysis of XRR data. They suggested that miscut induced interfacial roughness in a limited extent existed even far away from the original substrate/multilayer interface but diminished on the final surface for Si (001) - $4\times Si/Si_xGe_{1-x}$ multilayers. Lederman et al. (1997) quantitatively analyzed the surface roughness of GaN films grown under different Ga flux conditions using XRR. A higher Ga flux was found to induce significantly larger grain sizes and a lower fractal dimension

than the sample grown at a lower Ga flux, consistent with increasingly two-dimensional growth.

Lately, multilayer structures of alternating ferromagnetic and non-ferromagnetic layers have attracted much attention due to the giant magneto-resistance (GMR) effect with various possible applications such as read-write heads in HDD. One new comer in this field is the trilayer system NiMnSb/V/NiMnSb characterized by Sclomka et al. (1999) using X-ray and neutron reflectivity.

Other functional multilayer structures such as lamellar multilayer gratings (MLG), such as Mo/Si, Ni/C, and Pt/C layers with normal as well as lateral periodicities are extensively used in X-ray and ultraviolet (XUV) optics. X-ray reflectivity has been effectively utilized to characterize interface morphology in these structures (Lee et al.1998). Schlatmann, Shindler, and Verhoeven (1996) also tried to explain the evolution of surface morphology during growth and ion-polishing of Mo/Si multilayers during ion-beam assisted growth. Furthermore, Gupta et al. (1998) also employed the non-destructive nature of XRR during 100 MeV Ag ion irradiation on Ni/C and Pt/C multilayers, investigating time-resolved interface damage. In both cases, interfacial roughness was found to increase with irradiation dose, as expected. While Ni/C multilayers exhibit large ion-beam induced intermixing, no observable intermixing is observed in the case of Pt/C multilayers.

X-ray reflectivity allows one to characterize crystalline, amorphous, and polycrystalline gratings, since it investigates the distribution of the mean electron density. Thus, it is sensitive to the grating shape, and helps determine the quality of the interfaces.

Wide spread use of X-ray reflectivity followed the improved surface preparation techniques and advents in sources with higher brilliance, e.g. rotating anodes and synchrotrons.

4.2.1 X-ray Reflectivity and Density Profile: The Problem

The geometry of the reflection and transmission of a plane wave is illustrated in Figure 4.2.1. The initial layer is the free space (vacuum or air); layer 2 is the thin film (adsorbate layer) with finite thickness [$z=0$, $z=d$]; layer 3 is the substrate (semi-infinite subphase). In this Figure, the specular reflection of X-rays is considered where k_o, $k(z)$, and k_s are the z-components of the wave vectors, θ the incident angle, d the thickness of adsorbate layer, $\rho(z)$ the density profile, r the reflection coefficient, and t the transmission coefficient. In general, the problem is that one would like to infer density profile $\rho(z)$ given the measurements of the amplitudes of the reflected wave as a function of Q.

X-ray reflectivity is governed with the same principles as those underlying reflection and transmission of electromagnetic plane waves. Thus, for a mathematical treatment of X-ray reflection, it is necessary to solve the Helmholtz or wave equations for one dimension in the three layers (the subscript "o" and "s" stand for "free-space" and "substrate"; parameters without subscripts relate to the adsorbate layer):

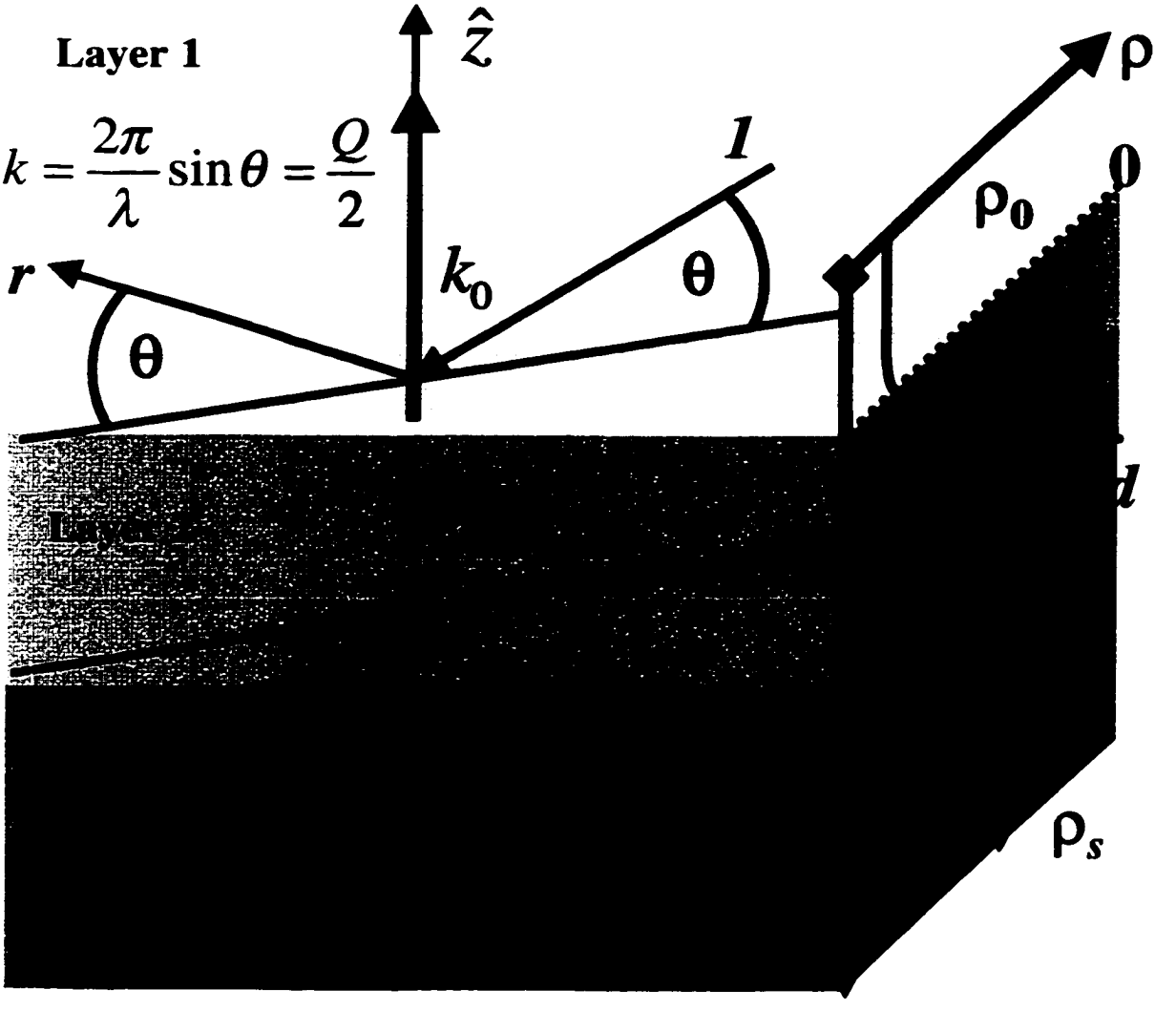

Figure 4.2.1 **Schematic illustration of specular reflectivity probing the density profile across the interface.**

$$\Psi''(z)+k_o{}^2\Psi(z)=0, \quad for \quad z\le 0 \quad , \tag{4.2.1a}$$

$$\Psi''(z)+k_o{}^2\Psi(z)=-(k^2-k_o{}^2)\Psi(z), \quad for \quad 0<z\le d \quad , \tag{4.2.1b}$$

$$\Psi''(z)+k_s{}^2\Psi(z)=0, \quad for \quad d<z \quad , \tag{4.2.1c}$$

where Ψ'' indicates second derivative with respect to z. For X-rays the wave numbers k_o, $k(z)$, and k_s can be expressed in terms of wavelength λ, the classical radius of electrons r_o, and the refractive index n as follows,

$$k_o{}^2=\left[\frac{2\pi}{\lambda}\sin\theta\right]^2, \tag{4.2.2a}$$

$$k^2=k_o{}^2-\left(\frac{2\pi}{\lambda}\right)^2\cdot(n^2-1), \tag{4.2.2b}$$

$$k_s{}^2=k_o{}^2-\left(\frac{2\pi}{\lambda}\right)^2\cdot(n_s{}^2-1) \ , \tag{4.2.2c}$$

$$n=1-\left(\frac{\lambda^2}{2\pi}\right)\rho(z)\cdot r_o, \tag{4.2.2d}$$

$$n_s=1-\left(\frac{\lambda^2}{2\pi}\right)\rho_s\cdot r_o. \tag{4.2.2e}$$

Solutions for $\Psi(z)$ in equations 4.2.1a and c using reflection and transmission coefficients can be expressed as

$$\Psi(z)=e^{ik_oz}+r\cdot e^{-ik_oz}, \quad for \quad z\le 0 \quad , \tag{4.2.3a}$$

$$\Psi(z)=t\cdot e^{-ik_sz}, \quad for \quad d<z \quad . \tag{4.2.3b}$$

Actually, one is only interested in the solution of equation 4.2.1b as it describes the wave in the sample with an *unknown* electron density profile for which an open-form expression can be derived using Green function (Zhou et al. 1991),

$$\Psi(z) = e^{ik_o z} + R \cdot e^{-ik_o z} + \frac{i}{2k_o}\int_0^d dz' \cdot \rho(z') \cdot \Psi(z')\left[e^{ik_o|z'-z|} + R \cdot e^{-ik_o(z'+z)}\right], \qquad (4.2.4)$$

where R denotes the Fresnel reflectance from the bare substrate-vacuum interface:

$$R = \frac{k_o - k_s}{k_o + k_s}. \qquad (4.2.5)$$

Unfortunately, unless $\rho(z)$ is known, there are only approximate solutions for equation 4.2.4. Once satisfactory approximations are done, one can obtain exact expressions for r and t terms by inserting the $\Psi(z)$ in the following equations:

$$r - R = \frac{i}{2k_o}\int_0^d dz' \cdot \rho(z') \cdot \Psi(z')\left[e^{ik_o z'} + R \cdot e^{-ik_o z'}\right], \qquad (4.2.6a)$$

$$t - T = \frac{i}{2k_o} T \cdot \int_0^d dz' \cdot \rho(z') \cdot \Psi(z') e^{ik_o z'}, \qquad (4.2.6.b)$$

where

$$T = \frac{2k_o}{k_o + k_s} \qquad (4.2.7)$$

These equations are the exact treatment of reflection and transmission coefficients for a simple three-layer system.

Based on the fundamentals of the refraction and reflection established earlier, dynamical theory of X-ray reflectivity for the multiple scattering events in a stratified

system can be obtained, exploiting several different approaches. A popular technique for neutron reflectivity, called the *matrix method*, utilizes a convenient matrix form (Born and Wolf 1975). Another widely accepted technique is the Parrat's recursion equations (Parrat 1954) where the scattering length density (SLD or $\rho(x)$) is partitioned into an *arbitrary* number of thin slices with finite sizes and the r from (j-1)th layer is related by a recursion relation to that of jth. Hence, reflectance between (j-1)th layer (with thickness d_{j-1}) and the jth layer (substrate) can be expressed by (Hamley and Pedersen 1994),

$$r'_{j-1,j} = \frac{r_{j-1,j} + r_{j-1,j}\exp(-iQ_j d_j)}{1 + r_{j-1,j}\, r_{j,j+1}\exp(-iQ_j d_j)}, \qquad (4.2.8)$$

where Q_j is $[Q^2 - (Q^c_j)^2]^{1/2}$ and Q^c_j is the critical wavevector transfer for medium j. The reflectances $r_{j,j+1}$ and the reflectance between layer (j-2) and (j-1), $r_{j-2,j-1}$, is approximated by

$$r_{j,j+1} = \frac{Q_{j+1} - Q_j}{Q_{j+1} + Q_j}, \qquad (4.2.9)$$

$$r'_{j-2,j-1} = \frac{r_{j-2,j-1} + r'_{j-1,j}\exp(-iQ_{j-1}d_{j-1})}{1 + r_{j-2,j-1}\, r'_{j-1,j}\exp(-iQ_{j-1}d_{j-1})}. \qquad (4.2.10)$$

This recursion scheme is applied till j-1=0 (free-space) and j=1 (surface layer), and then reflected intensities (ratio of reflected-to-incident) is calculated as

$$R(Q) = \left|\frac{E^r}{E}\right|^2 = |\, r'_{0,1}\,|^2. \qquad (4.2.11)$$

Kinematical approximation, unlike the its dynamical counterpart, does not take multiple reflections into account. In fact, the equation 4.2.9 is simplified to

$$r_{j,j+1} = \frac{2\pi(\rho_{j+1} - \rho_j)}{Q^2}, \tag{4.2.12}$$

considering $Q >> Q^c_j$ for all layers. Further approximation (Born and Wolf 1975) leads to substitution of complex recursion expression of reflectivity with a summation of reflected waves from each consecutive layer as

$$r = 4\pi \sum_{j=0}^{n} \left[\left(\frac{\rho_{j+1} - \rho_j}{Q^2} \right) \right] \exp(-iQd_j). \tag{4.2.13}$$

Consequently, one can simplify the expression for kinematical treatment of the reflectivity with d_j in the limit of dz and assuming a sharp interface between the adsorbate and the substrate,

$$R(Q) = R_F(Q) \times \left| \frac{1}{\rho_\infty} \int_{-\infty}^{\infty} \left[\frac{d\rho}{dz} \right] \exp(-iQ'z) dz \right|^2, \tag{4.2.14a}$$

$$R_F(Q) = \left| \frac{(Q - Q')}{(Q + Q')} \right|^2, \tag{4.2.14b}$$

$$Q' = \left[Q^2 - (Q^c_\infty)^2 \right]^{\frac{1}{2}}, \tag{4.2.14c}$$

where ρ_∞ is the density of the substrate, Q' the refraction-corrected wave-vector, Q^c_∞ the critical Q for the substrate and $R_F(Q)$ is the Fresnel reflectivity.

Derivation of kinematical theory involves crucial approximations, but the final expression (equation 4.2.14a) represents an important step in the *ab initio* analysis of reflectivity. The measured reflected intensities are related to the Fourier transform of the

real-space density fluctuations ($d\rho/dz$) along the path of X-rays in the adsorbate layer. Extraction of the density profile from the spectral response by an inverse Fourier transform requires the *correct* phases of the reflected waves Ψ for which only the intensity $<\Psi\Psi^*>$ is measurable.

If reliable and detailed a priori information about the system from other methods is available, the conventional ways for extracting the unknown density profiles often follow the path of optimizing the difference between calculated reflectivity (usually by recursion equation) and the measured data using parameterized box-like models in a least-squares sense (Pedersen 1992). Another one is the trial-and-error approach with box-like models. However, this approach requires ample knowledge about the system analyzed, which is sometimes not available or possibly wrong. Both of these techniques do little more than verifying the preconceptions about the actual structure and refining the initial input accordingly. They are both laborious and time-consuming. Recently, there have been significant developments in what is called *model-independent* techniques. Most of the model-independent approaches are build around the reflectivity analogue of the auto-correlation function (ACF) or Patterson function used in crystallography (Patterson 1934), and therefore are generally based on the kinematical approximation of the reflectivity. The peaks in a correlation function simply points out the distances between peaks in the density profile (SLD), which is related to the measured reflected intensities through a Fourier transform (equation 4.2.14a). Thus, this method introduces a degree of objectivity to the verification of SLD with limited a priori information.

In various forms, Patterson's method has been applied to the X-ray reflectivity by Penfold and Thomas (1990), Tidswell et al. (1990), Crowley et al. (1991), Sivia, Hamilton, and Smith (1991), Sivia, Hamilton, Smith, Rieker, and Pynn (1991), and Pedersen (1992). Among these, several merit further mentioning. The first is the maximum entropy technique (ME) employed by Sivia, Hamilton, and Smith (1991) and Sivia, Hamilton, Smith, Rieker, and Pynn (1991). One can suggest that ME is also a crossover from crystallography where it has been known and used for a long time (Bricogne 1984; Bricogne and Gilmore 1990; Gilmore et al. 1990). Simply, ME optimizes the likelihood of a $\rho(z)$ against a model (which may contain constraints on the $\rho(z)$) with the agreement of the reflectivity calculated from this model to measure the data. Although results are encouraging for systems with sharp interfaces, the method is severely hindered due to the non-unique correlation functions and limited resolution due to finite range (Q) of data. Even though marker techniques (e.g. speckle holography), are suggested to help with ambiguities of smoother and narrower correlation functions, the types of SLD (profiles up to 1000Å) that this technique could be useful are well in the limit of dynamical effects. On the other hand, Pedersen (1992) proposed a square-root deconvolution operation on the ACF leading to the density profile $\rho(z)$. Pedersen uses an indirect Fourier transformation using non-parametric cubic B-splines for the calculation of ACF, which avoids the artifacts due to limited range in Q. This method has been applied with varying success to the reflectivity curves from amphiphilic fluorocarbon molecules on water (Jacquemain et al. 1990) and 3-block layer liquid crystals at air-water interface (Ibn-Elhaj et al. 1997).

Another route followed by Singh et al. (1993) parameterizes the scattering density of multilayers using Fourier-series basis of sines and cosines. Using kinematical arguments, they have shown analytically that each coefficient of the Fourier series gives rise to a unique Bragg peak in the reflectivity data. A kinematical derivation is used to fit the data, determining each Fourier coefficient for the initial guess of scattering density, which may then be refined using a dynamical treatment. In a recent paper by Pedersen and Hamley (1994), the last two methods are extended for use with dynamical theory and applied to both aperiodic and periodic structures. Apart from these methods inspired by kinematical approximation, there is a handful of model-independent techniques attempting to invert $\rho(z)$ from highly-nonlinear dynamical treatment of reflectivity, such as studies by Zhou and Chen (1993), Berk and Majkrzak (1995), Kunz, Reiter, Gotzelmann, and Stamm (1993). All of these methods are originally proposed for the treatment of neutron reflectivity. This is because of the low contrast from polymers under X-ray scrutiny. Only the method proposed by Zhou and Chen is suggested to be directly applicable to XRR, although all of the cases that it has been applied to are neutron scattering experiments. Thus, the latter two take advantage of deuteration to enhance the contrast between the different components. Details of these methods and applications will not be reviewed here; interested readers are referred to the corresponding references.

4.2.1.1 Inversion of X-ray Reflectivity

The disposition of the classical *inverse problem* long-standing in quantum mechanics (Chadran and Sabatier 1977) and elsewhere fits well to the inversion of X-ray reflectivity. Direct inversion of dynamical reflectivity expression for special cases (e.g. two and three-layer box-like artificial models) are available with or without the missing phase information using exact formulations (Lekner 1991; Zhou and Chen 1993). However, in many cases with multilayers, even if the phase information were provided, it would still be very difficult to extract SLD by inverting recursion or matrix methods. This is simply due to the nonlinear behavior of the expressions involved. In fact, even with missing phases available, one has to use other techniques such as Gel'fand-Levitan and Marchenko methods which are directly applied through one-dimensional wave functions.

The inverse problem has been treated very rigorously in the literature for special 1-D cases (e.g. step problem, barrier problem, etc.). Some of the texts on these cases are listed by Aktosun and Sacks (1998) and Roberts (1991). Arguably, a shortcut around the inverse problem for X-ray reflectivity is to use kinematical approximation [§] in relating $\rho(z)$ to the reflected intensities through a single Fourier transformation. At this point, if the missing phases could be restored, one can happily use inverse Fourier transformations to extract the scattering density of the structure at the interface. In this format, the problem of extracting SLD is equivalent to the crystallographic phase retrieval problem

in XRD and/or TED. Development of direct methods for the crystallographic phase problem has been mentioned elsewhere in this chapter (section 4.1.1.1). Nonetheless, the phase problem is encountered in many different and unrelated fields such as image restoration (Gerchberg & Saxton 1972; Dainty & Feinup 1987) and Josephson junctions (Dynes & Fulton 1971). Phase restoration techniques in these fields developed nearly independently of each other. The common characteristics of such one-dimensional problems have been discussed reasonably in the literature (Klibanov, Sacks, and Tikhonravov 1995).

Clinton (1993) employed a phase retrieval-based approach (logarithmic dispersion relations, LDR) for the inversion of X-ray reflectivity for the first time. However, usage of LDR is limited to a number of special cases of density profiles which satisfy the condition that reflectivity is a complex analytic function that does not have any zeros in the upper half plane. Because its applicability depends on certain conditions that require ample knowledge on the density profile, this method is better suited to be a supplemental refinement routine for the model-dependent techniques where conditions permit its use.

At this point, one can always question the necessity for exact phases for a partial restoration, or may be tempted to use phases from a similar case where the solution is known. Hence, while the importance of the availability or measurement of the phases cannot be overemphasized, understanding the principles of phase restoration and

---

[§] In the limit $R(Q)<<1$ and large scattering vector, $Q>>0$, kinematical approximation is indistinguishable from exact considerations (Hamley & Pedersen 1993).

information enclosed in the phase of a wave are just as crucial. In this problem, we seek to find an unknown function $f(x)$ from the amplitude $|F(q)|$ of its Fourier transform.

Let's rewrite the equation 4.2.14a as,

$$I(Q) = \frac{R(Q)}{R_F(Q)} = \left| \int_{-\infty}^{\infty} \left[\frac{d\rho}{dz} \right] \exp(-iQ'z) dz \right|^2, \qquad (4.2.15a)$$

$$I(Q) = \left\langle \Psi \Psi^* \right\rangle = |\Psi|^2, \qquad (4.2.15b)$$

where,

$$\Psi = |\Psi(Q)| \exp(i\Phi(Q)) . \qquad (4.2.15c)$$

The expression in equation 4.2.15a is called the master formula (Als-Nielsen 1991) for reflectivity, where $I_O(Q)$ is the observed ideal reflected intensities and $\Phi(Q)$ the phase of the reflected wave Ψ which, if known, can be used to extract $\rho(z)$ directly by an inverse Fourier transform. Simply stated, one can say that the modulus $|\Psi(Q)|$ carries information about the size and shape of the scattering objects and domains, whereas the positional information regarding the scattering objects is locked in the phase $\Phi(Q)$. The following educational and elementary exercise may offer further clarity to the importance of phases: Figure 4.2.2 contains (76 pixel × 91 pixel) grayscale (8-bit) bitmap images of an apple and an orange. These images are Fourier transformed resulting in a complex valued image (A+*i*B) from which *modulus* $|A^2+B^2|$ and *phase* $\tan^{-1}(B/A)$ portions can easily be calculated.

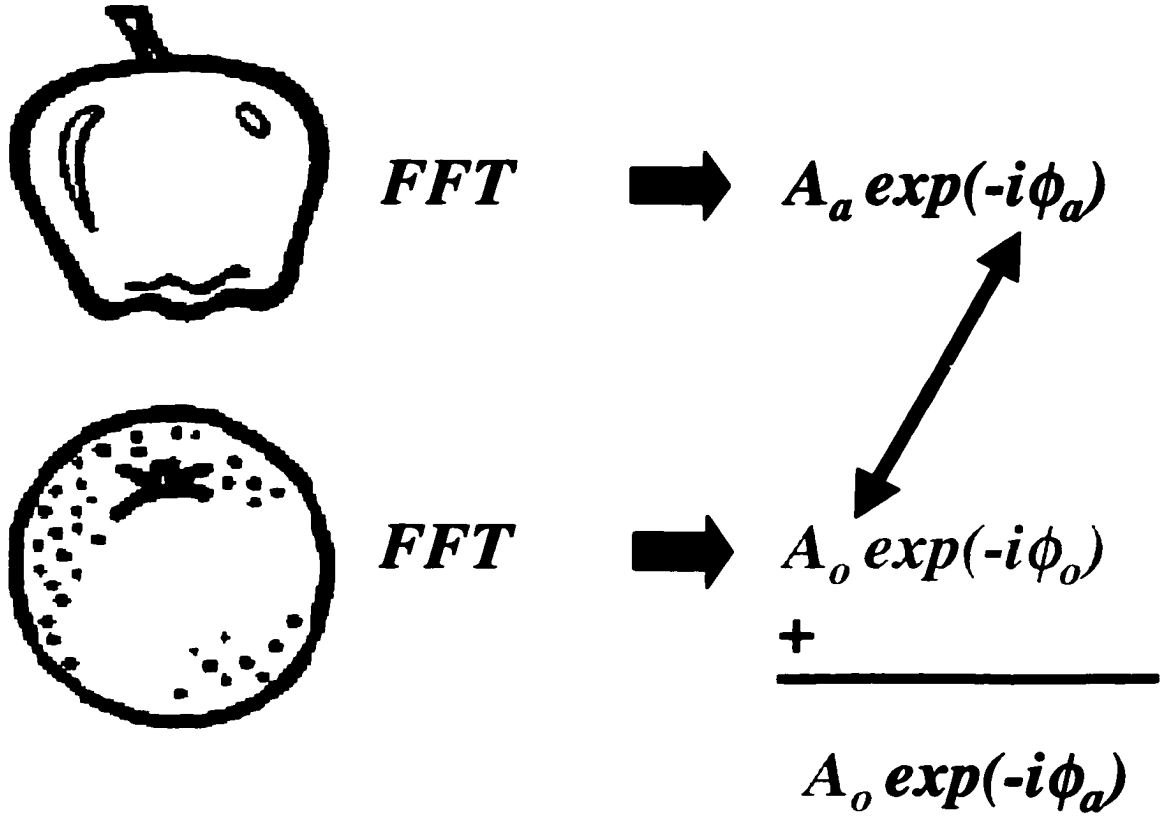

Figure 4.2.2 The bitmap images of an apple and an orange are Fourier transformed to get moduli and phases defining the 2-D images in the reciprocal space. FFT represents forward Fourier transformation.

Following this, modulus of the orange image is paired with the phase of the apple image, and then inverse Fourier transformed back into the real space. The resulting image is displayed in Figure 4.2.3; this image delineates an apple. It can be argued that images of the apple and the orange are not that different, and thus modulus of orange and apple would not be significantly different, resulting in the apple image in Figure 4.2.3. However, other reconstructions in Figures 4.2.4a and b with random and constant moduli, respectively, agree with the original postulation that information carried in the phase is decisive defining the features in an image. In fact, reconstructions with constant and random moduli are as good as, if not better, than the one with modulus of orange. Furthermore, another reconstruction with modulus of an apple and a random phase is displayed in Figure 4.2.5, which shows a featureless image.

Hence, the most common issue in constrained phase determination and other techniques that are trying to find a *feasible* solution for $f(x)$ from the moduli $|F(q)|$ of its Fourier transform is the uniqueness of the solutions. Indications are that a multitude number of solutions may exist for a given moduli $|F(q)|$. Yet, a function $f(x)$ can only be uniquely defined by its phase $\Phi(q)$ and not by its modulus, which may lead to dangerous ambiguities as shown by the earlier examples. For cases with two or higher dimensions, Bruck and Sodin (1979) suggested that there is *usually* a unique solution through the irreducibility of polynomial expressions of Fourier transformations. Although Fienup (1983;1987), Crimmins and Feinup (1983), Fiddy, Brames, and Dainty (1983) investigated in detail the theoretical and experimental extends where uniqueness

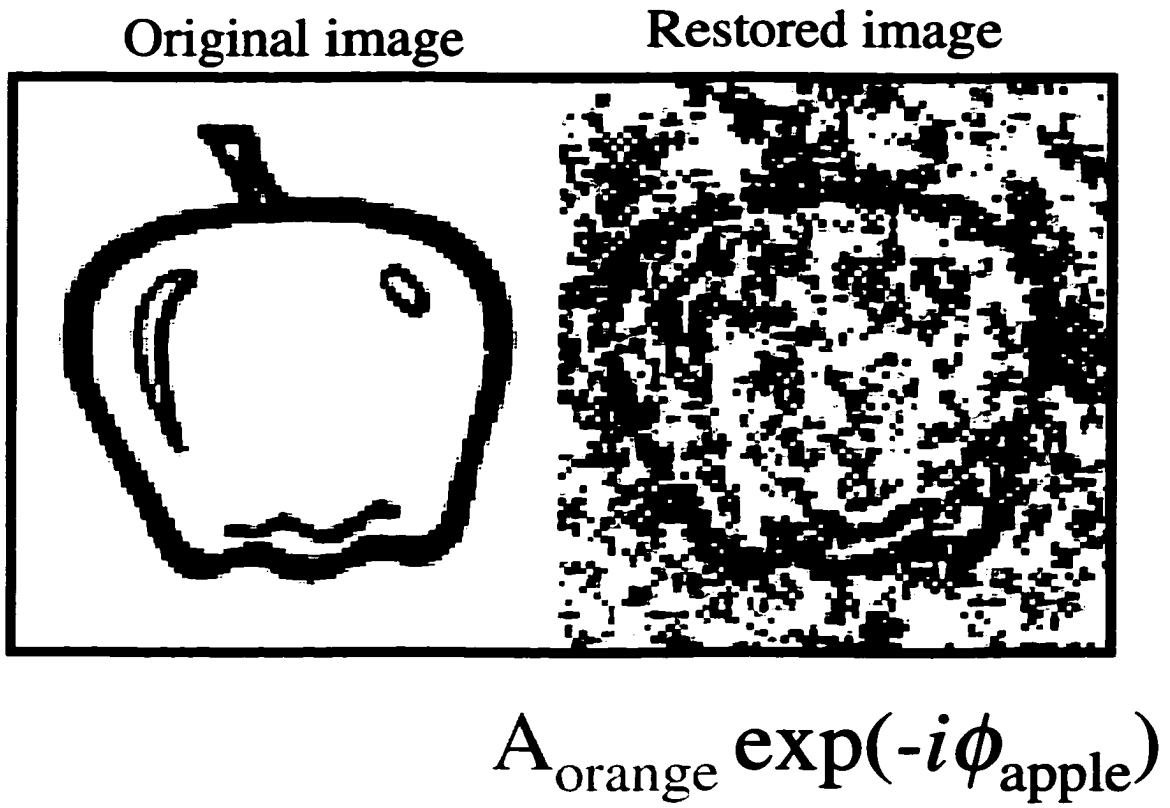

Figure 4.2.3 **The bitmap images of the apple and the restored image. The restoration is done by inverse transforming the reciprocal image composed of the moduli of orange and the phase of the apple. Despite the wrong moduli, the restored image shows the image of the apple.**

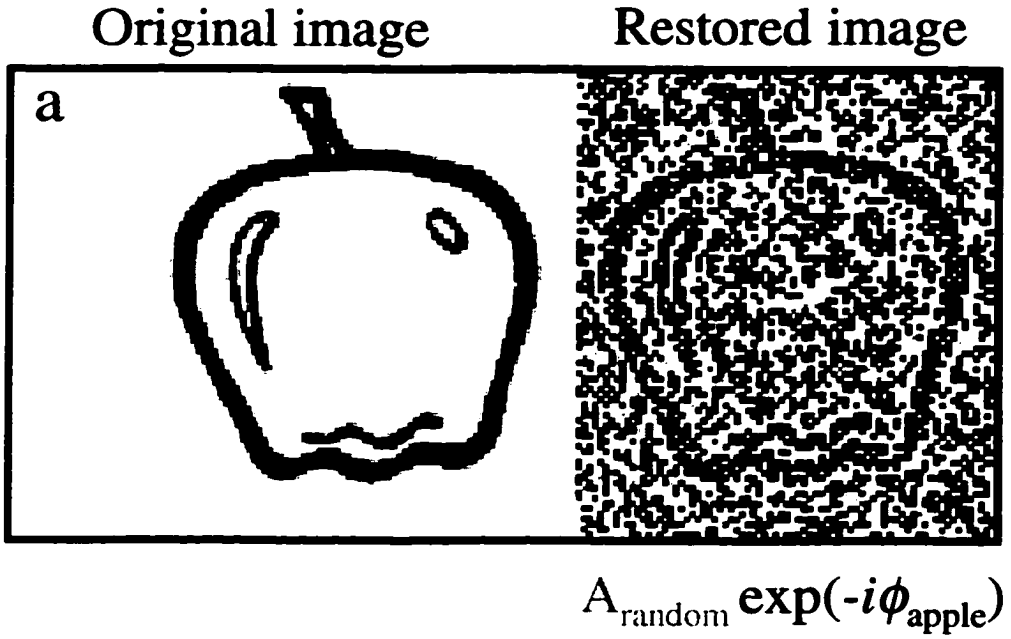

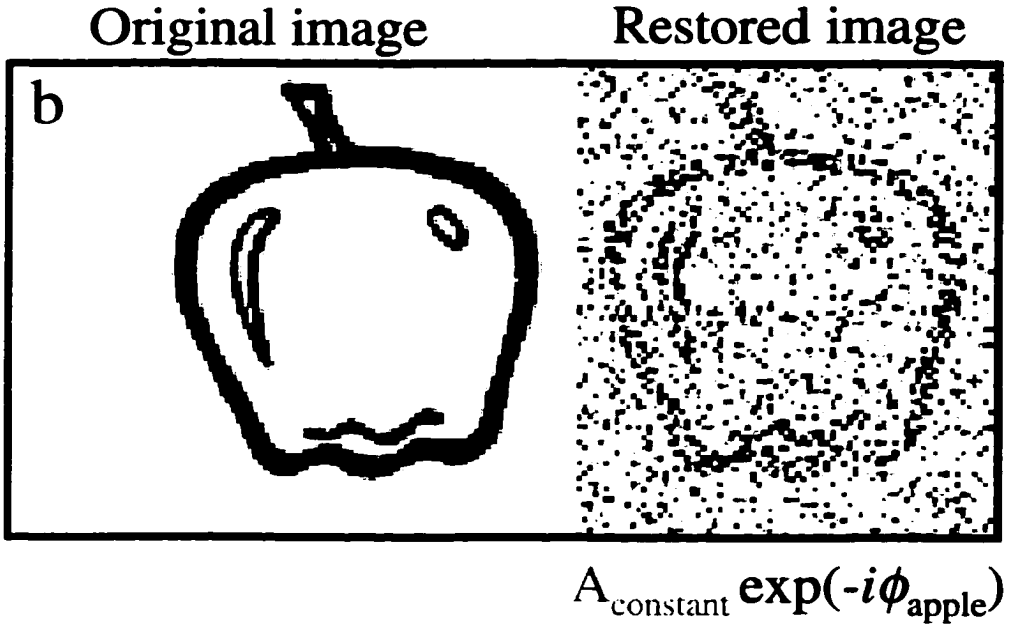

Figure 4.2.4 **The bitmap images of the apple and the restored images created from (a) a random and (b) a constant moduli and the phase of the apple. Both restored images with the wrong moduli show the image of the apple.**

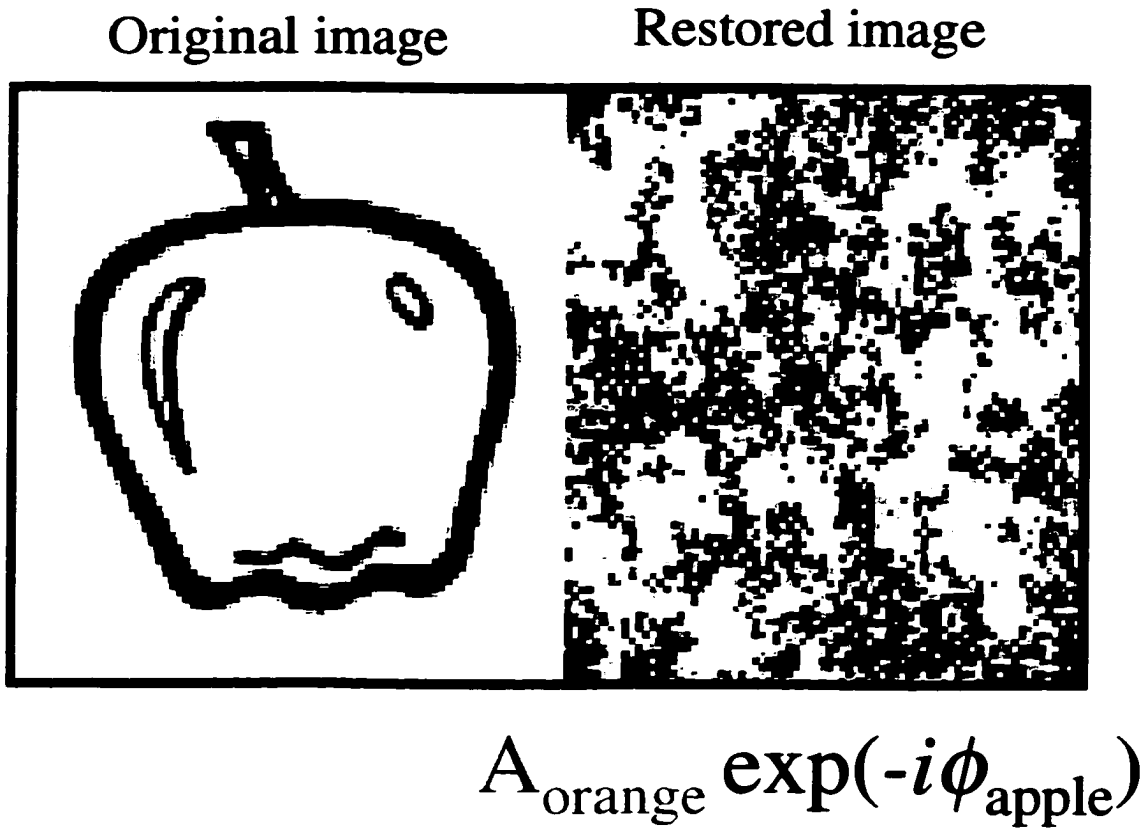

Figure 4.2.5 **The bitmap image for the restored image created by using the moduli of the apple and random phases. There are no observable features in the restoration.**

can be usually granted, Sivia et al. (1991) dismissed such considerations and called subscribers to this path "brave and perhaps foolish." Recent studies on the uniqueness issue (Klibanov et al. 1995) gives credit to earlier suggestions regarding the conditions granting uniqueness at higher dimensions, but puts strong emphasis on the use of every possible supplementary (a priori) information on $f(x)$ to decrease the ambiguity by limiting the plausible solution population for the much more difficult one-dimensional cases. Interested readers may find further discussions on this subject in texts by Hurt (1989) and Bates and McDonnell (1986) and references therein.

4.2.2 A Feasible Set Approach to X-ray Reflectivity

A methodology outlined by Combettes (1996) has been adopted, originally proposed for image recovery issues, as a new and unique way to reconstruct scattering length density by determining the phases in the case of x-ray reflectivity through kinematical considerations. One of the essential points in this method is to determine all admissible a priori information about the system, which are subsequently used as constraints during the solution process. For x-ray and neutron reflectivity, there are four constraints acting on the $\rho(z)$ (see Figure 4.2.6):

i- $\rho(z)$ is positive, (except for a few cases of neutron reflectivity).

ii- For the medium before the reflecting surface, generally vacuum, the value of $\rho(z)$ is known ($\rho(z)$=0).

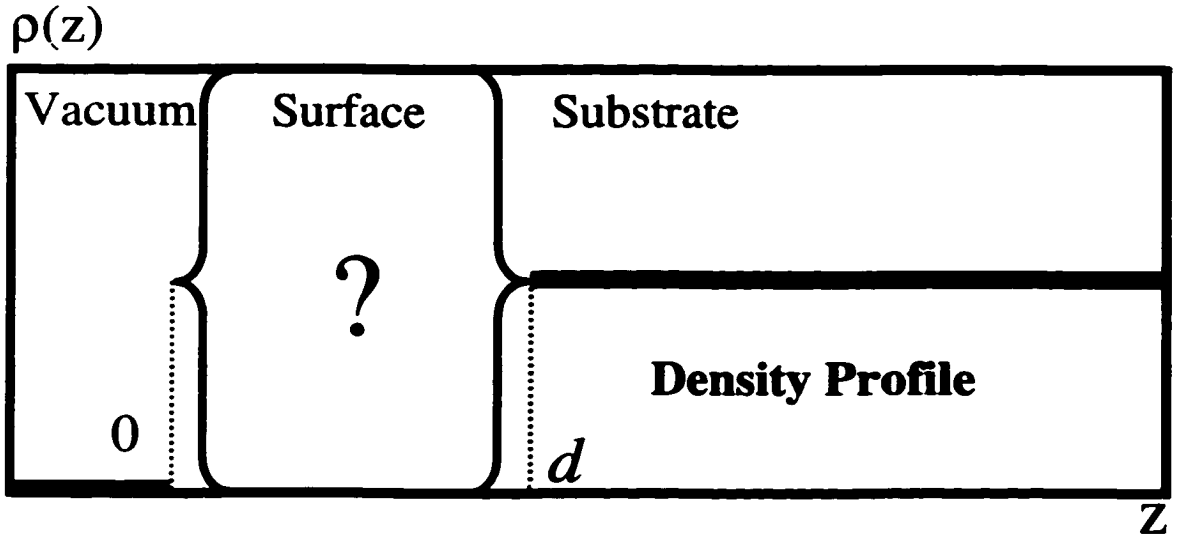

$$S_1 = \begin{cases} \rho(z) = 0: & z \in vacuum \\ \rho(z): & 0 \le \rho(z) \le D_{\max} \\ (1-\delta_2)\,\rho(z): & \rho(z) < 0 \\ D_{\max} - (\delta_2 - 1)\rho(z): & \rho(z) > D_{\max} \\ \rho(z) = D_{sub}: & z \ge d \end{cases}$$

Figure 4.2.6 A priori information on the density profile.

iii- In the bulk material below the reflecting surface, $\rho(z)$ is also known (D_{sub}).

iv- An upper bound to the value of $\rho(z)$ is usually available (D_{max}).

If the reflectivity problem was of "compact support"-i.e. outside of some particular region the derivative $d\rho(z)/dz$ is zero and this was the only constraint- it is known that a multiplicity of solutions may exist (Klibanov et al. 1995). Even with additional constraints, it is extremely difficult to ascertain numerically the existence of a unique solution for the reflectivity problem (i.e. an analytic proof), although numerical tests in this study indicate that this is often the case. For cases, where the solutions in a given set display a large degree of similarity and do not change with varying the parameters in the method, one can suggest the uniqueness of the solution. However, there will be always be a set of plausible solutions for $\rho(z)$, especially if one considers counting statistics and instrumental errors in the measurements. In this study, the motivation is to find this set of solutions, which may then act as the initial models for subsequent final refinement via some least-squares related approach. In other words, this set of solutions will act as the initial model input, and a degree of objectivity can be imparted to the process limiting the guesswork.

In this study, the method that has been used to analyze reflectivity data for plausible solutions of scattering density profiles by restoring the phases combines two separate algorithms:

a) The first finds a solution from some initial starting point that conforms the constraints (some of the phases). For this, a method of iterative projections is developed. Similar algorithms are characterized and tested by Feinup (1982; 1987).

b) The second is a global search algorithm to find the set of plausible solutions. This is achieved by employing a genetic algorithm similar to that used by E. Landree, C. Collazo-Davila, and L. D. Marks (1997).

The first algorithm involves projecting an initial estimate onto two constraint sets. This approach is initially employed as projection onto convex sets (POCS) which is a well-established technique used in fields for instance in computer-aided tomography (Herman 1980). A set is termed convex if all points on the line connecting any two elements of the set are also members. A general form of this technique including non-convex sets is termed as the *feasible set approach*. Reviews of the concepts involved can be found in an article by Sezan (1992), and formal analyses are available through articles in a book by Stark (1987) and the recent review article by Combettes (1996). Simply, this approach can be summarized by the following: given that there are m independent constraints, a *feasible* solution lies at the intersection of m constraint sets (Sezan 1992).

The flow diagram for an algorithm developed for the x-ray reflectivity problem based on feasible sets approach is given in Figure 4.2.7. The first set, S_1, consists of all solutions that obey constraints on $\rho(z)$, a real space object; Feinup (1987) argues complex-valued object can also be treated using similar methods with stronger

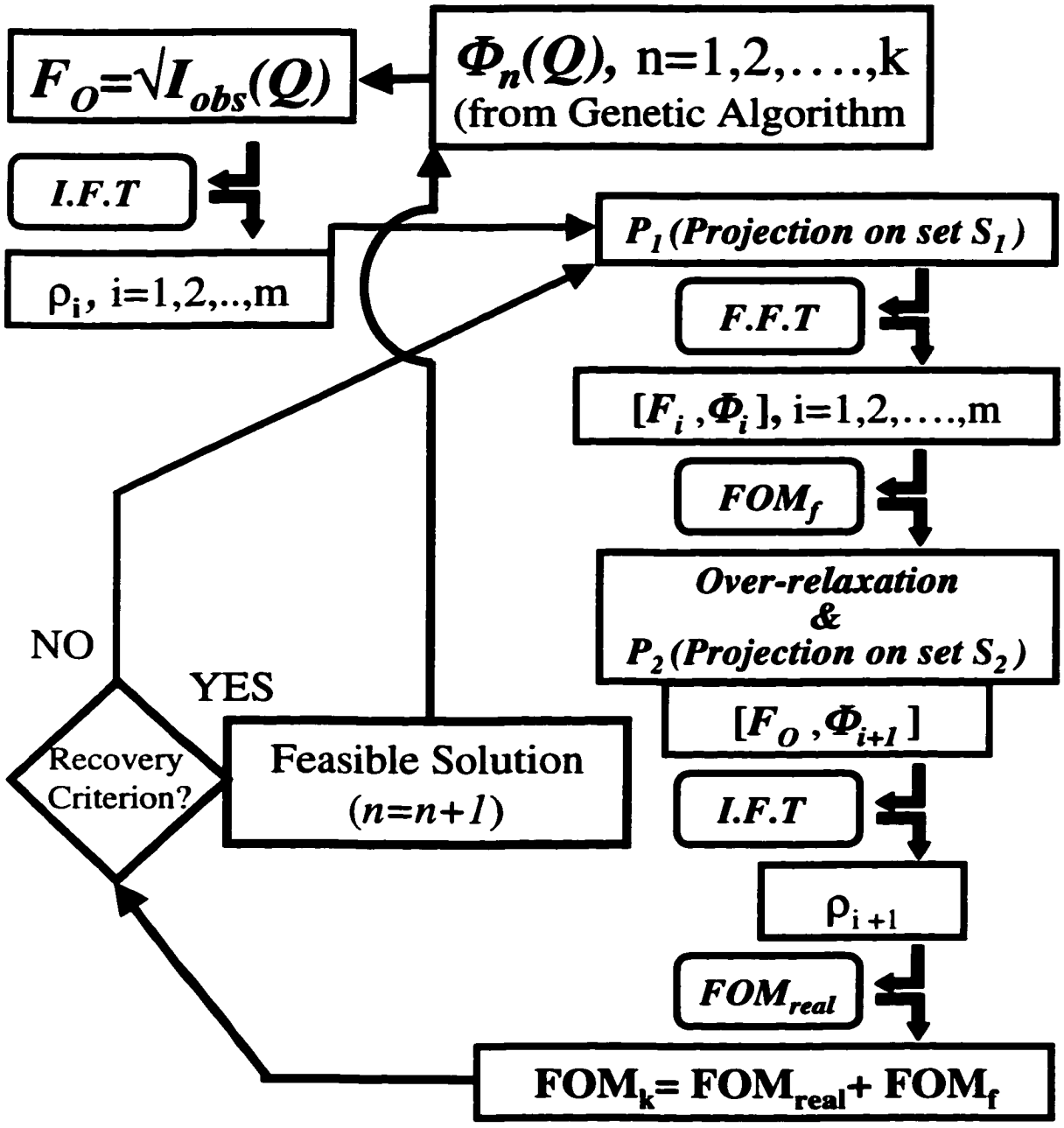

Figure 4.2.7 **The flow-chart of the algorithm used for the model-independent analysis of the x-ray reflectivity using feasible set approach.**

constraints. The second set, S_2, is the set of solutions whose moduli are equal to those measured experimentally. These sets can be expressed mathematically as:

$$S_1 = \left\{ \rho(z) \;\middle|\; \begin{array}{l} \rho(z) \in R^+ \\ D_{\max} \geq \rho(z) \geq 0 \\ \rho(z) = D_{sub}, \quad z \in Substrate \\ \rho(z) = 0, \quad z \in Vacuum \end{array} \right. , \tag{4.2.16a}$$

$$S_2 = \left\{ \rho(z) : \left| FT\{\frac{d\rho(z)}{dz}\} \right|^2 = I_o(Q) \right. , \tag{4.2.16b}$$

Here I_O is the observed ideal reflectivity data, D_{max} the maximum possible normalized density and D_{sub} the normalized substrate density. Using analyses by Sezan (1992), S_1 is a convex set while S_2 is a non-convex set. The projections involved can also be expressed as:

$$\rho_n(z) = T^{-1} P_2 T P_1 \rho_{n-1} , \tag{4.2.17}$$

where ρ_n is the current best estimate of $\rho(z)$ and ρ_{n-1} is the previous estimate of $\rho(z)$. P_1 and P_2 are relaxed projection operators. T is the operator for differentiation and Fourier transformation (FT), and T^{-1} is its inverse. Analytically P_1, P_2, and T can be expressed by

$$P_1 \rho(z) = \begin{cases} 0 : & z \in Vacuum \\ \rho(z) : & 0 \leq \rho(z) \leq D_{\max} \\ (1-\delta_1)\rho(z) : & \rho(z) < 0 \\ D_{\max} - (\delta_2 - 1)\rho(z) : & \rho(z) > D_{\max} \\ D_{sub} : & z \in Substrate \end{cases} , \tag{4.2.18a}$$

$$P_2 T \rho(z) = \sqrt{I_o(Q)} \left[\frac{T\rho(z)}{|T\rho(z)|} \right] , \tag{4.2.18b}$$

$$T\rho(z)=FT\left[\frac{d\rho(z)}{dz}\right] \quad , \qquad (4.2.18c)$$

where δ_1 and δ_2 are scalar constants between 1 and 2. P_2 corresponds to the correction of the object at the n-1th iteration, ρ_{n-1}, with the observed moduli $F_O(Q)$ ($=\sqrt{I_O(Q)}$), and P_1 is the correction for the real space constraints.

For the restoration of the phases, a genetic algorithm (GA) was used to implement a global search to find the best set of phases, Φ, (between 10 and 20 % strongest reflections were assigned phases) with regards to the constraints applied; this is attained by using a mathematical global Figure of merit (FOM) as a recovery criterion. In the algorithm, global FOM is a linear combination of FOM calculated in the reciprocal space (FOM_f), and FOM calculated in the real space (FOM_{real}). FOM_f is defined by

$$FOM_f = \sum \left|[F_n(Q),\Phi_n(Q)] - [F_{n-1}(Q),\Phi_{n-1}(Q)]\right|^2 + \sum \left|[F_n(Q),\Phi_n(Q)] - [F_O(Q),\Phi_n(Q)]\right|^2 \qquad (4.2.19)$$

where $F_n(Q)$ and $\Phi_n(Q)$ are the moduli and phase for the nth iteration, respectively, and $[F_O(Q),\Phi_n(Q)]$ is the observed moduli paired with the phases from the nth iteration. FOM_{real} is the L_2 mean between the unprojected $\rho(z)$ and $P_1\rho(z)$ except adsorbate layer. Successive projections onto the constraint sets refine the initial phases *locally*, but within the GA a *global* optimization is achieved by a method similar to "natural selection" favoring phases with better FOM values. Phases with good FOM values are chosen as "parents" for the next generation of "children." The output from the algorithm is a solution set where the solutions are listed in an ascending order with regards to their

FOMs. The first solution, the solution, has the lowest FOM and is considered to be the most plausible solution to the problem. Details on phase restoration using GAs and FOM selection can be found elsewhere in papers by Carmody et al. (1999), and Marks and Landree (1998). For further information on GA and the use of sharing algorithms that are required to implement fully global convergence avoiding local minima, the reader is recommended a text by Goldberg (1989).

4.2.2.1 Simulated Structures

In order to test the algorithm and solution method, four mock-models were prepared. Two of the models (Figures 4.2.8a and b) were designed after a monolayer of fluorocarbon amphiphilic molecules at air-water interface (Grayer Wolf et al. 1988; Jacquemain et al. 1990). First is a two-box model with one for the hydrophobic tail (ρ =1.7, l = 10 Å) and the other for the hydrophilic head (ρ =1.3, l = 10 Å). (ρ is normalized with respect to substrate, ρ_∞) . The second model, a three-box model, has three boxes roughly corresponding to the fluorocarbon tail (ρ =1.7, l =14 Å), ester group (ρ =1, l = 2 Å), and the glycyl head (ρ =2, l = 2 Å). The third system, a multilayer model, corresponds to five layers of Pt(20Å)/Si(40Å) on a SiO_2 substrate, Figure 4.2.8c. The final model, a four-step model (Figure 4.2.8d), examines the uniqueness issue which

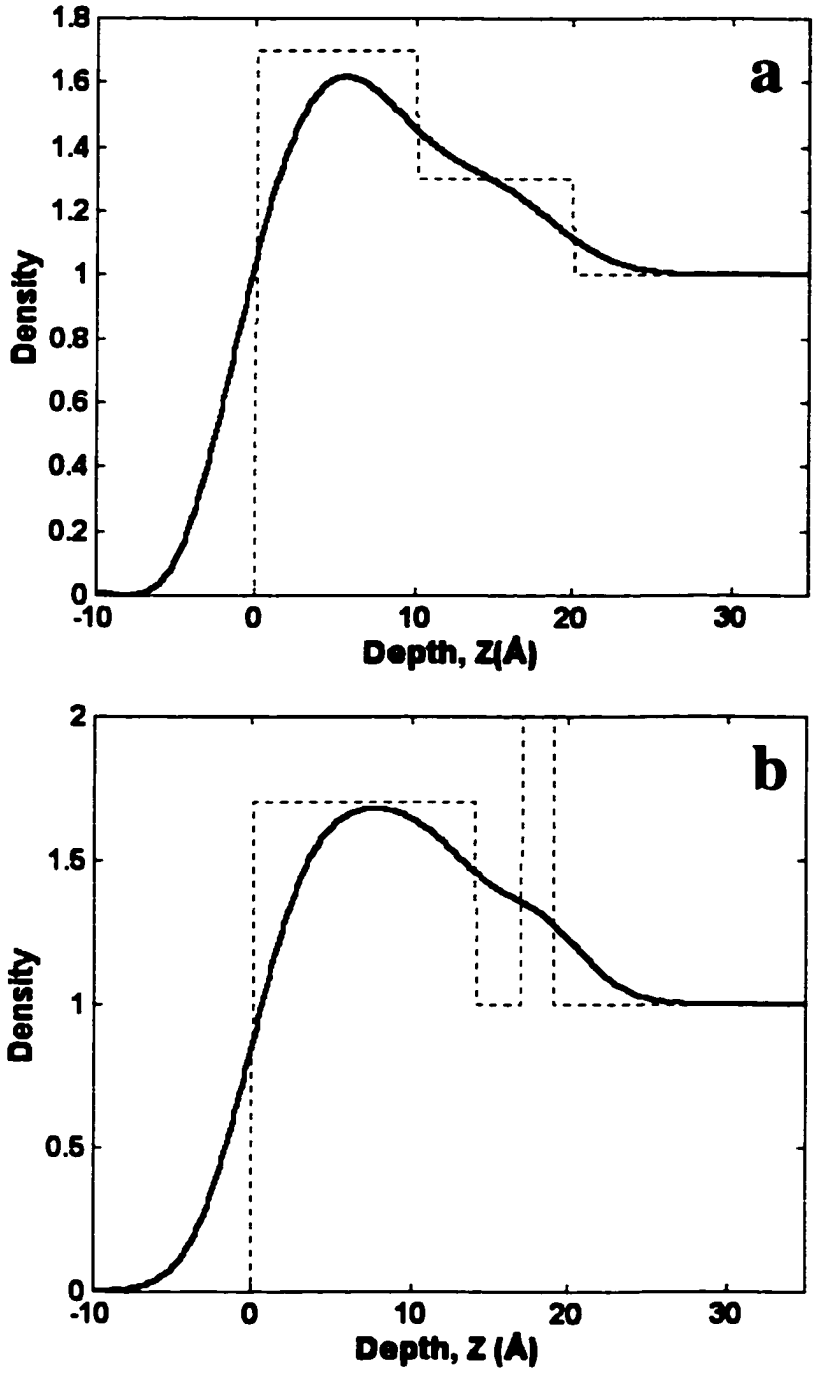

Figure 4.2.8 Simulated models used in testing the algorithm (dashed models are before the application of roughness) : a) two-box, b) three-box, c) multilayer model, and d) four-step model.

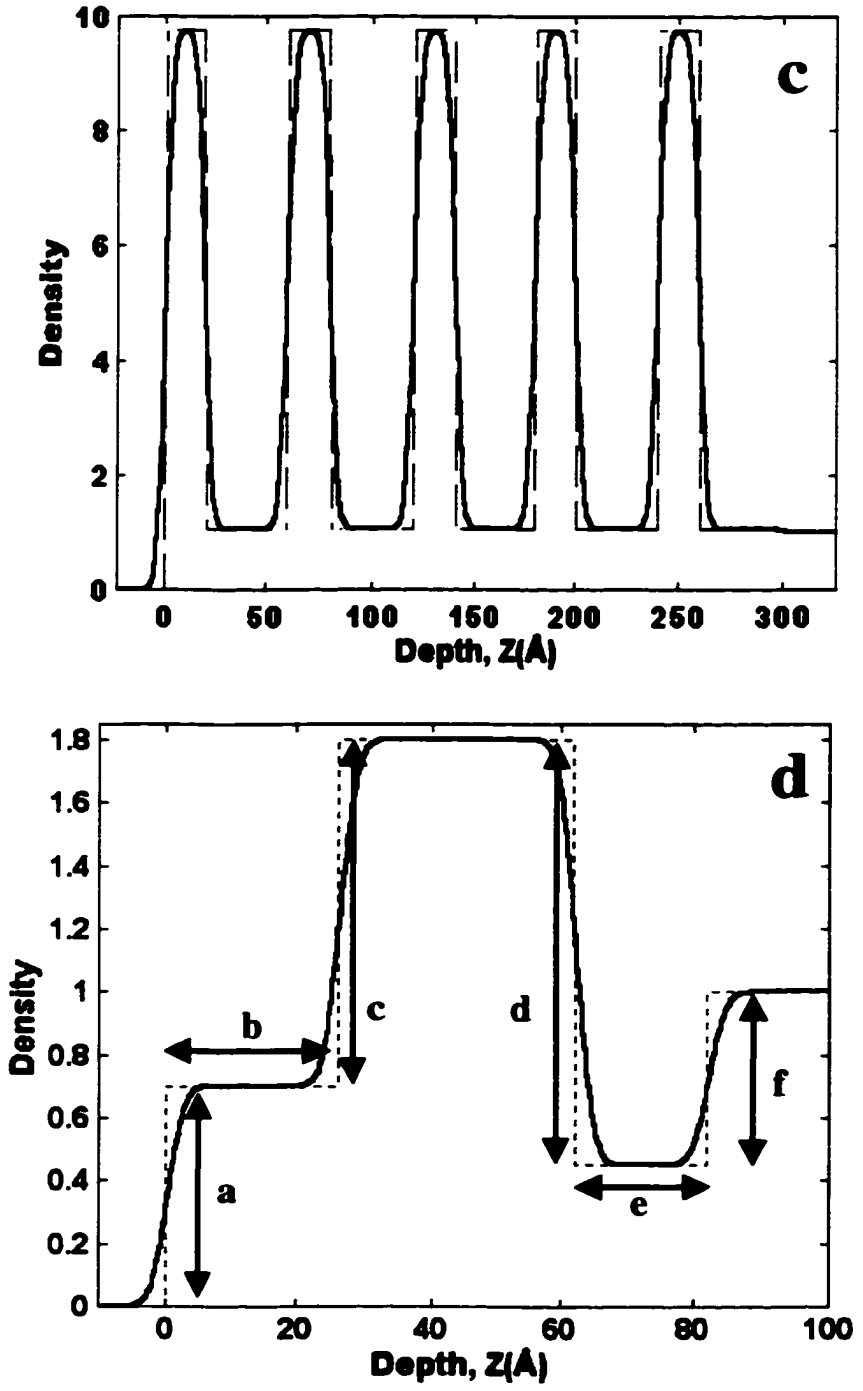

Figure 4.2.8 Simulated models used in testing the algorithm (dashed models are before the application of roughness) : c) multilayer model, and d) four-step model.

is inspired by a model used by Pedersen (1992) for the same purpose. This model, which is made up of three boxes, results in four steps and three plateaus in the final shape. Steps a-f (h_a=0.7 vs. h_f=0.58, h is step height) and c-d (h_c=1.1 vs. h_d=1.35, h is step height) are designed to have no more than 25% difference between them, as are plateaus b-e (w_b=25 Å vs. w_e=20 Å, w is step width). Thus, these similarities in the step heights and separations increase the degeneracy in the position of steps. For the correct solution, accuracy in the determination of the phases becomes imperative. A gaussian interface roughness of σ = 3.0 Å was used for all models.

The ideal reflectivity equation 4.2.15a (without absorption) is used to calculate the reflectivity curves displayed in Figure 4.2.9 for the analysis of the phase restoration algorithm. The GA algorithm performance was optimized earlier for best performance using similar models as outlined by studies conducted by Landree, Collazo-Davila and Marks (1997). The overall algorithm was set to search and reconstruct the phases for the largest 20 or 40 reflections of a total of 500 (40 for four-step). The input consisted of simulated ideal reflectivity intensities, reciprocal space constraint set S_2, and the constraints for the real space set S_1 for individual cases such as D_{sub} and D_{max}. Three- and two-box models have closely related real space objects and reflected intensities (R-factor[§] =0.1675), as shown in Figures 4.2.8 and Figure 4.2.9, respectively.

[§] R-factor is one of the standard methods used to quantify the agreement between two sets of numbers:

$$R \equiv \sum_{j=1}^{N} \left| I_j^1 - I_j^2 \right| \Big/ \sum_{j=1}^{N} I_j^1$$

where I^1 is the first set of numbers, I^2 the second and N is the length of each array.

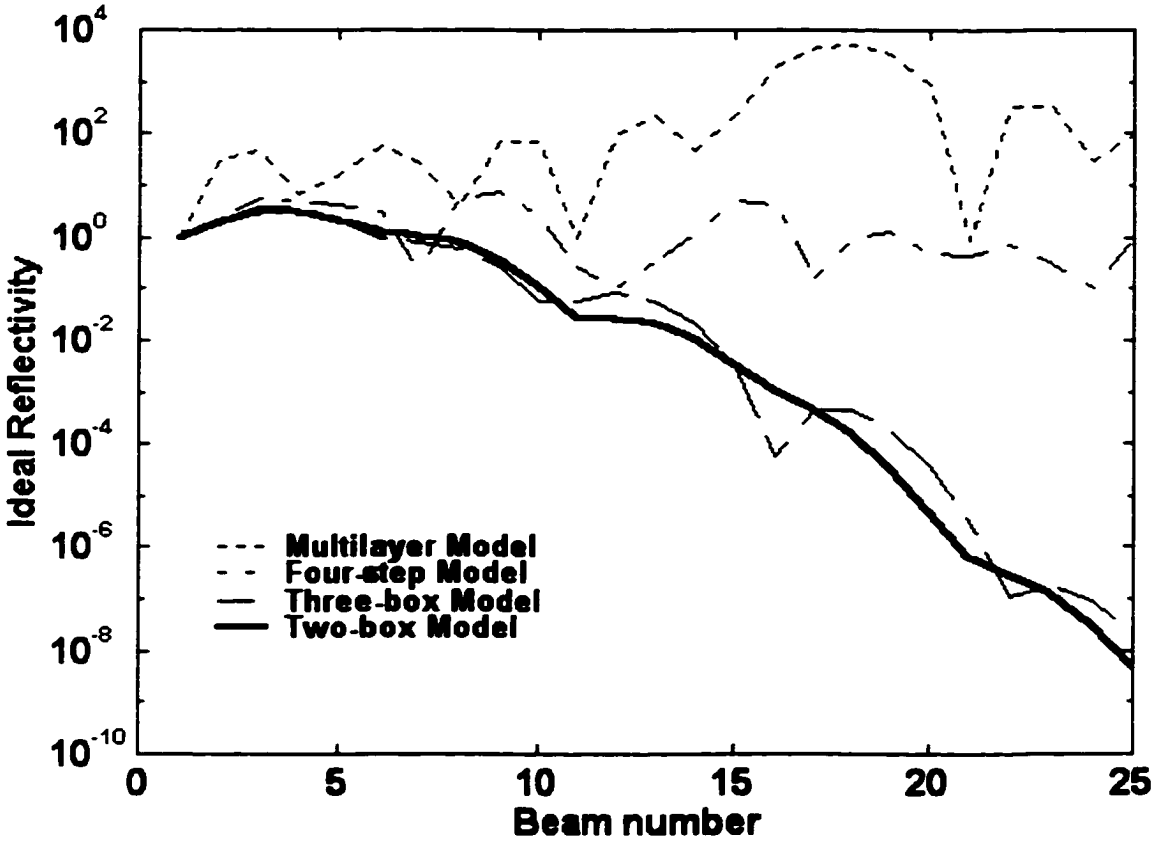

Figure 4.2.9 Calculated ideal reflectivity curves for the simulated models using the Equation 4.2.15 a in the text.

In fact, they are two plausible models proposed for the same structure, amphiphilic molecules on water (Pedersen 1992). The ambiguity in the reflectivity measurements and similar SLD has caused complications with earlier studies employing model-dependent approaches with limited data sets (Grayer Wolf 1988). In fact, there was not enough information to differentiate between the two as initial guess models without further a priori chemical information regarding the chemistry of the polymer. From a feasible set perspective, the real space constraints are the same and Fourier space constraints are very similar. However, as shown in Figure 4.2.10, the cosine plot (cos Φ_i) of the phases for the reflected waves suggests a reasonable difference between the models. A further analysis is conducted using a simple expression normalizing the difference between the phases within the interval [0,π],

$$\Delta\Phi_i = \cos^{-1}\left[\cos(\Phi_i^{original} - \Phi_i^{modified})\right] \quad for\, i = 1,2,...,n. \qquad (4.2.20)$$

where $\Delta\Phi$ is the normalized phase difference. The peaky behavior of the $\Delta\Phi$ histogram (for the first 50 reflections), shown in Figure 4.2.10 b, is in agreement with the previous finding. Therefore, the challenge posed for the phase reconstruction algorithm using these two cases has fundamental ramifications in terms of the reliability of the method used. The first is global optimization and the second is degree of sensitivity of the algorithm with respect to constraint sets.

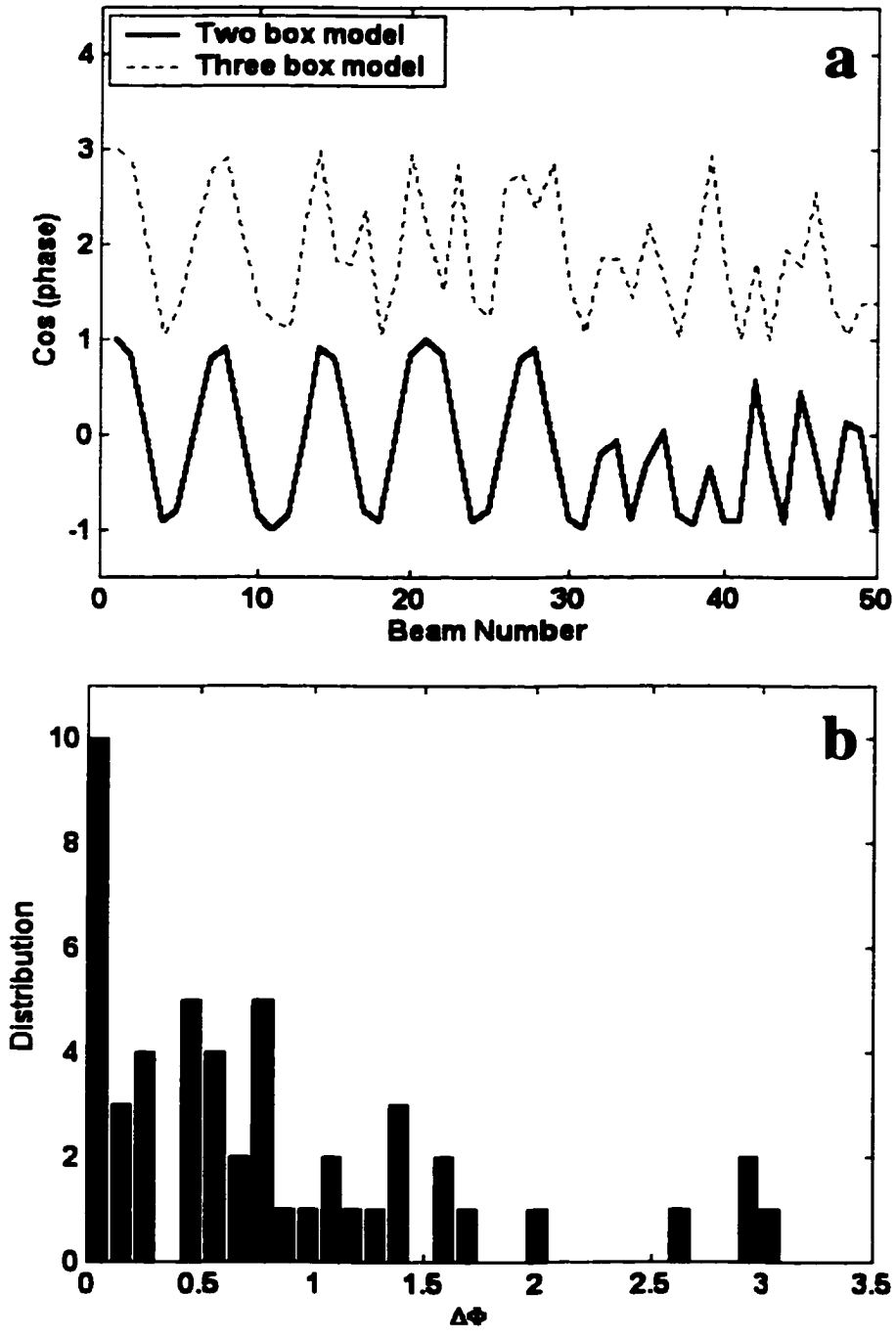

Figure 4.2.10 a) Plot of cosines of calculated phases for the two- and three-models; b) normalized phase difference plot showing a peaky distribution.

In conclusion, the algorithm was able to find considerably accurate solutions for these cases with only 16% difference between the measured intensities, only available non-degenerate constraint set. The results consisting of the top solutions for the two-box and three-box cases (given in Figure 4.2.11a and b, respectively), indicate that the algorithm was able to differentiate between these cases and match the original models very well. The fit is nearly exact if corrected for the displacements observed (indicated by Δ in the figures). A displacement in the real space corresponds to a systematic *phase shift* in reciprocal space with respect to the correct phases, which does not affect the shape of the solution, changing only the relative position of the solution with regard to a reference point. The displacement for the two-box solution is measured to be around 1 Å, while that of the three box model is approximately 2.5 Å. This insignificant effect can be overcome by implementing stricter constraints for the real space in the algorithm.

In Figures 4.2.11c and d, the first top ten solutions in the solution sets for the two-box and three-box case are given, respectively. The strong similarity between the solutions can be considered as an indication of these cases to be uniquely defined with the current constraints on the problems. Although, all of the solutions are closely related in both cases, only one solution in the set for the three-box case, #10 in Figure 4.2.11d, deviated slightly from the general appearance. However, this is expected as a global optimization is performed.

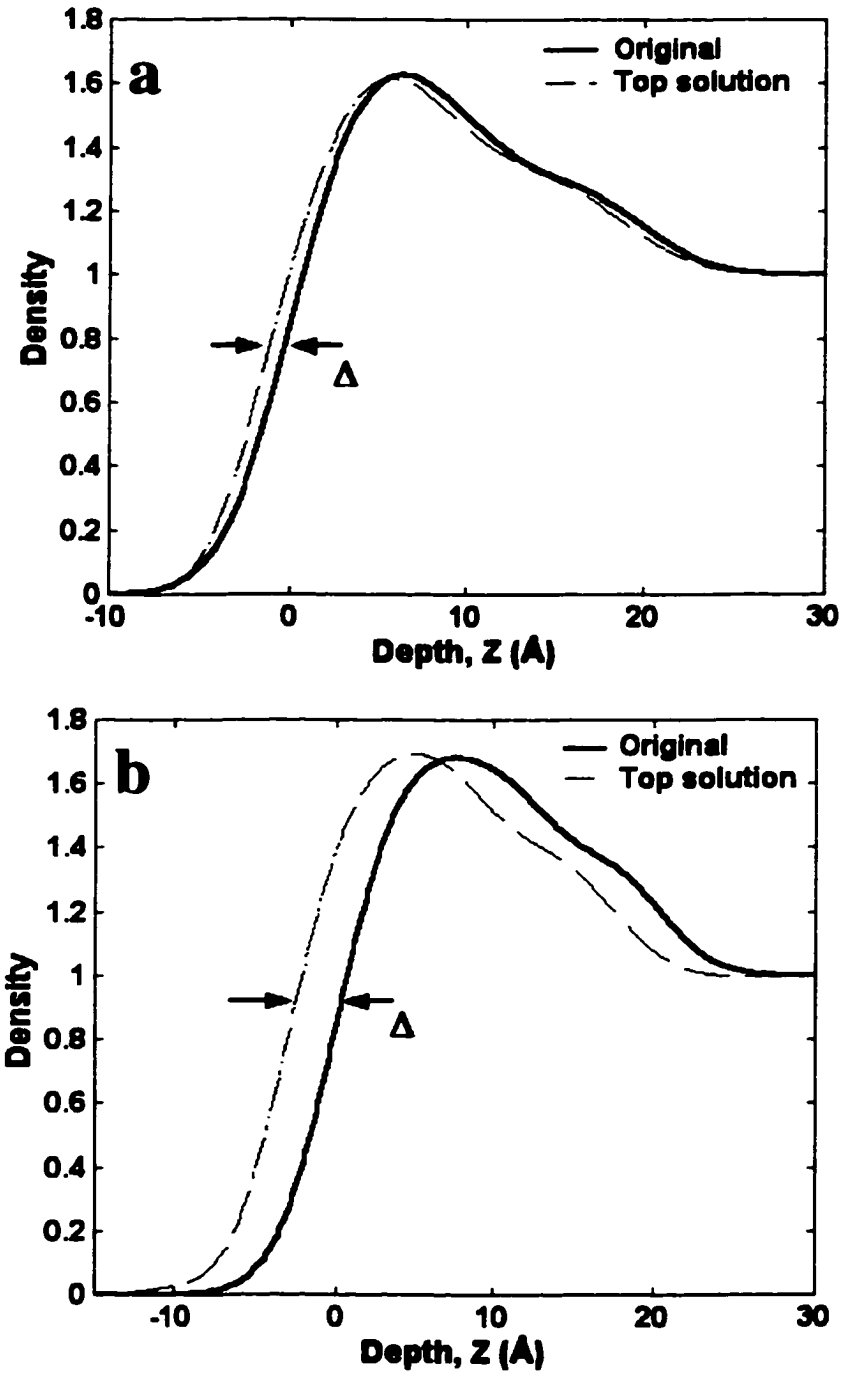

Figure 4.2.11 a) The top solution for the two-box model (dash-dotted curve); b) for the three box-model (dash-curve). Δ denotes translational shift in the solutions.

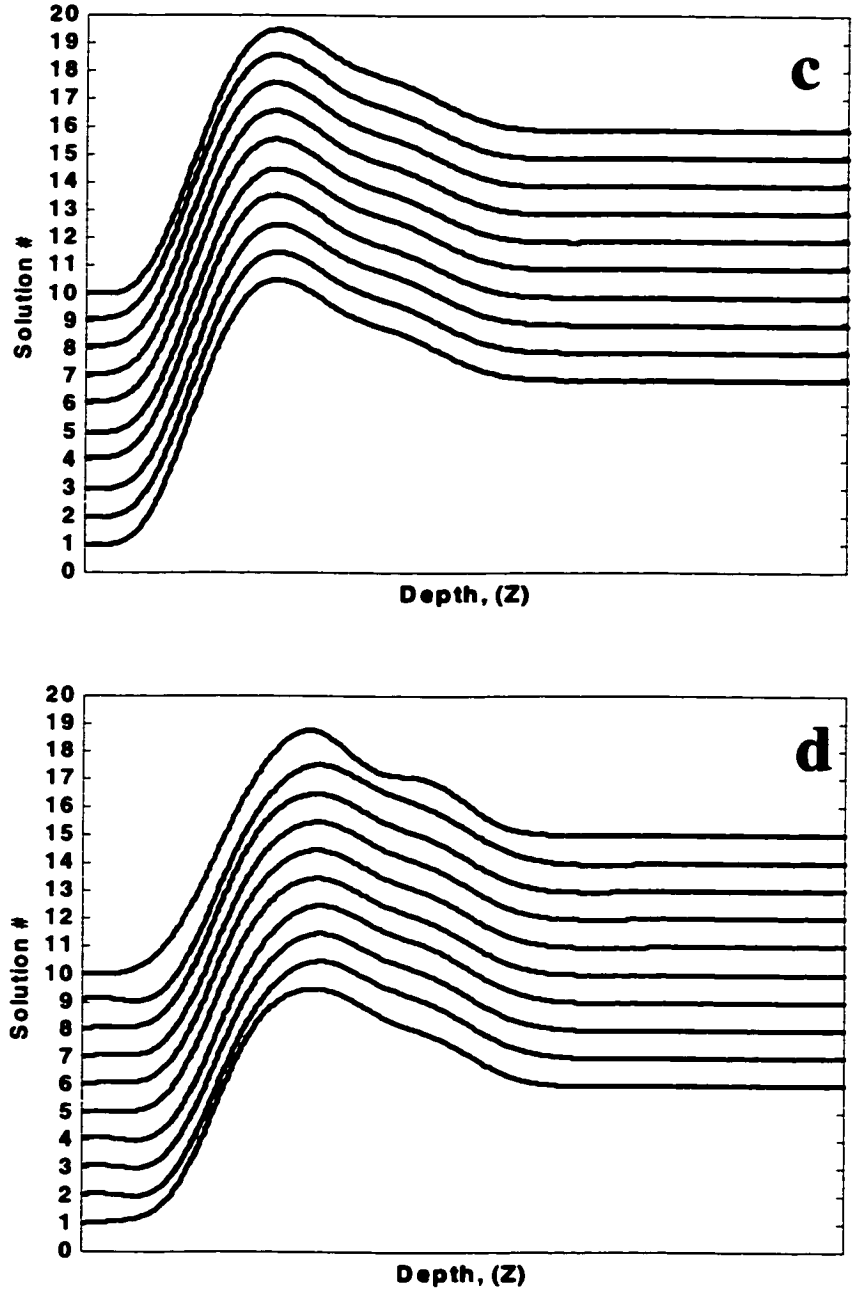

Figure 4.2.11 c) Plot of the top ten solution for the two-box model, and d) for the three box-model.

The four-step model, Figure 4.2.8d, poses a more difficult problem for the phase restoration process overall. The inset in Figure 4.2.12 illustrates calculated reflectivities from the $d\rho(z)/dz$ of the 4-step model (depicted as *original* in Figure 4.2.12) and another manufactured by replacing the first peak (from step a) with the fourth peak (from step f) in the original (*modified* in the Figure). The purpose of this exercise is to test whether the restoration algorithm and feasible set approach is stable against cases with a high degree of degeneracy (non-uniqueness that has been mentioned earlier). In fact, there is not an appreciable difference between the calculated reflected intensities of these two density profiles (inset in the Figure 4.2.12); the R-factor difference is roughly 0.1. Moreover, this similarity is also evident from the phases in Figure 4.2.13a, displaying the cosine plots of the phases with little difference. In Figure 4.2.13b, $\Delta\Phi$ histogram (over the phases of 50 largest reflections) also shows that more than 70% of the phases are shifted approximately an average of 0.1 radians. Most importantly, the same number is 80% of the phases for stronger reflections (first thirty-six reflections with intensity > 0.01). Therefore, this example is especially instructive in testing the stability of the algorithm against a small error while restoring the original phases, which can actually cause a non-unique solution with wrong positions to prevail in the solution sets. The top solution for the 4-step case from the algorithm using forty largest reflections for phase restoration, as shown in 4.2.14a is nearly an exact reconstruction of the SLD. When the top ten solutions for this case are examined in Figure 4.2.14b, deviations from the top solution can be observed, but they are slight, and the general trend in the solutions does not vary.

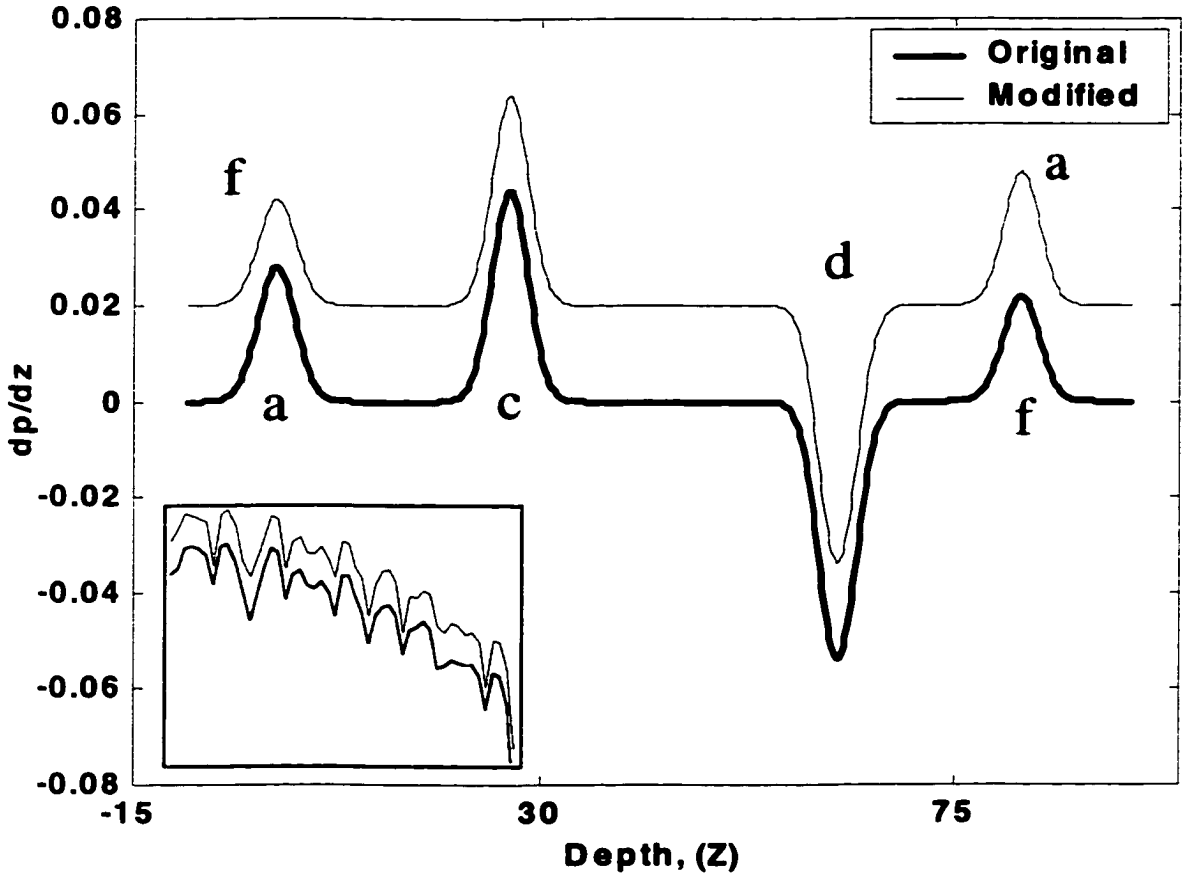

Figure 4.2.12 Plot of *dp/dz* vs. Z for the four-step model and modified four-step model. The modification is done by replacing the position of peak a and peak f. Peaks a,c,d, and f are due to the corresponding step edges of the original model in Figure 4.2.8d. The inset is the calculated reflectivities for these models.

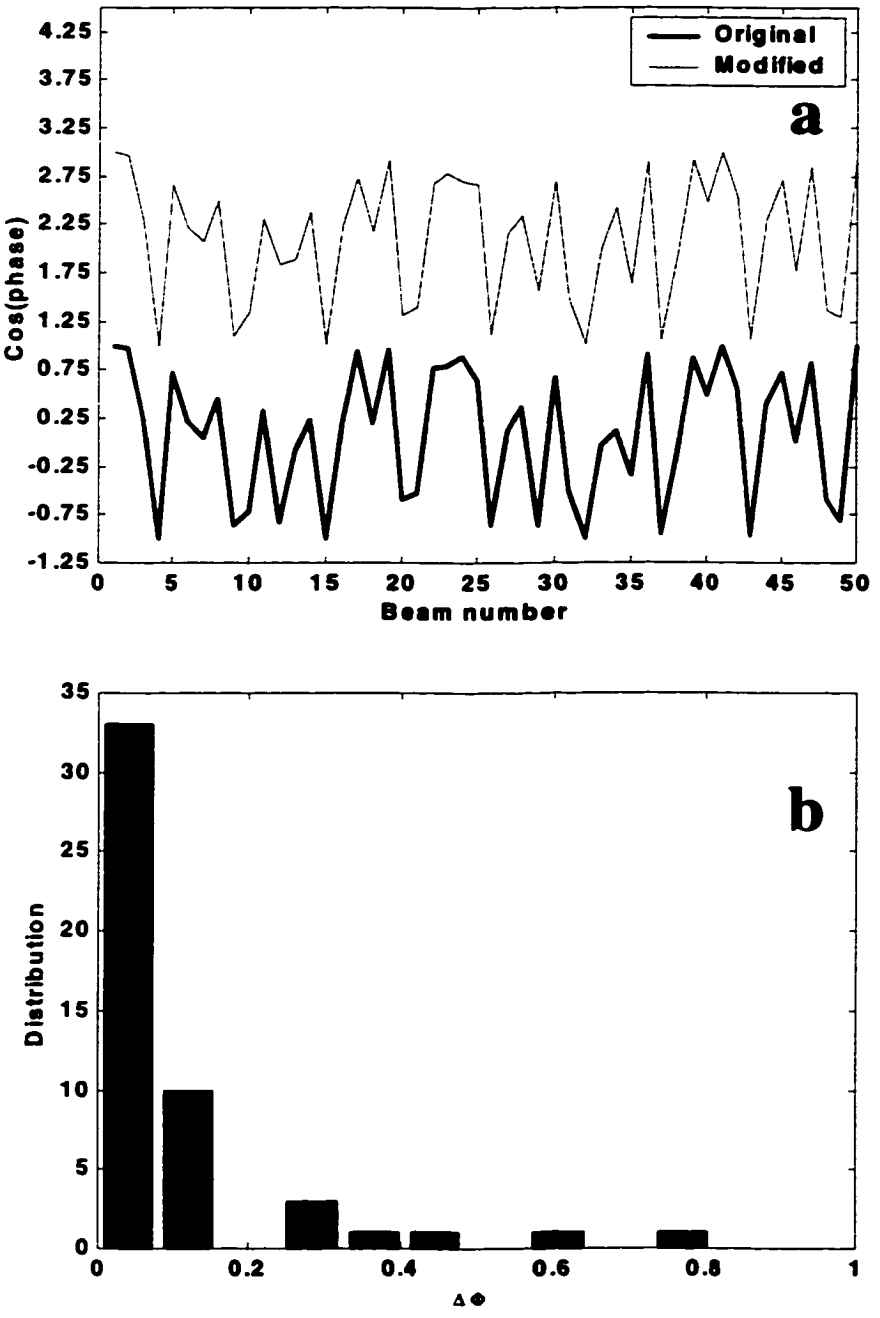

Figure 4.2.13 a) Plot of cosines of calculated phases for the original and modified versions of four-step models; b) normalized phase difference plot indicates a small shift (< 0.1 radians) for the majority of the phases.

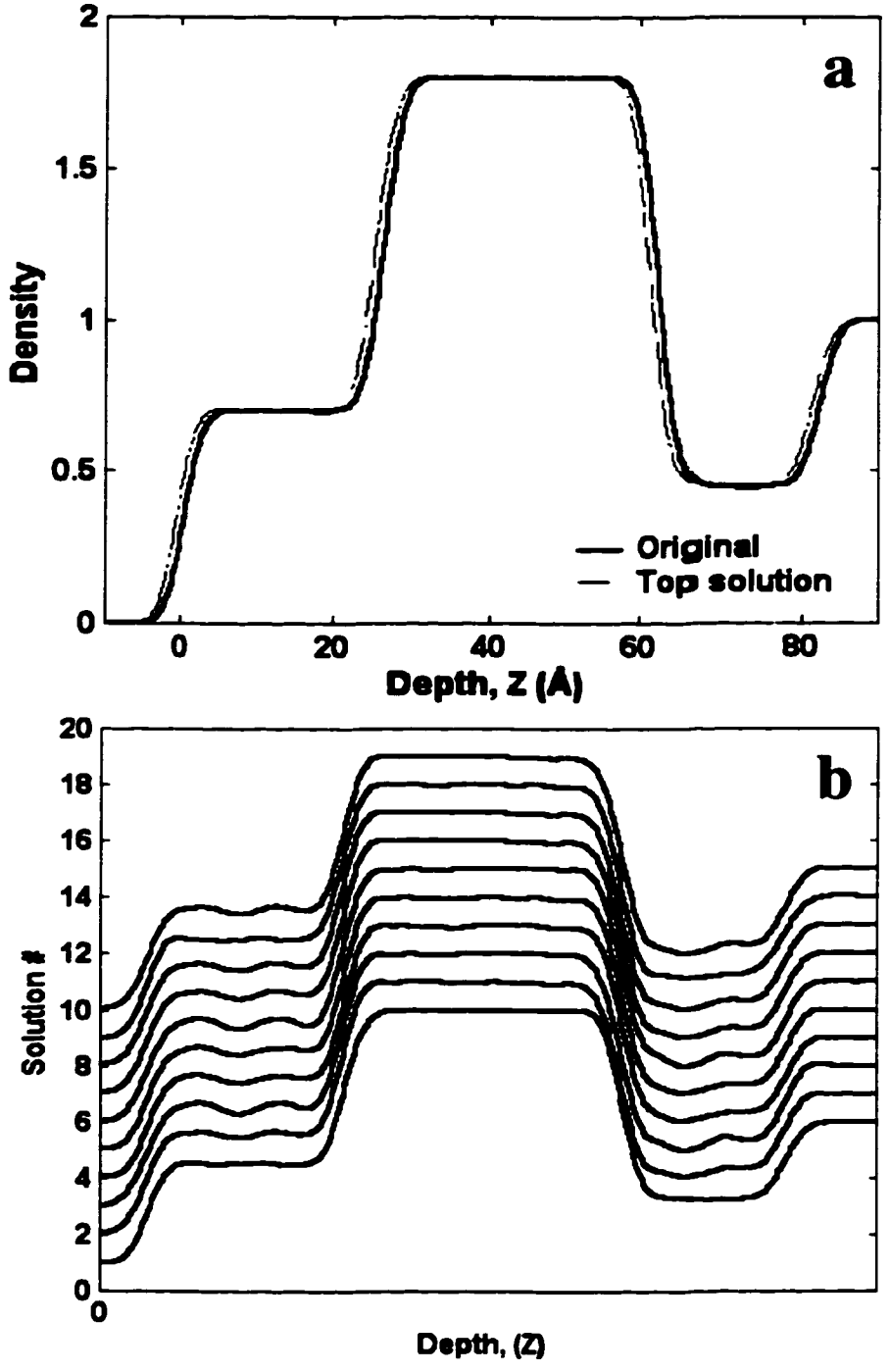

Figure 4.2.14 a) The top solution for the four-step model (dash-dotted curve); b) top ten models for the four-step.

The top solution for the multilayer model displays several deviations from the original model, especially in the low-density regions, indicated by an arrow in Figure 4.2.16a. However, the shape and the width of the high-density layers are correct. This result suggests that to the extent that reflectivity from a multilayer can be approximated using kinematical approach, the solutions from the algorithm can be used as starting points for a least-squares method. The same trend can be also observed in the top ten solutions for the multilayer case, Figure 4.2.16b. Although, the high-density regions in the solutions match to the model, low-density regions in six out of ten solutions are not very well fit. As in other models, there are no drastically different solutions in the set.

4.2.2.2 Structure of PFA On Water

Langmuir monolayers at the air-water interface display sharp discontinuities in their surface pressure-molecular area (π-A) diagrams, strongly suggesting phase transition. One of the few techniques that could be applied to the study of the structure of these films is specular x-ray reflectivity. Hence, the final phase of this study consists of applying the algorithm to the analysis of data from the x-ray reflectivity study of fluorocarbon amphiphile perfluorododecyl aspartate (PFA) monolayers on water by Jacquemain et al. (1990).

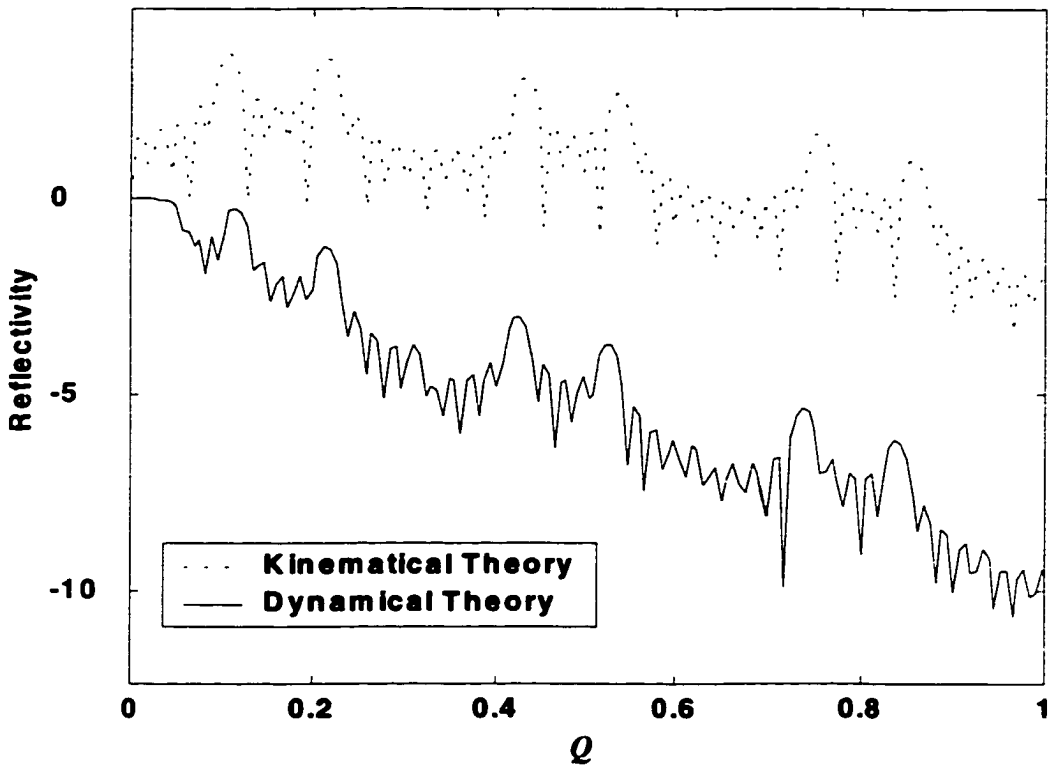

Figure 4.2.15 **Comparison of the calculated reflectivity curves from full dynamical theory and kinematical approximation for the multilayer model.**

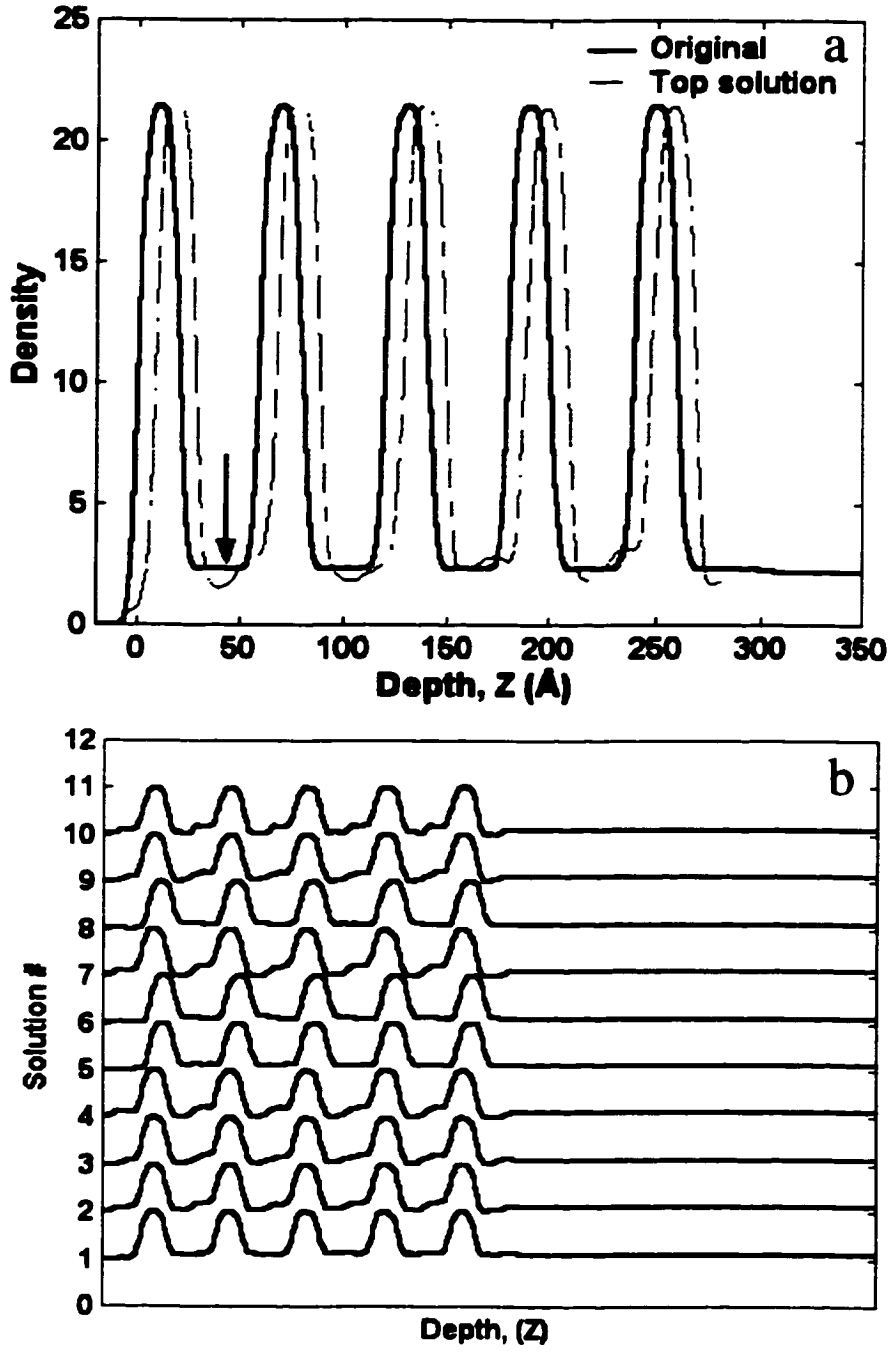

Figure 4.2.16 a) The top solution for the multilayer model (dash-dotted curve); b) top ten models for the multilayer model. The arrow in a) points to the deviations from the model in low density regions.

The X-ray measurements on PFA were conducted by using the liquid diffractometer on beam line D4 at Hasylab, DESY, Hamburg, Germany. For further information on the experimental detail refer to Jacquemain et al. (1990). The data consists of four sets, (Figure 4.2.17) acquired under the following conditions: I- pure water, surface pressure π = 13mNm^{-1}; II- pure water, high pressure π = 28mNm^{-1}; III- basic solution (KOH) with pH=11.2, π = 30mNm^{-1}; IV- basic solution (CsOH) with pH=11.1 π = 30mNm^{-1}. The original analysis of the data sets from the PFA/water system is given by Jacquemain et al. (1990) using a least-squares refinement. In addition, Pedersen (1992) has also analyzed the same data set using a method involving an auto-correlation function with non-parametric cubic splines. In general, the solutions for the SLD for the PFA/water system from both studies resembles the three-box case examined earlier, although the two-box case is also very similar.

In this analysis, again only the 20 largest beams are phased in the algorithm, although the whole set contained 31 beams as shown in Figure 4.2.17. The reflectivity values for $Q/Q_c < 1$ in the data sets are greater than unity, probably originating from instrumental resolution or other issues with data acquisition. The top solutions found by running the algorithm on this data set are provided in Figure 4.2.18.

The solution for the low-pressure water data set indicates a lower roughness than the rest of the cases which are under higher surface pressure (~ 30 mNm^{-1}) in full agreement with the previous results by Pedersen (1992) and Jacquemain et al. (1990).

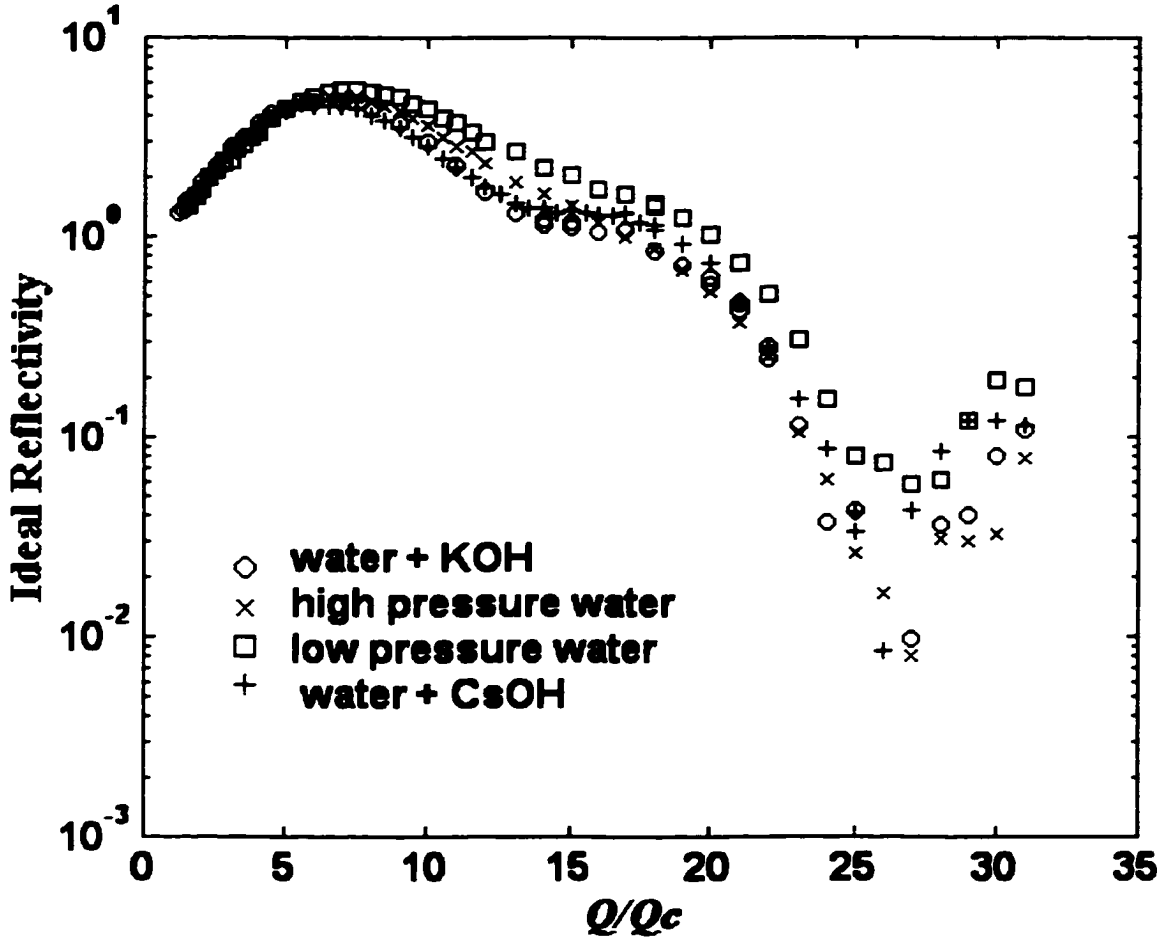

Figure 4.2.17 Experimental data from the x-ray reflectivity study of PFA monolayers on water (by Jacquemain et al., 1995): 'o', water + KOH solution, pH=11.2, π=30 mN m^{-1}; '×' pure water, π=28 mN m^{-1}; 'Y' pure water, π=13 mN m^{-1}; '+' water + CsOH solution, pH=11.1, π=30 mN m^{-1}.

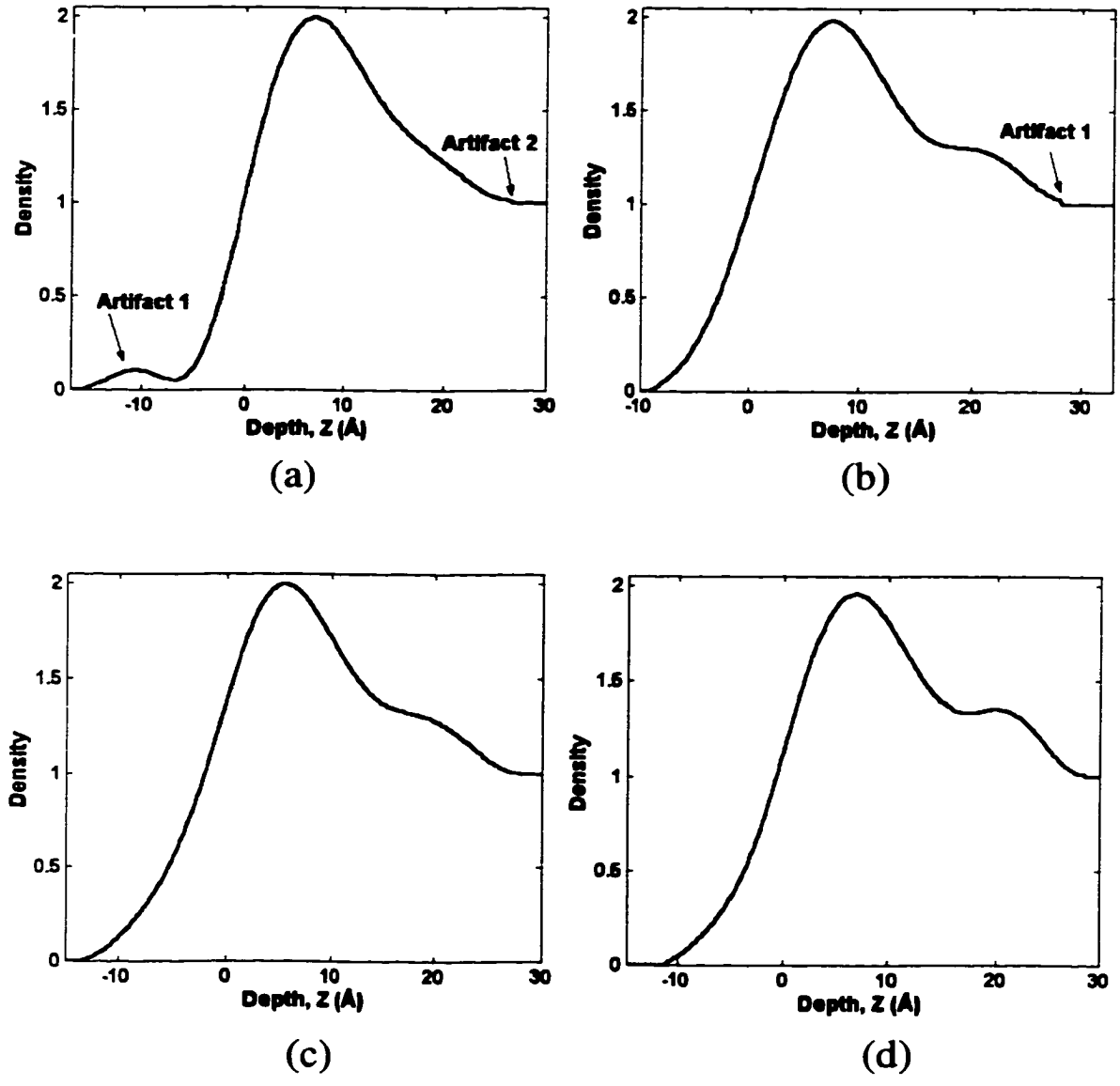

Figure 4.2.18 Top solutions for the a) pure water, π=13 mN m^{-1}; b) pure water, π=28 mN m^{-1}; c) water + KOH solution, pH=11.2, π=30 mN m^{-1}; d) water + CsOH solution, pH=11.1, π=30 mN m^{-1}.

However, there are two problem areas in the solution as shown in Figure 4.2.19a: (1) the hump in the surface region (artifact 2), and (2) the kink at the PFA-water interface (artifact 1). The cause for these can be a combination of the following among other possibilities: limited Q-range in the data (resolution) and/or placement of the constraints regarding regions where SLD is zero. In Figure 4.2.19b, there are solutions without artifact 2; however, the top five solutions display it. Solution #9 does not have a hump preceding the density profile, but it is still marginally different from solution #1 regarding the rest of the profile. The only solution which shows a marked difference than the common trend is solution #10.

The top solution for the high-pressure case also indicates the presence of a similar kink (artifact 1) in Figure 4.2.20a, but some solutions do not (e.g. #7). The top four high-pressure solutions display an extra density around the head region, where as low-pressure solutions did not have such a pronounced effect. This is also different from the findings of Pedersen (1992) and Jacquemain et al. (1990). There are some other solutions in the set that are different than top four solutions, such as #6 and #7 which are more similar to low-pressure solutions. The last three solutions in Figure 4.2.20b are markedly different from the top solutions. On the other hand, the top ten solutions for the KOH + water case are remarkably similar to each other, as shown in Figure 4.2.21a and b. Furthermore, the solutions match very well with the previously proposed models (Pedersen 1992) with the extra density for the head groups approximately located at 19 Å form the vacuum in Figure 4.2.21a (19.5 Å for Pedersen 1992).

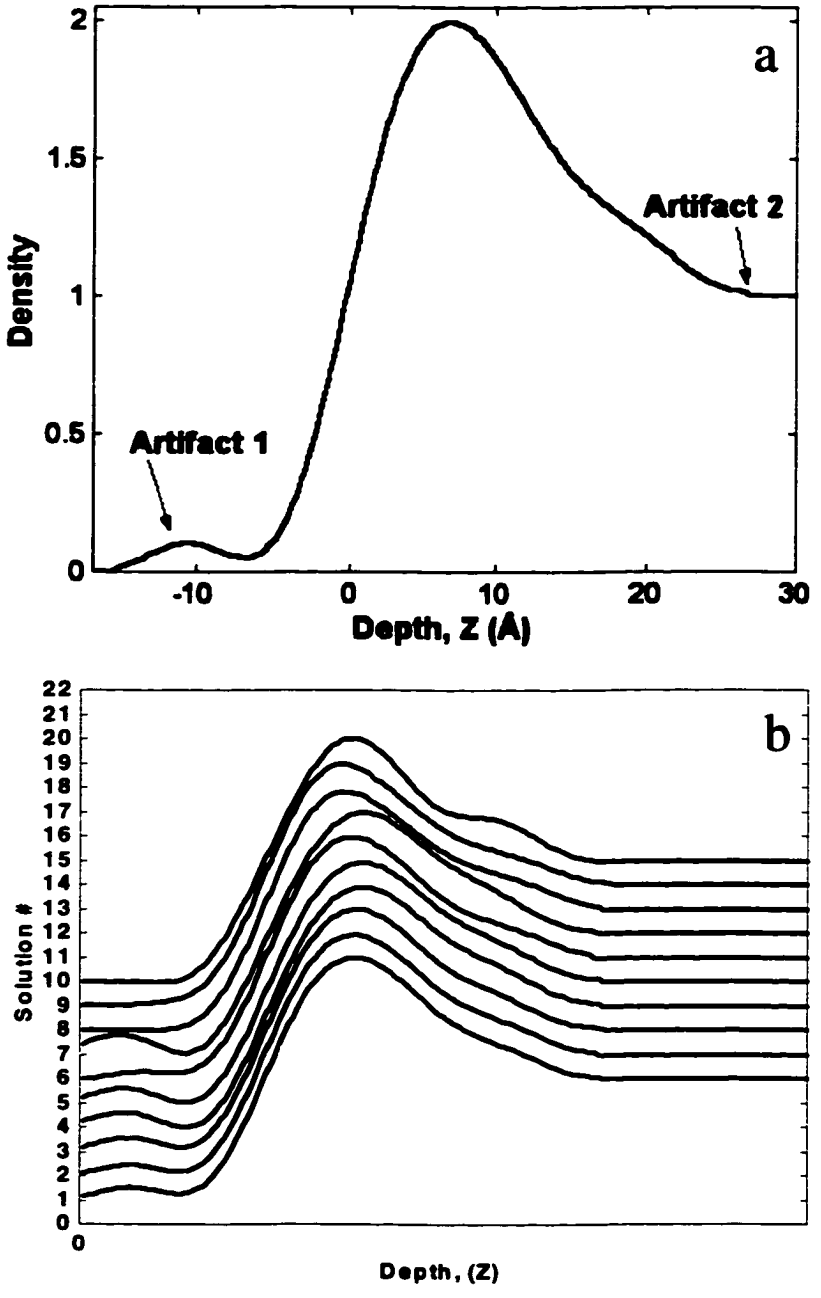

Figure 4.2.19 a) The top solution for the data obtained from pure water, π=13 mN m^{-1} (low pressure); b) top ten models for the solution set. Artifact 1 and 2 in a) are discussed in the text.

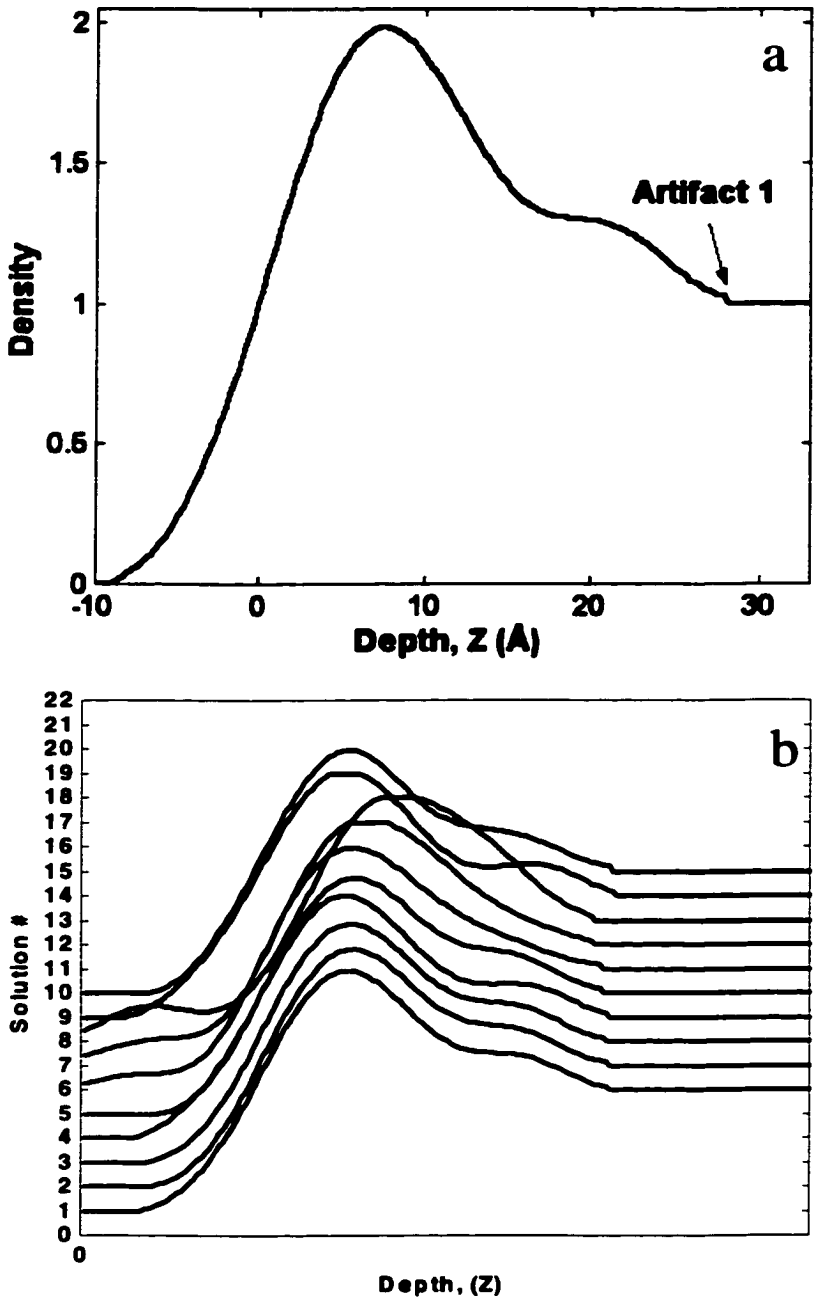

Figure 4.2.20 a) The top solution for the data obtained from water substrate at high pressure, π=28 mN m^{-1}; b) top ten models for the solution set.

The top ten solutions for the data obtained from CsOH + water substrate are also in fair agreement with each other, as shown in Figure 4.2.22a and b. Only two solutions display a slightly different character; the extra density of the head group for #7 and #9 are less pronounced closer to what is observed for the KOH + water case. Thus, models proposed by Pedersen and Jacquemain are similar to #7 and #9 with less extra density for CsOH than for KOH case. In fact, Jacquemain et al. (1990) predicted a higher occupancy (3:1) for the K^+ ions than the Cs^+ ions as occupancy depended on the number of electrons in these ions. Thus, in both reports, the differences in head group profile for CsOH + water was not as strong as for the top solutions in the current study.

4.2.3 Summary and Conclusions

In summary, a new model-independent method for the analysis of x-ray reflectivity data has been developed which has been the main motivation for this study. This new method is based on the reconstruction of the missing phase information through methods known in the image recovery field. This technique involves application of the feasible sets approach to the retrieval of the missing phases using constraint sets on the real space object (SLD) and the reciprocal space data (ideal reflectivity). The method and the algorithm have been tested using four different simulated cases, which resulted in nearly perfect reconstructions of the models in question. The algorithm proved to be stable when tested against models with a high degree of degeneracy.

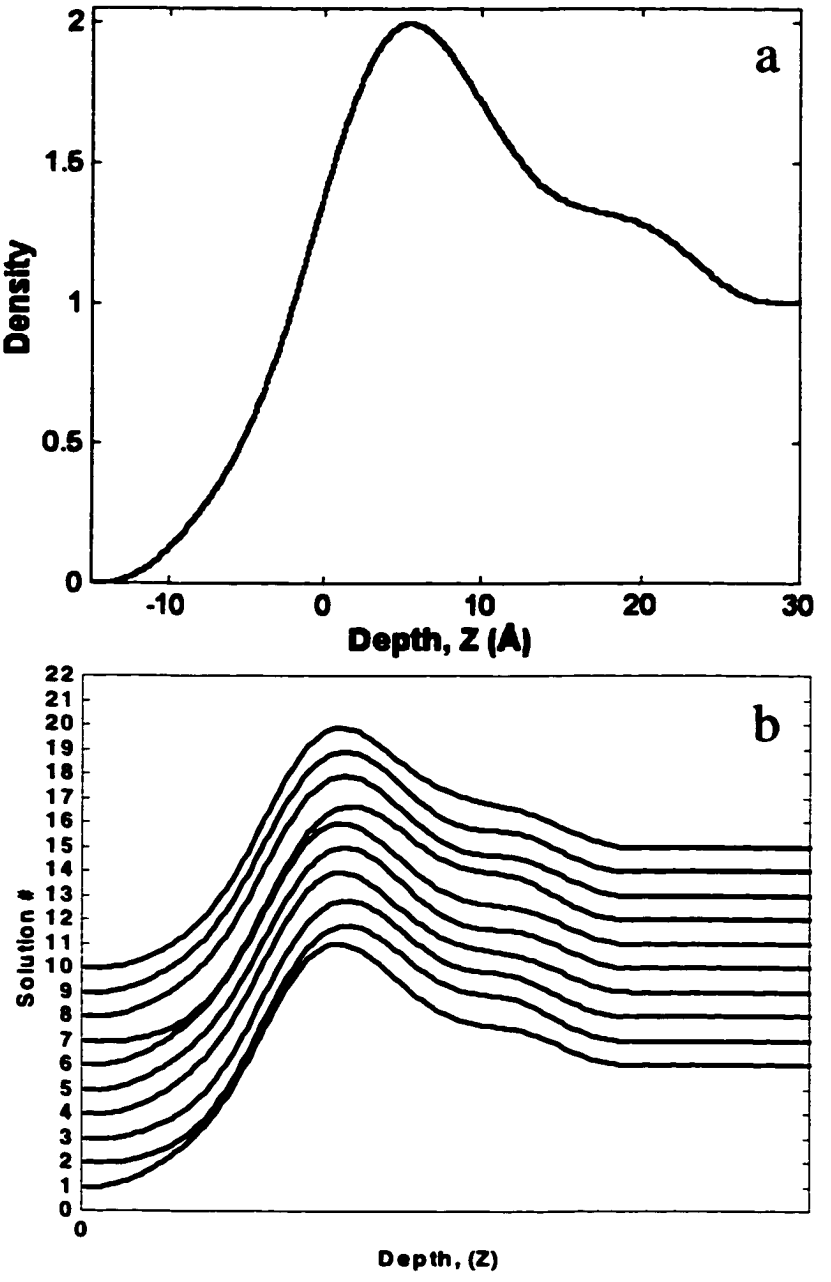

Figure 4.2.21 a) The top solution for the data obtained from water + KOH substrate, pH=11.1, π=30 mN m^{-1}; b) top ten models for the solution set.

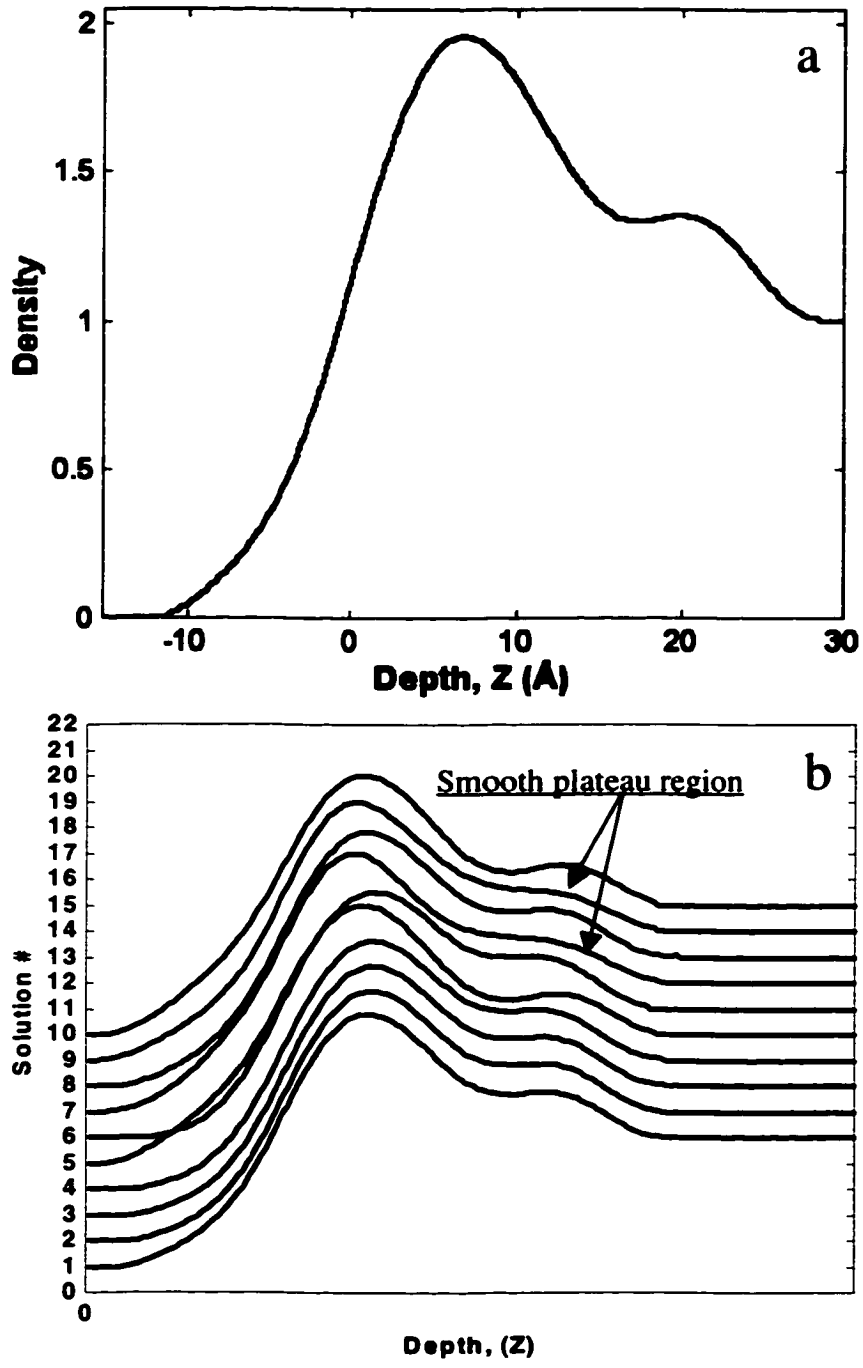

Figure 4.2.22 a) The top solution for the data obtained from water + CsOH solution, pH=11.1, π=30 mN m^{-1}; b) top ten models for the solution set.

In the light of results from the test cases, one can speculate that the X-ray reflectivity problem is a reasonably well-defined case with constraints on the problem for the feasible set algorithm to find a unique solution. The applicability of the technique to the real experimental data has been demonstrated using measurements from reflectivity studies of PFA on water. The solutions from the method are comparable to those obtained from least-squares fits of the molecular model by Jacquemain et al. (1990), although some differences are present in the high-pressure water and CsOH + water cases. The top solutions for these cases consistently indicated extra density for the head groups. This is somewhat expected for the latter one, as Cs^+ ions contribute a lot to the electron density at the interface, but it cannot explain the high-pressure case. Furthermore, the top ten solutions of these two cases indicate a variety of solutions than for the other two where nearly all off the solutions had remarkable similarity. Although this behavior cannot be addressed fully at the moment, it might pertain to measurement errors, which are omitted in this current version of the algorithm.

In conclusion, although this new method is not offered as a complete replacement of the model-dependent methods, it proved to be a useful tool for the fast analysis of x-ray reflectivity with minimal a priori information. One of the advantages of this method is that it requires very little a priori information about the system, which is generally readily available (e.g. density of the substrate). The solution method used in this study also enables the smoothness of the solutions, even if the data set has a limited range. Finally, it is strongly believed that this new method can be used routinely as a pre-refinement tool for providing the initial models for the refinement process. The multi-

solution nature of the genetic algorithms used in thus study suits very well with this purpose.

CHAPTER 5: FUTURE WORK

5.1 Phase problem

First, the current version of the algorithm performed well on the four sets of experimental data that was available. In order to evaluate the performance of the algorithm better, make improvements, more data sets should be analyzed. In addition, level of hardness for the simulated data sets could be increased by artificially inducing large random noise and by even limiting the resolution of the data set.

The current format of the X-ray reflectivity algorithm employs a kinematical treatment of the process. This is an approximation to the actual process, at its best, and is only valid when multiple scattering events and absorption are negligible. Thus, it limits the application of the technique to films with light atoms, i.e. LB films. The application fields of the algorithm can be extended with the dynamical treatment of the reflectivity process. This can be achieved by using the recursion formula (Parrat 1954), or the matrix method (Born and Wolf 1975). If this is done, then it will be possible to treat multilayer coatings with large variations in the density. This may also present a better chance for improving on the algorithm.

In addition, one of the techniques widely used for reflectivity studies of organic films is neutron reflectivity. However, positivity constraint does not apply for the case of neutron reflectivity. This would be a substantially harder problem for the algorithm and the methodology, but it will be useful in showing the limits of applicability.

5.2 Nanotubes

The amount of data available on the mechanical and electronic properties of single-wall BN nanotubes is insufficient. One of the reasons for this is the lack of experimental data regarding the atomic structure of these tubes. The information provided by this study can be used to quantitatively determine the mechanical and electronic properties of the BN nanotubes.

Highly strained bonds at the nanotube caps in 4-membered BN rings may be preferential sites for c-BN nucleation. Furthermore, previously proposed interface structures for diamond/graphite and c-BN/h-BN systems do not account for such a possibility (De Vita et al. 1996, Lambrecht et al. 1993, and Widany et al. 1996). These models only consider the 2:3 lattice matching between the (0002) planes of the graphitic phases and the (111) planes of the cubic phases. Especially, for the h-BN/c-BN system, there are several different interface configurations (Kester and Messier 1994).

5.3 C-BN/h-BN interface

The reports from Mehandru et al. (1992) regarding the hydrogenation induced curling of the graphitic sheets is very similar to what is observed for BN nanoarches (Collazo et al. 1999). It is possible to these use quantum mechanical calculations to test the viability of a similar response for hydrogenation in h-BN sheets. Repeating the same tests for other possible contaminants such as CO and CO_2 can reveal the chemistry behind the nanotube formation.

REFERENCES

Aizawa, N., Y. Homma. 1995. Annealing behavior of (7×7) domain boundaries on Si(111) observed by secondary electron imaging. *Surf. Sci.* 340:101-108.

Ajayan, P. M., S. Iijima. 1993. Capillarity-induced filling of carbon nanotubes. *Nature* 361: 333.

Aktosun, T., and P. E. Sacks. 1998. Inverse problem on the line without phase information. *Inverse Problems* 14:211-224.

Albe, K. 1997. Theoretical study of boron nitride modifications at hydrostatic pressures. *Phys. Rev. B* 55:6203-6210.

Alexandre, S. S., M. S. C. Mazzoni, H. Chacham. 1999. Stability, geometry, and electronic structure of the boron nitride $B_{36}N_{36}$ fullerene. *Appl. Phys. Lett.* 75:61-63.

Als-Neilsen, J., and H. Mohwald. 1991. *Sychrotron Irradiation*. Edited by S. Ebashi, M. Koch E. Rubenstein. New York: North-Holland p. 1-54.

Andujar, J. L., E. Bertran, and Y. Maniette. 1996. Microstructure of highly oriented, hexagonal, boron nitride thin films grown on crystalline silicon by radio frequency plasma-assisted chemical vapor deposition. *J. Appl. Phys.* 80:6553.

Badziag, P., and W. S. Verwoerd. 1989. Cluster calculations of the Si(111) 7×7 dimer-adatom-stacking-fault structure. *Phys. Rev. B* 40:1023-1029.

Banhart, F., M. Zwanger, and H. J. Muhr. 1994. The formation of curled concentric-shell clusters in boron-nitride under electron-irradiation. *Chem. Phys. Lett.* 231:98-104.

Banhart, F. and P. M. Ajayan. 1996. Carbon onions as nanoscopic pressure cells for diamond formation. *Nature* 382:433-435.

Banhart, F. 1997. The transformation of graphitic onions to diamond under electron irradiation. *J. Appl. Phys.* 8:3340-3344.

Barna, A., P. B. Barna, G. Radnoczi, G. Safran. 1985. In situ UHV-TEM study of the two dimensional growth of Al_2Au phase on Al(111) surface. *Ultramicroscopy* 15:101.

Bates, R. H. T. and M. J. McDonnell. 1986. *Image Restoration and Reconstruction.* Oxford:Clarendon.

Bauer, E. 1985. The resolution of the low-energy electron reflection microscope. *Ultramicroscopy* 17:51-56.

Bauer, E. 1991. The Si(111)-(5×1) Au structure. *Surf. Sci. Lett.* 250:L379-382.

Baughman, R. H., C. X. Cui, A. A. Zakhidov, Z. Iqbal, J. N. Barisci, G. M. Spinks, G. G. Wallace, A. Mazzoldi, D. De Rossi, A. G. Rinzler, O. Jaschinski, S. Roth, M. Kertesz. 1991. Carbon nanotube actuators. *Science* 284:1340.

Becker, R. S., J. A. Golovchenko, D. R. Hamman and B. S. Swartzentruber. 1985a. Real-space observation of surface states on Si(111) 7×7 with the tunneling microscope. *Phys. Rev. Lett.* 55:2032-2034.

Becker, R. S., J. A. Golovchenko, E. G. McRae, and B. S. Swartzentruber. 1985b. Tunelling images of atomic steps on the Si (111) 7×7 surface. *Phys. Rev. Lett.* 55: 2028-2030.

Becker, R. S., J. A. Golovchenko, G. S. Higashi, and B. S. Swartzentruber. 1986. New reconstruction on Silicon (111) surfaces. *Phys. Rev. Lett.* 57: 1020-1023.

Bengu, E., R. Plass, L. D. Marks, T. Ichihashi, P. M. Ajayan, and S. Iijima. 1996. Imaging the dimers in Si(111)-(7x7). *Phys. Rev. Lett.* 77:4226-4228.

Bengu, E., C. Collazo-Davila, D. Grozea, E. Landree, I. Widlow, M. Guruz, and L. D. Marks. 1998. In situ growth and characterization of ultrahard thin films. *Micros. Res. Tech.* 42:295-301.

Berber S. 1999. Private Communication.

Berk, N. F., and C. F. Majkrzak. 1995. Using parametric B splines to fit specular reflectivities. *Phys. Rev.* B 51:11296-11309.

Berns, D. H., M. A. Cappelli. 1996. Cubic boron nitride synthesis in low-density supersonic plasma flows. *Appl. Phys. Lett.* 19:2711-2713.

Binnig, G., H. Rohrer, C. H. Gerber and E. Weiber. 1983. 7×7 reconstructions on Si(111) resolved in real space. *Phys. Rev. Lett.* 50:120-123.

Blasé, X., A. Rubio, S. G. Louie, M. L. Cohen. 1994. Stability and band gap constancy of boron nitride nanotubes. *Europhys. Lett.* 28:335-340.

Blasé, X., A. Rubio, S. G. Louie, M. L. Cohen. 1995. Quasiparticle band structure of bulk hexagonal boron nitride and related systems. *Phys. Rev. Lett.* 51:6868-6874.

Blasé, X., A. De Vita, J. C. Charlier, R. Car. 1998. Frustration effects and microscopic growth mechanisms for BN nanotubes. *Phys. Rev. Lett.* 80:1666-1669.

Bohr, S., R. Haubner, B. Lux. 1995. Comparative aspects of C-BN and diamond CVD. *Diam. and Rel. Mat.* 4:714.

Bonevich, J. E. and L. D. Marks. 1992. Ultahigh vacuum electron microscopy of crystalline surfaces. *Microscopy: the Key Research Tool* 22:95-102.

Born, M., and E. Wolf. 1975. *Principles of Optics.* 5th Edition. Oxford: Pergamon Press.

Bouchier, D., A. Bossebouef. 1992. Nuclear reaction analyses of boron nitride films deposited by ion based techniques. *Nucl. Inst. Meth. In Phys. Res. B*64:765-769.

Bouchier, D., W. Moller. 1992. Boron nitride films synthesis by ion-beam-assisted deposition. *Surf. and Coat. Technol.* 51:190-196.

Bouchier, D., G. Sene, M. A. Djouadi, P. Moller. 1994. Effect of noble gas ions on the synthesis of c-BN by ion beam assisted deposition. *Nucl. Inst. Meth. In Phys. Res. B*89:369-372.

Boustani, I., A. Quandt, E. Hernandez, A. Rubio. 1999. New boron based nanostructured materials. *J. Chem. Phys.* 110:3176-3185.

Boulanger, L., B. Andriot, M. Cauchetier, and F. Willaime. 1995. Concentric shelled and plate-like graphitic boron-nitride nanoparticles produced by CO_2-laser pyrolysis. *Chem. Phys. Lett.* 234:227-232.

Braslau, A., P. S. Pershan, A. H. Weiss, J. Als-Neilsen. 1985. Surface-roughness of water measured by x-ray reflectivity. *Phys. Rev. Lett.* 54:114-117.

Braslau, A., P. S. Pershan, G. Sislow, B. Ocko, J. Als-Neilsen. 1988. Capillary waves on the surface of simple liquids measured by x-ray reflectivity. *Phys. Rev. A* 38:2457.

Bricogne, G. 1984. Maximum-entropy and the foundations of direct methods. *Acta Crystall. A* 40:410-445.

Bricogne, G., C. J. Gilmore. 1990. A multisolution method of phase determination by combined maximization of entropy and likelihood. I. theory, algorithms, and strategy. *Acta Crystall. A* 46:284-297.

Brown, D. 1998. Ion beam deposition takes the next step. *Data Storage* 5.

Buck, T. M., 1975. *Methods of Surface Analysis*. Edited by: A.W. Czanderna. New York: Elsevier. p75-102.

Bundy, F. P., H. T. Hall, and R. H. Wentorf. 1955. Direct transformation of hexagonal boron nitride to denser forms. *J. Chem. Phys.* 38:1144-1149.

Bundy, F. P., and R. H. Wentorf. 1963. Direct transformation of hexagonal boron nitride to denser forms. *J. Chem. Phys.* 38:1144-1149.

Cardinale, G. F., P. B. Mirkarimi, K. F. McCary, E. J. Klaus, D. L. Medlin, W. M. Clift, and D. G. Howitt. 1994. Effects of ambient conditions on the adhesion of cubic boron nitride films on silicon substrates. *Thin Solid Films* 253:130-135.

Cardinale, G. F., D. G. Howitt, K. F. McCarty, D. L. Medlin, P. B. Mirkarimi, and N. R. Moody. 1996. Analysis of residual stress in cubic boron nitride thin films using micromachined cantilever beams. *Diam. and Rel. Mat.* 5:1295-1302.

Cardinale, G. F., D. L. Medlin, P. B. Mirkarimi, K. F. McCarty, and D. G. Howitt. 1997. Orientation-dependence of elastic strain energy in hexagonal and cubic boron nitride layers in energetically deposited BN films. *J. Vac. Sci. Technol. A* 15:196-200.

Carmody, M., E. Landree, L. D. Marks. 1999. Determination of current density distribution in Josephson junctions. *Physica C* 315:145-153.

Carroll, D. L., P. Redlich, P. M. Ajayan, J. C. Charlier, X. Blasé, A. De Vita, and R. Car. 1997. Electronic structure and localized states at carbon nanotube tips. *Phys. Rev. Lett.* 78:2811.

Chadran, K., and P.C. Sabatier. 1977. *Inverse problems in quantum scattering theory*. New York: Springer.

Chai, W. P., Y. S. Gu, M. Li, Z. H. Mai, Q. Z. Li, L. Yuan, S. Pang. 1994a. Orientation influence of cubic boron-nitride crystal facets on the epitaxial-growth of diamond film by microwave plasma chemical-vapor-deposition. *Journal of Crystal Growth* 135:639-642.

Chai, W. P., Y. S. Gu, M. Li, Z. H. Mai, Q. Z. Li, L.Yuan, S. J. Pang. 1994b. Epitaxial-growth of diamond films on the (221) and (100) surfaces of C-BN with Microstructures full of (100) facets. *Appl. Phys. Lett.* 64:194-1943.

Charlier, J. C., X. Blasé, A. De Vita, R. Car. 1999. Microscopic growth mechanisms for carbon and boron-nitride nanotubes. *Appl. Phys. A* 68:267-273.

Chen, Y., L. T. Chadderton, J. F. Gerald, J. S. Williams. 1999. A solid-state process for formation of boron nitride nanotubes. *Appl. Phys. Lett.* 74:2960-2962.

Cherns, D. 1974. Direct resolution of surface atomic steps by transmission electron microscopy. *Phil. Mag.* 30:549-557.

Choi W. B., Chung D. S., Kang J. H., Kim H. Y., Jin Y. W., Han I. T., Lee Y. H., Jung J. E., Lee N. S., Park G. S., Kim J. M. 1999. Fully sealed, high-brightness carbon-nanotube field-emission display. *Appl. Phys. Lett.* 75:3129-3131.

Chopra, N. G., R. J. Luyken, K. Cherrey, V. H. Crespi, M. L. Cohen, S. G. Louie. A. Zettl. 1995. Boron Nitride Nanotubes. *Science* 269:966-967.

Chung, Y., C. S. Bahatia. 1998. Best bets in protective overcoats in hard disks. *Data Storage*. 5:7.

Clinton, W. L. 1993. Phase determination in x-ray and neutron reflectivity using logarithmic dispersion relations. *Phys. Rev. B* 48:1-5.

Cochran, W. 1955. Relations between the phases of structure factors. *Acta Cryst.* 8:473-478.

Collazo-Davila, C., E. Landree, D. Grozea, G. Jayaram, R. Plass, P. C. Stair, and L. D. Marks. 1995. Design and initial performance of an ultrahigh vacuum sample preparation evaluation analysis and reaction (SPEAR) system. *JMSA* 1:267-279.

Collazo-Davila, C., L. D. Marks, K. Nishii, and Y. Tanishiro. 1997. Atomic structure of the In on Si(111)(4x1) surface. *Surf. Rev. Lett.* 4:65-70.

Collazo-Davila, C., D. Grozea, E. Landree, and L. D. Marks. 1997. Transmission electron diffraction determination of the Ge(001)-(2x1) surface structure. *Surf. Sci.* 375:293-301.

Collazo-Davila, C., D. Grozea, and L. D. Marks. 1998. Determination and refinement of the Ag/Si(111)-(3x1) surface structure. *Phys. Rev. Lett.* 80:1678-1681.

Collazo-Davila, C., D. Grozea, L. D. Marks, R. Feidenhans'l, M. Nielsen, L. Seehofer, L. Lottermoser, G. Falkenberg, R. L. Johnson, M. Gothelid, and U. Karlsson. 1998. Direct Methods solution of the Ge(111)-(4x4)Ag surface. *Surf. Sci.* 418:395-406.

Collazo-Davila, C., E. Bengu, C. Leslie, L.D. Marks. 1998. Formation of BN nanoarches: possibly the key to cubic boron nitride film growth. *Appl. Phys. Lett.* 72:314-316.

Collazo-Davila, C., E. Bengu, L. D. Marks, M. Kirk. 1999. Nucleation of cubic boron nitride thin films. *Diam. and Rel. Mat.* 8:1091-1100.

Collazo-Davila, 1999. Ph.D. Dissertation.

Combettes, P. L. 1996. The convex feasibiltiy problem in image recovery. *Advances in Imaging and Electron Physics.* Vol 95, New York: Academic Press. Inc. p. 155.

Crimmins, T. R., and J. R. Feinup. 1983. Uniqueness of phase retrieval for functions with sufficiently disconnected support. *Journal of Opt. Soc. Am.* 73:218.

Crowley, T. L., E. M. Lee, E. A. Simister, R. K. Thomas. 1991. The use of contrast variation in the specular reflection on neutrons from interfaces. *Physica B* 173:143-156.

Dai, H. J., J. H. Hafner, A. G. Rinzler, D. T. Colbert, R. E. Smalley. 1996. Nanotubes as nanoprobes in scanning probe microscopy. *Nature* 384:147-150

Dainty, J. C. and J. R. Fienup. 1987. Phase retrival and Image Reconsturction for astronomy in *Image Recovery: Theory and Application.* Edited by: H. Stark. Orlando:Academic Press. p.231

Davison, C. J., and L. H. Germer. 1927. Diffraction of electrons by a crystal of nickel. *Phys. Rev.* 30:705-740.

Dean, K. A. and B. R. Chalamala. 1999a. Field emission microscopy of carbon nanotube caps. *J. Appl. Phys.* 85:3832-3836.

Dean, K. A. and B. R. Chalamala. 1999b. The environment stability of field emission from single-walled carbon nanotubes. *Appl. Phys. Lett.* 75:3017-3019.

De Vita, A., G. Galli, A. Canning, R. Car. 1996. A microscopic model for surface-induced diamond-to-graphite transitions. *Nature* 379:523-526.

Dewar, M. J. S., E. G. Zoebisch, E. F. Healy, and J. P. Steward. 1985. AM1: A new general purpose quantum mechanical molecular model. *J. Am. Chem. Soc.* 107:3902-3909.

Dillon, A. C., K. M. Joesn, T. A. Bekkedahi, C. H. Kiang, D. S. Bethune, M. J. Heben. 1997. Storage of hydrogen in single-walled carbon nanotubes. *Nature* 386:377-379.

Doll, G. L., J. A. Sell, C. A. Taylor II, and R. Clarke. 1991. Growth and characterization of epitaxial cubic boron nitride films on silicon. *Phys. Rev. B* 43:6816-6819.

Dorset, D. L. 1995. *Structural electron crystallography.* New York: Plenum Press.

Dorset, D. L. 1996. Electron crystallography. *Acta Cryst. B*52:753.

Dworschak, W., K. Jung, and H. Ehrhardt. 1995. Growth mechanism of cubic boron nitride in a r.f. glow discharge. *Thin Solid Films* 254:65-74.

Dunn, D. N., J. P. Zhang, and L. D. Marks. 1991. UHV microscopy of the reconstructed Au(001) surface. *Surf. Sci.* 260:220-270

Dunn, D. N., P. Xu, and L. D. Marks. 1993. UHV transmission electron microscopy of Ir (001) I, microstructure of the (1×1) and reconstructed (5×1) surfaces. *Surf. Sci.* 294:308-321.

Dynes, R. C., T. A. Fulton. 1971. Supercurrent density distribution in Josephson junctions. *Phys. Rev. B*3:3015.

Ebbesen, T. W., P. M. Ajayan. 1992. Large-scale synthesis of carbon nanotubes. *Nature* 358:220-222.

Ebbesen, T. W., H. J. Lezec, H. Hiura. 1996. Electrical conductivity of individual carbon nanotubes. *Nature* 382:54-56.

Eisenberger, P., and W. Marra. 1981. X-ray diffraction study of the Ge(001) reconstructed surface. *Phys. Rev. Lett.* 46:1081.

Endo, M., K. Takeuchi, S. Igarashi, K. Kobori, M. Shiraishi, H. W. Kroto. 1993. The production and structure of pyrolytic carbon nanotubes (PCNTS). *J. Phys. and Chem. of Solids.* 54:1841-1848.

Era, K., O. Mishima, Y. Wada, J. Tanaka, and S. Yamaoka. 1989. *Electroluminescence*. Edited by S. Shionoya and H. Kobayashi, Springer Proceedings in Physics, 38:386.

Erwin, S. C. 1995. New structural model for the alkali-induced Si(111)-(3x1) reconstruction from first principles. *Phys. Rev. Lett.* 75:1973-1976.

Erwin, S. C. and H. H. Weitering. 1998. Theory of the "Honeycomb Chain-Channel" reconstruction of M/ Si(111)-(3x1). *Phys. Rev. Lett.* 81:2296-2299.

Fan, Z. Y., N. Newman. 1998a. Precise control of atomic nitrogen production in an electron cyclotron resonance plasma using N-2 noble gas mixtures. *Appl. Phys. Lett.* 73:456-458.

Fan, Z. Y., N. Newman. 1998b, Kinetic energy distribution of nitrogen ions in an electron cyclotron resonance plasma. *J. Vac. Sci. Technol. A* 16:2132-2139.

Fasel, R., R. Aebi, R. G. Agostino, D. Naumovic, J. Osterwalder, A. Santaniello and L. Schlapbach. 1996. Orientation of adsorbed C_{60} molecules determined via x-ray photoelectron diffraction. *Phys. Rev. B* 76:4733-4736.

Fasel, R., R. G. Agostino, R. Aebi and L. Schlapbach. 1999. Unusual molecular orientation and frozen librational motion of C_{60} on Cu(110). *Phys. Rev. B* 60:4517-4520.

Fienup, J. R. 1982. Phase retrieval algorithms: a comparison. *Applied Optics*. 21:2758.

Fienup, J. R. 1983. Reconstruction of objects having latent reference points. *Opt. Soc. Am.* 73:1421-1426.

Fienup, J. R. 1987. Reconstruction of a complex-valued object from the modulus of its Fourier transform using a support constraint. *J. Opt. Soc. Am. A* 4:118-123.

Fiddy, M. A., B. J. Brames and J. C. Dainty. 1983. Enforcing irreducibility for phase retrival in two dimensions. *Optics Lett.* 8:96-98

Fowler, P. W., K. M. Rogers, G. Seifert. M. Terrones, H. Terrones. 1999. Pentagonal rings and nitrogen excess in fullerene-based BN cages and nanotube caps. *Chem. Phys. Lett.* 299:359-367.

Friedmann, T. A., L. J. Bernardez, K. F. McCarty, E. J. Klaus, D. K. Ottesen, H. A. Johnsen and W. M. Clift. 1993. Diamond deposition on polycrystalline films of cubic boron-nitride. *Appl. Phys. Lett.* 63:1342-1344.

Friedmann, T. A., P. B. Mirkarimi, D. L. Medlin, K. F. McCarty, E. J. Klaus, D. R. Boehme, H. A. Johnsen, M. J. Mills, D. K. Ottesen, and J. C. Barbour. 1994. Ion-assisted pulsed laser deposition of cubic boron nitride films. *J. Appl. Phys.* 76:3088-3101.

Geer, R. E., K. F. Thibodeaux, R. S. Duran. 1995. Interfacial sturcture and correlations in finite-sized liquid-crystalline polymer-films. *Europhys. Lett.* 32:419-424.

Gerchberg, R. W., and W. O. Saxton. 1972. A practical algorithm for the determination of phase from image and diffraction plane pictures. *Optik* 35:237-246.

Gibson, J. M., M. L. McDonald, F. C. Unterwald. 1985. Direct imaging of a novel silicon surface reconstruction. *Phys. Rev. Lett.* 55:1765.

Gilmore, C., G. Bricogne, C. Bannister. 1990. A multisolution method of phase determination by combined maximization of entropy and likelihood. 2. Application to small molecules. *Acta Cryst. A* 46:297-308.

Gilmore, C., K. Shankland, G. Bricogne. 1993. Applications of the maximum entropy method to powder diffraction and electron crystallography. *Proc R. Soc. Lond* A442:97-111.

Gilmore, C. J., L. D. Marks, D. Grozea, C. Collazo-Davila, E. Landree, and R. D. Twesten. 1997. Direct solutions of the Si(111) 7x7 structure. *Surf. Sci.* 381:77-91.

Goldberg, D. E. 1989. *Genetic algorithms in search, optimization, and machine language*. New York: Addison-Wesley Publishing Company, Inc.

Golberg, D. 1998. Octahedral boron nitride fullerenes formed by electron beam irradiation. *Appl. Phys. Lett.* 73:2441-2443.

Golberg, D., Y. Bando, M. Eremets, K. Takemura, K. Kurashima, K. Tamiya. 1997. Boron nitride nanotube growth defects and their annealing-out under electron irradiation. *Chem. Phys. Lett.* 191-196.

Golberg, D., Y. Bando, W. Han, K. Kurashima, T. Sato. 1999. Single-walled B-doped carbon, B/N-doped carbon and BN nanotubes synthesized from single-walled carbon nanotubes through a substitution reaction. *Chem. Phys. Lett.* 308:337-342.

Goodman, P. and A. F. Moodie. 1974. Numerical evaluation of N-beam wave functions in electron scattering by the multislice method. *Acta Cyrst. A* 30:280-295.

Guo, T., P. Nikolaev, A. G. Rinzler, D. Tomanek, D. T. Colbert, R. E. Smalley. 1995. Self-assembly of tubular fullerenes. *J. Phys. Chem.* 99:10694-10697.

Gupta, A., S. Pandita, D. K. Avasthi. 1998. Swift heavy ion irradiation effects in Pt/C and Ni/C multilayers. *Nucl. Inst. Meth. In Phys. Res. B* 146:265-270.

Grayer Wolf, S., M. Deutsch, E. M. Landau, M. Lavah, L. Leiserowitz, K. Kjaer, J. Als-Neilsen. 1988. A Synchrotron X-ray study of solid-solid phase transition in a two-dimensional crystal. *Science* 424:1286-1289.

Grozea, D., E. Landree, and L. D. Marks. 1997. Surface roughening by electron beam heating. *Appl. Phys. Lett.* 71:2301-2303.

Grozea, D., E. Landree, L. D. Marks, R. Feidenhans'l, M. Nielsen, and R. L. Johnson. 1998. Direct Methods determination of the Si(111)-(6x6)Au surface structure. *Surf. Sci.* 418:32-45.

Grozea, D., E. Bengu, C. Collazo-Davila, and L. D. Marks. 1999. Structure determination of the Ge(111)-(3x1)Ag surface reconstruction. *Surf. Rev. Lett.* in press.

Grozea, D., E. Landree, C. Collazo-Davila, E. Bengu, R. Plass, and L. D. Marks. 1999. Structural investigations of metal-semiconductor surfaces. *Micron* 30:41-49.

Hackenberger, L.B., L. J. Pilione, R. Messier, and G. P. Lamaze. 1994. Effect of stoichiometry on the phases present in boron nitride thin films. *J. Vac. Sci. Technol. A* 12:1569.

Hahn, J., F. Richter, R. Pintaske, M. Roder, E. Schneider, and T. Welzel. 1997. Formation of c-BN thin films under reduced ion impact. *Surf. & Coat. Technol.* 92:129-134.

Hamada, N., S. I. Sawada, A. Oshiyama. 1992. New one-dimensional conductors: graphitic microtubes. *Phys. Rev. Lett.* 68:1579-1581.

Hamley, I. W., J. S. Pedersen. 1994. Analysis of neutron and x-ray reflectivity Data I. Theory. *J. Appl. Cryst.* 27:29-35.

Han, W., Y. Bando, K. Kurashima and T. Sato. 1999. Formation of boron nitride (BN) fullerene-like nanoparticles and $(BN)_xC_y$ nonotubes using carbon nanotubes as templates. *Jpn. J. Appl. Phys.* 38:L755-L757.

Herman, G. T. 1980. *Image Reconstruction from Projections- the Fundamentals of Computerized Tomography.* New York: Academic Press.

Hobbs, L. W., F. W. Clinard, S. J. Zinkle, R. C. Ewing. 1994. Radiation effects in ceramics. *Journal of Nuclear Materials* 216:291-321.

Hofsäss, H., C. Ronning, R. Griesmeier, M. Gross, S. Reinke, M. Kuhr, J. Zweck, R. Fischer. 1995. Characterization of cubic boron nitride films grown by mass separated ion beam deposition. *Nucl. Inst. Meth. In Phys. Res. B*106:153-158.

Hofsäss, H., H. Feldermann, M. Sebastian, and C. Ronning. 1997. Thresholds for the phase formation of cubic boron nitride thin films. *Phys. Rev. B* 55:13230-13233.

Hofsäss, H., H. Feldermann, R. Merk, M. Sebastian, and C. Ronning. 1998. Cylindrical spike model for the formation of diamondlike thin films by ion deposition. *Appl. Phys. A* 66:153-181.

Horiuchi, S., L. L. He, and M. Akaishi. 1995. Semispiral structure of turbostratic boron nitride formed under high pressure and high temperature. *Jpn. J. Appl. Phys.* 34:L1612-L1615.

Huang H., S. Y. Tong, W.E. Packard and M. B. Webb. 1988. Atomic geometry of Si(111) 7×7 by dynamical low-energy electron diffraction. *Phys. Lett. A* 130:166-170.

Huang, Z. P., J. W. Xu, Z. F. Ren, J. H. Wang. 1998. Growth of highly oriented carbon nanotubes by plasma-enhanced hot filament chemical vapor deposition. *Appl. Phys. Lett.* 73:3845-3847.

Hurt, N. E., 1989. *Phase Retrieval and Zero Crossings.* Dordrecht: Kluwer.

Ibn-Ehaj, M., H. Regler, H. Mohwald, M. Schwendler, C. A. Helm. 1997. X-ray reflectivity study of layering transitions and the internal multilayer structure of films of three-block organosiloxane amphiphilic smectic liquid crystals on the air-water interface. *Phys. Rev. E* 56:1844-1852.

Ichihashi, T., and S. Iijima. 1994. Surface structure of silicon observed by ultrahigh vacuum transmission electron microscopy at atomic level. Proceedings of the 13th International Congress on Electron Microscopy 2B:1013-1014.

Ichiki, T., T. Momose, and T. Yoshida. 1994. Effects of the substrate bias on the formation of cubic boron nitride by inductively coupled plasma enhanced chemical vapor deposition. *J. Appl. Phys.* 75:1330-1334.

Ichiki, T., S. Amagi, T. Yoshida. 1996. Initial stage of cubic boron nitride film growth from vapor phase. *J. Appl. Phys.* 8:4381-4387.

Iijima, S. 1980. Direct observation of the tetrahedral bonding in graphatized carbon blacky by high resolution electron microscopy. *J. Crystl. Growth* 50:675-683.

Iijima, S. 1991. Helical microtubules of graphitic carbon. *Nature* 354:56.

Iijima, S., M. Yudasaka, R. Yamada, S. Bandow, K. Suenaga, F. Kokai, K. Takahashi. 1999. Nano-aggregates of single-walled graphitic carbon nano-horns. *Chem. Phys. Lett.* 309:165-170.

Ikeda, T. 1992. Cubic boron nitride films synthesized by low-energy ion-beam-enhanced vapor deposition. *Appl. Phys. Lett.* 61:786-788.

Ino, S., *In Reflection High-energy electron diffraction and reflection electron imaging of surfaces*. 1988. Edited by: P.K. Larsen, P.J.Dobson. New York: Plenum:p3-28.

Itoh, M., H. Tanaka, Y. Watanabe, M. Udagawa, and I. Sumita. 1993. Classification and structure analysis of domain boundaries on Si (111). *Phys. Rev. B* 47:2216-2227.

Jacquemain, D., S. Gayer Wolf, F. Leveiller, M. Lavan, L. Leiserowitz, M. Deutsch, K. Kjoer, J. Als-Neilsen. 1990. Dynamics of two-dimensional self-aggregation pressue and ph-induced structural changes in a florocarbon amphiphile at liquid-air interfaces. An x-ray synchrotron study. *J. of Am. Chem. Soc.* 112:7724-7736.

Jayaram, G., P. Xu, and L. D. Marks. 1993. Structure of Si(100)-(2x1) surface using UHV transmission electron diffraction. *Phys. Rev. Lett.* 71:3489-3492.

Jayaram, G., R. Plass, and L. D. Marks. 1995. UHV-HREM and diffraction of surfaces. *Interface Sci.* 2:379-395.

Jensen, R., H. Toflund. 1993. Structure and stability of C_{24} and $B_{12}N_{12}$ isomers. *Chem. Phys. Lett.* 201:89-96.

Jin, Z. S., X. Y. Lu, G. T. Zou. 1995. Heteroepitaxial growth of diamond film on cubic boron-nitride substrate by hot-filament chemical-vapor-deposition. *Chinese Phys. Lett.* 12:120-122.

Joshi, Vasant. 1999. Private communication.

Kaneda, K. and K. Shibata. 1994. A comparison of the effects of RF plasma discharge and ion beam supply on the growth of cubic boron nitride films formed by laser physical vapor deposition. *Jpn. J. Appl. Phys.* 33:266-269.

Karle, J., H. Hauptman. 1956. A theory of phase determination for the four types of non-centrosymmetric space groups $1P222_1$, 2P222, $3P_12$, $3P_22$. *Acta Cryst.* 9:635-651.

Kern, G., G. Kresse and J. Hofner. 1999. Ab initio calculations of the lattice dynamics and phase diagram of boron nitride. *Phys. Rev. B* 59:8551-8559.

Kester, D. J. and R. Messier. 1992. Phase control of cubic boron nitride thin films. *J. Appl. Phys.* 72:504-513.

Kester, D. J., K. S. Ailey, D. J. Lichtenwalner, and R. F. Davis. 1994. Growth and characterization of cubic boron nitride thin films. *J. Vac. Sci. Technol. A* 12:3074-3081.

Kidner, S., C. A. Taylor II, and R. Clarke. 1994. Low energy kinetic threshold in the growth of cubic boron nitride films. *Appl. Phys. Lett.* 64:1859-1861.

Klibanov, M. V., P. E. Sacks, and A. V. Tikhonrovov. 1995. The phase retrieval problem. *Inverse Problems* 11:1-28.

Kinchin, G. H., R. S. Pease. 1955. The displacement of atoms in solids by radiation. *Rep. Prog. Phys.* 18:1-51.

Koltover, I., T. Salditt, J. L. Rigaud. 1998. Stacked 2D crystalline sheets of the membrance-protein bacteriorhodopsin: a specular and diffuse reflectivity study. *Phy. Rev. Lett.* 81:2494-2497.

Kral, P., D. Tomanek. 1999. Laser driven atomic pump. *Phys. Rev. Lett.* 82:5373.

Kratschmer, W., L. D. Lamb, K. Fostiropoulos, D. R. Huffman. 1990. Solid C-60 – A new form of carbon. *Nature* 347:354-358.

Kroto, H. W., J. R. Heath, S. C. O'Brien, R. F. Curl, R. E. Smalley. 1985. C_{60}: Buckminsterfullerene. *Nature* 318:162-163.

Kulisch, W. and S. Reinke. 1997. Modeling of c-BN Thin Film Deposition. *Diam. Films and Tech.* 7:105-138.

Kunz, K., J. Reiter, A. Gotzelmann, M. Stomm. 1993. Model free-analysis of neutron reflectivity data from polymer thin films with the simulated annealing technicque. *Macromolecules* 26:4316-4323.

Kuznetsov, V., A. L. Chuvilin, Y. V. Butenko, I. Y. Mal'kov, and V. M. Titov. 1994. Onion-like carbon from ultra-disperse diamond. *Chem. Phys. Lett.* 222:343-348.

Kuznetsov, F. A., A. N. Golubenko, and M. L. Kosinova. 1997. A thermodynamic approach to chemical vapor deposition of boron nitride thin films from borozine. *Appl. Surf. Sci.* 114:638.

LaFemina, J. P. 1992. Total-energy calculations of semiconductor surface reconstrcutions. *Surf. Sci. Rep.* 16:138-248.

Lambrecht, W. R. L., Ch. H. Lee, B. Segall. J. C. Angus, Z. Li, M. Sunkara. 1993. Diamond nucleation by hydrogenation of the edges of graphitic precursors. *Nature* 364:607.

Landree, E., C. Collazo-Davila, and L. D. Marks. 1997. A multi-solution genetic algorithm approach to surface structure determination using Direct Methods. *Acta Cryst. B* 53:916-922.

Landree, E., D. Grozea, C. Collazo-Davila, and L. D. Marks. 1997. UHV high-resolution electron microscopy and chemical analysis of room-temperature Au deposition on Si(001)-2x1. *Phys. Rev. B* 55:7910-7916.

Latyshev, A., H. Minoda, Y. Tanishiro and K. Yagi. 1995. Ultra-high-vacuum reflection electron microscopy study of step-dislocation interaction on Si (111) surface. *Jap. J. Of Appl. Phys.* 34:5768-5773.

Leckner, J. 1991. Reflection theory and the analysis of neutron reflection data. *Physica B* 173:99-111.

Lederman, D., Z. H. Yu, T. H. Myers. 1997. Surface morphology of GaN films determined from quantitative x-ray reflectivity. *Appl. Phys. Lett.* 71:732-734.

Lee, D. R., Y. J. Park, S. H. Park. 1998. Resonant x-ray reflectivity measurements of a magnetic multilayer [Gd/Fe] (10). *Physica B* 248:146-151.

Leslie, C., E. Landree, C. Collazo-Davila, E. Bengu, D. Grozea and L. D. Marks. 1999. Electron Crystallography in surface structure analysis. *Microscopy Research and Technique* 46:160-177.

Li, Z., T. Suzuki, A. Argottia, P. Pirous, J. Angus. 1992. Orientation relationship between chemical vapor deposited and graphite substrates. *J. Appl. Phys.* 73:711-715.

Liao, K. and W. Wang. 1994. Cubic boron nitride/diamond films. *Physica Status Solidi A* 145:K25.

Lifshitz, Y., S. R. Kasi, J. W. Rabalais, and W. Eckstein. 1990. Subplantation model for film growth from hyperthermal species. *Phys. Rev. B* 41:10468-10480.

Litvinov, D., R. Clarke. 1997. Reduced bias growth of pure-phase cubic BN. *Appl. Phys. Lett.* 71:14.

Liu, A. Y. and M. L. Cohen.1989. Prediction of new low compressibility solids. *Science.* 245:841.

Loiseau, A., F. Willaime, N. Demoncy, G. Hug, H. Pascard. 1996. Boron nitride nanotubes with reduced numbers of layers synthesized by arc discharge. *Phys. Rev. Lett.* 76:4737-4740.

Logothetidis, S., M. Gioti, C. Charitidis. 1999. A new process for the development of hard and stable sputtered amorphous carbon films. *Vacuum* 53:61-65.

Long, C. A., H. J. Grabke. 1992. The formation of boron nitride on Fe-37Ni alloy. *Appl. Surf. Sci.* 59:207-217.

Lüthjie, H., K. Bewilogua, S. Daaud, M. Johansson, and L. Hultman. 1995. Preparation of cubic boron nitride films by use of electrically conductive boron carbide targets. *Thin Solid Films* 257:40.

Mackay, A. L., H. Terrones. 1991. Diamond from graphite. *Nature* 352:762.

Malik, A., M. K. Durbin, A. G. Richter. 1995. Structures of headgroup and tail-group monolayers in a Langmuir-Blodgett-film. *Phys Rev. B* 52:11654-11657.

Manorama, S., G.N. Chauderi, and V.J. Rao. 1993. Growth of BN by hot-filament assisted electron-beam deposition *J. of Phys.* D26:1793-1795.

Man Yu, K. and E. D.Bourret-Courchesne.1996. Anomalous ion damage in ZnSe. *Appl. Phys. Lett.* 69:2062

Margulis, L., G. Salitra, R. Tenne. 1993. Nested fullerene-like structures. *Nature* 365:113-114.

Marks, L. D. and D. J. Smith. 1983. Direct surface imaging in small metal particles. *Nature* 303:316-317.

Marks, L. D. 1988. Linear imaging and diffraction of an amorphous film. *Ultramicroscopy* 25:85-88.

Marks, L. D. 1991. Rigor, and plan-view simulation of surfaces. *Ultramicroscopy* 38:325-332.

Marks, L. D., T. S. Savage, J. P. Zhang, and R. Ai. 1991. Validity of the kinematical aproximation in tranmission electron diffraction from surfaces, revised. *Ultramicroscopy* 38:343-347.

Marks, L. D. 1992a. Registry and UHV transmission electron diffraction of surfaces. *Ultramicroscopy* 45:145-154.

Marks, L. D., P. Xu, D. N. Dunn and J. P. Zhung. 1992b. Atomic imaging of surfaces in plan view. *EMSA Bulletin* 22:65-69.

Marks, L. D., P. Xu, and D. N. Dunn. 1993. UHV transmission electron microscopy of Ir(001). II Atomic positions of the (5x1) reconstructed surface from HREM and R-factor refinements. *Surf. Sci.* 294:322-332.

Marks, L. D. 1996. Wiener-filter enhancement of noisy HREM images. *Ultramicroscopy* 62:43-52.

Marks, L. D., R. Plass, and D. Dorset. 1997. Imaging surface structures by direct phasing. *Surf. Rev. Lett.* 4:1-8.

Marks, L. D., E. Bengu, and C. J. Gilmore. 1997. New Methods of imaging surfaces (and buried interfaces). *J. of Electr. Micros.* 46:207-2144.

Marks, L. D., E. Bengu, C. Collazo-Davila, D. Grozea, E. Landree, C. Leslie, and W. Sinkler. 1998. Direct Methods for surfaces. *Surf. Rev. Lett.* 5:1087-1106.

Marks, L. D. and E. Landree. 1998. A Minimum Entropy algorithm for surface phasing problems. *Acta Cryst. A* 54:296-305.

Marks, L. D., W. Sinkler, and E. Landree. 1999. A feasible set approach to the crystallographic phase problem. *Acta Cryst. A* 55:601-612.

Marton, D. 1994. *Low energy ion-surface interactions.*Edited by: J.W. Rabalais. Chicester:John Wiley and Sons. p. 482.

McCarty, K. F., M. J. Mills, D. L. Medlin. 1994. Growth and characterization of epitaxial cubic boron nitride films on silicon-comment. *Phys. Rev. B.* 50:8907-8910.

McCarty, K. F., P. B. Mirkarimi, D. L. Medlin, T. A. Friedmann, and J. C. Barbour. 1996. On the low-temperature threshold for cubic boron nitride formation in energetic film depostion. *Diam. and Rel. Mat.* 5:1519-1526.

McCarty, K. F. and D. L. Medlin. 1997. How plastic deformation can produce texture in graphitic films of boron nitride, carbon nitride, and carbon. *Diam. and Rel. Mat.* 6:1219-1225.

McCarty, K. F. 1999. Preferred orientation in carbon and boron nitride: does a thermodynamic theory of elastic strain energy get it right? *J. Vac. Sci. Technol. A* 17:2749-2752.

McCulloch, D. G., D. R. Mc Kenzie, S. Prawer. 1995. Compressive stress induced formation of preferred orientation in glassy carbon following high-dose C^+ implantation. *Phil. Mag.* 72:1031-1041.

McFall, W. D., D. R. McKenzie, R. P. Netterfield. 1996. Use of in situ ellipsometry to observe phase transitions during boron nitride thin film deposition. *Surf. and Coat. Technol.* 81:72-78.

McKenzie, D. R. 1993. Generation and applications of compressive stress induced by low energy ion beam bombardment. *J. Vac. Sci. Tech. B* 11:1928-1935.

McKenzie, D. R., W. D. McFall, W. G. Sainty, C. A. Davis, and R. E. Collins. 1993. Compressive stress induced formation of cubic boron nitride. *Diam. and Rel. Mat.* 2:970-976.

McKenzie, D. R., W. D. McFall, H. Smith, B. Higgins, R. W. Boswell, A. Durandet, B. W. James, and I. S. Falconer. 1995. High pressure phases produced by low energy ion implantation with reference to cubic boron nitride. *Nucl. Inst. Meth. In Phys. Res. B* 106:90-95.

McKenzie, D. R., W. D. McFall, S. Reisch, B. W. James, I. S. Falconer, R. W. Boswell, H. Pershing, A. J. Perry, A. Durandet. 1996. Synthesis of cubic boron nitride thin films. *Surf. and Coat. Technol.* 78:255-262.

McKenzie, D. R., M. M. Bilek. 1998. Thermodynamic theory for preferred orientation in carbon and cubic BN. *J. Vac. Sci. Technol A.* 16:2733-2734.

McKinley, W. A., H. Feshbach. 1948. The coulomb scattering of relativistic electrons by nuclei. *Phys. Rev.* 74:1759-1763.

Medlin, D. L., T. A. Friedmann, P. B. Mirkarimi, M. J. Mills, and K. F. McCarty. 1994. Evidence for rhombohedral boron nitride in cubic boron nitride films grown by ion-assisted deposition. *Phys. Rev. B* 50:7884-7887.

Medlin, D. L., T. A. Friedmann, R. B. Mirkarimi, G. F. Cardinale, and K. F. McCarty. 1996. Crystallographic texture in cubic boron nitride thin films. *J. Appl. Phys.* 79:3567-3571.

Mehandru, S. P., A. B. Anderson, J. C. Angus. 1992. Hydrogenation of the {1010} graphite edge. Structural consideration from Band calculations. *J. Phys. Chem.* 96:10978-10982.

Menon, M., D. Srivastava. 1999. Structure of boron nitride nanotubes: tube closing versus chirality. *Chem. Phys. Lett.* 307:407-412.

Mieno, M. and T. Yoshida. 1990. Preparation of cubic boron nitride films by RF sputtering. *Jap. J. Appl. Phys.* 29:L1175-L1177.

Mineta, S., K. Kohata, N. Yasunaga, Y. Kikuta. 1990. Preparation of cubic boron nitride film by CO_2 laser physical vapour deposition with simultaneous nitrogen ion supply. *Thin Solid Films* 189:125-138.

Mikulik, P., T. Baumbach. 1999. X-ray reflection by rough multilayer gratings: dynamical and knimatical scattering. *Phys. Rev. B* 59:7632-7643.

Mirkarimi, P. B., K. F. McCarty, D. L. Medlin, W. G. Wolfer, T. A. Friedmann, E. J. Klaus, G. F. Cardinale, and D. G. Howitt. 1994. On the role of ions in the formation of cubic boron nitride films by ion-assisted deposition. *J. Mater. Res.* 9:2925-2938.

Mirkarimi, P. B., D. L. Medlin, K. F. McCarty, and J. C. Barbour. 1995. Growth of cubic BN films on β-SiC by ion-assisted pulsed laser deposition. *Appl. Phys. Lett.* 66:2813-2815.

Mirkarimi, P. B., K. F. McCarty, G. F. Cardinale, D. L. Medlin, D. K. Ottesen, and H. A. Johnsen. 1995. Substrate effects in cubic boron nitride film formation. *J. Vac. Sci. Technol. A* 14:251-255.

Mirkarimi, P. B., D. L. Medlin, K. F. McCarty, D. C. Dibble, W. M. Clift, J. A. Knapp, and J. C. Barbour. 1997. The synthesis, characterization, and mechanical properties of thick, ultrahard cubic boron nitride films deposited by ion-assisted sputtering. *J. Appl. Phys.* 82:1617-1625.

Mirkarimi, P. B., K. F. McCarty, and D. L. Medlin. 1997. Review of advances in cubic boron nitride film synthesis. *Mat. Sci. and Eng.* R21:47-100.

Miyamoto, Y., A. Rubio, M. L. Cohen, S. G. Louie. 1994a. Chiral tubes of hexagonal BC_2N. *Phys. Rev. B* 50:4976-1979.

Miyamoto, Y., A. Rubio, M. L. Cohen, S. G. Louie. 1994b. Electronic properties of tubule forms of hexagonal BC_3. *Phys. Rev B* 50:18360.

Mott, N. F. 1929. The scattering of fast electrons by atomic nuclei. *R. Soc. London A* 124:425-442.

Murakawa, M., S. Watanabe, S. Miyake. 1991. Manufacture of c-BN films with improved adhesion. *Materials Science and Engineering A* 140:753-758.

Murray, P. W., M. O. Pedersen, E. Laegsgaard, I. Stengaard, F. Besenbacher. 1997. Growth of C_{60} on Cu(110) and Ni(110) surfaces: C_{60}-induced roughening. *Phys. Rev. B* 55:9360-9363.

Nagashima, A., N. Tejima, Y. Gamou, T. Kawai and C. Oshima. 1995. Electronic structure of monlayer hexagonal boron nitride physisorbed on metal surfaces. *Phys. Rev. Lett.* 75:3918-3921.

Nagashima, A., N. Tejima, Y. Gamou, T. Kawai, M. Terai, M. Wakabayashi and C. Oshima. 1996. Electron spectroscopic studies of monolayer hexagonal boron nitride pysisorbed on metal surfaces. *Intern. J. of Modern Phys. B* 10:3517-3537.

Okamoto, M., H. Yokoyama, and Y. Osada. 1990. Formation of cubic boron nitride film on Si with boron buffer layers. *Jap. J. Appl. Phys.* 29:930-933.

Okamoto, M., Y. Utsumi, Y. Osaka. 1990. Formation of boron nitride films on diamond by plasma CVD technique. *Jpn. J. Appl. Phys.* 29:1004.

Okamoto, M., Y. Utsumi, Y. Osaka. 1992. Formation and properties of cubic boron nitride films on tungsten carbide by plasma chemical vapor deposition. *Jpn. J. Appl. Phys.* 31:3455-3460.

Osakabe, N., Y. Tanishiro, K. Yagi and G. Hunjo. 1980. Reflection electron microscopy of clean and gold deposited (111) silicon surfaces. *Surf. Sci.* 97:393-408.

Oshima, C., A. Nagashima. 1997. Ultra-thin epitaxial films of graphite and hexagonal boron nitride on solid surfaces. *J. of Phys.* 9:1-20.

Park, K. S., D. Y. Lee, K. J. Kim, and D. W. Moon. 1997. Observation of a hexagonal BN surface layer on the cubic BN film grown by dual ion beam sputter deposition. *Appl. Phys. Lett.* 70:315-317.

Parratt, L. G. 1954. Surface studies of solids by total reflection of x-rays. *Phys. Rev.* 95:359-359.

Pascallon, J., V. Stambouli, S. Ilias, D. Bouchier, G. Nouet, F. Silva, A. Gicquel. 1999a. Deposition of c-BN films on diamond: influence of the diamond roughness. *Mat. Sci. and Eng. B* 59:239-243.

Pascallon, J., V. Stambouli, S. Ilias, D. Bouchier, G. Nouet, F. Silva, A. Gicquel. 1999b. Microstructure of c-BN thin films deposited on diamond films. *Diam. and Rel. Mat.* 8:325-330.

Pascual, E., J. L. Andujar, S. Gimeno, A. Lousa, A. Bosch, M. El Kasmi, E. Bertran. 1996. Spectroscopic ellipsometric study of boron nitride thin films. *Diam. and Rel. Mat.* 5:539-543.

Pashley, D. W., M. J. Stowell, M. H. Jacobs, and T. J. Law. 1964. The growth and structure of gold and silver deposits formed by evaporation inside an electron microscope. *Phil. Mag.* 10:127-158.

Patterson, A. L. 1934. A Fourier series method for the determination of the components of interatomic distances in crystals. *Phys. Rev.* 46:372-376.

Pedersen, J. S., R. Feidenhans'l and M. Neilsen. 1988. X-ray diffraction study of the Ge(111) 5×5 and Ge(111) 7×7- Sn surfaces. *Phys. Rev. B* 38: 210-221.

Pedersen, J. S. 1992. Model-independent determination of the surface scattering-length-density profile from specular reflectivity data. *J. Appl. Cryst.* 25:129-145.

Pedersen, J. S., I. W. Hamley. 1994a. Analysis of neutron and x-ray reflectivity data by constrained least-squares methods. *Physica B* 198:16-23.

Pedersen, J. S., I. W. Hamley. 1994b. Analysis of neutron and x-ray reflectivity data II. Constrained least-squares methods. *J. Appl. Crystl.* 27:36-49.

Pederson, M. R., J. Q. Broughton. 1992. Nanocapillarity in fullerene tubules. *Phys. Rev. Lett.* 69:2689-2692.

Penfold, J., and R. K. Thomas. 1990. The application of the specular reflection of neutrons to the study of surfaces and interfaces. *Jour. Phys. 2*: 1369-1412.

Plass, R. and L. D. Marks. 1995. UHV transmission electron microscopy structure determination of the Si(111)-($\sqrt{3}$x$\sqrt{3}$)R30°Au surface. *Surf. Sci.* 342:233-249.

Poppa, H. R. 1983. Surface studies with clean supported metal particles and clusters. *Ultramicroscopy.* 11:105

Qin, L. C. and S. Iijima. 1996. Onion-like graphitic particles produced from diamond. *Chem. Phys. Lett.* 262:252-258.

Redlich, Ph., J. Loeffler, P. M. Ajayan, J. Bill, F. Aldinger, M. Ruhle. 1996. B-C-N nanotubes and boron doping of carbon nanotubes. *Chem. Phys. Lett.* 260:465-470.

Reinke, S., M. Kuhr, W. Kulisch, and R. Kassing. 1995. Recent results in cubic boron nitride deposition in light of the sputter model. *Diam. and Rel. Mat.* 4:272-283.

Reinke, S., M. Kuhr, W. Kulisch. 1996. Investigation of stress and adhersion of cubic boron nitride films. *Diam. and Rel. Mater.* 5:508-513.

Rinzler, A. G., J. H. Hafner, P. Nikolaev, L. Lou, S. G. Kim, D. Tomanek, P. Nordlander, D. T. Colbert, and R. E. Smalley. 1995. Unraveling nanotubes-field- emission from an atomic wire. *Science* 269:1550.

Roberts, T. M. 1991. Introduction to Schrodinger inverse scattering. *Physica B* 173:157-165.

Robertson, J. 1996. Deposition mechanism of cubic boron nitride. *Diam. and Rel. Mat.* 5:519-524.

Robinson, I. K., W. K. Waskiewicz, P. H. Fuoss, J. B. Stark, and P. A. Bennett. 1986. X-ray-diffraction evidence of adatoms in the Si(111) 7×7 recontructed surface. *Phys. Rev. B* 33:7013.

Robinson, M. T. 1994. Basic physics of radiation damage production. *J. of Nuc. Mat.* 219:1-28.

Rubio, A., J. Corkill, M. Cohen. 1994. Theory of graphitic boron nitride nanotubes. *Phys. Rev. B.* 49:5081-5084.

Rubio, A., Y. Miyamoto, X. Blasé, M. L. Cohen, S. G. Louie. 1996. Theoretical study of one-dimensional chains of metal atoms in nanotubes. *Phys. Rev.* 53:4023-4026.

Sachdev, H., R. Haubner, H. Hoth, and B. Lux. 1997. Investigation of the c-BN/h-BN phase transformation at normal pressure. *Diam. and Rel. Mat.* 6:286-292.

Saitoh, H. and W. A. Yarbrough. 1991. Growth of cubic boron nitride on diamond particles by microwave plasma enhanced chemical vapor deposition. *Appl. Phys. Lett.* 58:2482-2484.

Saitoh, H., T. Hirose, T. Ohtsuka and Y. Ichinose. 1994. Nucleation of boron nitride on cubic boron nitride microcrystallites using chemical vapor deposition. *Appl. Phys. Lett.* 64:1638.

Sayre, D. 1952. The squaring method: a new method for phase determination. *Acta Cryst.* 5:60-65.

Schiller, R. E., and H. E. Farnsworth. Structure and adsorption characteristics of clean surfaces of germanium and silicon. 1959. *J. of Chem. Phys.* 30: 917-926.

Schlatmann, R., J. D. Shindler, J. Verhoeven. 1996. Evolution of surface morphology during growth and ion erosion of thin films. *Phys. Rev. B* 54:10880-10889.

Schlomka, J. P., M. Tolan, W. Press. 1999. Interdiffusion in NiMnSb/V/NiMnSb: X-ray and neutron reflectivity investigation of ion beam sputtered trilayer systems. *J. Appl Phys.* 86:5146-5151.

Seitz, F. and J. S. Koehler. 1956. Displacement of atoms during irradiation. *Solid State Phys.* 2:305-448.

Sekine, T., T. Kobayashi, and H. Nameki. 1996. Effects of deviatoric stress and radial strain on the shock-induced diffusionless trasnformation in boron nitride. *J. Appl. Phys.* 81:527-529.

Semiconductor Industry Association. 1997. *The National Technology Roadmap for Semiconductors*. San Jose, California.

Sene, G., D. Bouchier, S. Ilias, M. A. Djouadi, J. Pascallon, V. Stambouli, P. Moller, and G. Hug. 1996. Correlation between microstructure and collisional effects in cubic boron nitride synthesized using IBAD. *Diam. and Rel. Mat.* 5:530-534.

Sezan, I., 1992. An overview of convex projections theory and its application to image recovery problems. *Ultramicroscopy* 40: 55-67.

Sheldrick, G. M. 1990. Phase annealing in SHELX-90-direct methods for larger structures. *Acta Cryst. A* 46:467-473.

Simmons J. H. 1965. *Radiation Damage in Graphite*. Oxford:Pergamon Press. p.38.

Singh, N., M. Tirrell, F. S. Bates. 1993. Applications of Fourier-sysnthesis methods to the analysis of specular reflectivity. *J. of Appl. Cryst.* 26:650-659.

Sivia, D. S., W. A. Hamilton, G. S. Smith. 1991. Analysis of neutron reflectivity data: maximum entropy, Bayesion spectral analysis and speckle holograhy. *Physica* B 173:121-138.

Sivia, D. S., W. A. Hamilton, G. S. Smith, T. P. Rieker, R. Pynn. 1991. A novel experimental procedure for removing ambiguity from the interpretation of neuton and x-ray reflectivity measurements: "speckle holography". *J. Appl. Physics* 70:732-738.

Smalley, R. E., D. T. Colbert. 1995. Self assembly of fullerene tubes and balls. Presented in "The Robert A Welch Foundation 39th Conference on Chemical Research: Nanophase Chemistry" which held in Houston, TX, Oct. 23-24, 1995.

Smalley, R. E., D. T. Colbert. 1995. Chemistry on the nanometer scale-introductory remarks.

Smalley, R. E. 1997. Discovering the fullerenes. *Rev. Mod. Phys.* 69:723-730.

Sokolowski, M. 1979. Deposition of wurtzite type bron nitride layers by reactive pulse plasma crystallization. *J. Cryst. Grwth.* 46:136-138.

Sokolowski, M., A. Sokolowska A. Rusek, Romanowski Z., B. Gokieli and M.Gajewska. 1981. Properties of growth of β-BN(Borazon) layers from a pulsed plasma under reduced pressure. *J. Cryst. Grwth* 52:165.

Solozhenko, V. L. 1993. Thermodynamics of dense boron nitride modifications and a new phase P,T diagram for BN. *Termochimica Acta* 218:221-227.

Solozhenko V. L. 1995. Current trends in the phase-diagram of boron-nitride. *J. of Hard Materials* 6:51.

Solozhenko, V. L., V. Z Turkevich. 1999. Refined phase diagram of boron nitride. *J. Phys. Chem. B* 103:2903-2905.

Song, Z., F. Zhang, Y. Guo, and G. Chen. 1994. Textured growth of cubic boron nitride film on nickel substrates. *Appl. Phys. Lett.* 65:2669-2671.

Spence, J. C. 1983. High-energy transmission electron diffraction and imaging studies of Silicon (111) 7×7 surface structure. *Ultramicroscopy* 11:117-123.

Stark, H. 1987. *Image recorvery: theory and application.* San Diego, California: Academic Press.

Steinfort, A. J., P. M. Scholte, F. Tuinstra. 1998. Characterisation of multilayers by x-ray reflection. *Surf. Sci.* 409:229-240.

Stephan, O., P. M. Ajayan, C. Colliex, P. Redlich, J. M. Lambert, P. Bernier, P. Lefin. 1994. Doping graphitic and carbon nanotubes structures with boron and nitrogen. *Science* 266:1683-1685.

Stephan, O., Y. Bando, A. Loiseau, F. Willaime, N. Shramchenko, T. Tamiyaa nd T. Sato. 1998. Formation of small single-layer and nested BN cages under electron irradiation of nanotubes and bulk material. *Appl. Phys.* A. 67:107-111.

Stone, V. W., A. M. Jonas, B. Nysten. 1999. Roughness of free surfaces of bulk amorphous polymers as studied by x-ray surface scattering and atomic force microscopy. *Phys. Rev. B* 60:5883-5894.

Takayanagi K., Y. Tanishiro, S. Takahashi, and M. Takahashi. 1985a. Structural analysis of Si(111)-7×7 by UHV transmission electron diffraction and microscopy. J. *Vac. Sci. Technol. A* 3:1502-1506.

Takayanagi, K., Y. Tanishiro, S. Takahashi, and M. Takahashi. 1985b. Structure analysis of Si(111)-7x7 reconstructed surface by transmission electron diffraction. *Surf. Sci.* 164:367-392.

Takayanagi, K. Y., Y. Tanishiro, K. Kajiyama. 1986. On the stability and structure of 5 × 5 and 7 × 7 reconsturction of the (111) surface of Si and Ge. *J. Vac. Sci. Technol. B* 4:1074-1078.

Tamura, R. and M. Tsukada. 1995. Electronic states of cap structure in the carbon nanotube. *Phys. Rev. Lett. B* 52:6015-6026.

Tanabe, N., T. Hayashi. 1992. Substrate temperature influence of c-BN thin film formation by IBED. *Diam. and Rel. Mat.* 151-156.

Tanaka, H. M., M. Itoh, T. Uchiyama, Y. Watanabe, T. Yokotsuko and I. Sumita. 1992. Si (111) 7×7 domain boundaries on vicinal surfaces. *Ultramicroscopy* 42:864-870.

Tanishiro, Y., K. Takayanagi, K. Yagi. 1986. Observations of lattice fringe of the Si (111) 7×7 structure by reflection electron microscopy. *J. Microsc.* 142:211.

Telieps, W., and E. Bauer. 1985. An analytical reflection and emmision UHV surface electron microscope. *Ultramicroscopy* 17:57-65.

Tenne, R., L. Margulis, M. Genut and G. Hodes. 1992. Polyhedral and cylindrical structures of tungsten disulphide. *Nature* 360:444-446.

Terrones, M., W. K. Hsu, H. Terrones, J. P. Zhang, S. Ramos, J. P. Hare, R. Castillo, K. Prassides, A. K. Cheetham, H. W. Kroto, D. R. M. Walton. 1996. Metal particle catalysed production of nanoscale BN structures. *Chem. Phys. Lett.* 259:568-573.

Tidswell, I. M., B. M. Ocko, P. S. Pershan, S. R. Waslerman, G. M. Whitesides, J. D. Axe. 1990. X-ray specular reflection studies of silicon coated by organic monolayers (alkylsiloxanes). *Physical Review B* 41:1111-1127.

Tomanek, D., W. Zhong, E. Krastev. 1993. Stability of multishell fullerenes. *Phys. Rev. B* 48:15461-15464.

Treacy, M. M. J., T. W. Ebbesen. J. M. Gibson. 1996. Exceptionally high Young's modulus observed for individual carbon nanotubes. *Nature* 381:678-680.

Trehan, R., Y. Lifshitz, J. W. Rabalais. 1990. Auger x-ray electron spectroscopy of hBN, cBN, and N_2^+ ion irradiation of boron and boron nitride. *J. Vac. Sci. Technol. A* 8:4026-4032.

Tsai, S. H., C. W. Chao, C. L. Lee, H. C. Shih. 1999. Bias-enhanced nucleation and growth of the aligned carbon nanotubes with open ends under microwave plasma synthesis. *Appl. Phys. Lett.* 74:3462-3464.

Twesten, R. D., J. M. Gibson, and F. M. Ross. 1994. Visualization of dynamic near-surface processes. *MRS Bull.* 6:38-43.

Twesten, R. D., and J. M. Gibson. 1995. Kinematic analysis of transmission electron diffraction data from Si (111)- 7×7. *Ultramicroscopy* 53:223-235.

Ugarte, D. 1992. Curling and closure of graphitic networks under electron-beam irradiation. *Nature* 359:707-709.

Ugarte, D. 1993. Formation mechanism of quasi-spherical carbon particles induced by electron bombardment. *Chem. Phys. Lett.* 207:473-479.

Ulrich, S., J. Scherer, J. Schwan, I. Barzen, K. Jung and H. Erhard. 1995. Radio-frequency ion plating-induced phase-transition from H-BN to nancrystalline C-BN. *Diam. and Rel. Mat.* 4:288.

Van Hove, M.A., W.H. Weinberg and C.M. Chan. 1986. *Low-energy electron diffraction: experiment, theory, and surface structure determination* . New York: Springer-Verlag.

Vel, L., G. Demazeau, and J. Etourneau. 1991. Cubic boron nitride: synthesis, physicochemical properties and applications. *Mat. Sci. and Eng. B* 10:149-164.

Veprek, S. 1999. The search for novel, superhard materials. *J. Vac. Sci. Technol. A* 17:2401.

Verinaud, F., E. Weissmantel. I. Grenier, A. Clerier, J. Machet. 1992. Investigation of hard BN films obtained by ion plating. *Thin Solid Films*. 209:59-66.

Verwoerd, W. S. 1994. Parallel v.s diagonal epitaxy models of diamond and c-BN on Si(001). *Diam. and Rel. Mat.* 3:457.

Verwoerd, W. S., K. Osuch, P. Badziag. 1994. Atomic structure calculation for epitaxy of c-BN on Si (001). *Surf. Sci.* 312:221-232.

Vineyard, G. H. 1982. Grazing-incidence diffraction and the distorted-wave approximation for the study of surfaces. *Phys. Rev.B* 26:4146.

Wada, T., N. Yamashita. 1992. Formation of cBN films by ion beam assisted deposition. *J. Vac. Sci. Technol. A* 10:515-519.

Watanabe, S., S. Miyake and M. Murakawa. 1991. Tribological properties of cubic, amorphous, and hexagonal boron nitride films. *Surf. and Coat. Technol.* 49:406-410.

Weisendanger, R., G. Tarrach, L. Scandella, H.-J. Guntherodt. 1990. *Ultramicroscopy* 32:291.

Weissmantel, C., K. Bewilogua, D. Dietrich, H.-J. Erler, H.-J. Hinneberg, S. Klose, W. Nowick and G. Reisse. 1980. Structure and properties of quasi-amorphous films prepared by ion beam techniques. *Thin Solid Films*. 72: 19-31.

Weitering, H. H., N. J. DiNardo, R. Pérez-Sandoz, J. Chen, and E. J. Mele. 1994. Structural model for the metal-induced Si(111) 3x1 reconstruction. *Phys. Rev. B* 49:16837-16840.

Weng-Sieh, Z., K. Cherrey, M. G. Chopra, X. Blase, Y. Miyamoto, A. Rubio, M. L. Cohen, S. G. Louie, A. Zettl, and R. Gronsky. 1995. Synthesis of $B_xC_yN_z$ Nanotubes. *Phys. Rev. B* 51:11229-11232.

Wentorf, R. H. 1957. Cubic form of boron nitride. *J. Chem. Phys.* 26:956.

Wentorf, R. H. 1961. Synthesis of the cubic form of boron nitride. *J. Chem. Phys.* 34:809-812.

Widany, J., T. Frauenheim, and W. R. L. Lambrecht. 1996. Investigation of the stability of the hexagonal-cubic boron nitride prism interface. *J. Mater. Chem.* 6:899-901.

Widany, J., T. Frauenheim, T. Kohler. 1996. Density-functional-based construction of transferable nonorthogonal tight-binding potentials for B, N, BN, BH, and NH. *Phys. Rev. B* 53:4443-4453.

Windschmann, H., 1991. Intrinsic stress in sputtering thin films. *J. Vac. Sci. Technol. A* 9:2431-2435.

Wiener, N. 1942. *Extrapolation, Interpolation, and Smooting of Stationary Time Series.* Cambridge, Massachusetts:MIT Press.

Woolfson, M. M. 1987. Direct Methods – from birth to maturity. *Acta Cryst. A* 43:593-612.

Woolfson, M. M. and H.-f. Fan. 1995. *Physical and non-physical methods of solving crystal structures.* Cambridge: University Press.

Wood, E. A. 1964. Vocabulary of surface crystallography. *J. Appl. Phys.* 35:1306-1311.

Wong, G. C. L., C. A. Lucas, D. Loretto, A. P. Payne, and P. H. Fuoss. 1994. Parallel adatom chains on Si(111) - a chemisorption-induced surface reconstruction. *Phys. Rev. Lett.* 73:991-994.

Wood, E. A. 1963. Vocabulary of surface crystallography. *J. Appl. Phys.* 35:1306-1311.

Woolfson, M. M. 1961. *Direct methods in crystallography.* Oxford: Clarendon Press.

Xu, P. and L. D. Marks. 1992. Intensities of surface diffraction spots in plan view. *Ultramicroscopy* 45:155-157.

Xu, P., D. N. Dunn, J. P. Zhang, and L. D. Marks. 1993. Atomic imaging of surfaces in plan view. *Surf. Sci.* 285:L479-L485.

Yagi, K., K. Takayanagi and G. Honjo. 1982. In-situ UHV electron microscopy of surfaces. *Crystals Growth Properties and Applications*. Edited by H. C. Freyhardt. Berlin: Springer-Verlag, pp. 48-74.

Yagi, K., K. Kobayashi, and K. Takayanagi. 1985. In situ electron microscope study of the initial stages of metal growth on metals. *Thin Solid Films* 126:95-105.

Yagi, K., A. Yamana, H. Sato, H. Ohse, S. Ozawa, Y. Tanishiro. 1991. UHV-Tem-REM studies of Si(111) surfaces. *Phil. Mag.* 30:549.

Yamada-Takamura, Y., O. Tsuda, H. Ichinose, T. Yashida. Atomic-scale structure at the nucleation site of cubic boron nitride deposited from the vapor phase. *Phys. Rev. B* 59:10351-10355.

Yao, N., V. Lordi. 1998. Carbon nanotube caps as springs: molecular dynamics simulations. *Phys. Rev. B* 58:649-651.

Yoshida,T. 1996. Vapor phase deposition of cubic boron nitride. *Diam. and Rel. Mat.* 5:501.

Yoshida, T. 1997. State-of-the-art vapor-phase deposition of cubic boron nitride. *Diam. Films and Tech.* 7:87-104.

Yoshikawa, M., H.Ishida, A. Ishitani, T. Murakami, S. Koizumi, T. Inuzuka. 1990. Study of crystallographic orientations in the diamond film on cubic boron-nitride using Raman microprobe. *Appl. Phys. Lett.* 57:428-431.

Yoshikawa, M., H. Ishida, A. Ishitani. 1991. Study of crystallographic orientations in the diamond film on the (100) surface of cubic boron nitride using a Raman microprobe. *Appl. Phys. Lett.* 58:1387-1388.

Yu, M., A. D. Bruck, L. G. Sodin. 1979. On the ambiguity of the image reconstruction problem. *Opt. Commun.* 30:304-308.

Yu, D. P., X. S. Sun, C. S. Lee, I. Bello, S. T. Bello, S. T. Lee, H. D. Gu, and K. Leung. 1998. Synthesis of boron nitride nanotubes by means of excimer laser ablation at high temperature. *Appl. Phys. Lett.* 72:1966-1968.

Yudasaka, M., R. Kikuchi, T. Matsui, Y. Ohki, S. Yoshimura. 1995. Specific conditions for Ni catalyzed carbon nanotube growth by chemical vapor deposition. *Appl. Phys. Lett.* 17:2477-2479.

Zaiser, M., F. Banhart. 1997. Radiation-induced transformation of graphite to diamond. *Phys. Rev. Lett.* 79:3680-3683.

Zangwill, A. 1988. *Physics at Surfaces*. Cambridge: Cambridge University Press.

Zeitler, M., S. Sienz, H. Neumann, M. Zeuner, J. W. Gerlach, B. Rauschenbach. 1998. In situ stress analysis of boron nitride films prepared by ion beam assisted deposition. *Nucl. Inst. Meth. Phys. Res. B*139:327-331.

Zeitler, M., S. Sienz, B. Rauschenbach. 1999. Study of stress evolution of boron nitride films prepared by ion assisted deposition. *J. Vac. Sci. Technol.* A 17:597-602.

Zettl, A. 1996. Non-carbon nanotubes. *Adv. Mater.* 8:443-445.

Zhang, F. Q., Y. P. Guo, Z. H. Song, and G.H. Chen. 1994. Deposition of high-quality cubic boron-nitride films of nickel substrates. *Appl. Phys. Lett.* 65:971.

Zhang, R. Q., J. L. Andujar, E. Bertran. 1997. Modeling interface structures of cubic boron nitride films deposited heteroepixially and via a hexagonal boron nitride interlayer on silicon (001) surface. *Diam. and Rel. Mat.* 6:589-593.

Zhang, Q., S. Yoan, J. Ahn, H. Yang. 1999. Study of hydrogenated diamond-like carbon films using x-ray reflectivity. *J. of Appl. Phys.* 86:289-296.

Zhou, X., G. P. Flecher, S. Chen. 1991. Closed-form expressions for neutron and x-ray reflection and transmission coefficients of a one-dimensional profile. *Physica B* 173:167-179.

Zhou, X., S. Chen. 1993. Model-independent method for reconstruction of scattering-length-density profiles using neutron or x-ray reflectivity data. *Phys. Rev. E* 47:3174-3190.

Zhou, W. L., Y. Ikuhara, and T. Suzuki. 1995. Orientational relationship between cubic boron nitride and hexagonal boron nitride in a thin film synthesized by ion plating. *Appl. Phys. Lett.* 67:3551-3553.

Zunger, A. 1974. A molecular calculation of electron properties of layered crystals: II. Periodic small cluster calculation for graphite and boron nitride. *J. Phys. C* 7:96.

Zunger, A., A. Katzir, and A. Halperin. 1976. Optical properties of heaxagonal boron nitride. *Phys. Rev. B* 13:5560.